## NOTICE

The quality of this microform is heavily dependent upon the quality of the original thesis submitted for microfilming. Every effort has been made to ensure the highest quality of reproduction possible.

If pages are missing, contact the university which granted the degree.

Some pages may have indistinct print especially if the original pages were typed with a poor typewriter ribbon or if the university sent us an inferior photocopy.

Reproduction in full or in part of this microform is governed by the Canadian Copyright Act, R.S.C. 1970, c. C 30, and subsequent amendments.

## AVIS

La qualité de cette microforme dépend grandement de la qualité de la thèse soumise au microfilmage. Nous avons tout fait pour assurer une qualité supérieure de reproduction.

S'il manque des pages, veuillez communiquer avec l'université qui a conféré le grade.

La qualité d'impression de certaines pages peut laisser à désirer, surtout si les pages originales ont été dactylographiées à l'aide d'un ruban usé ou si l'université nous a fait parvenir une photocopie de qualité inférieure.

La reproduction, même partielle, de cette microforme est soumise à la Loi canadienne sur le droit d'auteur, SRC 1970, c. C-30, et ses amendements subséquents.

# RECEIVING ANTENNAS FOR ELECTROMAGNETIC PULSES AND TRANSIENTS

by

Karunanayake P.A.P. Esselle

A thesis submitted to the
School of Graduate Studies and Research
in partial fulfillment of the requirements for the degree of

**DOCTOR OF PHILOSOPHY**

Ottawa-Carleton Institute for Electrical Engineering
Department of Electrical Engineering
Faculty of Engineering
University of Ottawa

ISBN 0-315-62312-8

UNIVERSITÉ D'OTTAWA
UNIVERSITY OF OTTAWA

# Abstract

The pulse receiving characteristics of several thin-wire antennas have been investigated in this thesis.

First, a loop antenna with a uniformly distributed impedance has been investigated, analytically, in the frequency domain. An equivalent circuit has been developed for the impedance-loaded loop antenna receiving an arbitrary steady-state electromagnetic field. The frequency- and time-domain receiving characteristics of a resistively loaded loop antenna have been obtained. It has been found that the loop antenna with a uniform distributed resistance has a broad receiving bandwidth. Nonetheless, the antenna is dispersive and is therefore not suitable for the reception of electromagnetic pulses or transients.

Second, pulse-receiving characteristics of resistively loaded straight dipole antennas have been investigated in the time domain. Frequency-domain receiving characteristics have been obtained using the Fast Fourier Transform method. Two types of resistively loaded straight dipole antenna designs have been considered. One design has a high distributed resistance and a low terminal resistance, and gives a broad bandwidth at the expense of the sensitivity. The other design has a low distributed resistance and a high terminal resistance. It does not sacrifice the sensitivity but requires an active high-impedance receiver circuit. It has been found that the Wu-King resistively loaded dipole has the maximally flat frequency response close to the upper roll-off frequency, when terminated with a high-impedance load.

Third, a time-domain stepping-in-time procedure has been developed for the analysis of unloaded and resistively loaded V-antennas. V-antennas with various terminations have

also been analyzed using the Numerical Electromagnetic Code. After identifying the limitations of resistively loaded straight and V-antennas in receiving fast pulses and transients, a passive compensation technique has been developed to significantly increase the upper frequency limit of the V-antenna. The new V-antenna consists of a resistively-loaded thin-wire V-dipole or monopole, a Response Equalizer Circuit and an oscilloscope probe (or other termination). For a given termination, the new antenna has a higher sensitivity and a much broader bandwidth compared with the Wu-King antenna. It is estimated to have a 3-dB bandwidth from 25 MHz to 10 GHz when used with a commercially available 500 Ω passive probe. The sensitivity is approximately 1 mV/(Vm$^{-1}$), taking into account the 20 dB attenuation of the probe. With a 50 Ω probe, this antenna has a 3-dB bandwidth from 110 MHz to 10 GHz, and a sensitivity better than 4 mV/(Vm$^{-1}$).

A V-antenna and a Wu-King monopole antenna have been fabricated using thin-film deposition technology. A time-domain antenna range has been built and used to measure the time-domain response of the experimental antennas. It has been found that the experimental V-antenna is capable of receiving a 520-ps approximately Gaussian pulse, without significant distortions. The frequency-domain receiving characteristics of the two antennas have been obtained using the Fast Fourier Transform method. The receiving response of the V-antenna has been measured in the frequency domain, using a TEM cell and network analyzers. The experimental thin-film V-antenna has a sensitivity of 1.12 mV/(Vm$^{-1}$) and a flat receiving response from 35 MHz to 3 GHz. It was not possible to measure the response beyond 3 GHz, due to limitations of the pulse generators available. The experimental thin-film Wu-King antenna has a sensitivity of 22 mV/(Vm$^{-1}$) and a upper roll-off frequency of about 300 MHz, which is limited by the bandwidth of the active receiver circuit.

# Acknowledgments

The author wishes to express his deepest gratitude to his supervisor Dr. S. S. Stuchly for his helpful advice, continuing guidance and encouragement throughout this work. Heartful thanks are also due to Dr. G. Costache, Dr. M. Stuchly and Dr. B. Syrett, for serving in the Thesis Advisory Committee and making valuable suggestions.

The author wishes to express his sincere thanks to Dr. M. Kanda and Mr. A. Ondrejka at the National Institute for Standards and Technology, Boulder, Colorado, for their hospitality, while visiting NIST.

The author extends his thanks to Dr. J. Chrostowski, Mr. M. Lee, Dr. A. Nyshadham, Mr. S. St-Andre and Dr. A. Thansandote for their help during the fabrication and testing of the experimental antennas. Special thanks are due to Dr. F. Cooray and Mr. C. Sibbald for reading the manuscript and making valuable comments and suggestions.

Heartfelt thanks are extended to all the staff members and graduate students of the Department of Electrical Engineering, University of Ottawa, who helped the author in numerous ways, in this research.

The author is grateful to the Canadian Commonwealth Scholarship Committee for its generous financial support during the course of this study.

# List of Symbols

| | |
|---|---|
| $c$ | velocity of light in free space |
| $f$ | frequency |
| $k$ | propagation constant in free space |
| $t$ | time |
| $\delta(x)$ | Dirac delta function |
| $\epsilon$ | permittivity of free space |
| $\lambda$ | wavelength |
| $\mu$ | permeability of free space |
| $\xi$ | intrinsic impedance of free space |
| $\tau$ | retarded time |
| $\omega$ | radian frequency |
| $\Gamma(x)$ | Gamma function |
| $\nabla$ | Del operator |
| $\partial$ | Partial derivation operator |
| $\Re(x)$ | Real part of a complex number |

# Contents

# List of Tables

# List of Figures

# Chapter 1

# INTRODUCTION

Even though some early experiments in electromagnetics were performed with pulse signals, more emphasis was placed later on time-harmonic electromagnetic fields and waves. The time-harmonic consideration significantly simplified the theoretical treatment of electromagnetic systems, eliminating the time-integral and time-differential operators in Maxwell's equations. On the practical side, very efficient sources and highly sensitive receivers were realized for the generation and detection of time-harmonic electromagnetic fields. Together with the development of efficient antennas for transmission and reception of such fields, complete and successful time-harmonic electromagnetic systems became a reality. Ideal time-harmonic signals, however, carry no information. When information is embedded in the signal in any form of modulation, the signal deviates from the ideal time-harmonic form. Practical time-harmonic systems operate with such quasi-time-harmonic signals having relatively narrow bandwidths.

In spite of the fact that systems and techniques based on quasi-time-harmonic signals are satisfactorily used in many electromagnetic applications, some electromagnetic phenomena are inherently non-time-harmonic and therefore should be treated differently. It is meaningless to measure very broadband electromagnetic fields generated by lightning, for example, using narrowband receiving systems designed for time-harmonic fields. Studies of pulse and transient electromagnetic fields, once left behind by the time-harmonic technology, are a

reality now, thanks to the recent advances in transient electromagnetic technology.

With the advent of short-pulse signal generators, interest has been growing in the exploitation of pulse electromagnetic fields in a wide spectrum of applications such as material measurements, radar, target identification, and remote sensing. Time-domain reflectometers and time-domain automatic network analyzers have been developed for the analysis of components and materials over a broad frequency range. Time-domain scattering analysis has several advantages over the conventional frequency-domain method. It does not need expensive anechoic chambers. Time-domain scattering data contains all the information over the frequency bandwidth of the excitation pulse. Frequency-domain parameters such as radar cross section can be obtained over this bandwidth, using numerical Fourier transformation techniques. Since the waveform of the scattered field is closely related to the target composition and geometry, it can be directly used for signature analysis and target identification. Time-domain scattering data can also be used to identify target scattering centers; an important step in the development of less-visible warfare and stealth technology. Experimental baseband (carrier-free) radar systems proved useful in a variety of applications ranging from automobile precollision sensors for airbag operation to airport ground traffic control systems [1]. Attempts have been made to identify the nature of the target by analyzing the return signal waveform of the baseband radar. Such sophisticated techniques have many potential applications in both civilian and military domains. One example is a baseband radar system developed for the detection and identification of metallic and non-metallic underground features such as buried utility lines, pipes, tunnels and mines [2].

Modern digital systems may be immune to low-power long-term interference such as noise, but they seem more vulnerable to high-power short-term interference due to transient electromagnetic fields. With the increasing popularity of digital systems in almost every field, including many safety-related and airborne applications, the electromagnetic compatibility (EMC) of electronic systems with transient radiation is becoming a critical issue. This raises the importance of characterizing unintentional transient electromagnetic radiation, and analyzing its influence on electronic systems.

## 1.1 Motivation

Many novel time-domain measurement techniques such as time-domain scattering measurements, transmission and reflection measurements of slabs, identification of debonding in multi-slab structures [3], and layer-peeling techniques [4], use *unguided* pulse electromagnetic fields. Some recently developed time-domain systems such as the baseband radar and target identification systems are also based on unguided pulsed fields [5]. For the full exploitation of their capabilities, one obviously needs good pulse-transmitting and pulse-receiving antennas. Good pulse-receiving antennas are also needed for the characterization of transient electromagnetic radiation from natural and man-made sources, such as lightning, electrostatic discharge (ESD) and nuclear electromagnetic pulse (NEMP).

Although pulse generators and receivers were considerably improved over the past two decades, antennas for pulse applications did not develop at the same rate. To be useful in pulse or transient applications, an antenna should not only have a broad bandwidth but also proper phase (precisely, time-delay) characteristics. This later condition excludes virtually all conventional broadband antennas designed for multi-frequency time-harmonic applications [6, 7]. When the pulse has a short rise time (transition duration), the antenna should respond without delay, *i.e.* it should be able operate at sufficiently high frequencies. When accurate measurements are to be made for an extended period of time, the antenna should also be able to operate at sufficiently low frequencies. These two requirements determine the antenna bandwidth for a given application.

The challenge of designing receiving antennas to operate at very low frequencies has been successfully dealt with recently. Electrically small dipole antennas terminated with high-impedance active circuits [8] and electrically small loop antennas terminated with low-impedance active circuits [9] allow measurements down to kilohertz or even lesser frequencies. At the other extreme, designing broadband antennas with short rise times still remains a challenge.

Some natural and man-made electromagnetic transients are suspected to have sub-nanosecond rise times. Many time-domain systems also need to operate with sub-nanosecond

pulses, either to extract broadband data or to achieve high spatial (or time) resolution. To work with such fast pulses and transients, one needs broadband receiving antennas operating up to 10 GHz or even higher frequencies. In the case of perfectly-conducting antennas such as spherical dipoles, conical dipoles and loops, the upper frequency limit is a fraction of the first resonant frequency of the antenna. Hence, such antennas are electrically small over the whole bandwidth of operation. These antennas are limited to receiving pulses and transients with rise times much longer than the antenna transit time. For sub-nanosecond operation, they have to be very small physically. In turn, they are less sensitive and difficult to fabricate.

The upper frequency limit of pulse-receiving antennas has been increased to several gigahertz, using resistive loading. Novel resistively loaded 'TEM' horns (with passive terminations) can operate up to 3 GHz [10]. Even these antennas may not be fast enough for some sub-nanosecond applications.

The need, and the lack of broadband antennas for the reception of sub-nanosecond electromagnetic pulses and transients have motivated this study.

## 1.2 Original Contributions

The primary objective of this study was to find a satisfactory solution to a practical problem of receiving sub-nanosecond electromagnetic pulses and transients. To this end, the thesis describes a novel antenna design based on a resistively loaded monopole and a passive compensation circuit, which is expected to have a 3-dB bandwidth better than 25 MHz- 10 GHz, and a sensitivity of 1 $mV/(Vm^{-1})$. This may be considered the major achievement and contribution of the thesis. The logical approach taken for the development of the new antenna is described in Chapter 5.

Other original contributions to the knowledge of pulse-receiving antennas are as follows:

- A loop antenna with uniform resistive loading is found broadband but dispersive. It may be useful for conventional multi-frequency applications but not for the reception of electromagnetic pulses and transients (Chapter 3).

- Considering resistively-loaded straight dipoles with high-impedance terminations (> 10 kΩ), the Wu-King distributed resistance is found to give the broadest ripple-free bandwidth. On the other hand, if the termination impedance is low (< 10 kΩ), a distributed resistance much higher than the Wu-King value is needed for broadband operation. In this mode of operation, the optimum distributed resistance is found as a compromise between the bandwidth and the sensitivity (Chapter 4).

Original contributions to the antenna analysis are as follows:

- An analytical frequency-domain solution is obtained to the problem of circular thin-wire loop antenna with uniform impedance loading. The receiving antenna problem is directly solved without using reciprocity, and therefore the solution is valid for arbitrary incident fields. An equivalent circuit is developed to describe the operation of the antenna. Theoretically obtained time-domain response of a resistively loaded loop antenna is presented for the first time in literature.

- A time-domain Method of Moments (stepping-in-time) solution is developed, using roof-top expansion functions, for the analysis of various resistively loaded and unloaded straight dipoles. To the best of author's knowledge, this is the first time-domain numerical analysis of the Wu-King resistively loaded dipole.

- A time-domain Method of Moments solution is developed, using roof-top expansion functions, for the analysis of resistively loaded and unloaded V-dipoles. Space-time distribution of current and charge in V-dipoles are presented for the first time. The resistively loaded V-dipole has never been analyzed in the time domain before.

## 1.3 Organization of the Thesis

In Chapter 2, the state of the art in pulse-transmitting and pulse-receiving antennas is reviewed. A summary of related work in antenna analysis is also included.

In Chapter 3, an analytical frequency-domain solution is obtained to the problem of the circular loop antenna with uniform impedance loading. An equivalent circuit is developed

to explain the receiving characteristics of the loop antenna. Frequency-domain receiving characteristics are presented for various values of distributed resistance, terminal resistance and several directions of the incident wave. Time-domain receiving responses of a resistively loaded loop antenna to monopolar and bipolar incident pulses are presented. The dispersion of the uniformly loaded loop antenna is explained using time delay characteristics.

In Chapter 4, the unloaded and resistively loaded straight dipole antennas are analyzed, directly in time-domain. Two different methods are used. A novel stepping-in-time procedure uses roof-top expansion functions to solve a time-domain integro-differential equation. The other method is to solve a Hallen-type time-domain integral equation, using Liu algorithm. Frequency-domain receiving characteristics of the straight dipoles are obtained using Fast Fourier Transform techniques. Emphasis is made on two different types of designs: (1) using a low distributed resistance (given by Wu-King expression) and high terminal resistance, (2) using a high distributed resistance and low terminal resistance.

In chapter 5, a time-domain stepping-in-time procedure is developed for the analysis of unloaded and resistively loaded V-antennas. Loaded and unloaded V-antennas with various terminations are also analyzed using the Numerical Electromagnetic Code. Frequency- and time-domain characteristics of V-antennas are presented. After identifying the limitations of resistively loaded straight and V-dipoles in receiving fast pulses and transients, a novel passive compensation technique is developed to significantly increase the upper frequency limit of the V-dipole.

Preliminary experimental results obtained with two prototype resistively loaded antennas are presented in Chapter 6. One is a V-monopole antenna terminated with a commercially-available 500 $\Omega$ oscilloscope probe (Tektronix P6510). Other is a Wu-King monopole antenna terminated with a high-impedance electronic circuit. The two antennas have been tested in a time-domain antenna range. Frequency-domain receiving characteristics have been obtained using the Fast Fourier Transform method. The V-monopole antenna has also been tested directly in the frequency domain, using a TEM cell and network analyzers.

A general discussion of this study is presented in Chapter 7. Possible improvements in

pulse-receiving antennas and in time-domain analysis techniques are also suggested.

# Chapter 2

# A REVIEW

## 2.1 Antennas for Pulse Applications

Some of the antennas designed for pulse applications are reviewed in this section. A few antennas described here work well only within a time interval and, hence, are useful only in pulse applications. Others can be used with time-harmonic signals as well.

### 2.1.1 Conical Antenna

The *infinite* conical antenna has an interesting geometry defined only by the angles. Hence, even if the antenna is scaled, it remains unchanged. Consequently, the input impedance and the electromagnetic field produced by the infinite conical antenna are frequency-independent. A *finite* conical antenna has a significantly different behavior under time-harmonic excitation. However, when a finite antenna is excited by a short pulse, the antenna behaves similarly to an infinite antenna, during a time interval determined by the dimensions of the antenna. Therefore, the finite conical antenna can be used as an ideal pulse transmitter, within a finite time window.

Many different forms of conical antennas have been described in the literature. Finite and infinite circular biconical antennas were analyzed by Schelkunoff and Friis [11]. Carrel

derived an expression for the input impedance of an infinite biconical antenna with arbitrary cross section [12]. The input impedance of the antenna was found to be real and frequency-independent. The symmetric and asymmetric circular biconical antennas, the biased (non-coaxial, inclined) circular biconical antenna and the coplanar and non-coplanar fin antenna were also treated as special cases. Frequency-domain expressions for the electromagnetic field from finite conical antennas were derived by Wait [13]. Dielectric loaded conical antennas were also considered. Pulse transmitting and receiving characteristics of the finite circular conical antenna were analyzed by Harrison and Williams [14]. It was found that, if the source impedance was matched to the antenna 'characteristic' impedance, a voltage pulse could be transmitted without distortion, within a time-window.

Foltz and Davis recently analyzed the input impedance of the infinite conical antenna with elliptic cross section [15]. The circular biconical antenna and the planar fin antenna (bow-tie) were also considered as special cases. Blume and Grafmüller used a mode matching technique to analyze the finite biconical antenna with elliptic cross section [16]. Far field of the finite asymmetrical circular biconical antenna was analyzed by Nagasawa and Matsuzuka [17]. Maloney *et. al.* analyzed the conical antenna using the Finite-Difference Time-domain technique [18].

The input impedance of an infinite circular monocone antenna is given by [17]

$$Z_c = \frac{\xi}{2\pi} \ln\left(\cot\frac{\theta_o}{2}\right) \tag{1}$$

where $\theta_o$ is the half-cone angle of the antenna. The electric field $E_\theta$ and the magnetic field $H_\phi$, at a distance $r$ from the apex and at an elevation angle $\theta$, is related to the input voltage $V_o$ by [17]

$$E_\theta(r,\theta,\omega) = \frac{V_o e^{-jkr}}{r\sin\theta \ln\left(\cot\frac{\theta_o}{2}\right)} \tag{2}$$

$$H_\phi(r,\theta,\omega) = \frac{E_\theta(r,\theta,\omega)}{\xi}. \tag{3}$$

In the time domain,

$$e_\theta(r,\theta,t) = \frac{v_o\left(t-\frac{r}{c}\right)}{r\sin\theta \ln\left(\cot\frac{\theta_o}{2}\right)} \tag{4}$$

$$h_\phi(r,\theta,t) = \frac{e_\theta(r,\theta,t)}{\xi}. \quad (5)$$

The circular conical antenna is omni-directional. The directivity of the antenna can be improved by slanting it (biasing). An alternative to the biased conical antenna, called the V-conical antenna, was recently proposed by Shen *et. al.* [19]. It is not only directive but also much easier to fabricate when compared with the biased conical antenna. The V-conical antenna is composed of two identical triangular sheets wrapped around a conical surface. Half of the antenna (with only one sheet) can be used in ground plane applications. As the V-conical antenna is completely described by only three angles, its input impedance and the fields are frequency-independent. Symmetrical and asymmetrical V-conical antennas and the triangular plate antenna were analyzed using a conformal mapping technique [19]. Due to the higher directivity, a stronger electromagnetic field can be obtained with the V-conical antenna when compared with the regular conical antenna.

In some applications, measurements are terminated before the reflection from the end of the finite conical antenna reaches the receiving antenna. Attempts have been made to minimize these reflections by burying the end of the conical antenna in electromagnetic absorbers [20].

### 2.1.2 Coaxial Horn Antenna

A coaxial horn antenna is commonly used as the receiving antenna in time-domain scattering ranges. Although not implied by the name, it is essentially an annular aperture on a ground plane, matched to a regular coaxial line using a tapered (conical) coaxial line section.

The coaxial horn antenna does not reproduce the incident electric field waveform at the output. In contrast, its output signal is approximately proportional to the time derivative of the incident pulse. This property has been exploited in time-domain scattering ranges to measure impulse response of scatterers. The scatterer is illuminated with a *step* incident field and the output of the coaxial horn antenna is taken as the *impulse* response.

Lamensdrof analyzed the transient response of the coaxial horn antenna, assuming a TEM field distribution at the aperture [21]. Since higher order modes are neglected in

this analysis, it is only valid for wavelengths much longer than the aperture dimension. Measurements have shown that the signal is distorted if this condition is not met. A constant characteristic impedance, usually 50 Ω, is maintained along the tapered section. This requires a constant radii ratio at every cross section. A larger aperture produces a stronger output signal at the expense of bandwidth. Low sensitivity is the major disadvantage of the coaxial horn antenna.

### 2.1.3 TEM Horn Antenna

The TEM horn antenna is one of the few electrically large antennas used for pulse reception. Several different forms of TEM horns have been described in the literature. Kanda analyzed a TEM antenna composed of two triangular conducting plates [22, 23]. This antenna can be approximated by a constant-impedance TEM transmission line if the aperture is much smaller than the wavelength and, hence, it is called the TEM horn. A distributed resistive loading was applied to smooth out the ripples in the frequency response of the perfectly conducting TEM horn [24].

A TEM horn with a tapered characteristic impedance was also considered [25, 26]. This antenna is the result of an attempt to 'match' a transmission line carrying a TEM wave to the unguided free-space. The width of each conducting plate varies along the length of the horn, forming an optimum impedance matching section. Input-end impedance of the matching section (horn) is equal to the characteristic impedance of the input transmission line, whereas the open-end impedance is rather arbitrarily chosen to be equal to the intrinsic impedance of free space. Possible reflections at the open end are further reduced by attaching resistive pads to the end of each plate.

The lately developed TEM horns have a constant-impedance perfectly conducting horn section and a resistively loaded parallel plate section [10]. The conducting horn generates the induced voltage (in the receiving mode) and the parallel plate section attenuates the reflections from the open ends. Lumped resistors are used to load the parallel plates. Very good receiving fidelity has been achieved with these TEM horns. The lower roll-off frequency of the TEM horn antenna was further reduced, using a high-impedance electronic circuit

connected to the horn output.

### 2.1.4 Loaded and Unloaded Dipoles

A perfectly conducting straight dipole excited by a time-harmonic voltage source exhibits a standing wave current pattern. Wu and King have shown that when such a dipole is loaded with a distributed (internal) impedance of proper value, the current forms an outward-traveling wave [27, 28]. The required distributed impedance varies along the length of the dipole and reaches infinity at the ends. It is determined by the dipole length, radius and the excitation frequency. It has been shown that the necessary distributed reactance is much smaller when compared with the distributed resistance provided that the dipole is electrically short [29]. Although an accurate implementation of the Wu-King (WK) nonreflecting dipole should have a distributed resistance as well as a reactance, for all practical purposes, it can be approximated by a resistively loaded dipole (*i.e.* a dipole with a distributed resistance).

Travelling-wave antennas such as rhombic antennas are known to have broad bandwidths [30]. Hence, the WK dipole was considered for broadband time-domain and frequency-domain applications. The WK dipole and other resistively loaded dipoles were analytically investigated by Sengupta and Liu [31]. Several numerical investigations have also been done in the frequency domain [32]. Kanda investigated the WK dipole and the corresponding monopole, both experimentally and theoretically [22, 33, 34]. A broad receiving bandwidth can be achieved by terminating the WK dipole with a high-impedance load. Kanda and Driver have successfully realized a broadband isotropic antenna based on the WK dipole [35]. However, this design uses a diode detector at the dipole terminals, and hence, is limited to the measurement of time-harmonic electromagnetic fields. For the measurement of pulse and transient electromagnetic fields, the WK dipole was coupled to a high-impedance electro-optic modulator [36, 37]. Capacitive loading of the straight thin-wire dipole was also considered [29].

Vollmer and Hinken described a tapered wire antenna, designed to have a constant gain over a broad bandwidth [38]. The profile (shape) of a perfectly conducting antenna was

synthesized first. Then, a resistive loading was applied close to the open end, in order to further reduce reflections. The final structure was analyzed using the method of moments. An experimental antenna had less than 8 dB gain variation in the frequency range from 1 GHz to 18 GHz.

Recently, a new class of pulse-receiving antennas was described by Shen *et. al.* [39]. The L-antenna and the V-antenna are simple thin-wire perfectly conducting monopoles, having the shapes of the letters 'L' and 'V', respectively. These antennas can be used to measure very fast electromagnetic pulses, within a time-window. The time-window is limited by the reflections from the open end. The V-antenna was found to have the best sensitivity. However, the very short time-window of this V-antenna may make it unsuitable for many practical applications. A simple calculation shows that the 82 mm V-antenna with 30° wedge angle, described in [39], has only a 37 ps distortion-free time-window. The time-window of the L-antenna can be increased by extending the 'tail' of the antenna. However, fairly long antennas are needed for measurements extending to several nanoseconds (approximately 15 cm length per ns).

### 2.1.5 Electrically Small Dipoles and Loops

Electrically small dipoles and loops have been widely used as electric and magnetic field sensors (receiving antennas) in frequency-domain applications. The advantages of such sensors are the simple relationship between the receiving transfer function and the geometry, and the small size. Baum and others have developed a wide collection of electrically-small sensors for time-domain applications [40]. These include dipole-type sensors for electric fields and loop-type sensors for magnetic fields, operating in both proportional (E-sensors and H-sensors) and differentiating ($\dot{\text{D}}$-sensors and $\dot{\text{B}}$-sensors) modes.

Electrically small perfectly conducting dipole-type antenna of any geometry can be represented by a frequency-independent vector effective height $\vec{l}_{e,eq}$ and a capacitance $C$ [40, 41]. The receiving mode equivalent circuit for such a dipole is shown in Figure 1(a), where $\vec{E}_{inc}$ is the incident electric field vector and $R$ is the load resistance. The received

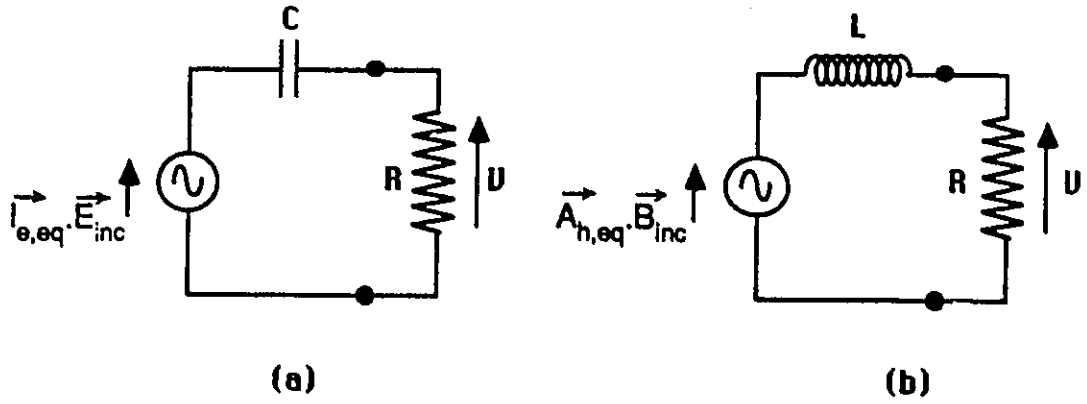


Figure 1: Equivalent circuits for electrically small antennas. (a) dipole, (b) loop.

voltage is simply given by

$$V = \left(\frac{R}{R + \frac{1}{j\omega C}}\right) \vec{l_{e,eq}}.\vec{E_{inc}}. \tag{6}$$

It is quite clear from this expression that: (1) for $\omega \ll \frac{1}{RC}$, the received signal represents the derivative of the incident electric field pulse; (2) for $\omega \gg \frac{1}{RC}$, the received signal reproduces the incident pulse. Different dipole-type geometries have been attempted to improve the bandwidth of each mode by increasing or decreasing the capacitance. Differentiating sensors such as asymptotic conical dipoles operating up to frequencies as high as 7.5 GHz have been reported [40, 42]. The parallel-plate dipole has a larger capacitance and therefore a broader proportional-mode bandwidth [43, 44].

Electrically small loops of any shape can similarly be represented by a frequency-independent vector equivalent area $\vec{A_{h,eq}}$ and an inductance $L$. Figure 1(b) shows the receiving mode equivalent circuit of such a loop, where $\vec{B_{in}}$ is the incident magnetic flux density vector. The received voltage waveform is similar to: (1) the derivative of the magnetic field waveform when $\omega \ll \frac{R}{L}$; (2) the magnetic field waveform itself when $\omega \gg \frac{R}{L}$. Sensors with various geometries have been realized to operate in both of these modes [40].

The new generation of electrically small antennas uses active electronic or optical circuits in order to reduce the lower frequency limit of the proportional-mode bandwidth. In the case of dipoles, the circuit should have a very high input impedance. This has been achieved by using commercially available high-impedance oscilloscope probes, FET source followers or electro-optical modulators [8, 45]. Thansandote *et. al.* reported a 5.6 cm diameter spherical antenna with a 3dB bandwidth from 60 Hz to 140 MHz and a sensitivity of 0.4 $mV/(Vm^{-1})$ [46]. In the case of loops, one needs an active circuit with a very low input impedance. This was achieved using a combination of a ferrite impedance transformer and a current follower circuit. Stuchly *et. al.* reported a loop antenna with a 3-dB bandwidth from 5 kHz to 100 MHz and a sensitivity better than 1 $mV/(Am^{-1})$ [9].

## 2.2 Antenna Transient Analysis

Theoretical analysis of antenna transients has been an interesting subject for more than two decades. This section summarizes some mathematical tools available for this task and their application to some specific antenna problems.

At present, analytical time-domain solutions are available only for a very few antenna problems. Few more antenna problems have analytical solutions only in the frequency domain, allowing numerical (Fourier inverse) transformation to the time domain. The vast majority of antenna geometries does not have analytical solutions. They are usually treated in one of the following three ways: (1) Numerical analysis in the frequency domain followed by numerical inverse Fourier transformation to the time domain, (2) Numerical analysis directly in the time domain, (3) Numerical analysis in the complex-frequency domain using the singularity expansion method (SEM) followed by inverse Laplace transformation to the time domain.

### 2.2.1 Analytical Solutions

It is widely accepted that an analytical solution provides physical insight and therefore is more valuable than a numerical solution. It is equally true that most problems in nature

(and their mathematical models) are so complicated that analytical solutions are almost impossible without many simplifications. Transient antenna analysis is no exception. For the sake of understanding the transient behavior of some basic antennas, many approximate investigations have been reported in the literature.

The transient response of a perfectly conducting straight dipole is characterized by two processes: (1) Propagation of a current pulse along the dipole, (2) Reflection of the current pulse at the driving point and at the two ends. Accurate numerical solutions and experimental results suggest that the current pulse undergoes both attenuation (drop of peak value) and dispersion (increase of pulse width) during the propagation along the dipole. In an approximate analysis, however, both of these effects are usually neglected. In other words, all frequency components are assumed to be propagating with the same velocity without any attenuation, as in a lossless transmission line.

King and Schmitt investigated the transient response of the straight dipole antenna, analytically [47]. Approximate expressions were derived for the reflection coefficient at the driving point and the radiated electromagnetic field. Many investigators either assumed a perfect reflection of the current pulse at the ends, or used an experimentally determined approximate reflection coefficient [48, 49]. Franceschetti and Papas analyzed the transient response of several radiating elements [50]. Using the analogy between a straight dipole and an open-ended lossless transmission line, they derived an approximate expression for the impulse response of the dipole.

Attempts have been made to account for the attenuation of the current pulse during propagation. The attenuation function was determined experimentally. This technique gave good results when applied to the rhombic wire antenna [51, 52]. The transmission line concept has been extended for the analysis of coupled straight dipoles and V-dipoles [53, 54].

Recently, Chen analyzed the ideal travelling wave antenna [55]. Expressions for the electromagnetic field at an arbitrary point were derived by inverse transforming frequency-domain expressions. Similar expressions were derived, directly in the time domain, by Zhan and Qin [56]. Fang and Wenbing also derived somewhat different expressions for the electromagnetic field from a travelling wave antenna [57]. They also considered the effect

of the first reflection from the open end.

Ross analyzed the pulse-receiving response of the straight dipole [58]. The large-current radiator was analyzed in time-domain, assuming a uniform current distribution on the radiating sheet [59, 60, 61].

Rigorous analytical solutions were obtained for the infinite perfectly conducting straight dipole, excited by a unit step voltage pulse [62]-[66]. Franceschetti derived expressions for the time-domain electromagnetic field from a spherical antenna [67]. Early time response of the spherical antenna was also investigated by Kotulski [68].

### 2.2.2 Numerical Solutions

The process of numerically solving a general antenna or scattering problem, in the frequency domain, normally involves two steps: (1) formulation of an integral equation, (2) solving the integral equation. The widely used integral equations are: the electric field integral equation (EFIE), the magnetic field integral equation (MFIE) and the hybrid field integral equation (HFIE). The EFIE is commonly used for thin wire structures. The integral equation is solved using the method of moments (MOM). This procedure is very well documented in the literature [69, 70].

Time-domain versions of the EFIE and MFIE can be derived from Maxwell's time-domain equations [71]. They can also be found by inverse transforming the corresponding frequency-domain equations [69]. As in the case of its frequency-domain counterpart, the time-domain MFIE is more suitable for smooth three dimensional surfaces. The kernel of the MFIE is less singular and therefore its numerical representation requires less sophisticated expansion functions. On the other hand, thin-wire and thin-sheet structures and bodies with edges are invariably treated with the EFIE, due to the instability of the MFIE when applied to such problems.

Some basic antennas such as dipoles and loops are essentially thin-wire structures. Even surface antennas can be conveniently approximated using thin-wire grids. Due to these reasons and the obvious simplicity (when compared with the surface antenna analysis), thin-wire antenna analysis plays a major role in the literature. The common assumptions made

in the thin-wire analysis are: (1) current is parallel to the axis; (2) current is concentrated at the axis as a filament. These assumptions are valid only if the wire radius is sufficiently shorter than the pulse width and the wire length. The unknown current is then a scalar function of only one variable: the distance along the wire axis.

Several different EFIEs specialized for thin-wire structures have been reported. One equation derived by Auckenthaler and Bennet does not involve time or spatial derivatives with respect to source coordinates [72]. Miller *et. al.* described an integral equation which is valid for both straight and curved wires [73]-[76]. All the derivatives in this integral equation are evaluated with respect to source coordinates. Poggio also reported an alternate equation which reduced to a derivative-free form when applied to straight wires [77, 78, 79].

The development of MOM time-stepping algorithms to solve time-domain integral equations is well explained in the literature [73]. Alternatively, the conjugate gradient method (CGM) can be used to solve these integral equations [80, 81]. In CGM, the solution is allowed to converge to a specific level at each time step, by iteration. Hence, a more accurate solution can be expected, with a small additional computing overhead.

The singularity expansion method (SEM) has been used for the analysis of antennas and scatterers in the complex-frequency ($s$) domain [82]-[86]. The solution obtained by SEM in the s-domain is often simple enough to allow direct transformation to the time domain. In the SEM, the unknown response is expanded in terms of known natural modes of the system. It can be shown that the response of a finite-size perfectly conducting object in free space can be expressed as [84]

$$\vec{J}(\vec{x},s) = \sum_{\alpha} \frac{\eta_\alpha(s)\vec{\nu}_\alpha(\vec{x})}{(s-s_\alpha)^{m_\alpha}} + \vec{W}(\vec{x},s) \tag{7}$$

where $s_\alpha$ is a natural frequency (pole) of order $m_\alpha$, $\nu_\alpha(\vec{x})$ is the corresponding natural mode, $\eta_\alpha(s)$ is the corresponding coupling coefficient and $\vec{W}(\vec{x},s)$ is an entire function to be added for completeness. The natural frequencies are the values of $s$ for which the system can have a response even without an excitation. The corresponding response is a natural mode.

Some simple geometries allow analytical determination of natural frequencies and modes,

at least approximately. For more complicated geometries common to antennas and scatterers, these can be found numerically, by solving an eigenvalue problem. Since both natural frequencies and natural modes are related to the source-free problem, they are independent of the excitation. Only the coupling coefficients and the entire function depend on the excitation.

The SEM is efficient in computing the late-time response of antennas and scatterers. Direct time domain techniques are more suitable for the calculation of early-time response.

# Chapter 3

# THE CIRCULAR LOOP

## 3.1 Introduction

The perfectly conducting loop has been considered as one of the fundamental antennas. For decades, it has been widely used in UHF receivers and magnetic-field sensors. The theoretical analysis of the loop antenna also has a long history. The thin-wire loop of the circular shape was theoretically attractive, mainly because this geometry leads to an analytical solution for the antenna problem. Wu analyzed the perfectly conducting circular loop antenna excited by a delta-function (in space) time-harmonic voltage source using the Fourier Series Expansion Method, and obtained closed-form expressions for the loop current and input admittance [87]. King and Prasad simplified these expressions for electrically small loops [88]. They also derived expressions for the electromagnetic field radiated by electrically small circular loops.

In many conventional applications, loop antennas are operated either at resonance or below resonance and they usually have terminations between 50 Ω and 300 Ω. This mode of operation is inherently narrowband for two reasons: the resonance of the loop and the finite resistance of the termination. It has been known that by decreasing the terminal resistance, it is possible to increase the receiving bandwidth of the loop antenna. However, this concept was not exploited until recently [9]. Even loops with such 'light' terminations

are subjected to natural resonance at higher frequencies, and therefore their use is limited to the frequencies where the loop is electrically small.

It can be expected that a distributed resistance applied to the loop would dampen the resonance and therefore extend the receiving bandwidth to higher frequencies. Circular loops loaded with a distributed resistance, or more generally a distributed impedance, have been analyzed by several investigators. Blackburn and Wilton used the Singularity Expansion Method for the analysis of the loop antenna with a uniformly distributed impedance [89]. Although they did not attempt to calculate the receiving characteristics or the bandwidth of the antenna, their approach explained the behavior of the system poles when the distributed load is varied. Kanda approximated the distributed resistance by a series of lumped loads and combined the theories of the perfectly conducting antenna and multi-port networks to calculate the receiving characteristics of the uniformly-loaded loop antenna [90, 91]. Alternatively, the loop antenna with a distributed load can be analyzed using a numerical method such as the Method of Moments [92]. In this chapter, a closed-form analytical solution is obtained for the thin-wire circular loop antenna with a uniformly distributed impedance [93, 94].

The integral equation for the current in a uniformly-loaded loop is derived in the next section. In Section 3.3, the analytical solution of the integral equation is obtained using the Fourier Series Expansion Method. An equivalent circuit is developed for the loaded loop antenna. Numerical results describing the frequency- and time-domain receiving characteristics of the loop antenna, obtained from a new Fortran code called LLOOP, are presented in Section 3.4. Some results obtained from the LLOOP code are compared with the results obtained from the Numerical Electromagnetic Code (NEC) [95]. The chapter is completed with a brief discussion in Section 3.5.

## 3.2 The Integral Equation

Consider the circular loop shown in Figure 2. The wire radius is denoted by $a$ and the loop

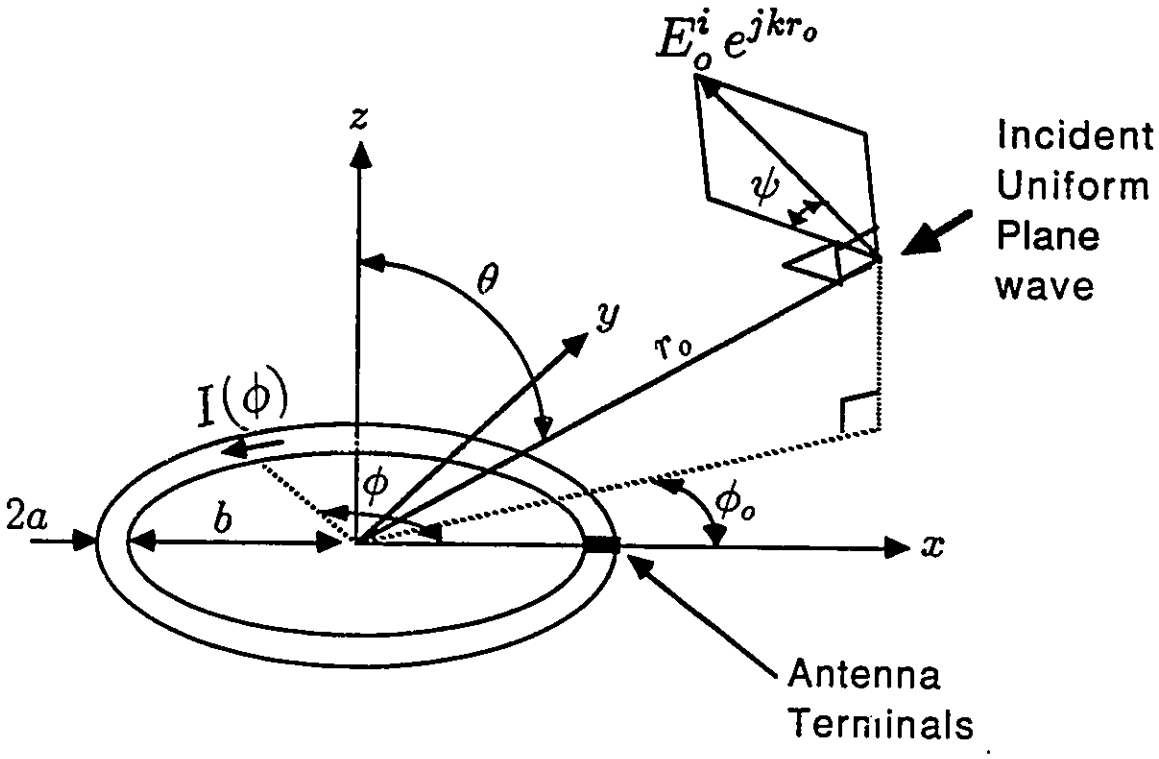


Figure 2: Geometry of the circular loop antenna.

radius is denoted by $b$. Assume that the loop is physically and electrically thin, *i.e.*,

$$a \ll b \tag{8}$$

and

$$ka \ll 1 \tag{9}$$

where $k$ is the free-space propagation constant. The loop current at the position $\phi = \phi'$ is, say, $I(\phi')$. The electromagnetic field produced by the loop current, commonly known as the scattered field, can be determined using the scalar electric potential $\Psi$, and vector magnetic potential $\vec{A}$, as follows. Since the scattered electric field is given by

$$\vec{E}^s = -\nabla\Psi - j\omega\vec{A}, \tag{10}$$

the component of the scattered electric field tangential to the loop surface, $E^s_\phi$, is found as

$$E^s_\phi = -\frac{1}{b}\frac{\partial\Psi}{\partial\phi} - j\omega A_\phi. \tag{11}$$

It has been shown that in the case of the circular loop, $\Psi$ and $A_\phi$ are related to the loop current by the expressions [88]:

$$\Psi = -\frac{1}{4\pi b j\omega\epsilon}\int_{-\pi}^{\pi}\frac{\partial I(\phi')}{\partial\phi'}W(\phi-\phi')d\phi' \tag{12}$$

$$A_\phi = \frac{\mu}{4\pi}\int_{-\pi}^{\pi} I(\phi')W(\phi-\phi')\cos(\phi-\phi')d\phi' \tag{13}$$

where the kernel $W(\alpha)$ may be approximated by

$$W(\alpha) = \frac{b}{2\pi}\int_{-\pi}^{\pi}\frac{e^{-jkr}}{r}d\theta \tag{14}$$

with

$$r = 2\sqrt{a^2\sin^2(\theta/2) + b^2\sin^2(\alpha/2)}. \tag{15}$$

Substitution of these expressions into (11) results in the following expression for $E^s_\phi$:

$$E^s_\phi = -\frac{j\xi}{4\pi b}\int_{-\pi}^{\pi} L(\phi-\phi')I(\phi')d\phi' \tag{16}$$

where the new kernel is given by

$$L(\phi-\phi') = [kb\cos(\phi-\phi') + \frac{1}{kb}\frac{\partial^2}{\partial\phi^2}]\frac{b}{2\pi}\int_{-\pi}^{\pi}\frac{e^{-jkr}}{r}d\theta \tag{17}$$

and $\xi$ is the intrinsic impedance of free space.

Since the wire is electrically thin, one can assume that at a given cross section the loop current is uniformly distributed over the wire periphery. Therefore, the current density at $\phi$ is given by

$$J(\phi) = \frac{I(\phi)}{2\pi a}. \tag{18}$$

Let the surface impedance of the wire be constant along the length and equal to $Z_s$. This surface impedance may be due to the skin effect in the case of a loop with good conductivity or it may be due to the thin resistive coating in the case of a resistively loaded loop. The tangential component of the *total* electric field is then related to the current density according to

$$E_\phi^t(\phi) = Z_s J(\phi). \tag{19}$$

Substituting $J(\phi)$ from (18), one obtains

$$E_\phi^t(\phi) = \frac{Z_s}{2\pi a}I(\phi). \tag{20}$$

We may now define the internal impedance of the wire as

$$Z_i = \frac{Z_s}{2\pi a} \tag{21}$$

and the *total* distributed impedance as

$$Z_T = 2\pi b Z_i \tag{22}$$

and hence obtain the following expressions for the total field:

$$E_\phi^t(\phi) = Z_i I(\phi) \tag{23}$$

$$= \frac{Z_T}{2\pi b}I(\phi). \tag{24}$$

The total electric field is the sum of the scattered and applied fields:

$$E_\phi^t(\phi) = E_\phi^s(\phi) + E_\phi^a(\phi) \tag{25}$$

where $E_\phi^a(\phi)$ is the component of the applied electric field tangential to the wire surface. The applied field may be due to sources connected to the antenna terminals or electromagnetic fields incident on the antenna. To be more general, assume that a zero-impedance source with voltage $V_s$ is connected to the terminals located at $\phi = 0$ and at the same time, the antenna is also excited by an incident electromagnetic field. Let the incident field have a tangential electric field of $E_\phi^i(\phi)$. The tangential electric field produced by the Dirac function voltage source can be expressed as

$$E_\phi^v(\phi) = \frac{V_s \delta(\phi)}{b} \tag{26}$$

and therefore

$$E_\phi^a(\phi) = \frac{V_s}{b}\delta(\phi) + E_\phi^i(\phi). \tag{27}$$

Combining expressions (16),(24),(25) and (27), one finally obtains the following frequency-domain integral equation for the impedance-loaded circular loop antenna:

$$V_s\delta(\phi) + bE_\phi^i(\phi) = \frac{j\xi}{4\pi}\int_{-\pi}^{\pi} L(\phi-\phi')I(\phi')d\phi' + \frac{Z_T}{2\pi}I(\phi) \tag{28}$$

This is clearly a generalization of the integral equations published previously [87, 89].

## 3.3 The Analytical Solution

The integral equation for the uniformly loaded circular loop antenna (28) can be solved, analytically, by extending the Fourier Series Expansion Method (FSEM) used in [88]. First, the kernel is expanded in a Fourier series:

$$L(\phi-\phi') = \sum_{n=-\infty}^{\infty} a_n e^{-jn(\phi-\phi')} \tag{29}$$

where the Fourier coefficients $a_n$ are given by

$$a_n = \frac{1}{2\pi}\int_{-\pi}^{\pi} L(\phi)e^{jn\phi}d\phi. \tag{30}$$

The source field and the incident field terms are also expanded as

$$V_s\delta(\phi) = \frac{V_s}{2\pi}\sum_{n=-\infty}^{\infty} e^{-jn\phi}, \tag{31}$$

$$E^i_\phi(\phi) = E^i_o \sum_{n=-\infty}^{\infty} f_n e^{-jn\phi} \tag{32}$$

where

$$f_n = \frac{1}{2\pi E^i_o}\int_{-\pi}^{\pi} E^i_\phi(\phi)e^{jn\phi}d\phi \tag{33}$$

and $E^i_o$ is the electric field at the center of the loop.

Finally, the unknown current is expanded in a Fourier series as

$$I(\phi) = \sum_{n=-\infty}^{\infty} I_n e^{-jn\phi}. \tag{34}$$

At this point, the similarity between the FSEM and the Method of Moments (MOM) is apparent. The only difference between the MOM and the FSEM is that, in the latter, not only the unknown response function but also the kernel and the known excitation functions are expanded using complex exponentials.

Consider the integrand in (28). Substituting for $L(\phi-\phi')$ and $I(\phi)$ from (29) and (34), respectively, and exploiting the orthogonal property of complex exponential functions, i.e.

$$\int_{-\pi}^{\pi}[e^{jm\phi}.e^{-jn\phi}]d\phi = \begin{cases} 2\pi, & m = n \\ 0, & m \neq n \end{cases} \tag{35}$$

one can simplify this term as follows:

$$\begin{aligned} &\int_{-\pi}^{\pi} L(\phi-\phi')I(\phi')d\phi' \\ &= \int_{-\pi}^{\pi}[\sum_{m=-\infty}^{\infty} a_m e^{-jm(\phi-\phi')}][\sum_{n=-\infty}^{\infty} I_n e^{-jn\phi'}]d\phi' \\ &= \sum_{m=-\infty}^{\infty}\sum_{n=-\infty}^{\infty} a_m e^{-jm\phi} I_n \int_{-\pi}^{\pi}[e^{jm\phi'}.e^{-jn\phi'}]d\phi' \\ &= 2\pi\sum_{m=-\infty}^{\infty} a_m I_m e^{-jm\phi} \end{aligned} \tag{36}$$

Expressions (31),(32),(34) and (36) are now substituted in the integral equation (28). The results is

$$\frac{V_s}{2\pi}\sum_{m=-\infty}^{\infty} e^{-jm\phi} + bE_o^i \sum_{m=-\infty}^{\infty} f_m e^{-jm\phi} = \frac{j\xi}{2}\sum_{m=-\infty}^{\infty} a_m I_m e^{-jm\phi} + \frac{Z_T}{2\pi}\sum_{m=-\infty}^{\infty} I_m e^{-jm\phi}. \tag{37}$$

Finally, this is multiplied by $e^{jn\phi}$ and integrated over the range of $\phi$ from $-\pi$ to $\pi$. This is equivalent to the 'testing' in the MOM. Due to the orthogonal property given in (35), it is now possible to obtain the following *analytical* solution for $I_n$:

$$I_n = \frac{V_s + 2\pi b f_n E_o^i}{Z_T + j\pi\xi a_n}. \tag{38}$$

Substitution of this expression for $I_n$ into (34) yields the solution for the loop current $I(\phi)$.

In terms of the MOM, the particular expansion and testing used leads to a *diagonal* 'impedance matrix' of infinite order. Because of this diagonality, analytical inversion of the matrix, and therefore the analytical solution for the unknown, was possible.

When the loop antenna is transmitting, $E_o^i = 0$. The input admittance of the antenna is therefore given by

$$Y = \frac{I(\phi = 0)}{V_s} = \sum_{n=-\infty}^{\infty} \frac{1}{Z_T + j\pi\xi a_n}. \tag{39}$$

In the receiving mode, $V_s = 0$. Assuming that the receiving antenna is terminated with a zero impedance load, the terminal current (usually known as the short circuit current) is found from (34) and (38) as

$$I_{sc} = I(\phi = 0) = \sum_{n=-\infty}^{\infty} \frac{2\pi b f_n E_o^i}{Z_T + j\pi\xi a_n}. \tag{40}$$

In the general receiving case where the terminal load is not zero but a finite impedance $Z_L$, the terminal current can be found using the Norton equivalent theorem, as

$$I_L = \frac{I_{sc}}{Z_L Y + 1}. \tag{41}$$

At this point, it is necessary to define a parameter to represent the frequency-domain receiving characteristics of the antenna. A dimensionless parameter is more convenient when

the antenna is scaled. The normalized receiving transfer function $R$ of the loop antenna is therefore defined as

$$R = \frac{I_L \xi}{2bE_o^i}. \tag{42}$$

The magnitude of $R$ defines the "sensitivity" of the loop antenna for incident steady-state electromagnetic fields whereas its argument represents the phase delay. The normalized receiving transfer function of the impedance-loaded loop antenna is obtained by combining expressions (39)-(42) as,

$$R = \frac{\sum_{n=-\infty}^{\infty} (\pi \xi f_n)/(Z_T + j\pi\xi a_n)}{1 + \sum_{n=-\infty}^{\infty} Z_L/(Z_T + j\pi\xi a_n)}. \tag{43}$$

The solution for the loop current and the expression for the transfer function derived above are valid for an arbitrary incident field as long as it is in steady state. Consider the case where the incident field is an uniform plane wave (UPW). The UPW is incident in the $(\theta, \phi_o)$ direction, as shown in Figure 2, and the electric field has a polarization angle of $\psi$. The component of the incident electric field tangential to the loop, at $\phi$, is found as [90]

$$E_\phi^i(\phi) = E_o^i[\cos\psi\cos(\phi - \phi_o) + \sin\psi\sin(\phi - \phi_o)\cos\theta]\, e^{jkb\cos(\phi-\phi_o)\sin\theta}. \tag{44}$$

The Fourier coefficients associated with the UPW can be obtained by substituting the above expression into (33). With the use of the Bessel function identities [96]:

$$\int_o^{2\pi} e^{jx\cos\beta}\cos n\beta d\beta = 2\pi j^n J_n(x) \tag{45}$$

$$\int_o^{2\pi} e^{jx\cos\beta}\sin n\beta d\beta = 0 \tag{46}$$

$$J_{n-1}(x) - J_{n+1}(x) = 2J_n'(x) \tag{47}$$

$$J_{n-1}(x) + J_{n+1}(x) = \frac{2n}{x} J_n(x) \tag{48}$$

one obtains the following expression for $f_n$:

$$f_n = j^{n-1}\cos\psi\, e^{jn\phi_o} J_n'(kb\sin\theta) + j^n \sin\psi\cos\theta\, e^{jn\phi_o} \frac{nJ_n(kb\sin\theta)}{kb\sin\theta} \tag{49}$$

where

$$J_n'(x) = d[J_n(x)]/dx$$

and $J_n(x)$ is the Bessel function of first kind.

A lengthy discussion of the coefficients $a_n$ is available in the literature [88]. This has led to a considerable simplification of the expression (30). This procedure is briefly examined below. A new coefficient $N_n$ is defined as

$$N_n = \frac{b}{4\pi^2}\int_{-\pi}^{\pi}\int_{-\pi}^{\pi}\frac{e^{jn(\theta)}e^{-jkr}}{r}d\alpha\, d\theta. \tag{50}$$

It can be shown that the two coefficients $a_n$ and $N_n$ are related by

$$a_n = a_{-n} = \frac{kb}{2}(N_{n+1} + N_{n-1}) - \frac{n^2}{kb}N_n. \tag{51}$$

Assuming that $b \gg a$, $ka \ll 1$ and $n \not\gg (b/a)$, the expression for $N_n$ can be simplified to the following, more convenient, forms [88]:

$$N_0 = \frac{1}{\pi}\ln\left(\frac{8b}{a}\right) - \frac{1}{2}\int_0^{2kb}[\Omega_0(x) + jJ_0(x)]dx \tag{52}$$

$$N_n = N_{-n} = \frac{1}{\pi}[I_0\left(\frac{na}{b}\right)K_0\left(\frac{na}{b}\right) + \ln(4n) + \gamma - 2\sum_{m=0}^{n-1}\frac{1}{2m+1}] - \frac{1}{2}\int_0^{2kb}[\Omega_{2n}(x) + jJ_{2n}(x)]dx, \quad n \neq 0 \tag{53}$$

where $\Omega_n(x)$ is the Lommel-Weber function defined as

$$\Omega_n(x) = \frac{1}{\pi}\int_o^{\pi}\sin(x\sin\beta - n\beta)d\beta, \tag{54}$$

$I_n(x)$ is the modified Bessel function of first kind, $K_n(x)$ is the modified Bessel function of second kind and $\gamma$ is the Euler's constant, which is approximately 0.54772.

### 3.3.1 The Equivalent Circuit

A receiving-mode equivalent circuit for the impedance-loaded circular loop antenna is developed in this section, using the results of the theoretical analysis reported in the previous section. The receiving loop antenna can indeed be represented by the simple Norton equivalent circuit shown in Figure 3(a). The antenna admittance $Y$ and the current source $I_{sc}$

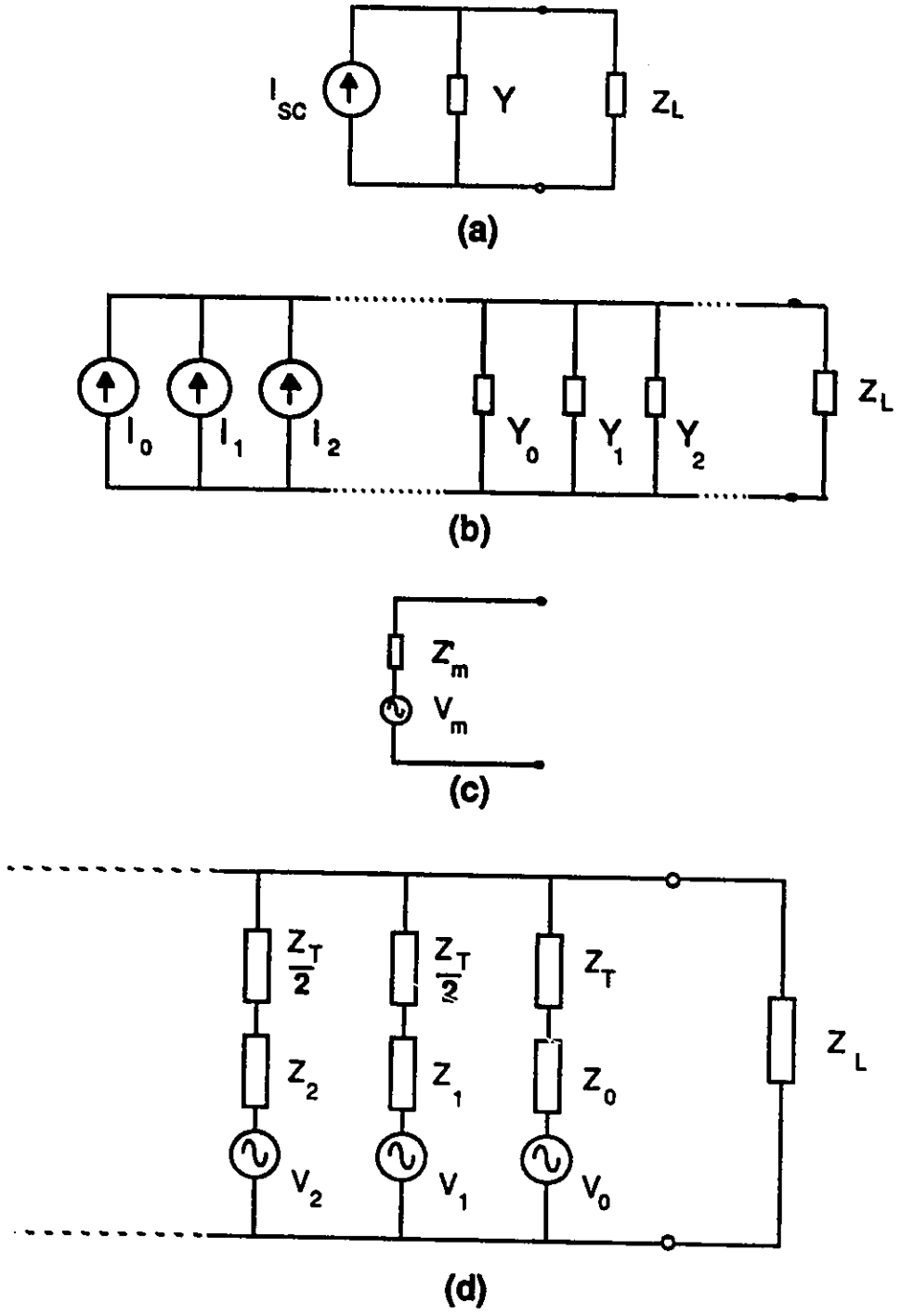


Figure 3: Development of equivalent circuits for the loaded loop antenna in receiving mode.

can be determined using the expressions (39) and (40), respectively. Nonetheless, these expressions are fairly complicated and therefore don't provide much physical insight. Interestingly, the current source can be decomposed into infinite number of modal current sources, all connected in parallel. The $m^{th}$ modal current, which is in fact the contribution to the short-circuit current from the $m^{th}$ and $-m^{th}$ Fourier components of the electric field $E^i_\phi$, is given by

$$I_m = \frac{2\pi b g_m E^i_o}{Z_T + j\pi\xi a_m} \tag{55}$$

where

$$g_m = \begin{cases} f_m + f_{-m} & , \quad m \neq 0 \\ f_o & , \quad m = 0. \end{cases} \tag{56}$$

The admittance can also be decomposed similarly, resulting an infinite number of modal admittances connected in parallel. The $m^{th}$ modal admittance is given by

$$Y_m = \frac{\delta_m}{Z_T + j\pi\xi a_m} \tag{57}$$

where

$$\delta_m = \begin{cases} 2, & m \neq 0 \\ 1, & m = 0. \end{cases} \tag{58}$$

The decomposed Norton Equivalent circuit takes the form shown in Figure 3(b). Let us now combine the $m^{th}$ modal current with the $m^{th}$ modal admittance and then replace it with the equivalent Thévenin circuit. This results in a single branch with a voltage source and an impedance connected in series, as shown in Figure 3(c). This branch conveniently represents the total effect of the $m^{th}$ Fourier mode. The modal voltage source $V_m$ and the modal impedance $Z'_m$ are given by the following much simpler expressions:

$$\begin{aligned} V_m = \frac{I_m}{Y_m} &= \frac{2\pi b g_m E^i_o}{\delta_m} \\ &= \pi b (f_m + f_{-m}) E^i_o \end{aligned} \tag{59}$$

$$Z'_m = \frac{1}{Y_m} = \frac{Z_T + j\pi\xi a_m}{\delta_m}. \tag{60}$$

The complete equivalent circuit of the receiving loop antenna can be obtained by combining all the branches as shown in Figure 3(d) where

$$Z_m = \frac{j\pi\xi a_m}{\delta_m}. \tag{61}$$

Substitution of (33) in (59) leads to the following alternate expression for $V_m$:

$$V_m = b\int_{-\pi}^{\pi} E_\phi^i(\phi)\cos m\phi d\phi. \tag{62}$$

The operation of the impedance-loaded circular loop as a receiving antenna can be understood with the aid of the equivalent circuit. Each Fourier mode of the incident electric field, more precisely the tangential component of the incident electric field ($E_\phi^i$), develops a voltage according to (62). This voltage drives the corresponding modal current $I_m$. When the antenna terminals are short-circuited, *i.e.* $Z_L = 0$, the modal currents are independent of each other and are determined by only two impedances- the antenna's inherent unloaded modal impedance $Z_m$ and the distributed load impedance $Z_T$. It should be noted that the effect of the distributed load is the same for all modes except $m = 0$. When the terminal impedance is finite, all the modal currents are coupled through $Z_L$ and therefore each of them is determined by *all* the modal impedances.

The frequency dependence of the impedance $Z_m$ is determined by that of the Fourier coefficient $a_m$. The graphs of $1/a_o$, $1/a_1$ and $1/a_2$ versus $kb$ are available in the literature [88]. It was found that in the case of electrically small loops ($kb \ll 1$), all coefficients except $a_o$ are extremely large, and $a_o$ is primarily real. Therefore, according to (61), all impedances but $Z_o$ are extremely large and $Z_o$ is primarily reactive. As a result, all the branches except the $m = 0$ branch in the equivalent circuit are practically open-circuited by the large modal impedances. The only significant current in an electrically small loop is the $0^{th}$ order modal current given by

$$I_o = \frac{V_o}{Z_o + Z_T + Z_L}. \tag{63}$$

Interestingly, the effect of the distributed load $Z_T$ and the effect of the terminal load $Z_L$, on the loop current, seem identical in the case of small loops. In other words, the distributed load is effectively lumped in series with the terminal load. For small loops, the expression

for $Z_o$ can be further simplified using the low-frequency asymptotic expression for $a_o$ [97]. It was found that in the case of small loops,

$$Z_o = j\omega L \tag{64}$$

where $L$ is the self inductance of the loop approximately given by

$$L = \mu b(\ln \frac{8b}{a} - 2). \tag{65}$$

Hence we obtain the simplified equivalent circuit for electrically small loop antennas, described in Chapter 2.

The sole driving force in an electrically small loop is the modal voltage $V_o$. Using (62) and Faraday's Law of Induction, it is possible to derive the following alternate expression for $V_o$:

$$\begin{aligned} V_o &= b\int_{-\pi}^{\pi} E_\phi^i(\phi)d\phi \\ &= \int_{Area} j\omega\mu H_n(s)ds \end{aligned} \tag{66}$$

where the surface integration is carried out over the loop area and $H_n(s)$ is the magnetic field orthogonal to the plane of the loop. When the loop is small, the magnetic field may be assumed uniform over the loop area. Then, (66) reduces to

$$V_o = j\omega\mu\pi b^2 H_n \tag{67}$$

where $H_n$ is the constant orthogonal magnetic field. The loop antenna hence becomes a "magnetic field sensor" when it is electrically small, producing a response that is directly proportional to the orthogonal magnetic field. This is known as the "magnetic response" of the loop antenna. In the special case where the electromagnetic field does not have an orthogonal magnetic field, $V_o = 0$ and therefore the magnetic response disappears. Yet a small loop may produce a finite but very weak response due to higher order modal voltages. Such a response is sometimes referred to as the "electrical response" of the loop antenna even though these terms are somewhat misleading.

## 3.4 Numerical Results

### 3.4.1 Code Description

Numerical results presented in the next section were obtained using the LLOOP Fortran code listed in Appendix B. The code uses the following notation:

| | | | |
|---|---|---|---|
| BBYA | $= b/a$ | PHI0 | $= \phi_o$ |
| ZL | $= Z_L$ | ZT | $= Z_T$ |
| SC | $= R$ | YC | $= Y\xi$ |
| KB | $= kb$ | PI | $= \pi$ |
| NC(N) | $= N_n$ | AC(N) | $= a_n$ |
| WINT(N) | $= \int_o^{2kb} \Omega_{2n}(x)dx$ | | |
| BINT(N) | $= \int_o^{2kb} J_{2n}(x)dx$ | | |

LIMIT is the number of terms calculated in the series in expressions (39), (40) and (43). ISC is the normalized short circuit current defined as

$$\text{ISC} = \frac{I_{sc}\xi}{2bE_o^i}.$$

The subroutine INT is used to evaluate WINT(N) and BINT(N). Coefficients $N_n$ are calculated according to (52) and (53). $I_o(na/b)$ and $K_o(na/b)$ are evaluated using the IMSL functions MMBSI0 and MMBSK0 [98]. The expression (51) is used to calculate $a_n$.

Substituting $\vartheta = 90°$ and $\psi = 0°$ in (49) and using the Bessel identity [96]

$$2J_n'(x) = J_{n-1}(x) - J_{n+1}(x), \tag{68}$$

one obtains the following expression for $f_n$:

$$\begin{aligned} f_n &= j^{n-1}e^{jn\phi_o}J_n'(kb) \\ &= \frac{1}{2}e^{j(n-1)\pi/2}e^{jn\phi_o}[J_{n-1}(kb) - J_{n+1}(kb)]. \end{aligned} \tag{69}$$

Using the identity [96]

$$J_{-n}(x) = (-1)^n J_n(x) \tag{70}$$

it can be shown that

$$f_{-n} = \frac{1}{2} e^{j(n-1)\pi/2} e^{-jn\phi_o} [J_{n-1}(kb) - J_{n+1}(kb)]. \tag{71}$$

Noting that $a_{-n} = a_n$ and using (40), the following expression for ISC can be derived:

$$\begin{aligned} \mathsf{ISC} &= \frac{I_{sc}\xi}{2bE_o^i} \\ &= \sum_{n=-\infty}^{\infty} \frac{\pi f_n \xi}{Z_T + j\pi\xi a_n} \\ &\approx \frac{-jf_o}{a_o + (Z_T/j\pi\xi)} + \sum_{n=1}^{LIMIT-1} \frac{-j(f_n + f_{-n})}{a_n + (Z_T/j\pi\xi)} \\ &\approx \frac{LC(0)}{a_o + (Z_T/j\pi\xi)} + \sum_{n=1}^{LIMIT-1} \frac{LC(n)}{a_n + (Z_T/j\pi\xi)} \end{aligned} \tag{72}$$

where

$$LC(0) = -jf_o = J_1(kb) \tag{73}$$

and

$$LC(n) = -j(f_n + f_{-n}) = -e^{jn\pi/2} \cos n\phi_o [J_{n-1}(kb) - J_{n+1}(kb)], \quad n \neq 0. \tag{74}$$

LC(N) is calculated according to above expressions. The IMSL subroutine MMBSJN is used to evaluate $J_n(kb)$. The normalized admittance $Y\xi$ is calculated according to (39). ISC is calculated according to (72). Finally, the normalized receiving transfer function is evaluated according to

$$\mathsf{SC} = \frac{\mathsf{ISC}}{(\mathsf{ZL} * \mathsf{YC})/(120\pi) + 1} \tag{75}$$

The value of $kb$ is increased in steps of KBSTEP. The subroutine INTAZ is used to integrate $\Omega_{2n}(z)$ and $J_{2n}(z)$ from $z$ =(KB-KBSTEP) to $z$ =KB where KB is the next value of $kb$. These contributions are added to WINT(N) and BINT(N) vectors.

The subroutine INT evaluates $\int_o^z \Omega_{2n}(x)dx$ and $\int_o^z J_{2n}(x)dx$ using the trapezoidal rule. Values of $\Omega_{2n}(x)$ are obtained by calling the subroutine WEB2NX. $J_{2n}(x)$ is assumed to be zero if $2n > 10$ and $x \leq 1.0$; otherwise it is evaluated by calling the IMSL subroutine MMBSJN. Similarly, the subroutine INTAZ evaluates $\int_a^z \Omega_{2n}(x)dx$ and $\int_a^z J_{2n}(x)dx$ for $a \neq 0$.

Consider the function $E_n(x)$ defined as

$$E_n(x) = \frac{1}{\pi}\int_o^\pi \sin(n\beta - x\sin\beta)d\beta. \tag{76}$$

When $n$ is an even integer, it can be expanded as [99]

$$E_n(x) = -(-1)^{n/2}\sum_{m=0}^{\infty}\frac{(-1)^m(x/2)^{2m+1}}{\Gamma(m-n/2+3/2)\Gamma(m+n/2+3/2)}. \tag{77}$$

Comparing (76) with the definition of $\Omega_n(x)$ in (54), we find that

$$\begin{aligned}\Omega_{2n}(x) &= -E_{2n}(x)\\ &= (-1)^n\sum_{m=0}^{\infty}\frac{(-1)^m(x/2)^{2m+1}}{\Gamma(m-n+3/2)\Gamma(m+n+3/2)}.\end{aligned} \tag{78}$$

WEB2NX subroutine calculates $\Omega_{2n}(x)$ according to this expression. The IMSL function GAMMA calculates the Gamma function for positive arguments. When the argument is negative, the following property is exploited [96]:

$$\Gamma(1-z) = \frac{\pi z}{\Gamma(1+z)\sin\pi z}. \tag{79}$$

Substituting $x = 1 - z$ where $x < 0$, one obtains

$$\Gamma(x) = \frac{\pi(1-x)}{\Gamma(2-x)\sin[\pi(1-x)]}. \tag{80}$$

This is used in GAMMAA to calculate Gamma function for negative arguments.

### 3.4.2 Frequency-Domain Results

#### Input Admittance

The LLOOP Fortran code has been used to calculate the frequency-domain parameters of resistively loaded loop antennas. The input conductance $G$ and susceptance $B$ have been calculated for loops with radii ratio $(b/a)$ of 23.6 (equivalent to a thickness parameter $\Omega = 2\ln(2\pi b/a)$ of 10.0). These results are illustrated in Figure 4 and Figure 5, in normalized form, for various values of the distributed resistance.

Resonance in unloaded and lightly loaded loops gives rise to rapidly changing conductance and susceptance curves, as seen in Figure 4 and Figure 5. The 1000 Ω loop, on the

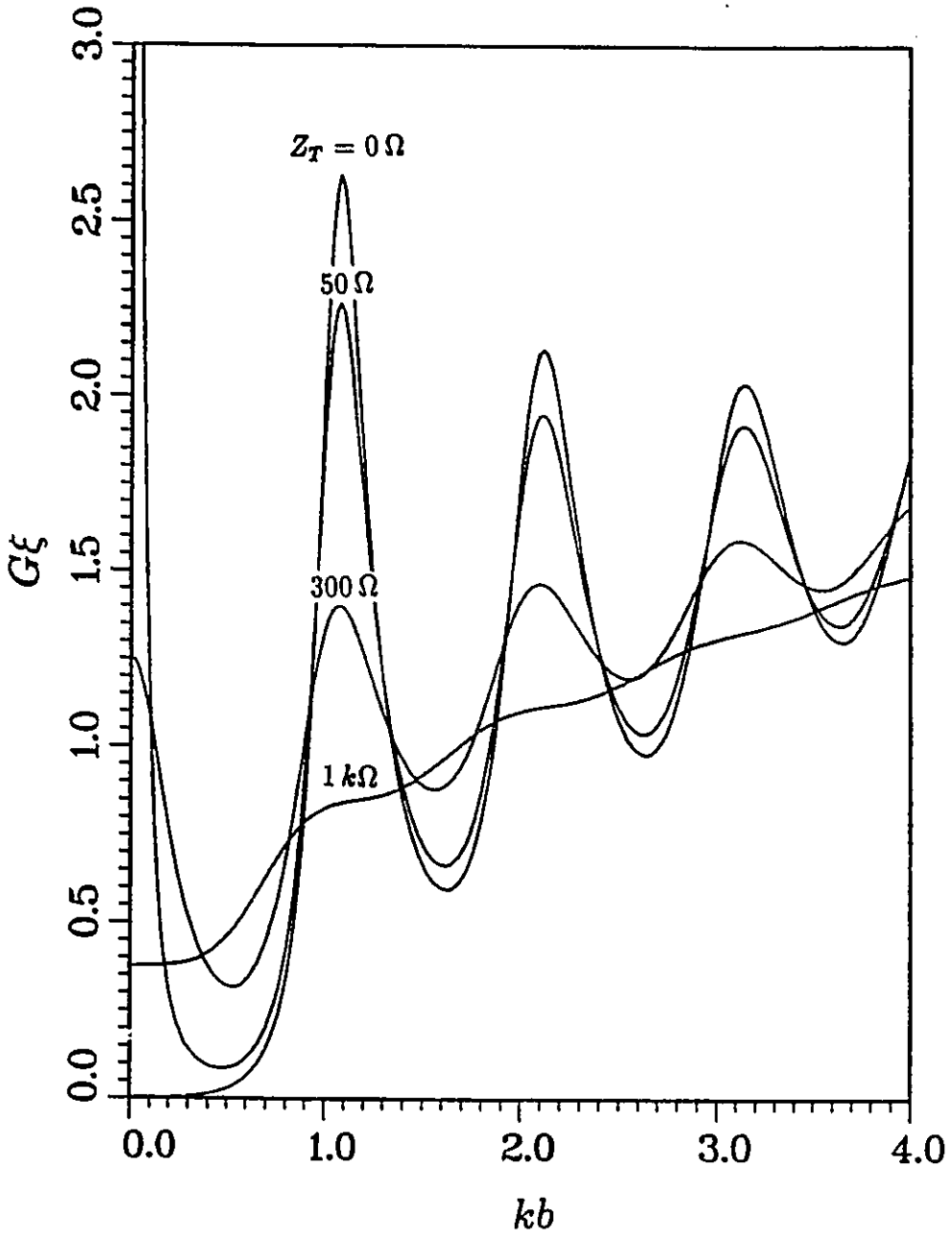


Figure 4: Normalized input conductance of the resistively loaded loop antenna versus normalized frequency. $b/a = 23.6$, $Z_T$ = distributed resistance.

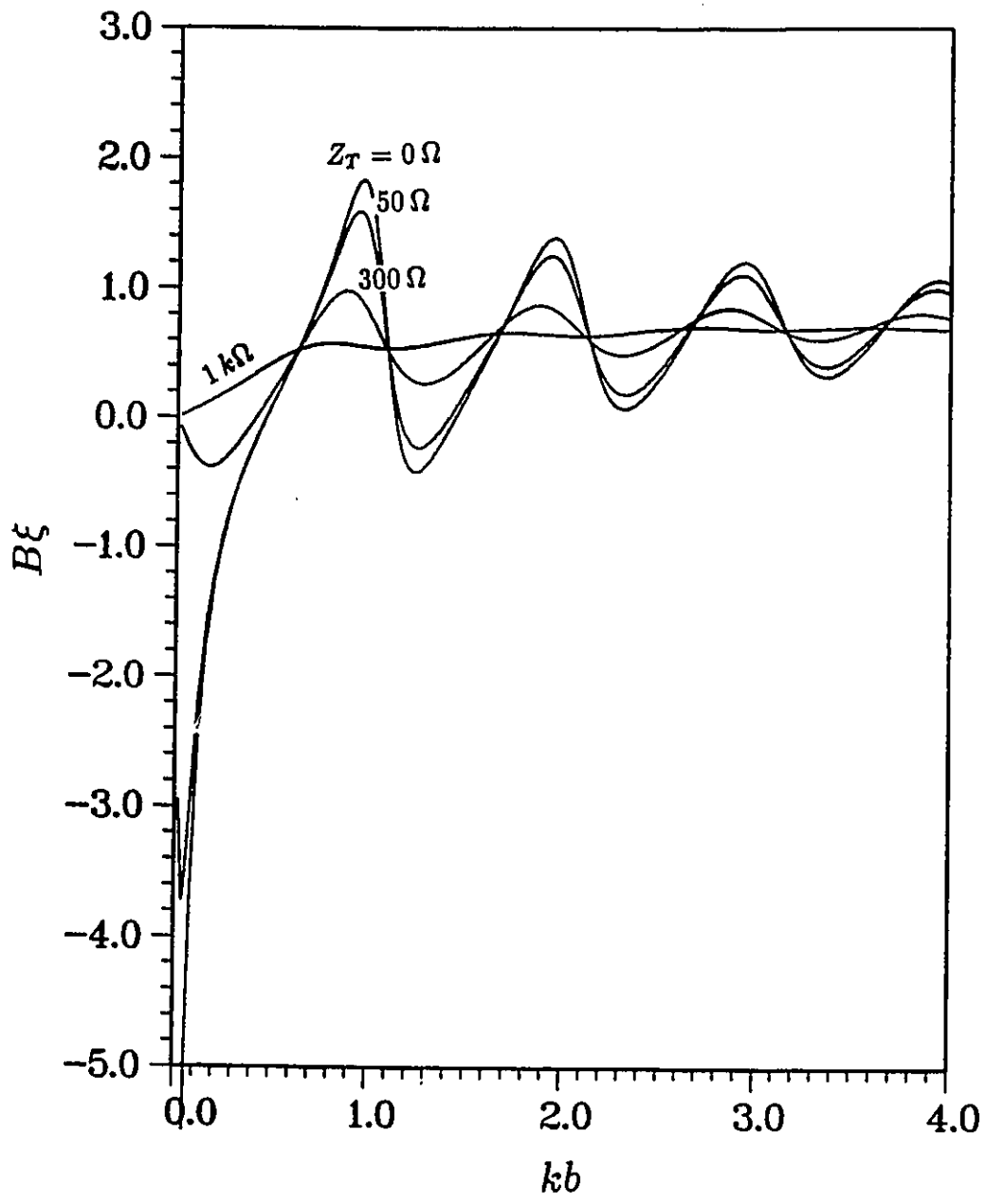


Figure 5: Normalized input susceptance of the resistively loaded loop antenna versus normalized frequency. $b/a = 23.6$, $Z_T$ = distributed resistance.

other hand, exhibits a nearly smooth variation. The conductance approaches $1/Z_T$ as the frequency approaches zero except for the unloaded case where it approaches zero. This behavior can also be predicted using the low-frequency equivalent circuit of the loaded loop antenna. It should be noted that the input admittance (or impedance) of any lossy loop is determined by the loss resistance at very low frequencies whereas that of a perfectly conducting loop is determined by the loop inductance.

The susceptance of the unloaded loop varies according to $1/f$ at low frequencies, again due to its dominant reactive nature, while the susceptance of loaded loops vanishes as frequency approaches zero. As expected, lightly loaded loops have negative susceptances and therefore are inductive at low frequencies. It is interesting to see that heavily loaded loops are capacitive even at very low frequencies. This exceptional behavior cannot be explained using the conventional low frequency equivalent circuit that neglects all $Z_m$s except $Z_o$. To understand this capacitive effect, we should take into account both $m = 0$ and $m = 1$ branches in the general equivalent circuit in Figure 3(d), even at low frequencies. It has been shown that the impedance $Z_1$ represents a capacitance $C$ when $kb \ll 1$ where $C$ is approximately given by [97]

$$C = \frac{2\epsilon b}{\ln \frac{8b}{a} - 2}. \tag{81}$$

In the case of heavily loaded loops, the electric energy stored in this capacitance exceeds the magnetic energy stored in the loop inductance [expression (65)], making the loop capacitive.

### Directional Properties

Consider an unloaded loop antenna excited by a horizontally polarized ($\psi = 0°$) incident wave propagating along the plane of the loop ($\theta = 90°$). The $b/a$ ratio of the loop is 23.6 and the loop antenna is terminated with a 50 Ω load. The normalized receiving transfer function magnitude $|R(\omega)|$ of this antenna is plotted against normalized frequency $kb$ in Figure 6 for several directions of the incident wave ($\phi_o$). It can be seen that for all but one ($\phi_o = 180°$) directions of the incident wave, $|R(\omega)|$ changes very rapidly with frequency. The curve for $\phi_o = 180°$ has a pronounced peak close to $kb = 1$ but it becomes smoother

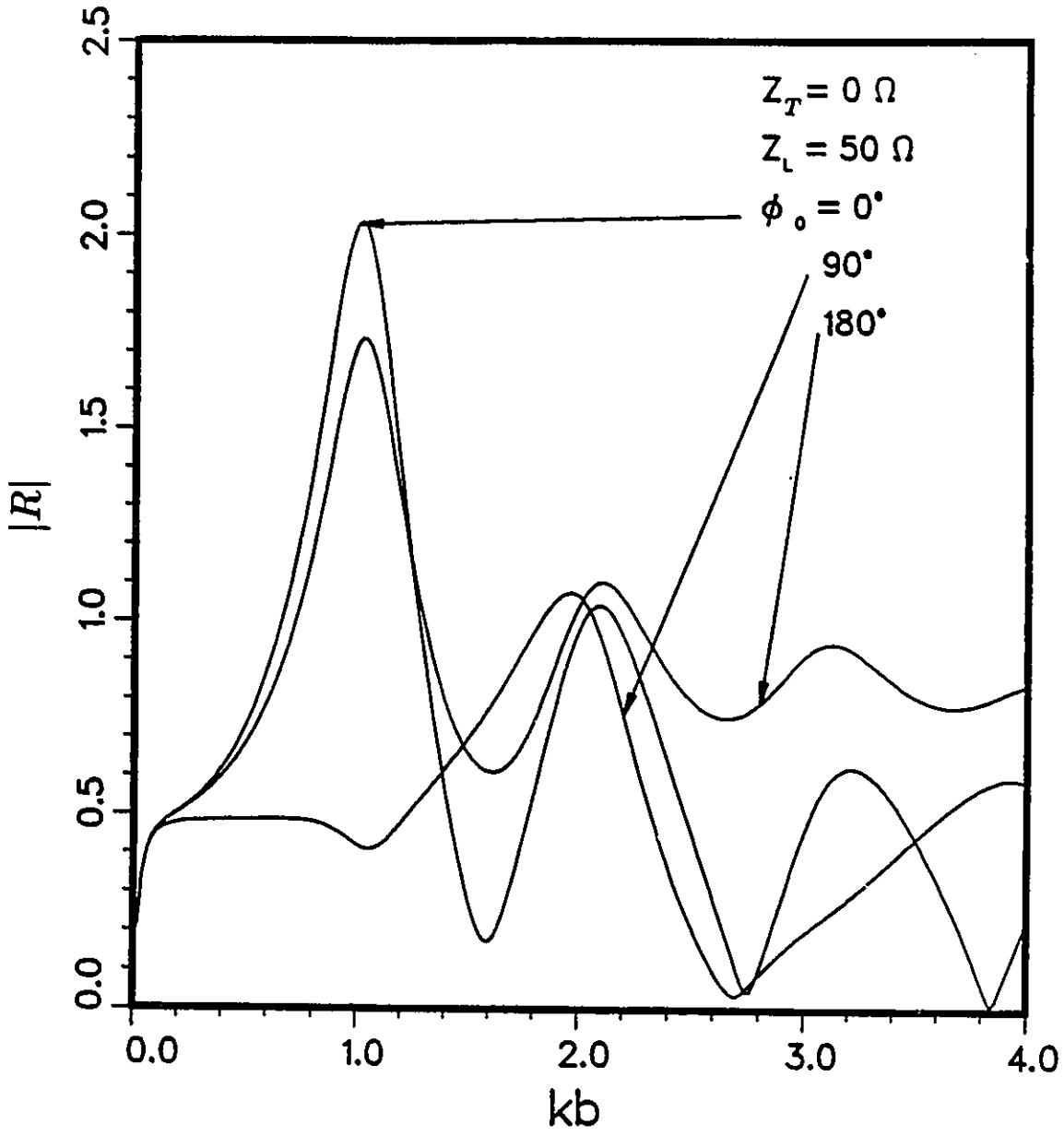


Figure 6: Receiving transfer function versus frequency for different directions of the incident wave. $Z_T = 0\Omega$, $Z_L = 50\Omega$, $b/a = 23.6$, $\theta = 90°$ and $\psi = 0°$.

at higher frequencies.

When the same loop is loaded with a distributed resistance of 300Ω, $|R(\omega)|$ curves take the form shown in Figure 7. Again, the best frequency response is produced by the waves incident in $\phi_o = 180°$ direction. Based on these results, it is assumed that the orientation of the loop that provides the maximum bandwidth is $\theta = 90°, \phi_o = 180°$.

### Effect of the Distributed Load

Figure 8 and Figure 9 illustrate the effect of the distributed resistance on the receiving transfer function magnitude $|R(\omega)|$ and phase $ARG[R(\omega)]$, respectively. A 50 Ω termination has been assumed. The loop has a radii ratio $(b/a)$ of 23.6 and the incident wave is such that $\theta = 90°, \phi_o = 180°, \psi = 0°$.

It can be seen that a fairly flat transfer function (magnitude) can be obtained by properly loading the loop. Overloading will result a considerable loss of sensitivity. A distributed resistance in the range from 300 Ω to 1 kΩ should be sufficient for most practical applications. It should be noted that these resistively loaded loops are not sensitive at low frequencies, usually below $kb = 0.5$. The phase curves of the loaded loops are fairly linear except at low frequencies.

### Effect of the Terminal Load

It was seen that the resonance in a loop antenna can be very much suppressed by applying a proper distributed load, resulting in a flat receiving response. It is interesting to see whether the same result can be obtained using different terminal loads rather than distributed loads. Figures 10 and 11 show the transfer function magnitude and phase curves, respectively, for an unloaded loop terminated with different resistances. Obviously, the results are not very encouraging. The most uniform magnitude curve is obtained with terminations close to 300 Ω. Comparing this with the results in Figure 8 shows that the loop with 300 Ω distributed resistance has not only a more uniform frequency response but also a better overall sensitivity. In Figure 10, an interesting behavior is observed approximately at $kb = 0.5$. At this frequency, input reactance is zero whereas the input resistance is equal to the

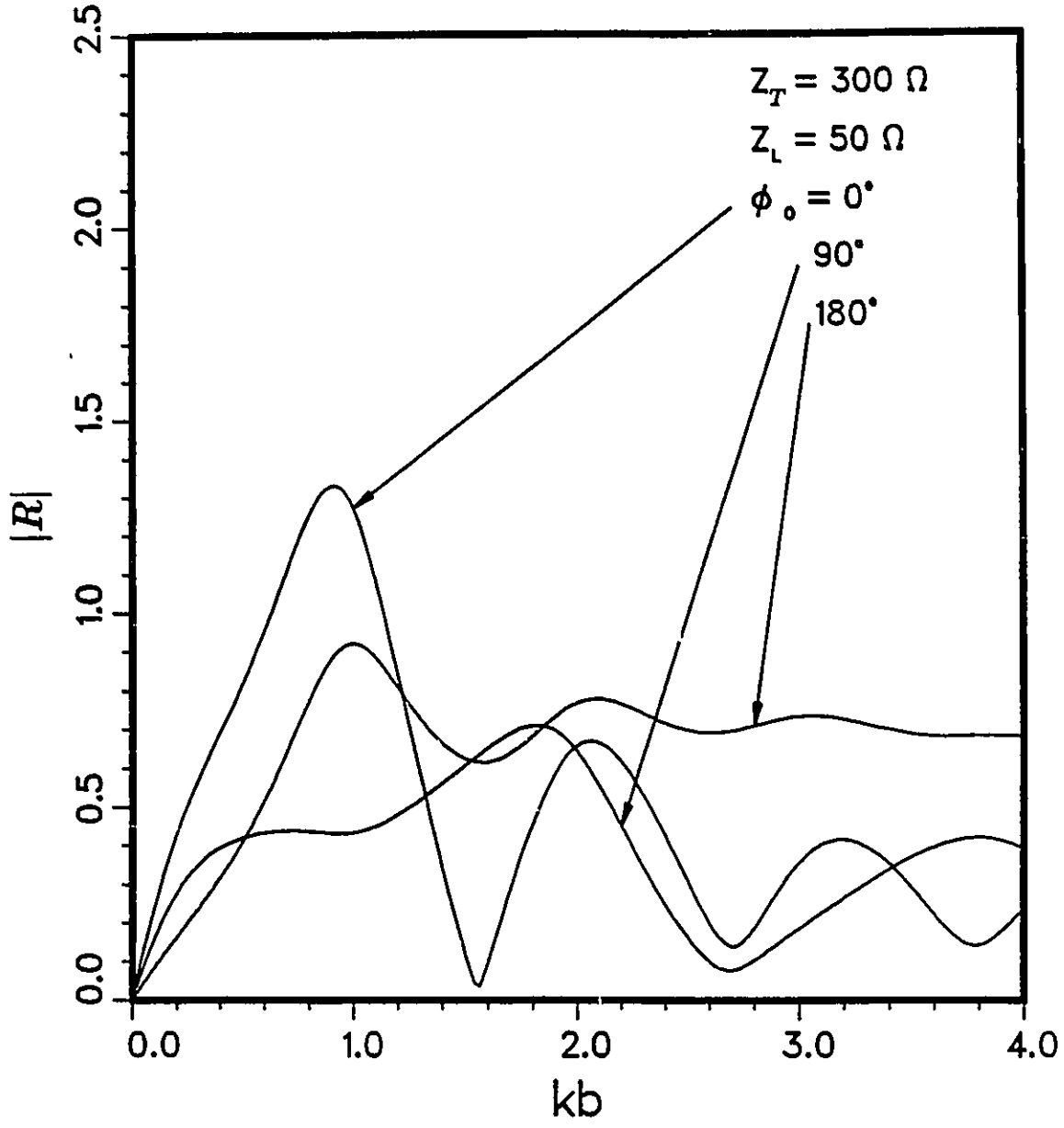


Figure 7: Receiving transfer function versus frequency for different directions of the incident wave. $Z_T = 300\Omega$, $Z_L = 50\Omega$, $b/a = 23.6$, $\theta = 90°$ and $\psi = 0°$.

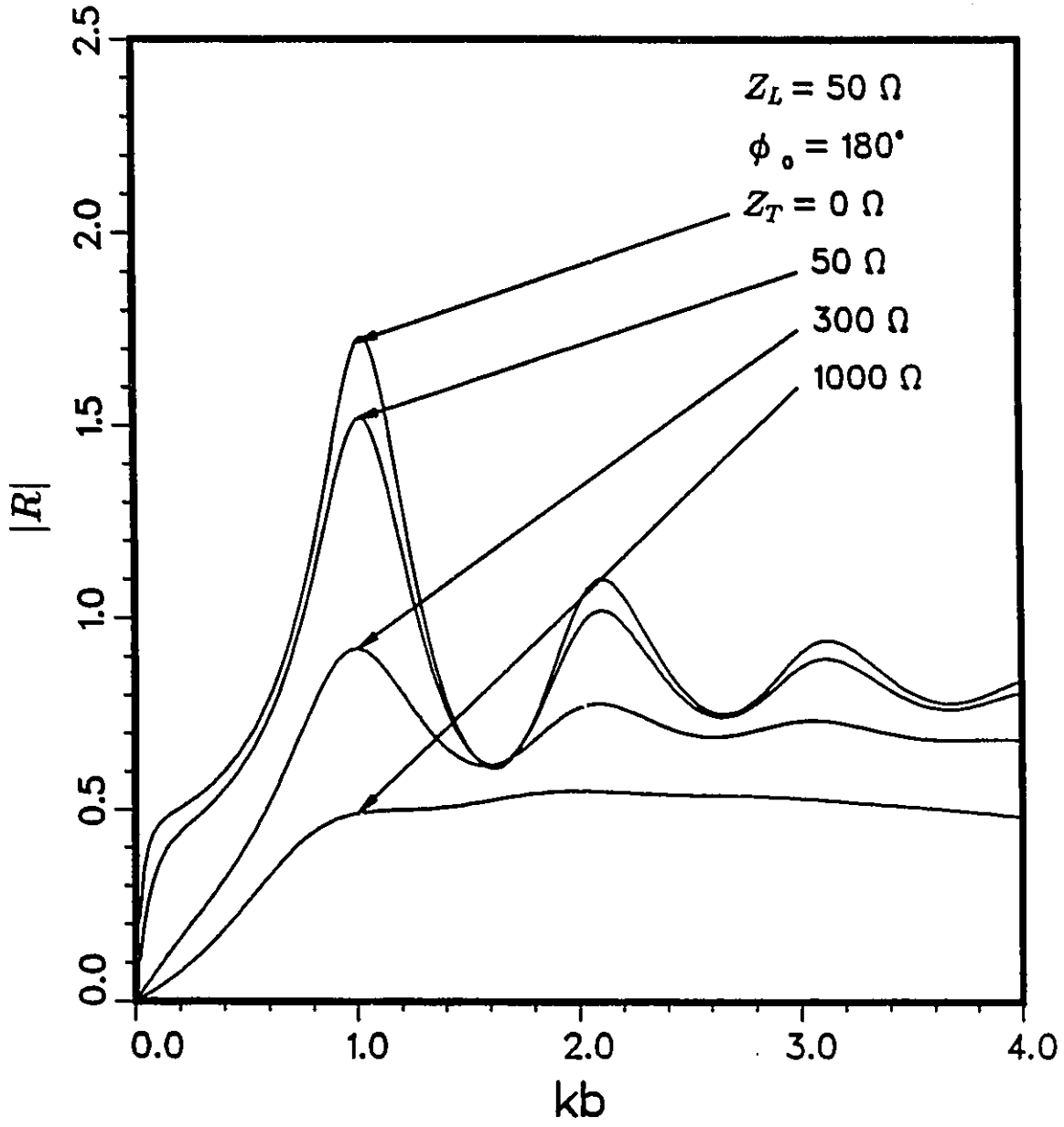


Figure 8: Effect of the distributed resistance on the frequency response of the loop antenna. $Z_L = 50\Omega$, $b/a = 23.6$, $\theta = 90°$, $\psi = 0°$ and $\phi_o = 180°$.

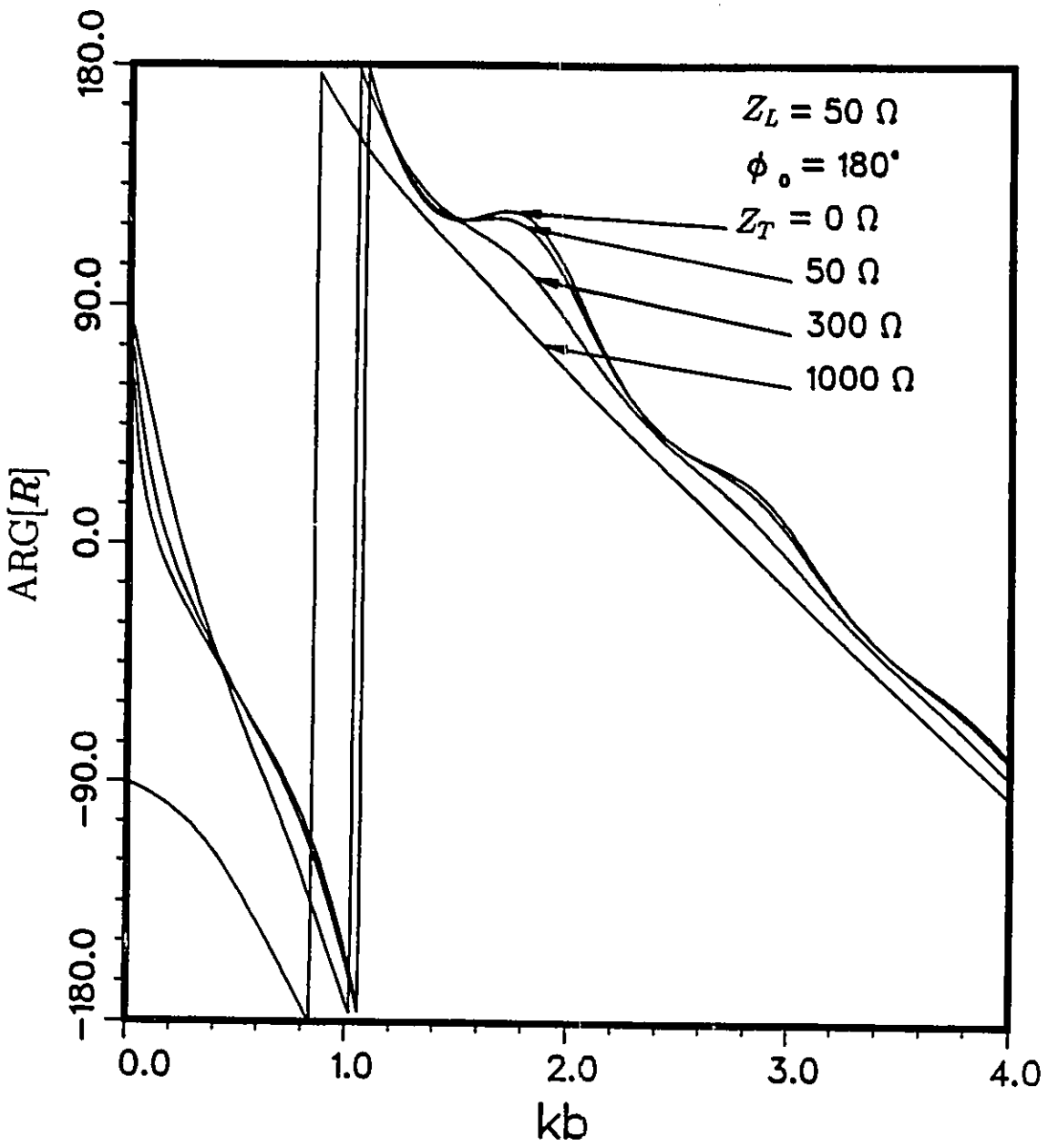


Figure 9: Effect of the distributed resistance on the phase response of the loop antenna. $Z_L = 50\Omega$, $b/a = 23.6$, $\theta = 90°$, $\psi = 0°$ and $\phi_o = 180°$.

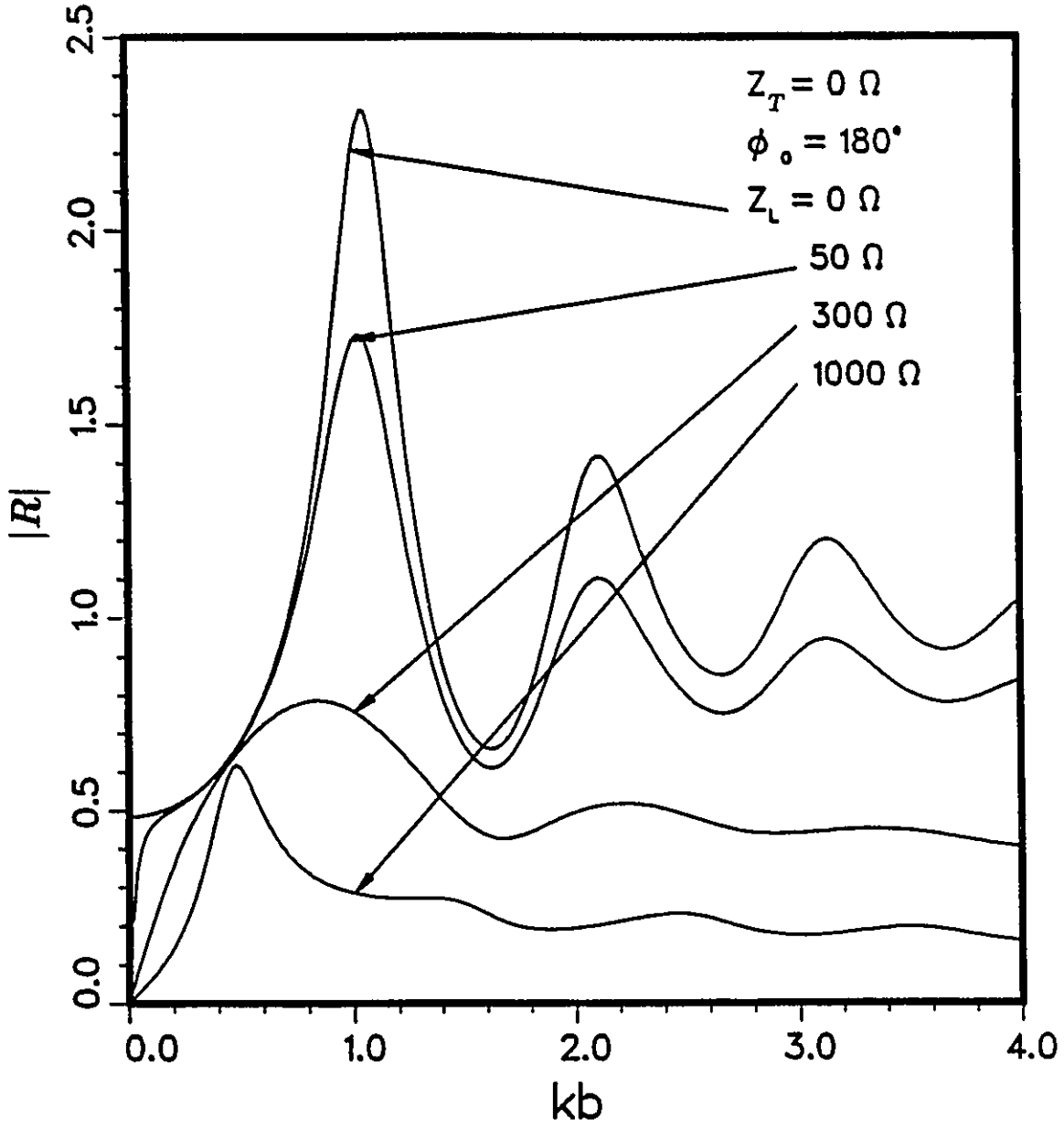


Figure 10: Effect of the terminal resistance on the frequency response of unloaded loops. $Z_T = 0\Omega$, $b/a = 23.6$, $\theta = 90°$, $\psi = 0°$ and $\phi_o = 180°$.

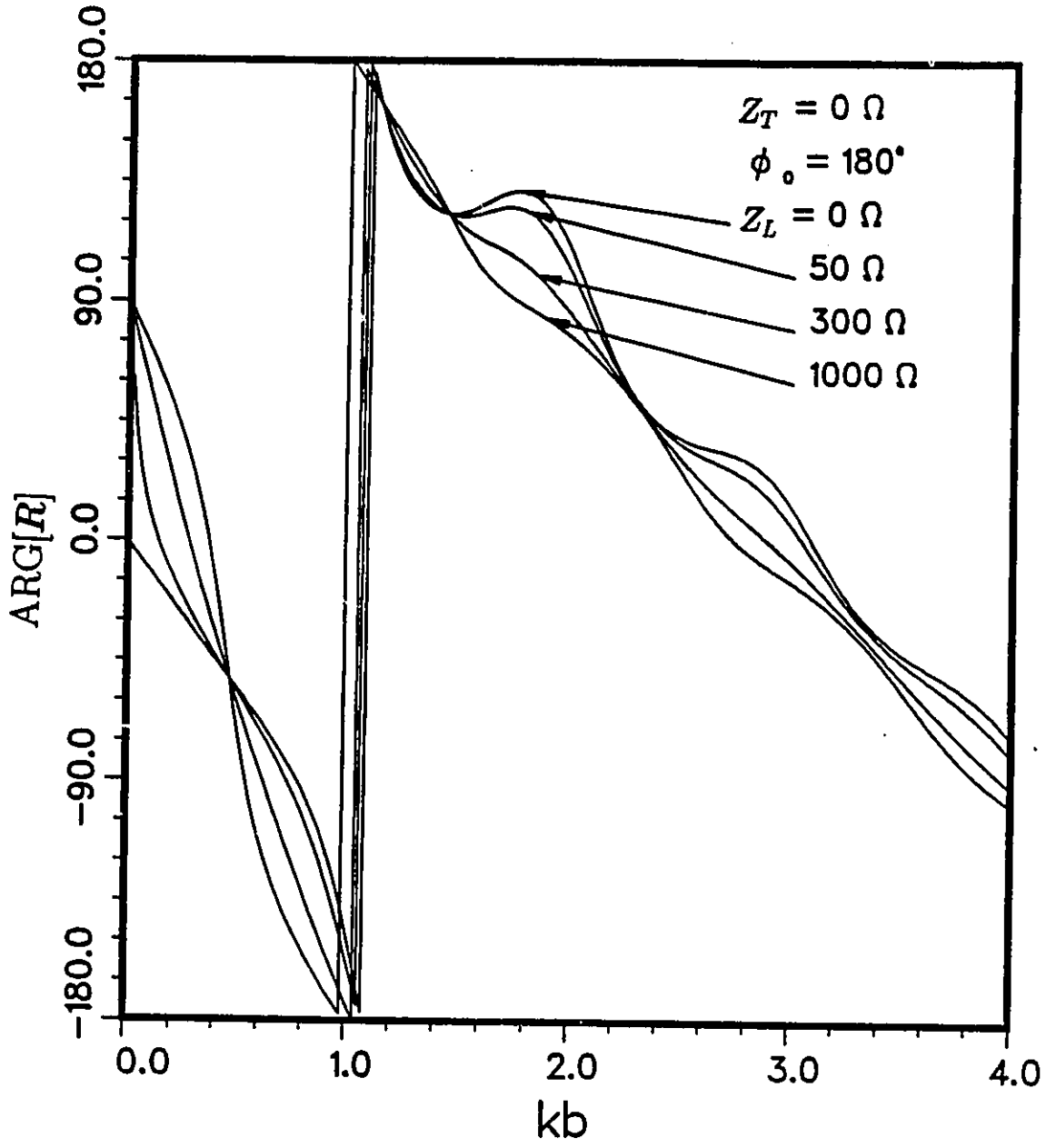


Figure 11: Effect of the terminal resistance on the phase response of unloaded loops. $Z_T = 0\Omega$, $b/a = 23.6$, $\theta = 90°$, $\psi = 0°$ and $\phi_o = 180°$.

fairly high radiation resistance. Therefore, with moderate terminations ($Z_L < 1k\Omega$), the loop acts as an ideal current source and delivers a terminal current almost independent of the terminal resistance. As seen in Figure 11, the phase of $R(\omega)$ is independent of the terminal resistance at all frequencies where the input impedance is purely resistive.

### Time Delay in Reception

According to the definition of $R$ in (42), the phase of $R$ is the difference between the phase of $I_L$ and that of $E_o^i$. Let us now define the time delay associated with the receiving process as

$$\tau_d = \frac{ARG[E_T^i(\omega)] - ARG[I_L(\omega)]}{\omega} \tag{82}$$

where $E_T^i$ is the incident electric field at the antenna terminals. Assuming that the wave is incident from $\theta = 90°, \phi_o = 180°$ direction, the above expression can be simplified to

$$\tau_d = -\frac{ARG[R(\omega)]}{\omega} - \frac{b}{c}. \tag{83}$$

The time delay has been calculated for 300 Ω and 1 kΩ loops. Each antenna has a $b/a$ of 23.6 and is terminated with a 50 Ω resistive load. The results are illustrated in Figure 12. Even though these antennas have approximately linear phase curves at higher frequencies, it can be seen that the time delay experienced by each spectral component is frequency dependent and therefore the antennas are *dispersive*. Good time-domain performance cannot be expected from such dispersive antennas because this dispersion eventually causes distortion of the output waveform.

It should be stressed here that the flat magnitude curve and linear phase curve are necessary *but not sufficient* for good time-domain performance. For that, the system should also have a frequency-independent time delay (or advance). In other words, the linear part of the phase curve should be represented by an equation of the form

$$ARG[R(f)] = \alpha f + n\pi \tag{84}$$

where $n$ is an integer and $\alpha$ is a constant. Unfortunately, the phase curves of the resistively loaded loops, shown in Figure 9, have a different form. If a straight line is fitted to the

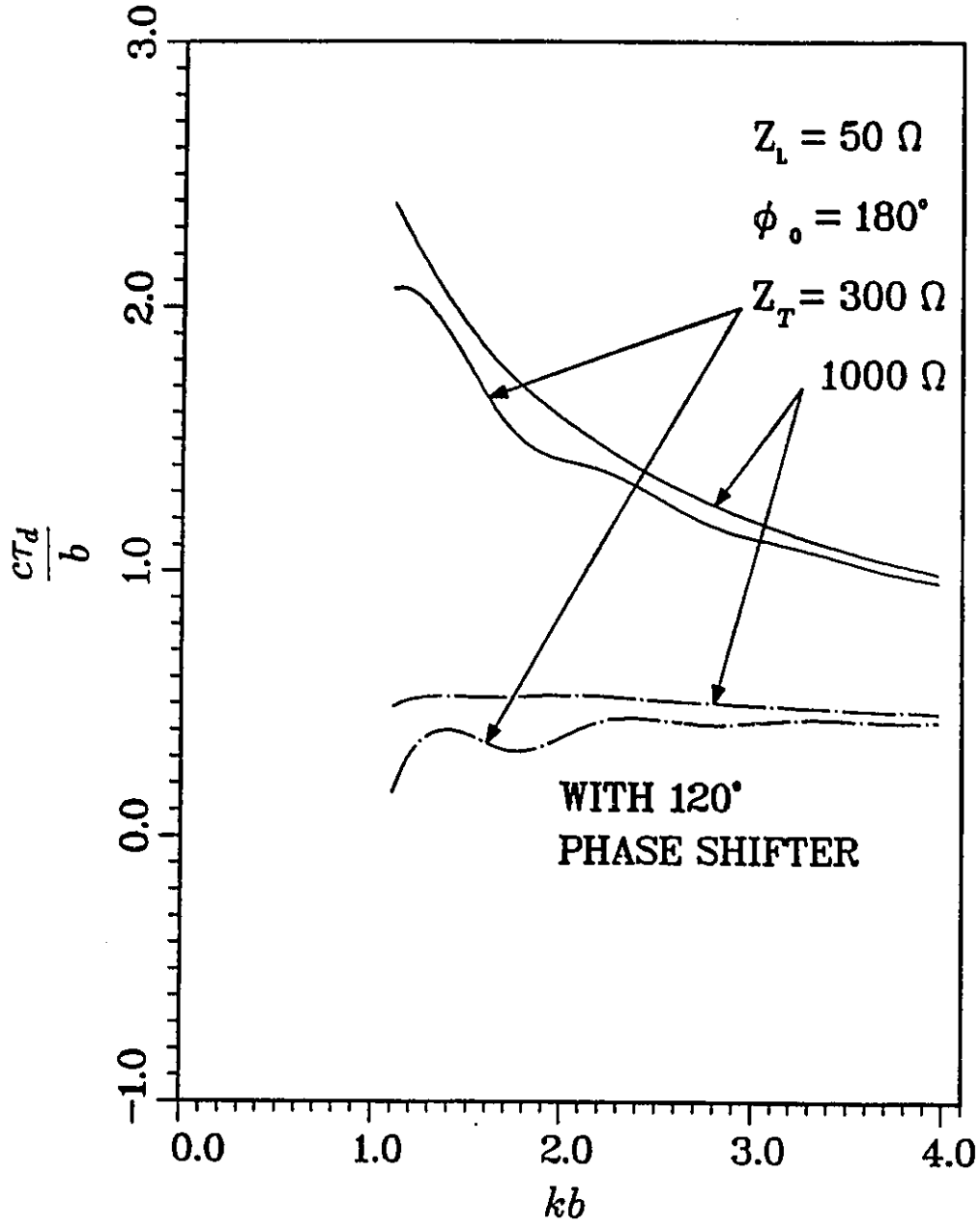


Figure 12: Normalized time delay versus normalized frequency. $Z_L = 50\Omega$, $b/a = 23.6$, $\theta = 90°$, $\psi = 0°$ and $\phi_o = 180°$.

approximately linear section (*i.e.* $kb > 1$ ) of these curves, an intercept of approximately 240 degrees ($4\pi/3$ radians) is found. This undesirable phase shift leads to the dispersion of the antenna. The loop antenna dispersion may be corrected by connecting a frequency-independent $-240^o$ phase shifter to the terminals. Unfortunately, such broadband phase shifters are not feasible.

### Comparison with NEC

For comparison, the receiving transfer function of several resistively loaded loop antennas were also calculated using the NEC [95]. A loop with $b/a$ of 23.6 was approximated by a regular polygon with 20 sides and was divided into 60 segments. The results for loops with distributed resistances of 300 Ω and 1 kΩ, obtained from the NEC, are shown in Figure 13. Results obtained from the LLOOP code (shown in Figure 8 before) are also shown. A terminal resistance of 50 Ω was assumed in all cases. Despite the polygon approximation, a good agreement between the two results can be seen.

## 3.4.3 Time-Domain Results

The time-domain response of various resistively loaded loop antennas for various incident electromagnetic pulses were calculated using the LLOOP code and a 1024-point Fast Fourier Transform (FFT) algorithm. Some of the results obtained for the 300 Ω loop with 50 Ω termination are shown in Figure 14 and Figure 15. In both cases, the direction and polarization of the incident pulses are given by $\theta = 90^o$, $\psi = 0^o$ and $\phi_o = 180^o$ and the loop has $b/a$ of 100. The normalized time and terminal current plotted in the figures are defined as

$$t_N = \frac{ct}{2\pi b} \tag{85}$$

and

$$i_{L,N}(t) = \frac{i_L(t)\xi}{2b}. \tag{86}$$

In Figure 14, the incident electric field pulse has a Gaussian waveform given by

$$e_T^i(t) = e^{-(t/\tau)^2} \tag{87}$$

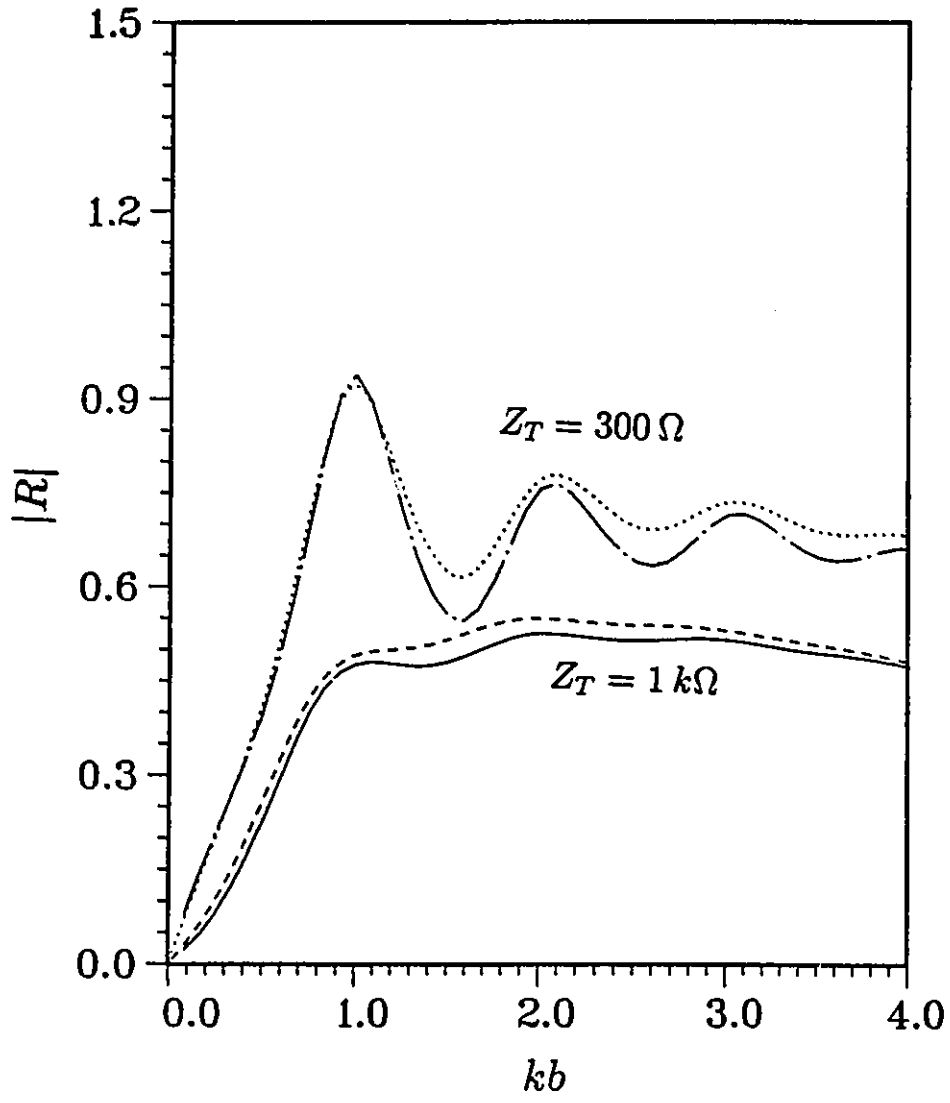


Figure 13: Comparison of results from LLOOP and NEC. Solid line- NEC results for 1 kΩ loop; dash line- LLOOP results for 1 kΩ loop; broken line- NEC results for 300 Ω loop; dotted line- LLOOP results for 300 Ω loop; $Z_L = 50\Omega$, $b/a = 23.6$, $\theta = 90°$, $\psi = 0°$ and $\phi_o = 180°$.

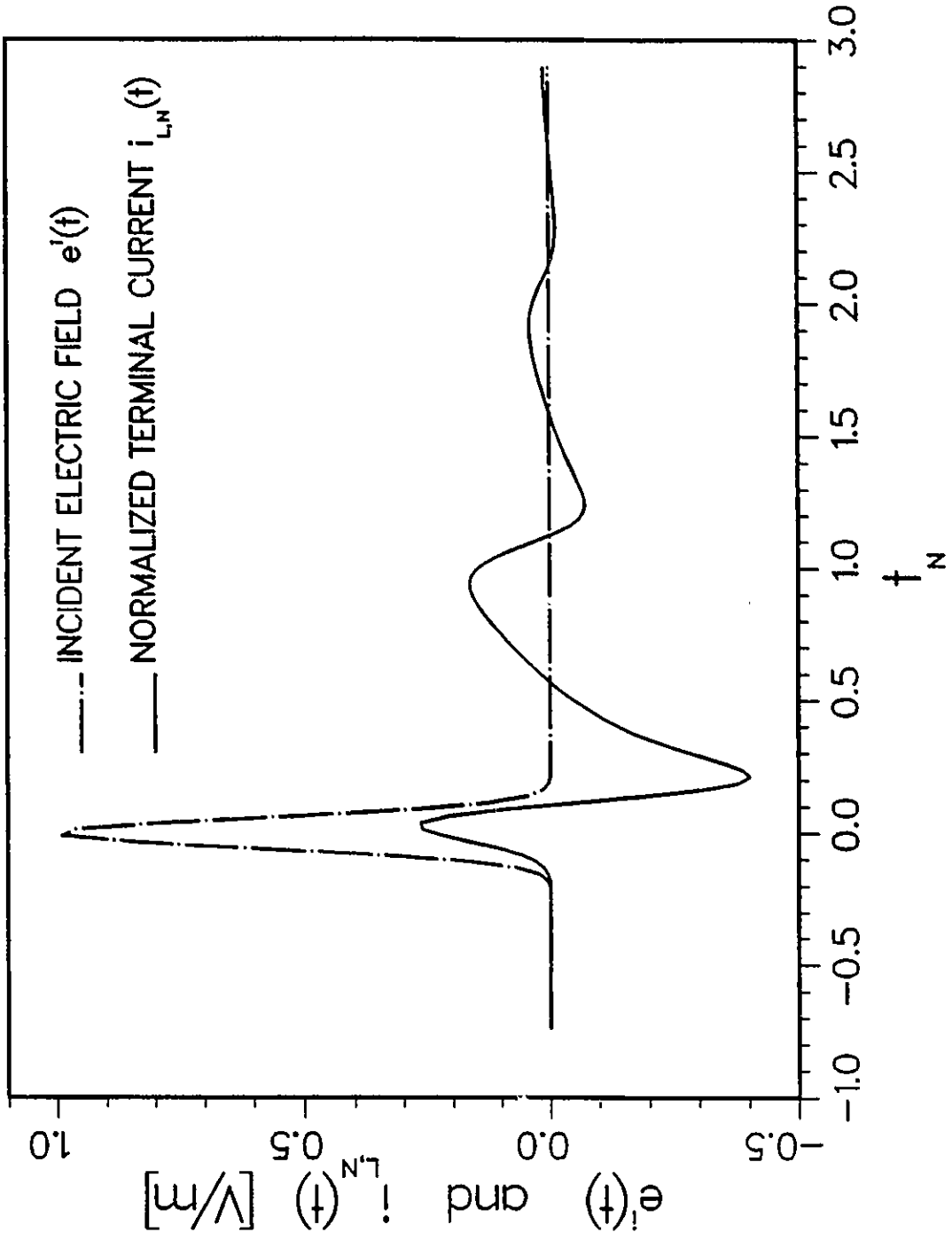


Figure 14: Time-Domain response of the loaded loop to an incident electromagnetic pulse with Gaussian waveform. $Z_T = 300\Omega$, $Z_L = 50\Omega$, $b/a = 100$, $\theta = 90°$, $\psi = 0°$ and $\phi_o = 180°$.

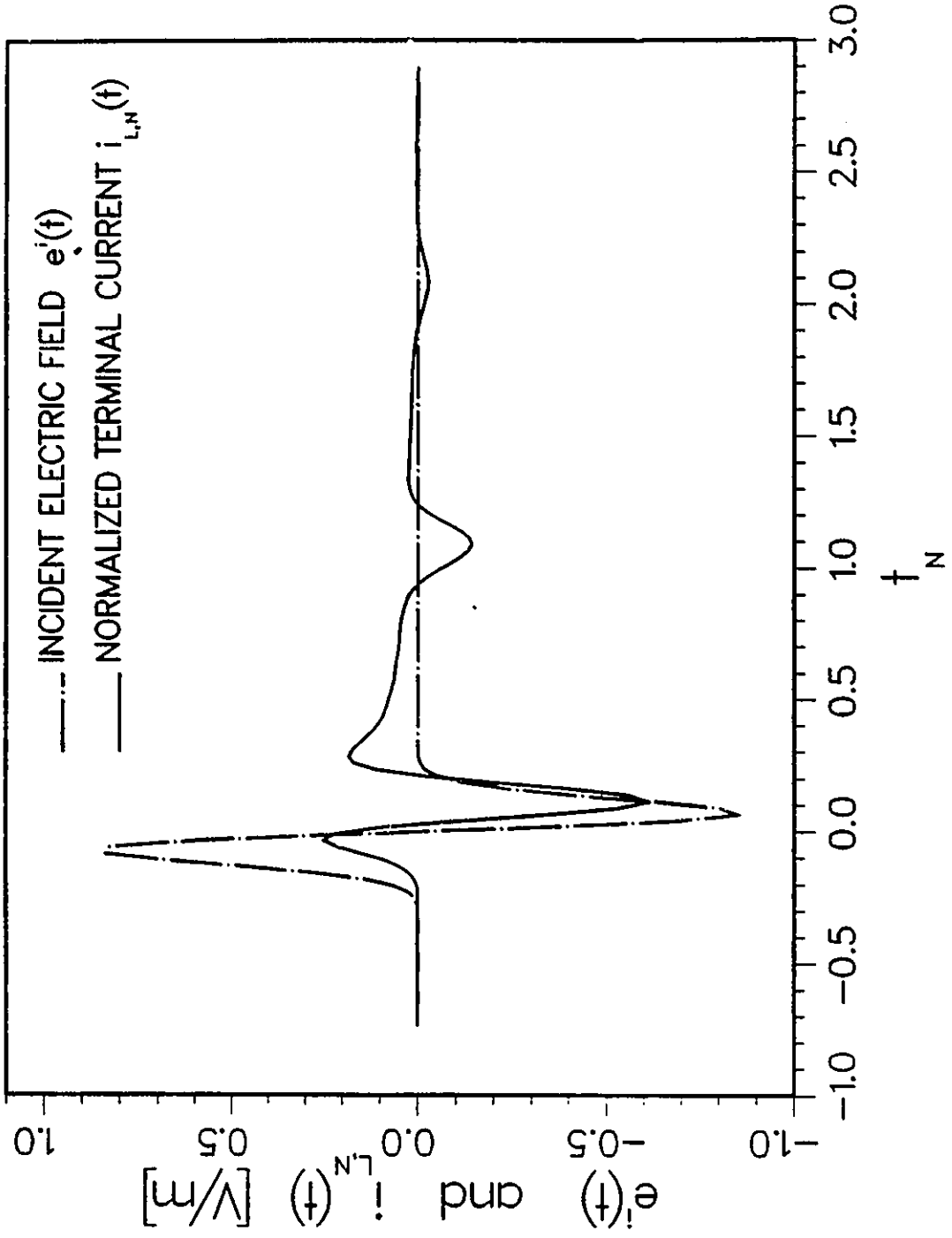


Figure 15: Time-Domain response of the loaded loop to an incident electromagnetic pulse with differentiated-Gaussian waveform. $Z_T = 300\Omega$, $Z_L = 50\Omega$, $b/a = 100$, $\theta = 90°$, $\psi = 0°$ and $\phi_o = 180°$.

where $\tau = \pi b/(5c)$. It can be seen that the output waveform is heavily distorted. In fact, this waveform distortion should be due to both the dispersion and the low-frequency cut-off of the loop antenna. In Figure 15, the incident pulse has a differentiated-Gaussian bipolar waveform given by

$$e^i(t) = -(2t/\tau)\, e^{-(t/\tau)^2}. \tag{88}$$

The output seems to be a distorted (unbalanced) bipolar pulse followed by many weaker negative pulses, each delayed by the antenna transit time $2\pi b/c$. Since the incident pulse has a negligible amount of spectral energy at frequencies below $kb = 1$, the low-frequency cut-off of the loop antenna should not produce much distortion in this case. Therefore this distortion is almost totally attributed to the dispersion of the loop antenna.

## 3.5 Discussion

According to the numerical results presented here, a circular loop antenna with a uniform distributed resistance has a broad receiving bandwidth, at least for uniform plane waves incident in $\theta = 90°, \phi_o = 180°$ direction. Nonetheless, the antenna is dispersive and therefore not suitable for the reception of electromagnetic pulses or transients. In theory, this dispersion can be eliminated using a broadband phase shifter; but it seems not practical.

One may also consider the use of loop antennas with *nonuniform* resistive loads as well as reactive loads. The Fourier Series Expansion method presented here can be modified to analyze nonuniformly loaded circular loops. However, in that case, modal currents interact with each other through the distributed load (besides the terminal load) and therefore an analytical solution to the problem is not possible. One would obtain an infinite matrix problem, which can be truncated and solved numerically. On the other hand, one can also use standard numerical methods (such as the Method of Moments) to solve the nonuniformly loaded loop problem. For example, the Numerical Electromagnetic Code can be used for this purpose, without much user effort [95].

# Chapter 4

# THE STRAIGHT DIPOLE

## 4.1 Introduction

One interesting broadband antenna is the nonreflecting dipole proposed by Wu and King [27]. Although for accurate implementation of the Wu-King (WK) concept the dipole should have a distributed resistance as well as a reactance, for all practical purposes, it can be approximated by a resistively loaded dipole. The WK dipole and other resistively loaded straight dipoles were analytically investigated by Sengupta and Liu [31]. Several numerical investigations have also been done in the frequency domain [32, 33, 34]. In this chapter, we analyze the unloaded straight dipole, the WK dipole and a few other resistively loaded straight dipoles, using two different time-domain techniques [100]. Numerical results obtained from the two methods are compared. Time-domain results so obtained are numerically transformed to the frequency domain using the Fast Fourier Transform (FFT) technique. Frequency-domain results are compared with the results obtained from a direct frequency-domain (MOM) analysis.

The time-domain equations describing the unloaded and resistively loaded straight thin-wire dipoles are presented in the next section. These integral and integro-differential equations are numerically solved in Section 4.3, directly in the time domain. The time-domain and frequency-domain results are presented in Section 4.4. Applicability of resistively loaded

straight dipoles, for the reception of electromagnetic pulses and transients is discussed in Section 4.5.

## 4.2 Time-Domain Equations

Several time-domain equations are available to describe the current induced in a resistively loaded straight dipole when it is excited by a voltage source or an incident electromagnetic field. In this section, two such equations are presented- a Pockington-type integro-differential equation and a Hallen-type integral equation. Both of these equations assume that the dipole is electrically thin over the whole frequency spectrum.

### 4.2.1 The Integro-Differential Equation

Consider the electric field $\vec{E}^s(P,t)$ at a point P in free space produced by a current element $\vec{I}(S,t)$ and a charge element $q(S,t)$ located at point S, as shown in Figure 16(a). If $\vec{R}_s$ is the vector from S to P, the electric field is given by [60]

$$\begin{aligned} 4\pi\epsilon\vec{E}^s(P,t) = & \\ & \frac{q(S,\tau)\vec{R}_s}{R_s^3} + \frac{[\vec{I}(S,\tau).\vec{R}_s]\vec{R}_s}{cR_s^4} \\ & - \frac{\vec{R}_s \times [\vec{I}(S,\tau) \times \vec{R}_s]}{cR_s^4} - \frac{\vec{R}_s \times [\dot{\vec{I}}(S,\tau) \times \vec{R}_s]}{c^2 R_s^3} \end{aligned} \tag{89}$$

where $R_s = |\vec{R}_s|$ and $\tau = t - R_s/c$.

Let the point P be on the surface of the wire and the point S be on the axis of the wire of a dipole, as shown in Figure 16(b). The unit vector along the wire axis is $\hat{s}$. It is assumed here that the current and its associated charge are concentrated at the center of the wire. This "thin-wire" assumption is valid as long as the wire radius is much smaller than all the wavelengths considered. For the derivation of the integral equation for the dipole, we need to evaluate the component of the scattered electric field tangential to the wire surface, given by

$$E^s(P,t) = \vec{E}^s(P,t).\hat{s}\ . \tag{90}$$

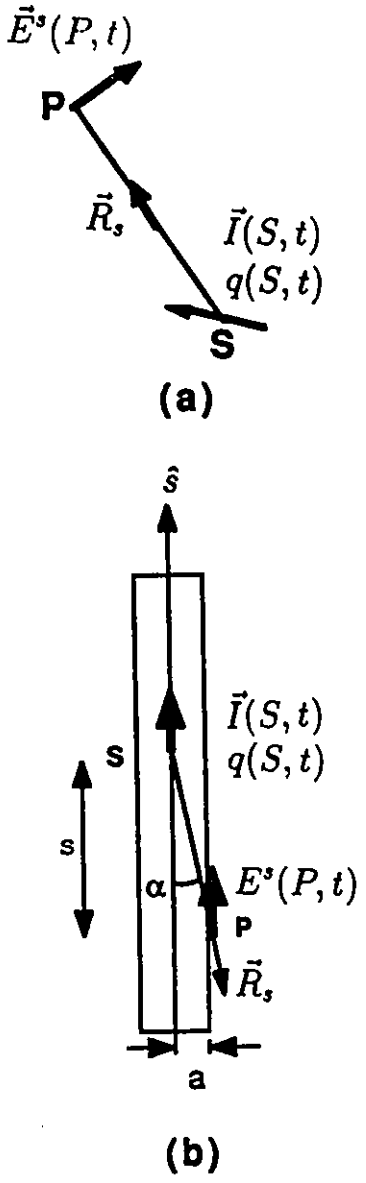


Figure 16: Elemental current and charge on the straight dipole.

The elemental current at S can be expressed as

$$\vec{I}(S,t) = I(S,t)\,\hat{s}. \tag{91}$$

Equation (89) is scalar-multiplied by $\hat{s}$ and hence $4\pi\epsilon E^s(P,t)$ is found. Then, expression (91) is substituted for $\vec{I}(S,t)$. Vector multiples are replaced using following equations.

$$\vec{R}_s.\hat{s} \;=\; -R_s\cos\alpha \tag{92}$$

$$[\vec{R}_s \times (\hat{s} \times \vec{R}_s)].\hat{s} = -R_s^2\sin^2\alpha \tag{93}$$

where $\alpha$ is the angle between $\vec{R}_s$ and $-\hat{s}$. Then, the tangential electric field at the surface of the wire produced by an elemental source on the axis of the wire is found as

$$4\pi\epsilon E^s(P,t) = \\ -\frac{q(S,\tau)}{R_s^2}\cos\alpha + \frac{I(S,\tau)}{cR_s^2}(\cos^2\alpha - \sin^2\alpha) + \frac{\dot{I}(S,\tau)}{c^2R_s}\sin^2\alpha. \tag{94}$$

Substitution for $\sin\alpha$ and $\cos\alpha$ leads to

$$4\pi\epsilon E^s(P,t) = \\ \frac{q(S,\tau)s}{(s^2+a^2)^{3/2}} + \frac{I(S,\tau)(s^2-a^2)}{c(s^2+a^2)^{3/2}} - \frac{\dot{I}(S,\tau)a^2}{c^2(s^2+a^2)^{3/2}} \tag{95}$$

where $a$ is the wire radius and $s$ is the axial separation between S and P. The total scattered field is obtained by integrating the field from elemental sources over the wire:

$$4\pi\epsilon E^s(P,t) = \\ \int_{wire}\left\{\frac{q(S,\tau)s}{(s^2+a^2)^{3/2}} + \frac{I(S,\tau)(s^2-a^2)}{c(s^2+a^2)^{3/2}} - \frac{\dot{I}(S,\tau)c^2}{c^2(s^2+a^2)^{3/2}}\right\}ds. \tag{96}$$

The total tangential electric field is the sum of the tangential scattered field and the tangential incident field, given by

$$E^t(P,t) = E^s(P,t) + E^i(P,t). \tag{97}$$

For a perfectly conducting dipole, $E^t(P,t)$ must be zero. When the the antenna is loaded with a surface resistance $\rho(P)$,

$$E^t(P,t) = \rho(P)\,J(P,t) = \rho(P)\,\frac{I(P,t)}{2\pi a} \tag{98}$$

where $J(P,t)$ is the current density. Substitution of (98) in (97) leads to

$$\frac{2\epsilon}{a}\rho(P)I(P,t) = 4\pi\epsilon E^s(P,t) + 4\pi\epsilon E^i(P,t). \tag{99}$$

Finally, expression (96) is substituted for $4\pi\epsilon E^s(P,t)$ and the following equation for the resistively loaded straight dipole antenna is obtained:

$$\begin{aligned} 4\pi\epsilon E^i(P,t) = & \\ & \frac{2\epsilon}{a}\rho(P)I(P,t) \\ - & \int_{wire}\left\{\frac{q(S,\tau)s}{(s^2+a^2)^{3/2}} + \frac{I(S,\tau)(s^2-a^2)}{c(s^2+a^2)^{3/2}} - \frac{\dot{I}(S,\tau)a^2}{c^2(s^2+a^2)^{3/2}}\right\}ds. \end{aligned} \tag{100}$$

The charge $q(S,t)$ is directly related to the current $I(S,t)$ by the continuity equation. As this relationship involves the spatial derivative of current, (100) is essentially an *integro-differential* equation with only one unknown -the current. This may be compared with the Pockington's frequency-domain integro-differential equation. Equation (100) can be solved for the current, directly in the time domain, as shown later. Alternatively, it can be transformed to the frequency domain and can be solved using conventional frequency-domain numerical methods [92]. The frequency-domain current solution can be transformed to the time domain later, using numerical Fourier transform techniques.

### 4.2.2 The Integral Equation

It has been shown that the current in an unloaded or loaded straight dipole can be represented by a Hallen-type time-domain integral equation. The derivation of this equation is available in literature [78, 79]. Let $e^i(z,t)$ be the incident or applied electric field tangential to the dipole. The length of the dipole is $2l$ and the radius is $a$. The internal resistance at a distance $z$ from the terminals $\sigma(z)$ is related to the surface resistance $\rho(z)$ by

$$\sigma(z) = \frac{\rho(z)}{2\pi a}. \tag{101}$$

A resistive lumped load $R_L$ is connected to the terminals. The time-domain integral equation for the current $i(z,t)$ in this dipole is [78]

$$\int_{-l}^{l}\left[\int_{-\pi}^{\pi}\frac{d\phi'}{8\pi^2\sqrt{(z-z')^2+4a^2\sin^2(\phi'/2)}}+\frac{\sigma(z')}{2\xi}\right] i\left(z',t-\frac{|z-z'|}{c}\right)\,dz'$$
$$=\frac{1}{2\xi}\int_{-l}^{l}e^{i}\left(z',t-\frac{|z-z'|}{c}\right)dz'-R_L\,i\left(0,t-\frac{|z|}{c}\right)$$
$$+f_1(ct-z)+f_2(ct+z) \qquad (102)$$

where $f_1(x)$ and $f_2(x)$ are determined during the solution process by considering the boundary conditions

$$i(-l,t)=i(l,t)=0. \qquad (103)$$

## 4.3 Numerical Solutions

### 4.3.1 The Integro-Differential Equation

The time-domain integro-differential equation for the straight-dipole antenna is numerically solved in this section. The algorithm developed here is based on the stepping-in-time method. The stepping-in-time method is a specialization of the method of moments (MOM) where causality is made use of. This allows one to calculate the current distribution in the two wires, step by step, in time. The excitation (incident field or applied voltage) waveform is arbitrary as long as it is causal and sufficiently bandlimited to justify the thin-wire assumption.

#### Expansion and Testing

The unknown in the integral equation (100) is the wire current, which is a function of two variables- space and time. The roof-top function shown in Figure 17(a) is used for the expansion of the unknown in its domain. It is a triangular function in time and a pulse function in space. The $\Delta T$ in this figure is the time step. Use of triangular functions in time means the current is linearly interpolated along time axis. Pulse expansion in space means each wire is divided into many segments and the current is assumed to be uniform along

each segment. Therefore, according to the continuity equation, no charge does exist along a segment. Nonetheless, the discontinuity of current distribution at segment boundaries creates concentrated charges at these discrete locations. This representation is obviously an approximation to the actual continuous charge distribution. The advantage of using pulses for spatial expansion is that one doesn't have to perform an explicit matrix inversion in solving the integral equation. The spatial length of each segment $\Delta Z$ is equal to $2c\Delta T$. Two dimensional Dirac functions are used for testing. In other words, the equality in (100) is enforced only at several points on the space-time plane.

It is assumed that the electromagnetic pulse is incident perpendicular to the dipole. The dipole is therefore symmetrically excited and the current in the lower half is identical to that in upper half, both in magnitude and sense. Hence, one has to solve only for the current in the top half. In turn, testing points are needed only on the top half of the dipole. Figure 17(b) shows a dipole divided into $(2N + 1)$ segments. The space-time plane over which the current is calculated is also shown. The $(i, j)$ Dirac testing function is physically located at the center of the $i^{th}$ segment. Along time axis, it is at the $j^{th}$ time step. The $(l, m)$ expansion function is centered at the $(l, m)$ testing point, as shown in the same figure.

### Scattered Field from Segments

In this section, the electric field produced at the $(i, j)$ testing point by a general $(l, m)$ expansion function is determined. It can be seen from (95) that only the current and charge at $t = \tau$ contribute to the scattered field. The $\tau$ curve for the $(i, j)$ testing point is shown in Figure 17(b). If the $(l, m)$ expansion function is completely above this curve, there will be no scattered field at the $(i, j)$ testing point due to the $(l, m)$ expansion function. If the $\tau$ curve passes through the expansion function, it will generate a scattered field both due to its currents and charges. If the expansion function is completely below the curve, the scattered field is only due to charges associated with the expansion function. It should be noted that the roof-top expansion function has charges only at the two ends (segment boundaries).

Consider the electric field at the $(i, j)$ testing point due to its own $(i, j)$ expansion

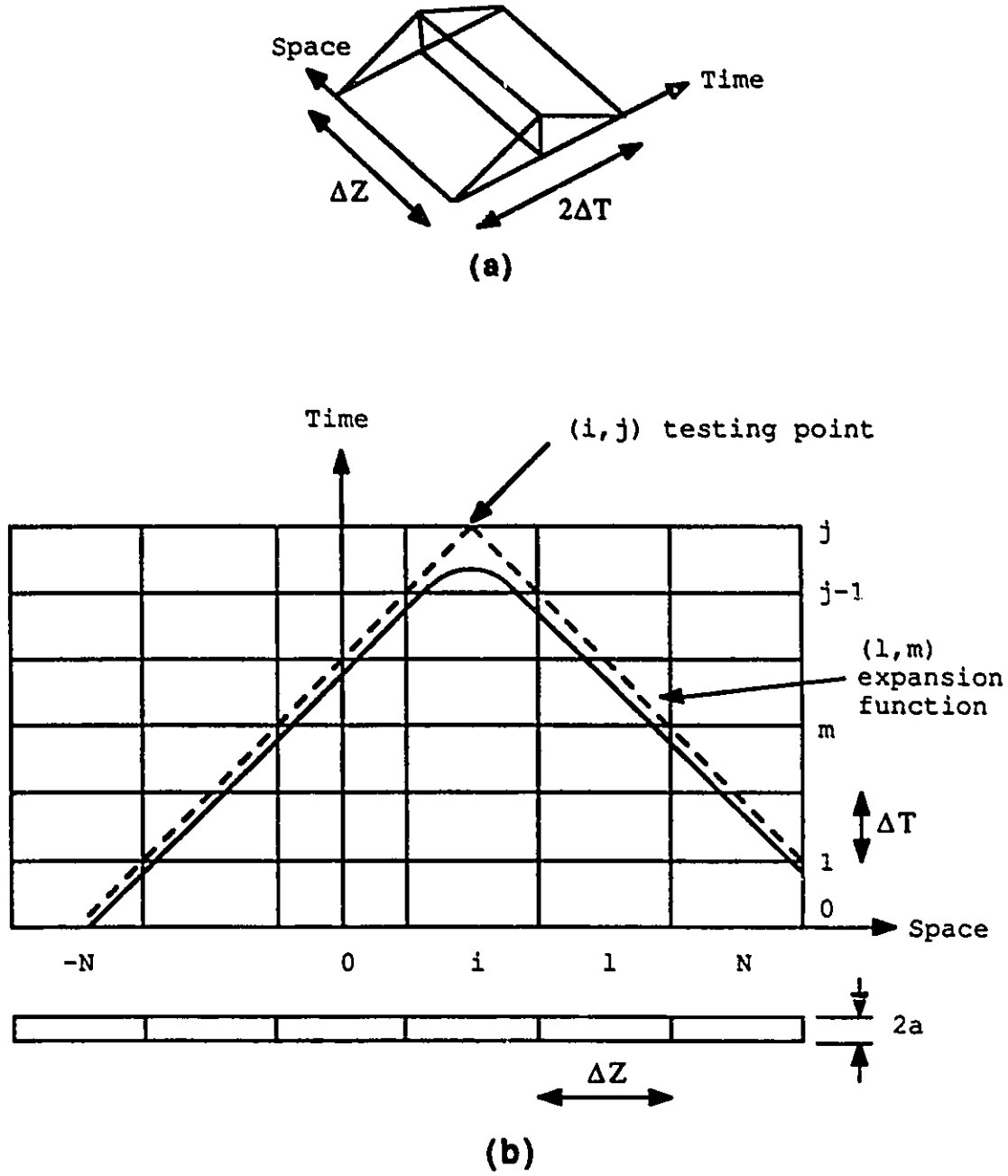


Figure 17: (a) Roof-top expansion function (b) Discretized space-time plane.

function. The $\tau$ curve for this case is shown in Figure 18. Consider a current element at a distance $s$ from the center of the segment. The $\tau$ curve leaves the expansion function at $s = \pm s_1$ where

$$s_1 = \sqrt{c^2\Delta T^2 - a^2}. \tag{104}$$

Since the $\tau$ curve does not cross the segment boundary, there is no contribution from the $(i,j)$ expansion function charges to the electric field at the $(i,j)$ testing point. The current contribution is found as follows. The contribution from the the current element at $s$ is determined first. Then it is integrated from $-s_1$ to $s_1$ to find the total scattered field.

The current in the lower half of the $(i,j)$ expansion function can be expressed as

$$I(S,t) = I_{i,j}\frac{t-(j-1)\Delta T}{\Delta T} \tag{105}$$

where $I_{i,j}$ is the current of the $i^{th}$ segment at $t = j\Delta T$. The retarded time $\tau$ for this case is

$$\begin{aligned} \tau &= j\Delta T - \frac{R_s}{c} \\ &= j\Delta T - \frac{\sqrt{s^2+a^2}}{c}. \end{aligned} \tag{106}$$

Therefore,

$$I(s,\tau) = I_{i,j}\left[1 - \frac{\sqrt{s^2+a^2}}{c\Delta T}\right] \tag{107}$$

and

$$\dot{I}(s,\tau) = \frac{I_{i,j}}{\Delta T}. \tag{108}$$

The electric field due to the current element at $s$ can be determined by substituting above expressions for $I(s,\tau)$ and $\dot{I}(s,\tau)$ into (94). The charge-term in (94) is neglected. Finally, the resulting expression is integrated from $-s_1$ to $s_1$ and hence the scattered field at the $(i,j)$ testing point due to the $(i,j)$ expansion function is found as

$$4\pi\epsilon acE^s = A_0 I_{i,j} \tag{109}$$

where

$$A_0 = -\frac{2}{\psi}\sinh^{-1}\sqrt{\psi^2-1} = -\frac{2}{\psi}\ln(\psi + \sqrt{\psi^2-1}) \tag{110}$$

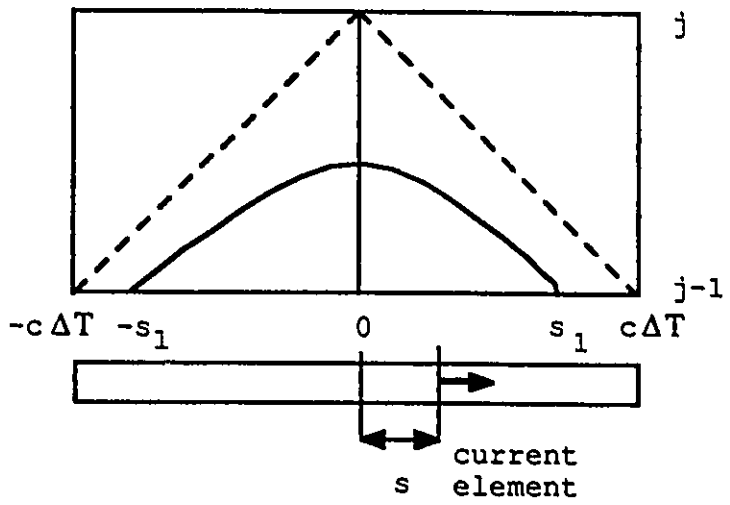


Figure 18: $\tau$ curve in the $(i, j)$ expansion function

and

$$\psi = \frac{c\Delta T}{a}. \tag{111}$$

This process is repeated to calculate the electric field at the $(i,j)$ testing point due to other expansion functions on the $i^{th}$ segment. The lengthy process is not included here. At last, one obtains the following expression for the scattered field at the $(i,j)$ testing point due to all the $i^{th}$ segment currents and charges:

$$4\pi\epsilon acE^s = A_0 I_{i,j} + A_1 I_{i,j-1} + A_2 I_{i,j-2} + A_3 \sum_{k=1}^{j-3} I_{i,k}. \tag{112}$$

where the coefficients are given by

$$A_0 = -\frac{2}{\psi}\ln(\psi + \sqrt{\psi^2 - 1}) \tag{113}$$

$$A_1 = \frac{4}{\psi}\ln(\psi + \sqrt{\psi^2 - 1}) - \frac{2}{\psi}\ln(\psi + \sqrt{\psi^2 + 1}) - \frac{3\psi^2 - 1}{(\psi^2 + 1)^{3/2}} \tag{114}$$

$$A_2 = \frac{2}{\psi}\ln(\psi + \sqrt{\psi^2 + 1}) - \frac{2}{\psi}\ln(\psi + \sqrt{\psi^2 - 1}) - \frac{2\psi^2 + 1}{(\psi^2 + 1)^{3/2}} \tag{115}$$

$$A_3 = -\frac{2\psi^2}{(\psi^2 + 1)^{3/2}}. \tag{116}$$

In the stepping-in-time method, the current $I_{i,j}$ is in fact the unknown being evaluated. Therefore, it is convenient to split the scattered field into known and unknown parts, as

$$4\pi\epsilon acE^s = 4\pi\epsilon acE^{s,i}_{i,j} + A_0 I_{i,j} \tag{117}$$

where

$$4\pi\epsilon acE^{s,i}_{i,j} = A_1 I_{i,j-1} + A_2 I_{i,j-2} + A_3 \sum_{k=1}^{j-3} I_{i,k}. \tag{118}$$

The contribution from other segments can be calculated similarly. The scattered field at the $(i,j)$ testing point due to the $(i \pm l)^{th}$ segment charges and currents $(l > 0)$ is found as

$$\begin{aligned} 4\pi\epsilon acE^{s,i\pm l}_{i,j} = & \\ & B_{0,l} I_{i\pm l,j-2l+1} + B_{1,l} I_{i\pm l,j-2l} + B_{2,l} I_{i\pm l,j-2l-1} \\ & + B_{3,l} I_{i\pm l,j-2l-2} + B_{4,l} \sum_{k=1}^{j-2l-3} I_{i\pm l,k} \end{aligned} \tag{119}$$

where the coefficients are given by

$$B_{0,l} = -\frac{1}{\psi}\sinh^{-1}\sqrt{4l^2\psi^2-1}+\frac{1}{\psi}\sinh^{-1}[(2l-1)\psi] + \frac{(2l-1)}{2}\frac{(4l-1)\psi^2-1}{[(2l-1)^2\psi^2+1]^{3/2}} \quad (120)$$

$$B_{1,l} = \frac{1}{\psi}\{2\sinh^{-1}\sqrt{4l^2\psi^2-1}-\sinh^{-1}\sqrt{(2l+1)^2\psi^2-1}-\sinh^{-1}[(2l-1)\psi]\} \frac{(2l-1)(2\psi^2+1)}{2[(2l-1)^2\psi^2+1]^{3/2}} \quad (121)$$

$$B_{2,l} = \frac{1}{\psi}\ln\left[\frac{(2l+1)\psi+\sqrt{(2l+1)^2\psi^2-1}}{2l\psi+\sqrt{4l^2\psi^2-1}}\right] -\frac{1}{\psi}\ln\left[\frac{(2l+1)\psi+\sqrt{(2l+1)^2\psi^2+1}}{(2l+1)\psi+\sqrt{(2l+1)^2\psi^2-1}}\right] -\frac{(2l+1)[(4l+3)\psi^2-1]}{2[(2l+1)^2\psi^2+1]^{3/2}}+\frac{(2l-1)\psi^2}{[(2l-1)^2\psi^2+1]^{3/2}} \quad (122)$$

$$B_{3,l} = \frac{1}{\psi}\sinh^{-1}[(2l+1)\psi]-\frac{1}{\psi}\sinh^{-1}\sqrt{(2l+1)^2\psi^2-1} +\frac{(2l-1)\psi^2}{[(2l-1)^2\psi^2+1]^{3/2}}-\frac{(2l+1)(2\psi^2+1)}{2[(2l+1)^2\psi^2+1]^{3/2}} \quad (123)$$

$$B_{4,l} = \psi^2\left\{\frac{2l-1}{[(2l-1)^2\psi^2+1]^{3/2}}-\frac{2l+1}{[(2l+1)^2\psi^2+1]^{3/2}}\right\}. \quad (124)$$

The total scattered field is therefore equal to

$$4\pi\epsilon acE^s_{i,j} = A_0 I_{i,j} + \sum_{m=-N}^{N} 4\pi\epsilon acE^{s,m}_{i,j}. \quad (125)$$

The expression (99) is now written in the discrete form as

$$2\epsilon c\rho_i I_{i,j} = 4\pi\epsilon acE^s_{i,j} + 4\pi\epsilon acE^i_{i,j} \quad (126)$$

where $\rho_i$ is the surface resistance at the $i^{th}$ segment and $E^i_{i,j}$ is the tangential component of the incident electric field at the $(i,j)$ testing point. By substituting for $4\pi\epsilon acE^s_{i,j}$ from (125) and rearranging the equation, one obtains

$$(2\epsilon c\rho_i - A_0)I_{i,j} = 4\pi\epsilon acE^i_{i,j} + \sum_{m=-N}^{N} 4\pi\epsilon acE^{s,m}_{i,j}. \quad (127)$$

Finally, free-space values are substituted for $\epsilon$ and $c$ and hence the following expression for the unknown current is obtained.

$$I_{i,j} = \frac{\frac{E^i_{i,j}}{30} + \sum_{m=-N}^{N} 4\pi\epsilon a c E^{s,m}_{i,j}}{\frac{\rho_i}{60\pi} - A_0}. \tag{128}$$

where $4\pi\epsilon a c E^{s,m}_{i,j}$ is given by (118) if $m = i$ or by (119) otherwise. The expression (128) is used in the Fortran code SDIP1 for the calculation of the dipole current.

### 4.3.2 The Integral Equation

A numerical technique to solve the time-domain integral equation (102) was developed by Liu [78, 79]. In this thesis, his algorithm is used to solve the unloaded and resistively loaded antenna problems. Therefore, this section is *not* an original contribution from the author. Liu's algorithm is briefly described in the following pages. The algorithm was implemented in a fortran code called SDIP2, as described in the next section. This allows us to compare the results obtained from the two codes (SDIP1 and SDIP2).

Two assumptions have been made in the derivation of equation (102). The current is assumed to be parallel to the dipole axis. The effect of the wire radius on time retardation is completely neglected. This second assumption leads to the much simpler expression for the retarded time

$$\tau = t - \frac{|z - z'|}{c}$$

instead of the exact expression

$$\tau = t - \frac{\sqrt{(z - z')^2 + a^2}}{c}$$

where $z$ is the location of the testing point, $z'$ is the location of the source point and $a$ is the wire radius. Therefore, the $\tau$ curves become straight lines, as shown in Figure 19.

The space-time plane is divided into a rhombic grid and the current is defined at cross-points (grid points). Two closest grid points are separated by $\Delta Z$ in space and $\Delta T$ in time, where

$$\Delta Z = c\Delta T.$$

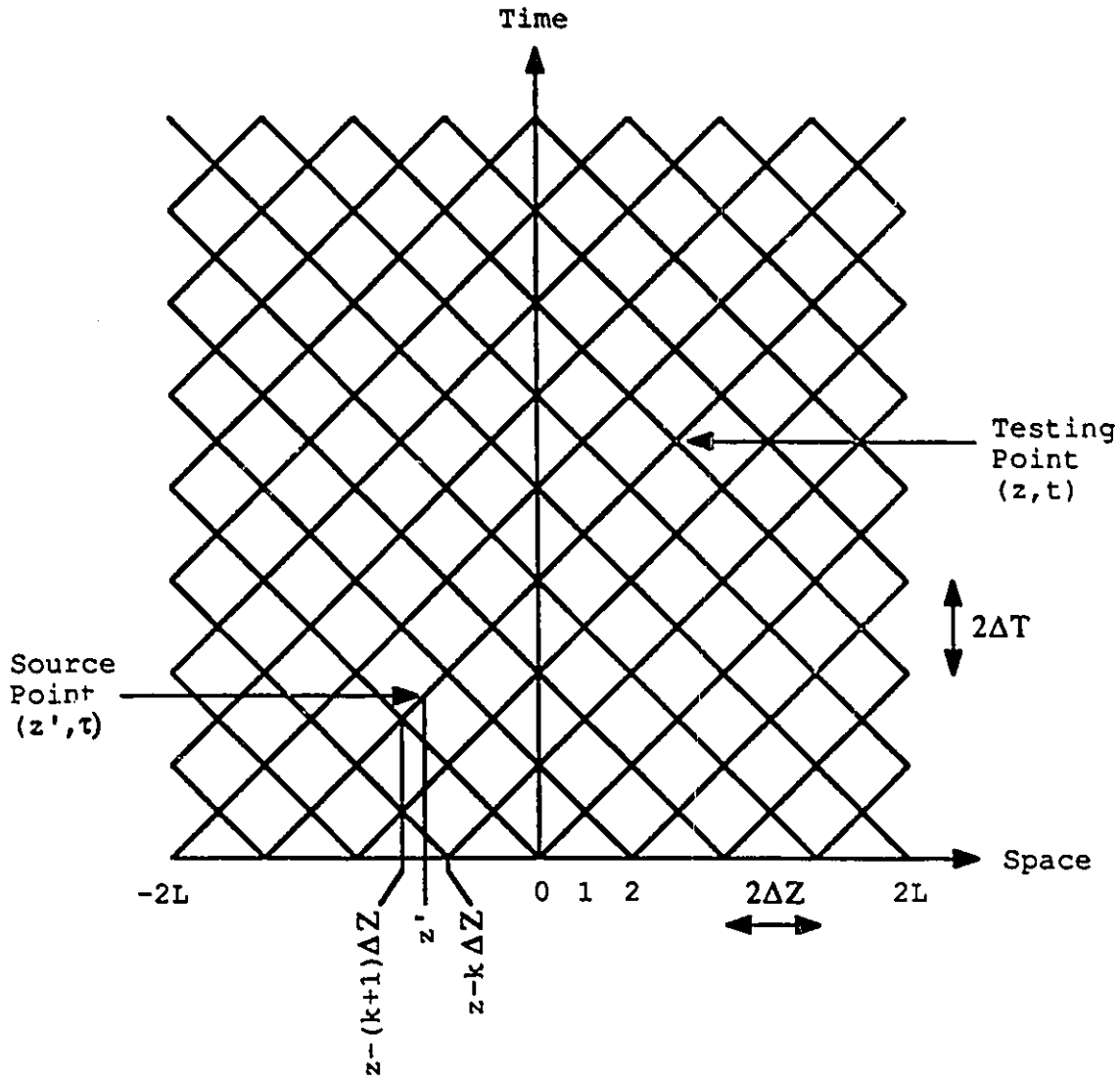


Figure 19: Discretization of space-time plane for Liu algorithm.

Let the dipole (with length $2l$) be divided into $4L+1$ number of points such that

$$\Delta Z = \frac{l}{2L}.$$

At time step $j = 0$ and all other even time steps, current is defined only at even numbered points. At all odd time steps, current is defined only at odd numbered points. Current at any point on any diagonal line can be obtained by interpolating the currents at the two closest grid points.

Assume that the current at $(z,t)$ grid point is to be calculated. According to (102), this involves the evaluation of two current integrals from $-l$ to $l$. The point $(z', t-|z-z'|/c)$ lies on one of two diagonal lines passing through $(z,t)$. Let it be between the two grid points $(z-k\Delta Z, t-k\Delta T)$ and $(z-(k+1)\Delta Z, t-(k+1)\Delta T)$. It is also assumed that the currents at these grid points are $I_k$ and $I_{k+1}$, respectively. By interpolation, the current $i(z', t-|z-z'|/c)$ can then be expressed in terms of $I_k$ and $I_{k+1}$ as

$$i(z', t-|z-z'|/c) = I_k + \frac{z'-z+k\Delta Z}{\Delta Z}(I_k - I_{k+1}). \tag{129}$$

Now the first current integral can be evaluated from $z-(k+1)\Delta Z$ to $z-k\Delta Z$, as

$$\int_{z-(k+1)\Delta Z}^{z-k\Delta Z}\int_{-\pi}^{\pi} \frac{i(z', t-|z-z'|/c)\, d\phi'\, dz'}{8\pi^2\sqrt{(z-z')^2+4a^2\sin^2(\phi'/2)}} = T_1^k I_k + T_2^k I_{k+1} \tag{130}$$

where

$$T_1^k = \frac{(k+1)S_1^k + S_2^k}{8\pi^2} \tag{131}$$

$$T_2^k = -\frac{kS_1^k + S_2^k}{8\pi^2} \tag{132}$$

and

$$S_1^k = 2\int_{-(k+1)\Delta Z}^{-k\Delta Z}\int_0^{\pi} \frac{d\phi' dz'}{\sqrt{z'^2+4a^2\sin^2(\phi'/2)}} \tag{133}$$

$$S_2^k = \frac{2}{\Delta Z}\int_{-(k+1)\Delta Z}^{-k\Delta Z}\int_0^{\pi} \frac{z' d\phi' dz'}{\sqrt{z'^2+4a^2\sin^2(\phi'/2)}}. \tag{134}$$

When $k \neq 0$, above expressions for $S_1^k$ and $S_2^k$ can be approximated by the following closed form expressions:

$$S_1^k = 2\pi \ln\left[\frac{-k\psi + \sqrt{k^2\psi^2+1}}{-(k+1)\psi + \sqrt{(k+1)^2\psi^2+1}}\right] \tag{135}$$

$$S_2^k = 2\pi\left[\sqrt{k^2+\frac{1}{\psi^2}} - \sqrt{(k+1)^2+\frac{1}{\psi^2}}\right] \tag{136}$$

where

$$\psi = \frac{\Delta Z}{a}. \tag{137}$$

$S_1^0$ and $S_2^0$ can be numerically evaluated using following expressions:

$$\begin{aligned} S_1^0 &= 2\psi \sinh^{-1}\left(\frac{2}{\psi}\right) + 4\sinh^{-1}\left(\frac{\psi}{2}\right) \\ &\quad +4\int_0^{\pi/2} \ln\left[\frac{\psi}{2\sin\theta} + \sqrt{1+(\frac{\psi}{2\sin\theta})^2}\right](1-\cos\theta)\,d\theta \end{aligned} \tag{138}$$

$$\begin{aligned} S_2^0 &= \frac{4}{\psi} - 2\sqrt{1+\frac{4}{\psi^2}} - \psi \ln\left(\frac{2}{\psi} + \sqrt{1+\frac{4}{\psi^2}}\right) \\ &\quad -4\int_0^{\pi/2}\left[\sqrt{1+\frac{4\sin^2\theta}{\psi^2}} - \frac{2\sin\theta}{\psi}\right](1-\cos\theta)\,d\theta. \end{aligned} \tag{139}$$

It has been shown that the first current integral from $z+k\Delta Z$ to $z+(k+1)\Delta Z$ can also be expressed as

$$\int_{z+k\Delta Z}^{z+(k+1)\Delta Z}\int_{-\pi}^{\pi} \frac{i(z',t-|z-z'|/c)d\phi' dz'}{8\pi^2\sqrt{(z-z')^2+4a^2\sin^2(\phi'/2)}} = T_1^k I_k' + T_2^k I_{k+1}' \tag{140}$$

where $I_k'$ and $I_{k+1}'$ are the currents at $(z+k\Delta Z, t-k\Delta T)$ and $(z+(k+1)\Delta Z, t-(k+1)\Delta T)$ grid points, respectively.

Let the internal resistance at point $z+k\Delta Z$ be $r_k$. The internal resistance $r(z')$ at a point $z'$ between $(z+k\Delta Z)$ and $(z+(k+1)\Delta Z)$ grid-points is found by linear interpolation of $r_k$ and $r_{k+1}$ as:

$$r(z') = r_k + \frac{z'-z-k\Delta Z}{\Delta Z}(r_{k+1}-r_k). \tag{141}$$

Then, the second current integral in (102) can be evaluated from $(z + k\Delta Z)$ to $(z + (k + 1)\Delta Z)$. This results

$$\int_{z+k\Delta Z}^{z+(k+1)\Delta Z} \frac{r(z')i(z', t - |z - z'|/c)}{2\xi} dz' = \frac{\Delta Z}{12\xi}(2r_k + r_{k+1})I_k + \frac{\Delta Z}{12\xi}(r_k + 2r_{k+1})I_{k+1}. \quad (142)$$

From now on, a new notation is used for current and internal resistance. $I_{m,n}$ represents the current at $(m\Delta Z, n\Delta T)$ point and $r_m$ represents the internal resistance at $z = m\Delta Z$. The two current integrals are now evaluated along the whole wire. The final result is

$$\begin{aligned}
&\int_{-l}^{l} \left[ \int_{-\pi}^{\pi} \frac{d\phi'}{8\pi^2\sqrt{(z - z')^2 + 4a^2 \sin^2(\phi'/2)}} + \frac{\sigma(z')}{2\xi} \right] i\left(z', t - \frac{|z - z'|}{c}\right) dz' \\
&= \left[2T_1^0 + \frac{\Delta Z}{12\xi}(r_{m+1} + 4r_m + r_{m-1})\right] I_{m,n} \\
&\quad + \sum_{k=1}^{M_2-1} \left[T_1^k + T_2^{k-1} + \frac{\Delta Z}{12\xi}(r_{m+k+1} + 4r_{m+k} + r_{m+k-1})\right] I_{m+k,n-k} \\
&\quad + \sum_{k=1}^{M_1-1} \left[T_1^k + T_2^{k-1} + \frac{\Delta Z}{12\xi}(r_{m-k+1} + 4r_{m-k} + r_{m-k-1})\right] I_{m-k,n-k} \qquad (143)
\end{aligned}$$

where $M_1$ and $M_2$ are the number of points to the left and right, respectively, from the testing point. They are given by

$$M_1 = MIN(n, 2L + m) \qquad (144)$$

$$M_2 = MIN(n, 2L - m). \qquad (145)$$

The expression (143) can also be written as

$$\begin{aligned}
&\int_{-l}^{l} \left[ \int_{-\pi}^{\pi} \frac{d\phi'}{8\pi^2\sqrt{(z - z')^2 + 4a^2 \sin^2(\phi'/2)}} + \frac{\sigma(z')}{2\xi} \right] i\left(z', t - \frac{|z - z'|}{c}\right) dz' \\
&= \left[2T_1^0 + \frac{\Delta Z}{12\xi}(r_{m+1} + 4r_m + r_{m-1})\right] I_{m,n} + X_{m,n} \qquad (146)
\end{aligned}$$

where $X_{m,n}$ is the contribution from known currents, given by

$$\begin{aligned}
X_{m,n} = &\sum_{k=1}^{M_2-1} \left[T_1^k + T_2^{k-1} + \frac{\Delta Z}{12\xi}(r_{m+k+1} + 4r_{m+k} + r_{m+k-1})\right] I_{m+k,n-k} \\
&+ \sum_{k=1}^{M_1-1} \left[T_1^k + T_2^{k-1} + \frac{\Delta Z}{12\xi}(r_{m-k+1} + 4r_{m-k} + r_{m-k-1})\right] I_{m-k,n-k}. \qquad (147)
\end{aligned}$$

In SDIP2 code, it is assumed that the electromagnetic pulse is incident perpendicular to the dipole. Therefore, at a given time, electric field is the same all along the dipole. Let $e_n = e^i(n\Delta T)$. The retarded electric field integral is evaluated using the trapezoidal rule:

$$\int_{-l}^{l} e^i\left(z', t - \frac{|z-z'|}{c}\right) dz' = e_n + \frac{1}{2}e_{n-M_1} + \frac{1}{2}e_{n-M_2} + \sum_{k=1}^{M_2-1} e_{n-k} + \sum_{k=1}^{M_1-1} e_{n-k}. \quad (148)$$

Let this value be equal to $Y_{m,n}$.

The function $f_1$ in (102) is a constant along a given 'characteristic line' with a positive gradient. ('characteristic lines' are simply the diagonal straight lines shown in Figure 19.) This constant value of $f_1$ is denoted by $\alpha$. Similarly, $f_2$ is constant, denoted by $\beta$, along a given characteristic line with negative slope. All the positive-slope lines which meet $t = 0$ axis has zero $\alpha$ value. All such negative-slope lines have zero $\beta$ value. All other positive-slope lines start at some point on $z = -l$ axis. The value of $\alpha$ for these lines is evaluated at this point, by considering the boundary condition $I_{-2L,n} = 0$. Similarly, $\beta$ for all other negative-slope lines are evaluated at the points they start, considering $I_{2L,n} = 0$. As the dipole is symmetrically excited, $\alpha$ and $\beta$ values are the same for corresponding lines, and therefore only $\alpha$ needs to be computed.

Combining (102), (146), (147) and (148), the unknown current $I_{m,n}$ can be calculated when $m \neq 2L$. This is further described in the next section. When $m = 2L$, the current is zero and then, $\alpha$ is calculated.

### 4.3.3 Description of Codes

#### SDIP1

The SDIP1 Fortran code is listed in Appendix C. The code uses the the following notation:

| | | |
|---|---|---|
| dipole length (m) | $l$ | LEN |
| dipole radius (m) | $a$ | RAD |
| no. of segments | $2N+1$ | 2*RANGE+1 |
| segment length (m) | $\Delta Z$ | DELZ |
| time step (s) | $\Delta T$ | DELT |
| | $\psi$ | PSI |
| time (ns) | $t$ | TIME |
| current (A) | $I_{i,j}$ | C(I,J) |
| current sum (A) | $\sum_{k=1}^{j} I_{i,k}$ | CS(I,J) |
| surface resistance ($\Omega/\square$) | $\rho_i$ | RHO(I) |
| internal resistance ($\Omega$/m) | $\rho_i/(2\pi a)$ | R(I) |
| terminal resistance ($\Omega$) | $R_L$ | RLOAD |
| incident field (V/m) | $E^i_{i,j}$ | EINC(I) |
| $A$-coefficients | $A_0 - A_3$ | ASEL0-ASEL3 |
| $B$-coefficients | $B_{0,l} - B_{4,l}$ | AMUT0(L)-AMUT4(L) |

The terminal resistance is distributed along the $0^{th}$ segment. The coefficients $A_0 - A_3$ are calculated according to (113-116) and $B_{0,l} - B_{4,l}$ according to (120-124). All the segment-currents at $1^{st}$ time-step are calculated first, starting from the $0^{th}$ segment. Then, it jumps to $2^{nd}$ time-step. This is repeated as much as needed. The total number of steps is equal to TOP.

When the current C(I,J) is calculated, the contribution to the scattered field at the $(i,j)$ testing point due to known $i^{th}$ segment currents is evaluated and stored as SELF. Then, the contribution from all the other segments is calculated (OTHERS). Finally the contribution from the incident field is added and the unknown current is calculated according to (123). Due to the symmetrical excitation of the dipole, C(-I,J)=C(I,J).

## SDIP2

The Fortran code SDIP2 is listed in Appendix D. This code uses the following notation:

| | | |
|---|---|---|
| dipole length (m) | $l$ | LEN |
| dipole radius (m) | $a$ | RAD |
| no. of points | $4L+1$ | 4*L+1 |
| point separation (m) | $\Delta Z$ | DELZ |
| time step (s) | $\Delta T$ | DELT |
| | $\psi$ | PSI |
| time (ns) | $t$ | TIME |
| norm. current (V) | $\xi I_{m,n}$ | C(M,N) |
| internal resistance ($\Omega$/m) | $r_i$ | R(I) |
| norm. internal resistance | $(r_i\Delta Z)/\xi$ | RD(I) |
| norm. terminal resistance | $R_L/\xi$ | RL |
| incident field (V/m) | $e_k$ | EINC(K) |
| | $S_1^K, S_2^K$ | S1K, S2K |
| | $T_1^k, T_2^k$ | T1(K), T2(K) |
| | $f_1(k\Delta Z - l)$ | ALPHA(K) |
| | $f_2(k\Delta Z + l)$ | ALPHA(K) |
| | $M_2$ | NN |
| | $M_1$ | MM |

$S_1^0$ and $S_2^0$ are calculated following (138) and (139). Approximate expressions (135) and (136) are used to calculate $S_1^k$ and $S_2^k$, for $k \neq 0$. $T_1^k$ and $T_2^k$ are calculated following (131) and (132). The electric field integral is evaluated according to (148). The V(K) in the code is in fact equal to $e_k\Delta Z$. The contribution from known currents is calculated according to (147).

Finally, the current is calculated as follows. If the $m^{th}$ point is the end point at $z = l$ (*i.e.* $m = 2L$), then current is zero. In this case, the value of ALPHA(N) is calculated according to the following expression, which is derived from (102);

$$\alpha_n = X_{m,n} - Y_{m,n} + \frac{R_L}{2\xi} I_{0,n-2L} - \alpha_{n-4L}. \tag{149}$$

If $n \leq 2L$, the term due to terminal resistance can be neglected. If $n \leq 4L$, $\alpha_{n-4L}$ is zero.

If $m = 0$, the contribution from the terminal resistance also involves the unknown current $I_{0,n}$. In this case, current is calculated according to

$$\left[2T_1^0 + \frac{\Delta Z}{12\xi}(r_1 + 4r_0 + r_1) + \frac{R_L}{2\xi}\right] I_{0,n} = Y_{0,n} - X_{0,n} + 2\alpha_{n-2L}. \tag{150}$$

If $m$ is neither equal to zero nor $2L$, the current is calculated according to

$$\left[2T_1^0 + \frac{\Delta Z}{12\xi}(r_{m+1} + 4r_m + r_{m-1})\right] I_{0,n} = Y_{m,n} - X_{m,n} - \frac{R_L}{2\xi} I_{0,n-m} + \alpha_{m+n-2L} + \alpha_{n-m-2L}. \tag{151}$$

Because of symmetrical excitation,

$$I_{-m,n} = I_{m,n}.$$

## 4.4 Numerical Results

### From SDIP1

A Gaussian electromagnetic pulse with a half-magnitude pulse width (PWHM) of .53 ns and a peak magnitude of 1 V/m is incident on a 1m-long unloaded dipole, from a direction perpendicular to the dipole. The incident electric field is parallel to the dipole. The diameter of the dipole is 8.3 mm ($l/a = 120$). Assume that the terminals are short-circuited. The dipole was divided into 61 segments and the current was computed using the SDIP1 code. The current distribution in one half of the dipole is shown in Figure 20. When the dipole is terminated with a 100 Ω resistance, the current distribution is as shown in Figure 21. Both figures show the 'reflections' from the two ends, which propagate back and forth at the speed of light. In addition, Figure 21 shows some reflections starting at the terminals. This must be due to the 'mismatch' caused by the 100 Ω termination. The current in the terminated dipole decays much faster than in the short-circuited dipole, obviously due to the dissipation at the termination.

Current distribution in several resistively-loaded straight dipoles was also calculated. These dipoles have the same dimensions as the unloaded dipole. All of them have the

parabolic resistance profile given by

$$r(z) = \frac{r(0)\, l}{l - |z|} \tag{152}$$

where $r(z)$ is the internal resistance at a distance $z$ from the terminals and $l$ is the half length of the dipole. Such a loaded dipole, terminated with a resistance $R_L$, is shown in Figure 22. A dipole with this resistance profile approximates the WK nonreflecting dipole when $r(0)$ is equal to the particular value given by [27]

$$r(0) = \frac{\xi}{2\pi l} \Re(\Psi) \tag{153}$$

where

$$\Psi = 2[\sinh^{-1} \frac{l}{a} - C(2ka, 2kl) - jS(2ka, 2kl)] + \frac{j}{kl}(1 - e^{-j2kl}) \tag{154}$$

$$C(\alpha, x) = \int_0^x \frac{1 - \cos\sqrt{u^2 + \alpha^2}}{\sqrt{u^2 + \alpha^2}}\, du \tag{155}$$

$$S(\alpha, x) = \int_0^x \frac{\sin\sqrt{u^2 + \alpha^2}}{\sqrt{u^2 + \alpha^2}}\, du \tag{156}$$

and $a$ is the dipole radius. Since a perfectly conducting dipole has the first resonant frequency approximately at $c/(4l)$, for broadband operation, the WK dipole is usually made nonreflective at this frequency. Therefore, when $\Psi$ is calculated, it is assumed that $kl = \pi/2$. Nonetheless, it has been shown that the real part of $\Psi$ is a slowly varying function of frequency for $kl \leq \pi/2$ [29]. According to above expressions, a 1 m long, 8.3 mm thick WK dipole has an internal resistance of 919.6 $\Omega$/m at the center of the dipole.

The current distribution in the WK dipole excited by the .53 ns Gaussian incident pulse is shown in Figure 23. The terminals are short-circuited. It can be seen that the 'reflections' from the ends have virtually disappeared as a result of the internal resistance. If the internal resistance of the dipole is increased by a factor 5, the current distribution will be as shown in Figure 24. One significant effect of this 'overloading' is that the peak current along the dipole now has an almost linear variation in space. If the internal resistance of the WK dipole is reduced by a factor of 5, the current distribution will be as shown in Figure 25. This internal resistance is not sufficient to suppress the end 'reflections'.

When the WK dipole is terminated with a 100 Ω resistance, the current distribution takes the shape shown in Figure 26. It can be seen that the current maximum no longer occurs at the terminals. If the termination resistance is increased to 1 kΩ, the terminal current will drop significantly, as shown in Figure 27. The terminal current waveform also changes significantly.

### From SDIP2

The same WK antenna described in the previous section was analyzed using the SDIP2 code. The same .53 ns Gaussian incident pulse was used as the excitation. The current was computed using 81 points on the dipole. The current distribution in the dipole, terminated with a 100 Ω resistance, is shown in Figure 28. This may be compared with the current distribution obtained from SDIP1 (shown in Figure 26). The terminal current waveform obtained from SDIP1 is compared with the waveform obtained from SDIP2, in Figure 29. An excellent agreement between the two methods can be noticed.

Numerical results to follow are normalized so that one can easily adopt them to dipoles with different lengths. The distributed resistance is normalized according to

$$\gamma(z) = \frac{\tau(z)\, l}{\xi}. \tag{157}$$

A half-length to radius ratio ($l/a$) of 120 is assumed in all cases. For a WK dipole, this results $\gamma(0) = 1.2$. The time-domain response of the WK antenna, terminated with a 100Ω resistance is shown in Figure 30 (which also corresponds to a WK monopole with a 50 Ω termination.) The incident pulse has a Gaussian waveform with a PWHM of $0.24l/c$. It can be seen that the WK dipole has a slower rise time and decay time, when compared with the incident pulse. The 24% undershoot and the stretching of the pulse caused by the WK dipole is clearly unacceptable in many time-domain applications. In order to improve the pulse-receiving characteristics, one may consider using a distributed resistance much higher than the WK value. Consider a heavily loaded (HL) dipole, with $\gamma(0) = 20$, terminated with a 100 Ω resistance. It has the terminal voltage waveform shown in Figure 31, when excited by the $0.24l/c$ Gaussian pulse. The voltage waveform peak is now well-placed due to the fast rise time of the dipole. The fast decay time of the dipole results almost negligible

pulse stretching. The undershoot has been reduced to 2%. All these advantages come at the cost of considerable loss of sensitivity (approximately 5 times) . The time-domain response of the WK and HL dipoles were transformed to the frequency domain, using a Fast Fourier Transform algorithm. The normalized receiving transfer function, defined as

$$R_N(\omega) = \frac{V_L(\omega)}{E^i(\omega)\, l} \tag{158}$$

has been calculated. The magnitude and phase of the transfer function are shown in Figures 32 and 33, respectively. It can be seen that the HL dipole provides a broader bandwidth at the expense of peak sensitivity; its 3dB bandwidth ranges from $l/\lambda = 0.014$ to $l/\lambda = 3.0$. The peak normalized sensitivity is approximately 0.01 which is an order of magnitude lower than for the WK dipole.

The WK dipole is expected to have good pulse receiving characteristics when it is terminated with a highly resistive load. The response of the WK dipole, terminated with a 100 k$\Omega$ resistance is shown in Figure 34. In this case, the incident Gaussian pulse has a PWHM of $1.18l/c$. The response is significantly better when compared with a 100 $\Omega$ termination. The small delay of the peak of the response is due to the inherently slow rise time of the WK antenna, which is almost independent of the termination. The normalized receiving transfer function of the WK dipoles with different resistive terminations has been calculated and the results are shown in Figures 35 and 36. These results can be compared with the data available in the literature [34]. It is clear that the low frequency limit of the WK dipole can be lowered using a higher terminal resistance. The upper frequency limit is almost independent of the terminal resistance as long as the terminal resistance is sufficiently high ($> 1$ k$\Omega$). The WK dipole with a 100 k$\Omega$ termination has a 3dB bandwidth from $l/\lambda = 0.001$ to 0.4. For comparison, the normalized receiving transfer function of a WK dipole with a 10 k$\Omega$ termination has been calculated, directly in frequency domain, using the Numerical Electromagnetic Code (NEC) [95]. The magnitude and phase of $R_N$ are shown in Figures 37 and 38, respectively.

The normalized receiving transfer function of several resistively loaded dipoles, each with a 100 k$\Omega$ resistive termination, has been calculated and is presented in Figures 39

and 40. The internal resistance of the dipoles varies from $\gamma(0) = 0.3$ to $\gamma(0) = 4.8$. The objective of this analysis is to identify the dipole which performs best at higher frequencies. It can be seen that, the WK dipole with $\gamma(0) = 1.2$ has approximately the 'maximally flat' response at higher frequencies. Dipoles with lower distributed resistance have overshoots whereas those with higher distributed resistance have lower roll-off frequencies.

## 4.5 Discussion

It has been shown that an incident pulse can be distorted in several ways during reception. An antenna with slow rise time delays the peak of the response. Slow decay time of the antenna leads to a stretched response. A negative undershoot or a 'tail' is observed very often, usually after the duration of the incident pulse. It has been found that the rise time and decay time of the antenna are associated with the high frequency response while the undershoot or tail is determined by the low frequency response. In the case of a broadband nondispersive antenna, pulse stretching or the delay of the peak determines the fastest pulse the antenna can receive without distortion (*i.e.* the time-resolution of the antenna). The maximum duration of the pulse (that relates to the lower roll-off frequency or the frequency-resolution of the antenna) is determined by the undershoot or the 'tail' of the response.

The WK nonreflecting monopole, when terminated with a 50 $\Omega$ transmission line, does not have a sufficient bandwidth for the reception of electromagnetic pulses. One possible way of increasing the bandwidth is by increasing the distributed resistance, as done in the HL monopole. This type of design gives a broader bandwidth at the expense of the receiving sensitivity. A broader bandwidth can also be achieved, without sacrificing sensitivity, by terminating the WK monopole with a high-resistance load. Although such a design promises a higher sensitivity, an active (electronic or optical) transducer is needed to realize the high input resistance. The WK monopole terminated with a highly resistive load has the 'maximally flat' frequency response close to the upper roll-off frequency.

Design and performance parameters of a WK monopole and a HL monopole designed to

| Monopole type | HL | WK |
|---|---|---|
| Termination ($\Omega$) | 50 | 50 k |
| Upper 3 dB frequency (GHz) | 3 | 3 |
| Monopole length (cm) | 30 | 4 |
| Lower 3 dB frequency (MHz) | 14 | 7.5 |
| Peak sensitivity ($mV/(Vm^{-1})$) | 1.8 | 16.4 |
| Distributed resistance at center (k$\Omega$/m) | 25.1 | 11.3 |

Table 1: Comparison of WK and HL dipoles.

operate up to 3 GHz are listed in Table 1. The WK monopole is smaller in size, provides a broader bandwidth and better sensitivity, but requires a higher termination resistance(>5 k$\Omega$). The HL monopole is 7.5 times longer, operates with a conventional 50 $\Omega$ transmission line but has a two times narrower bandwidth and nine times lower sensitivity. The greatest advantage of such a monopole is that it can be connected to the oscilloscope or the recording device using a standard 50 $\Omega$ coaxial line, without additional hardware.

In summary, the pulse receiving characteristics of several resistively loaded straight dipoles have been analyzed in the time-domain. The frequency-domain receiving transfer function has been obtained using a Fast Fourier Transform algorithm. Two broadband antenna designs based on resistively loaded straight dipoles were considered and their advantages and limitations were discussed.

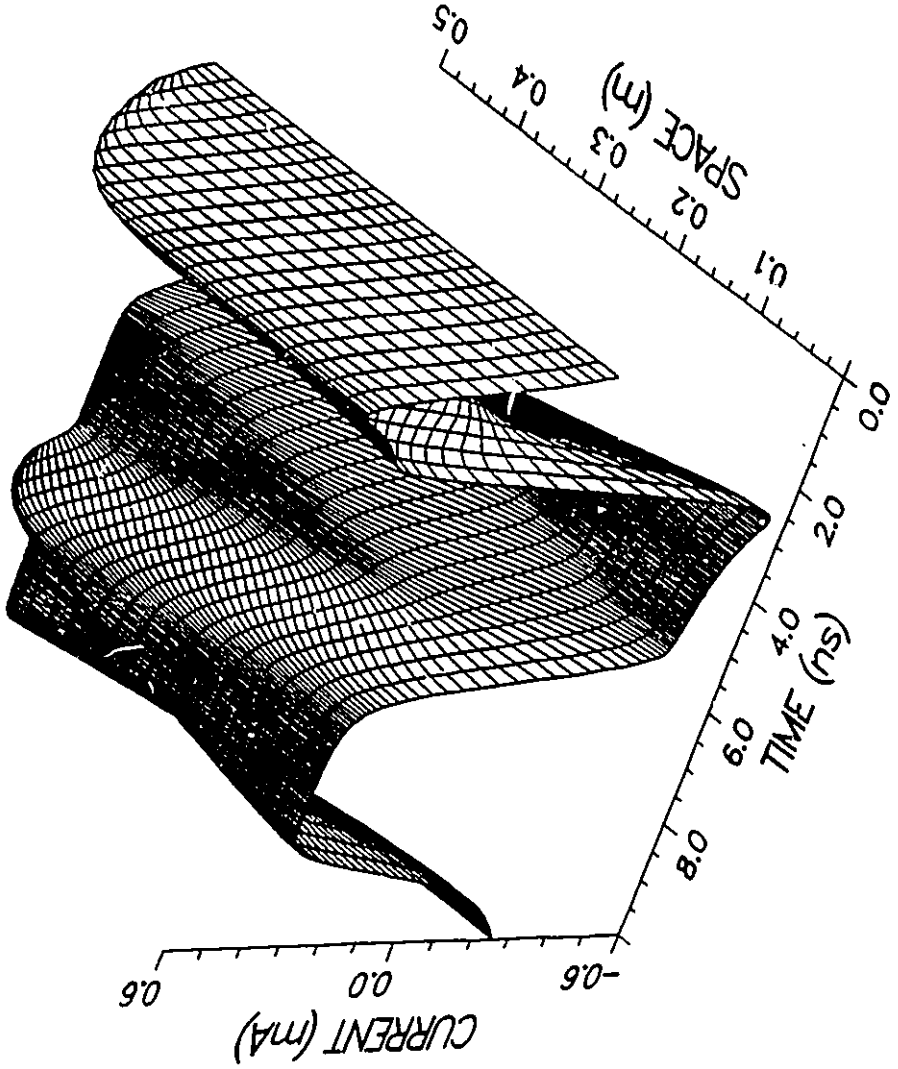


Figure 20: Current distribution in the unloaded dipole with 0 Ω termination.

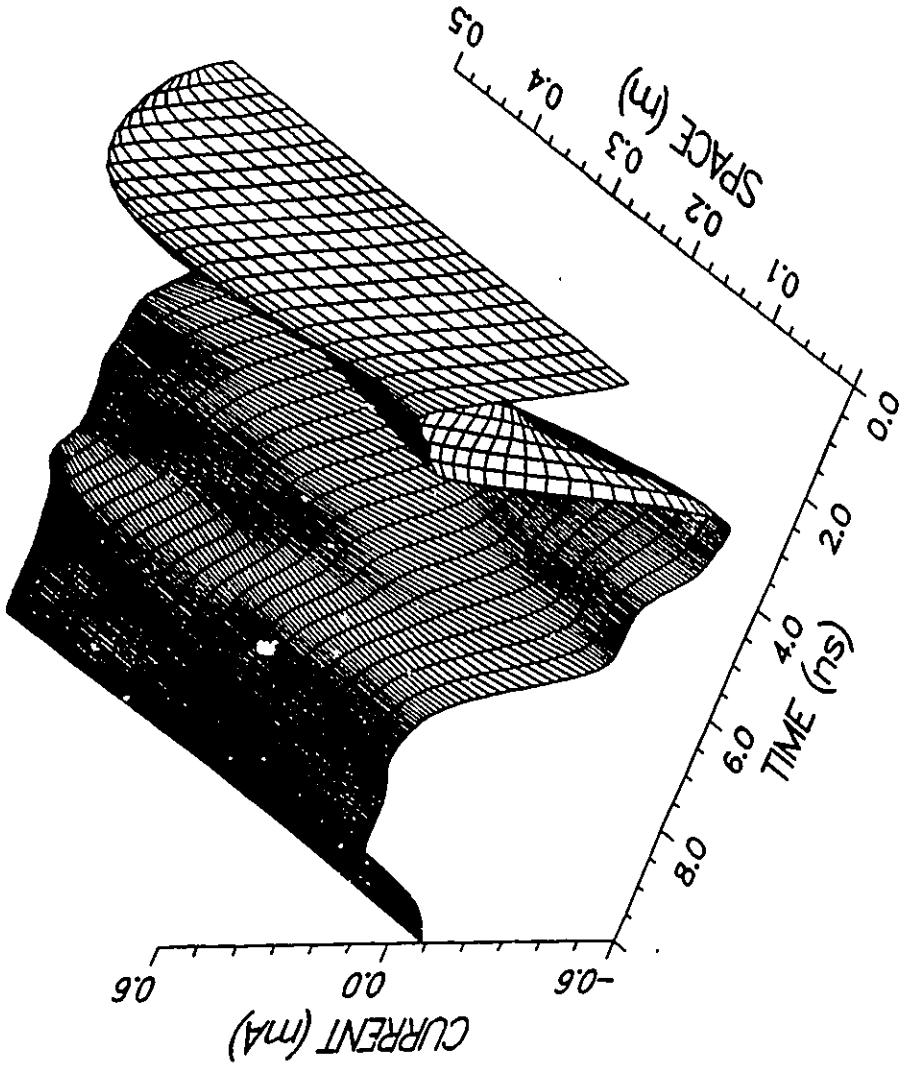


Figure 21: Current distribution in the unloaded dipole with 100 Ω termination.

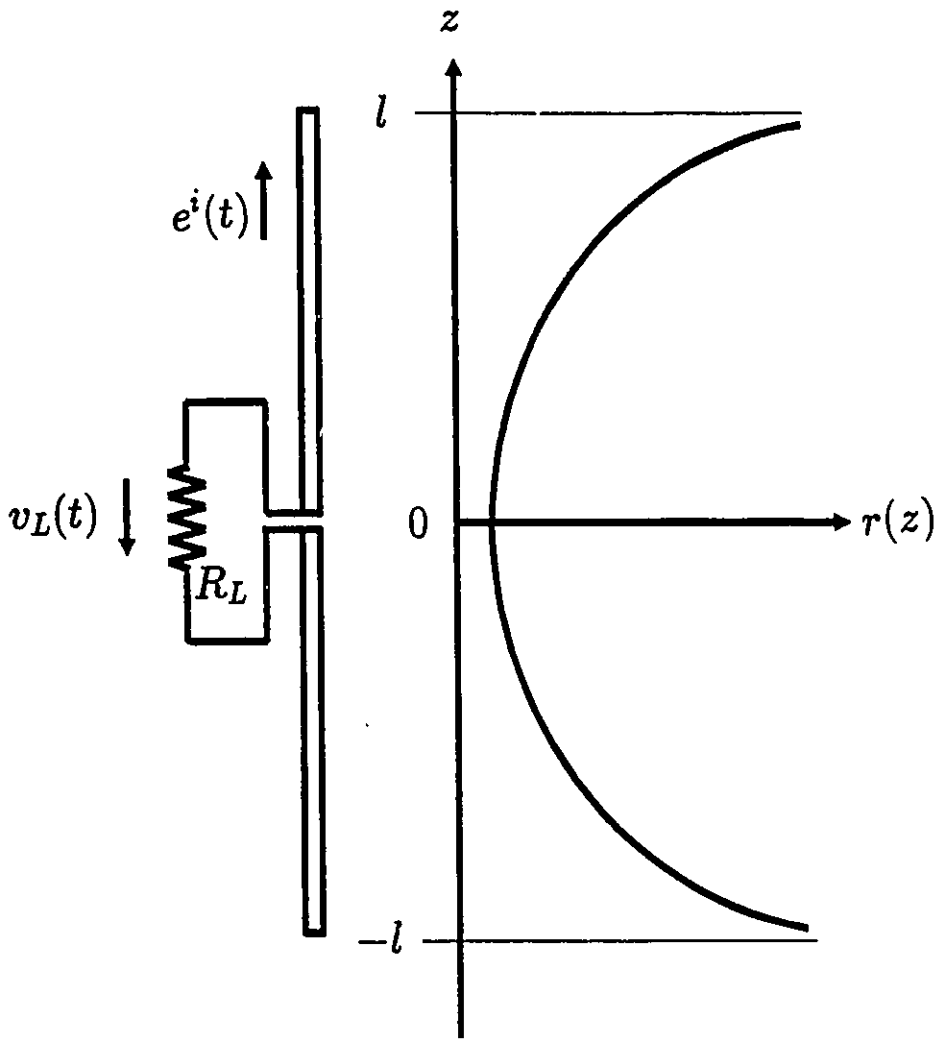


Figure 22: Resistively loaded straight dipole and the distributed resistance profile.

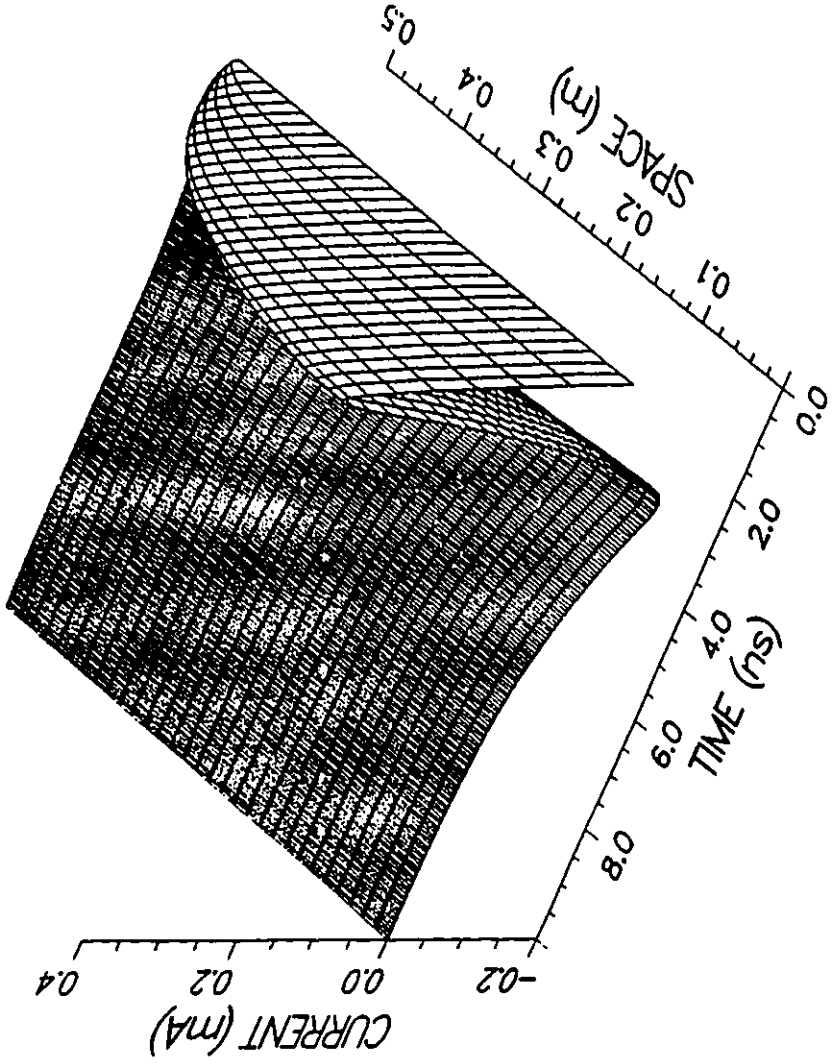


Figure 23: Current distribution in the WK dipole with 0 Ω termination.

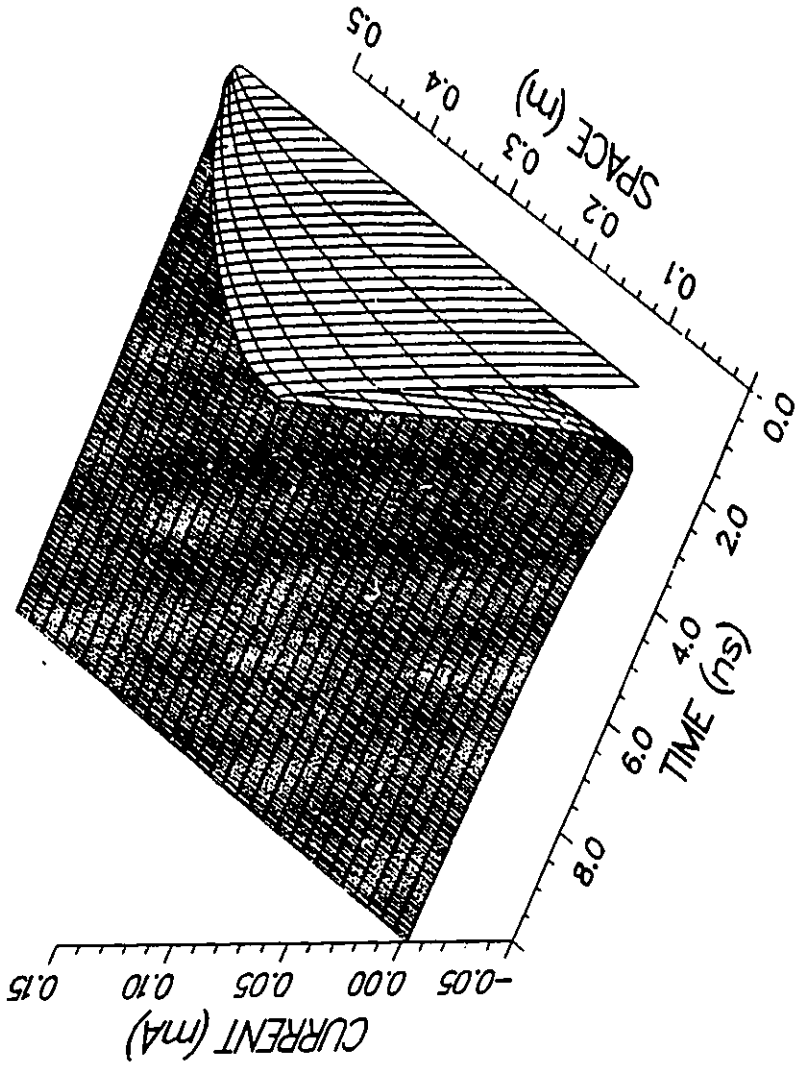


Figure 24: Current distribution in an 'overloaded' dipole with 0 Ω termination.

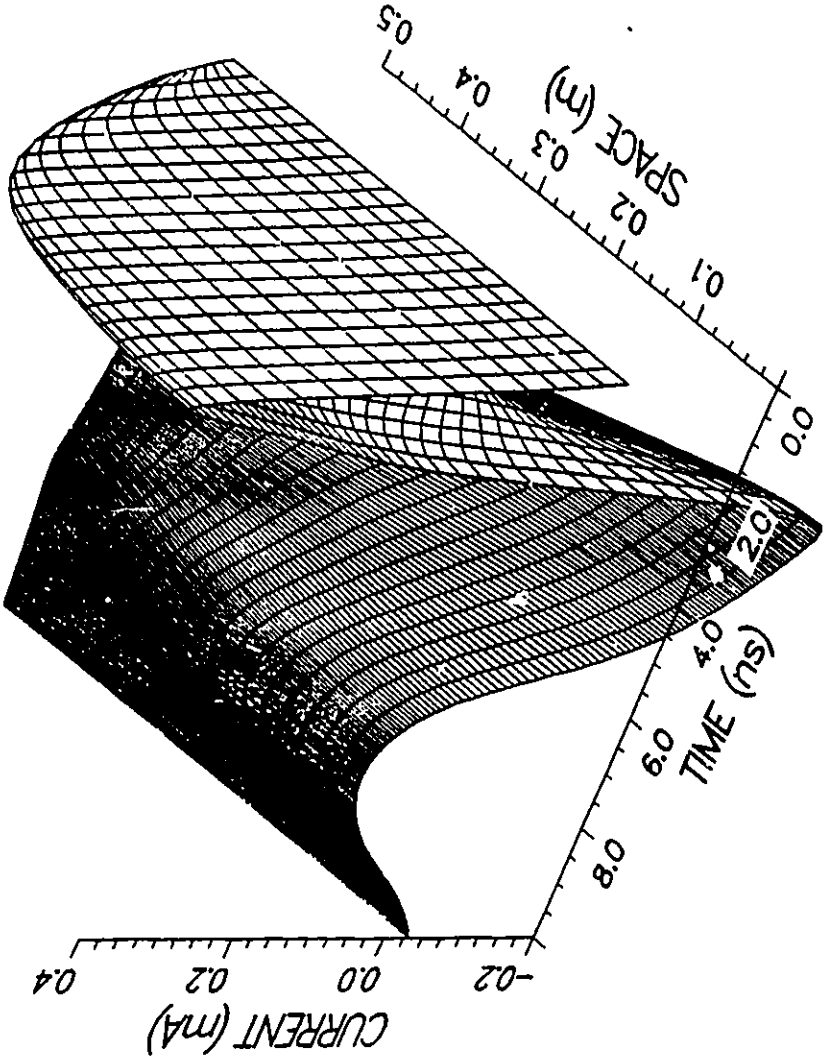


Figure 25: Current distribution in an 'underloaded' dipole with 0 Ω termination.

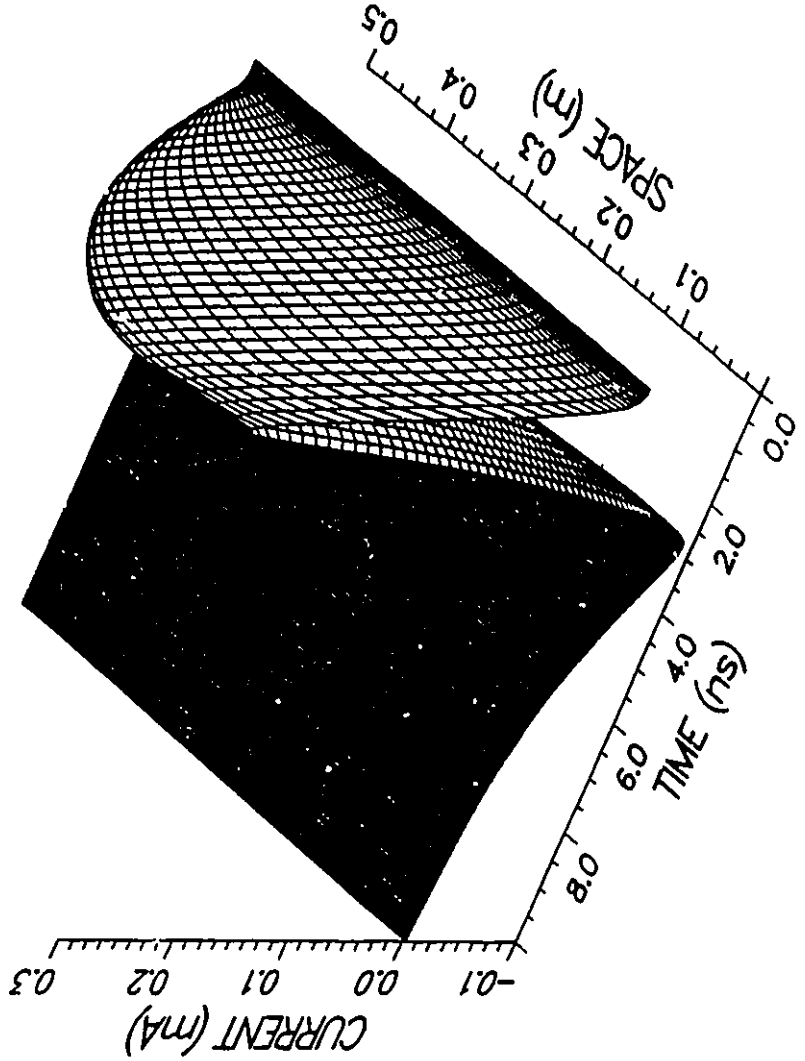


Figure 26: Current distribution in the WK dipole with 100 Ω termination- from SDIP1.

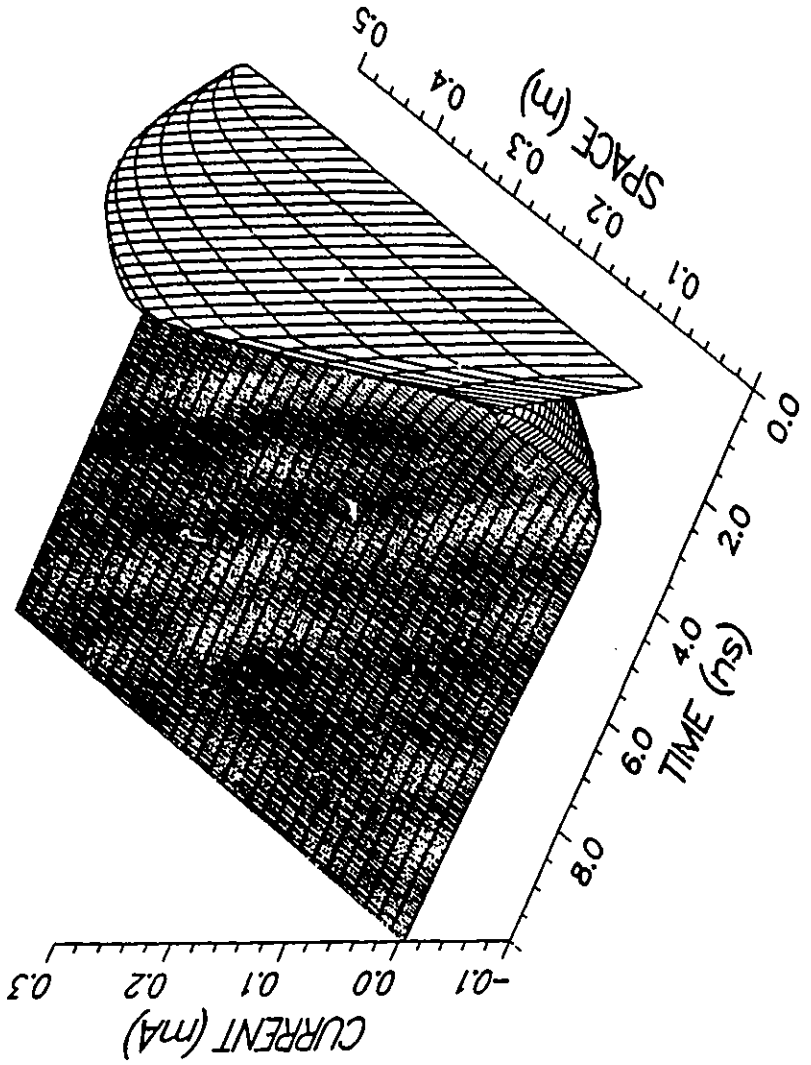


Figure 27: Current distribution in the WK dipole with 1 kΩ termination.

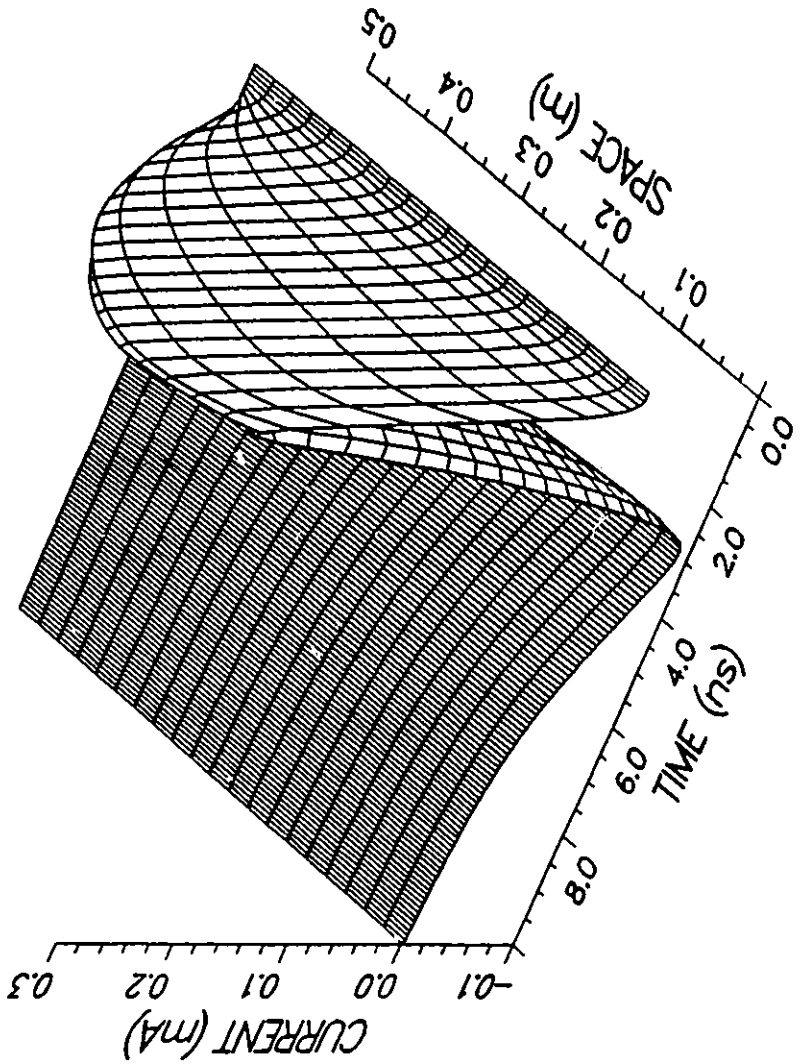


Figure 28: Current distribution in the WK dipole with 100 Ω termination- from SDIP2

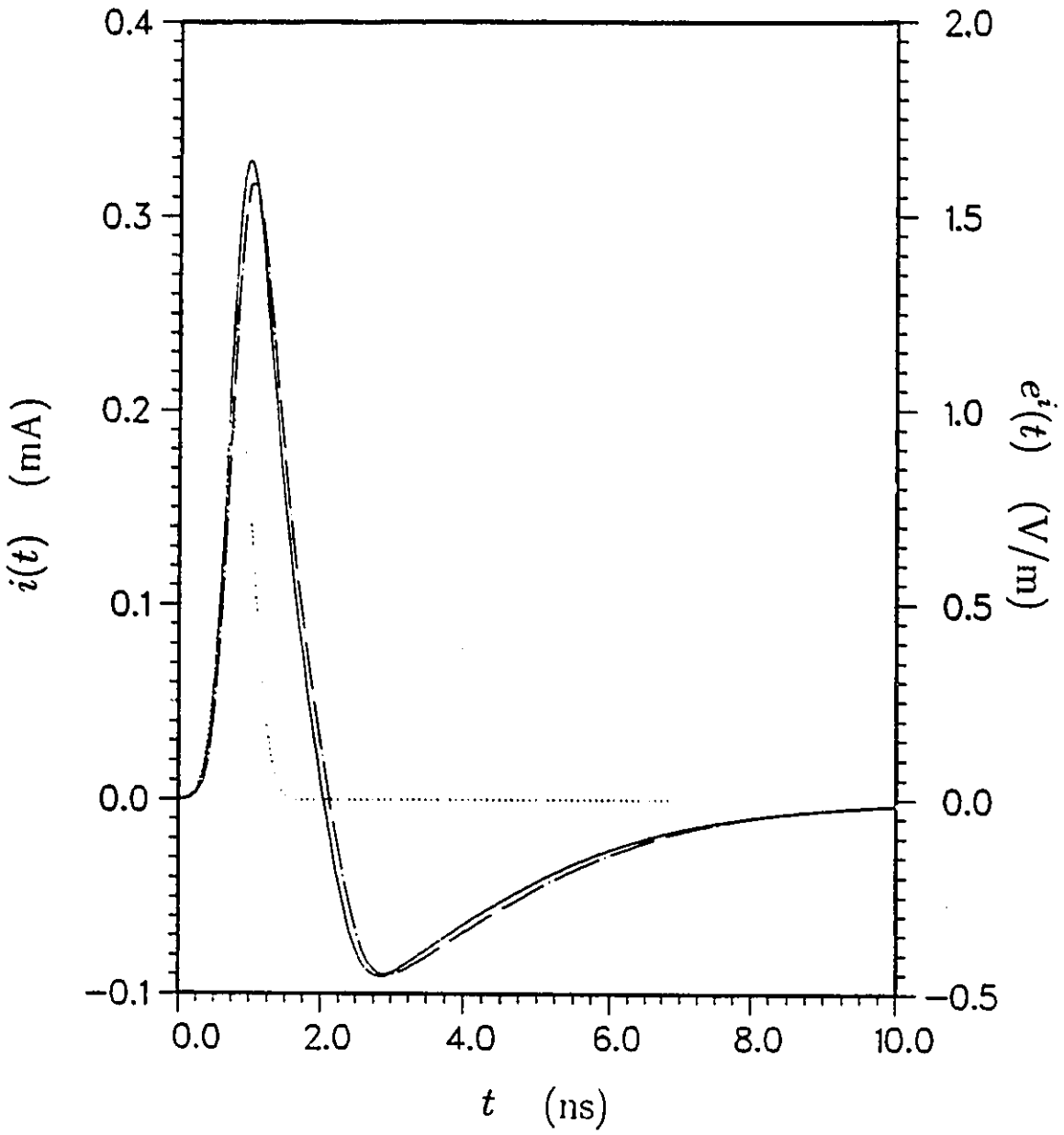


Figure 29: Terminal current waveform in the WK dipole with 100 Ω termination. Continuous line: from SDIP1, broken line: from SDIP2, dotted line: incident pulse.

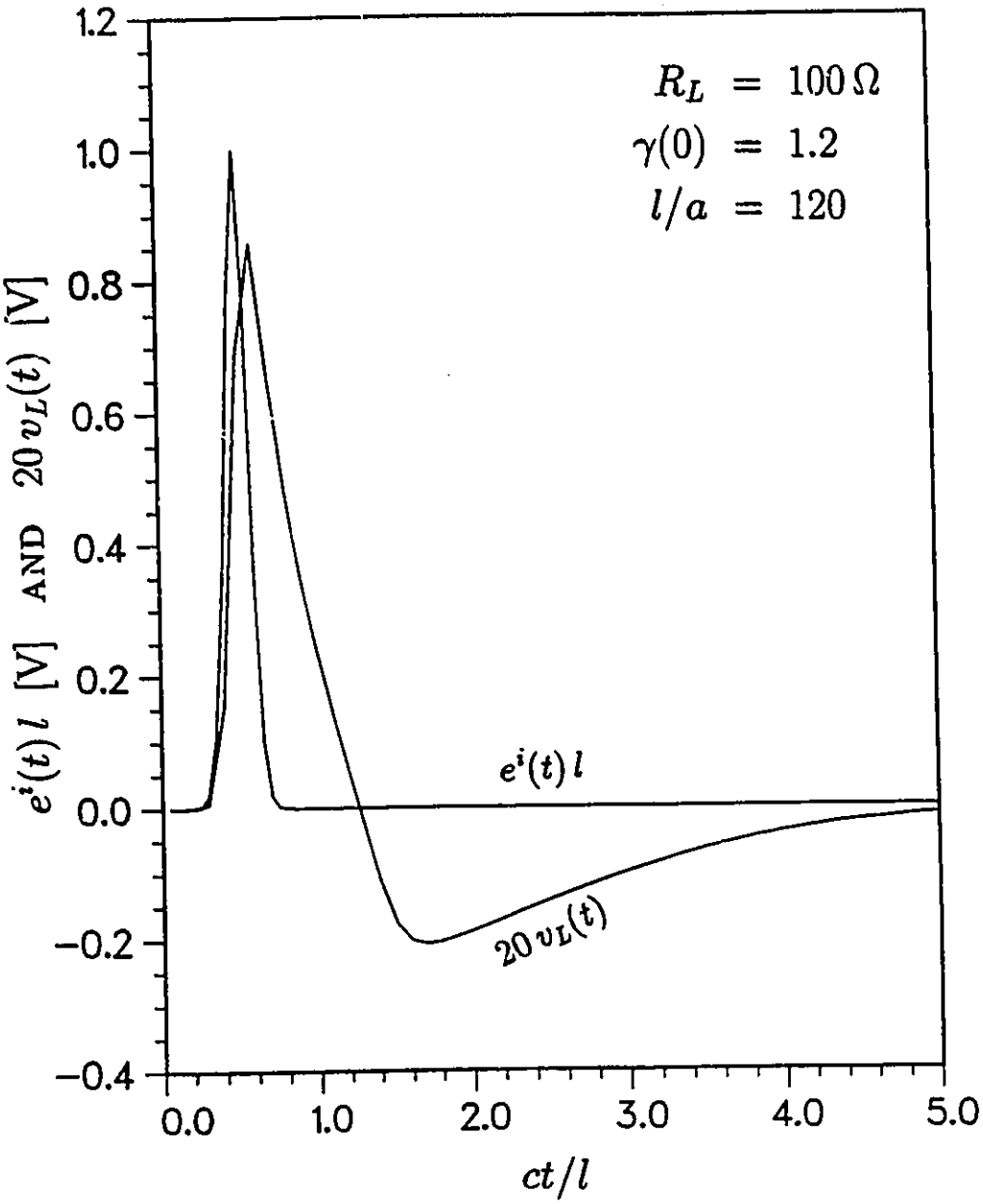


Figure 30: Time-domain response of the the WK dipole with 100 Ω termination.

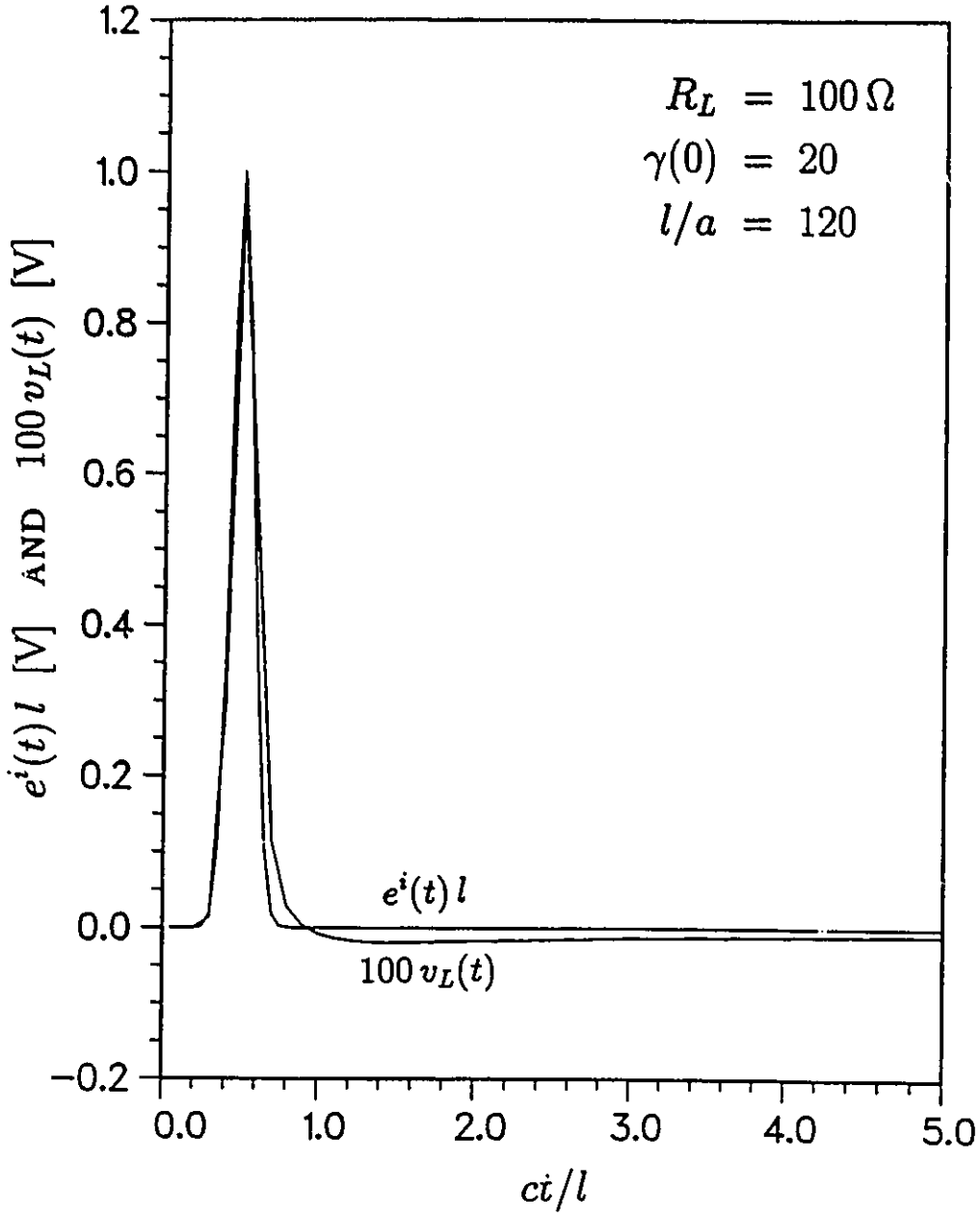


Figure 31: Time-domain response of the HL dipole with 100 Ω termination.

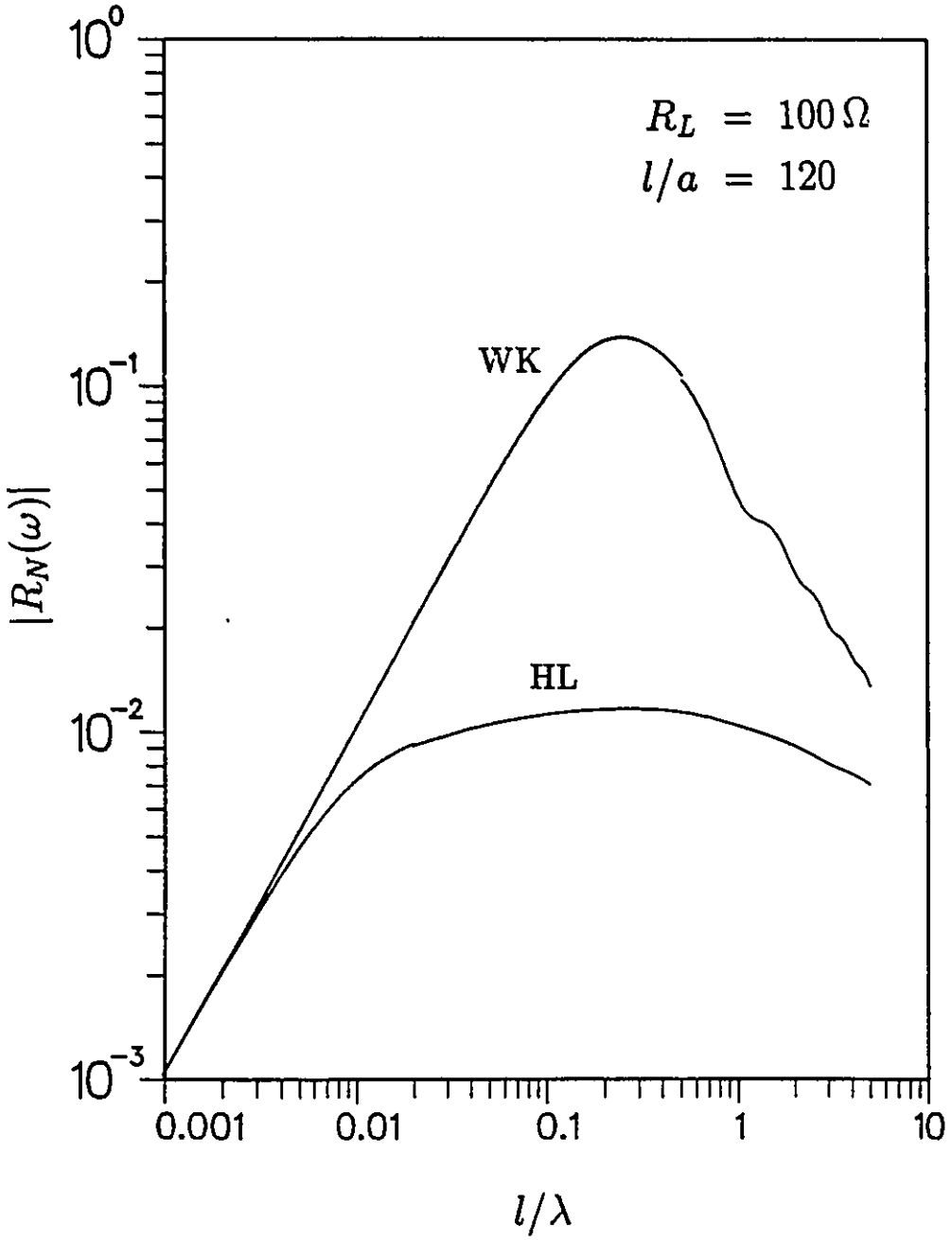


Figure 32: $|R_N|$ of the WK and HL dipoles with 100 Ω terminations.

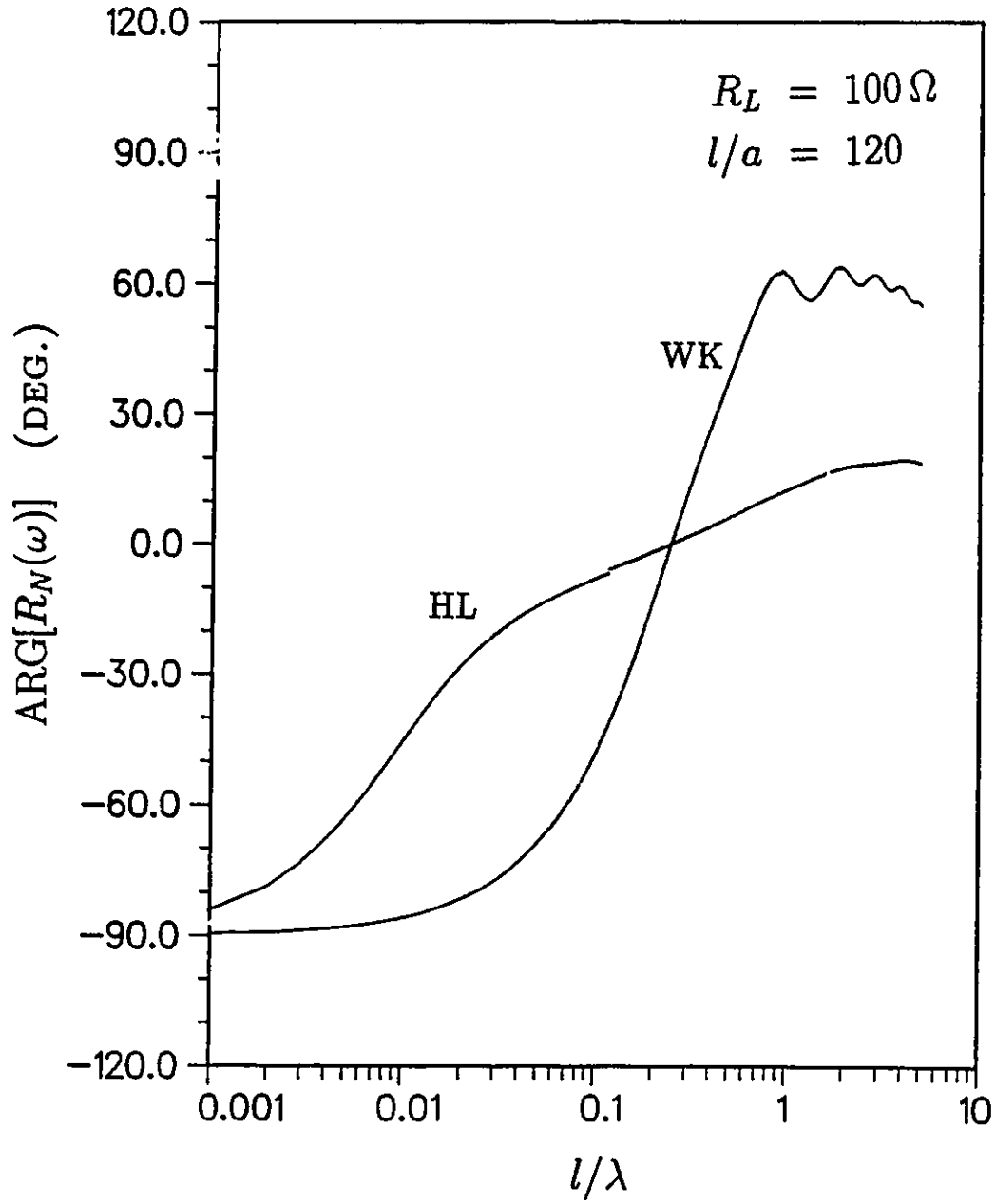


Figure 33: ARG($R_N$) of the WK and HL dipoles with 100 Ω terminations.

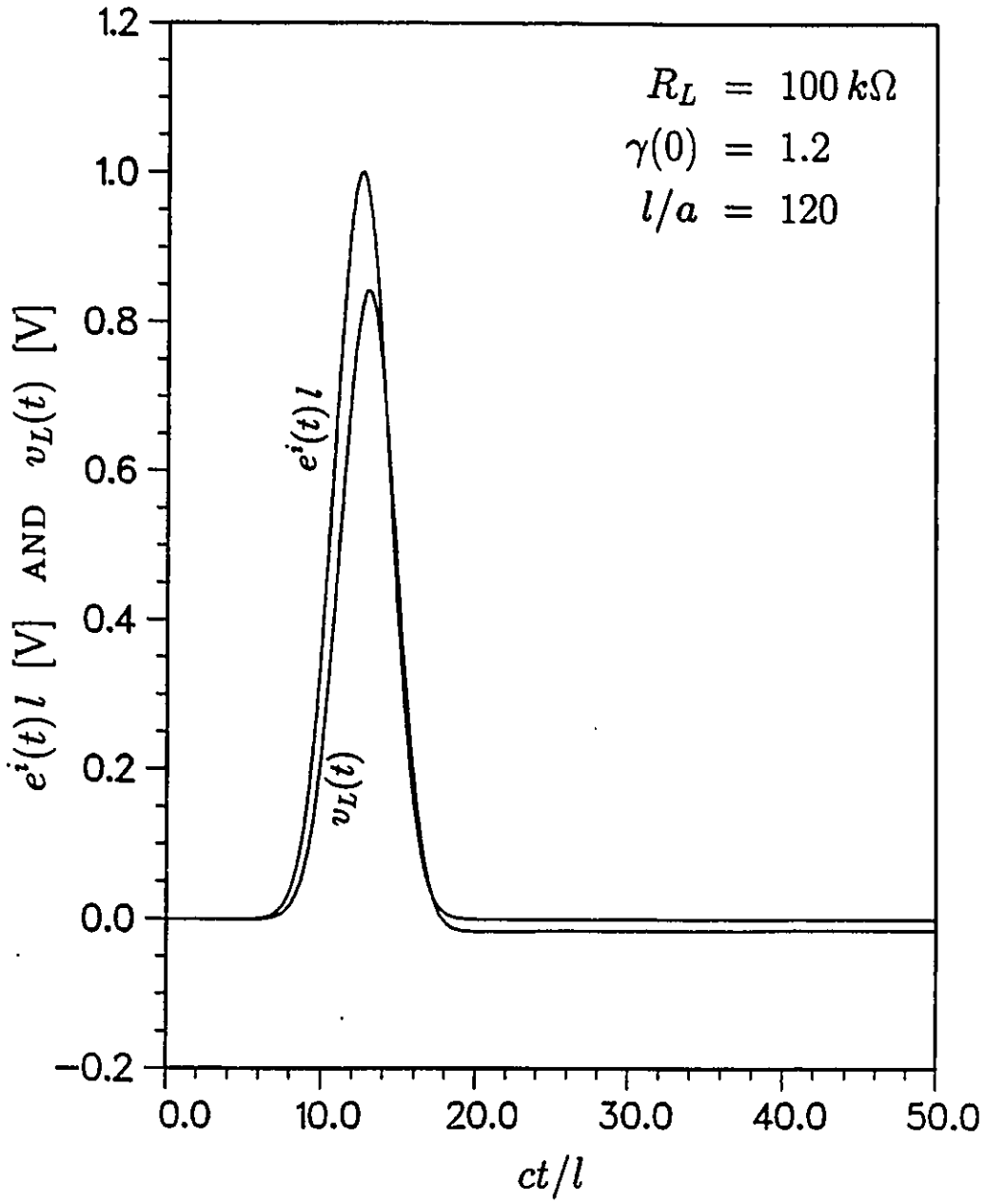


Figure 34: Time-domain response of the WK dipole with 100 kΩ termination.

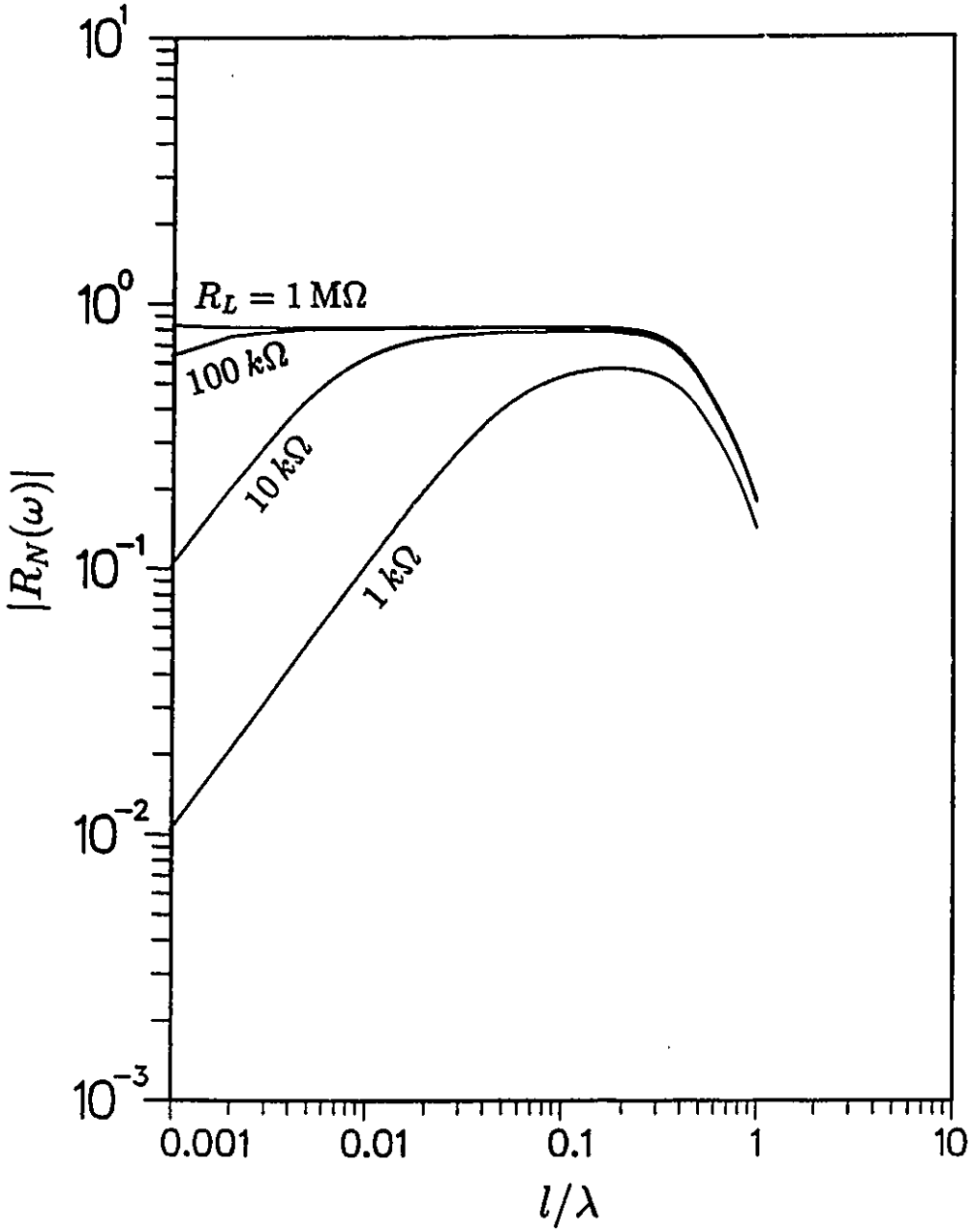


Figure 35: $|R_N|$ of the WK dipole with a high-resistance termination. Terminal resistance $R_L$ is shown as a parameter.

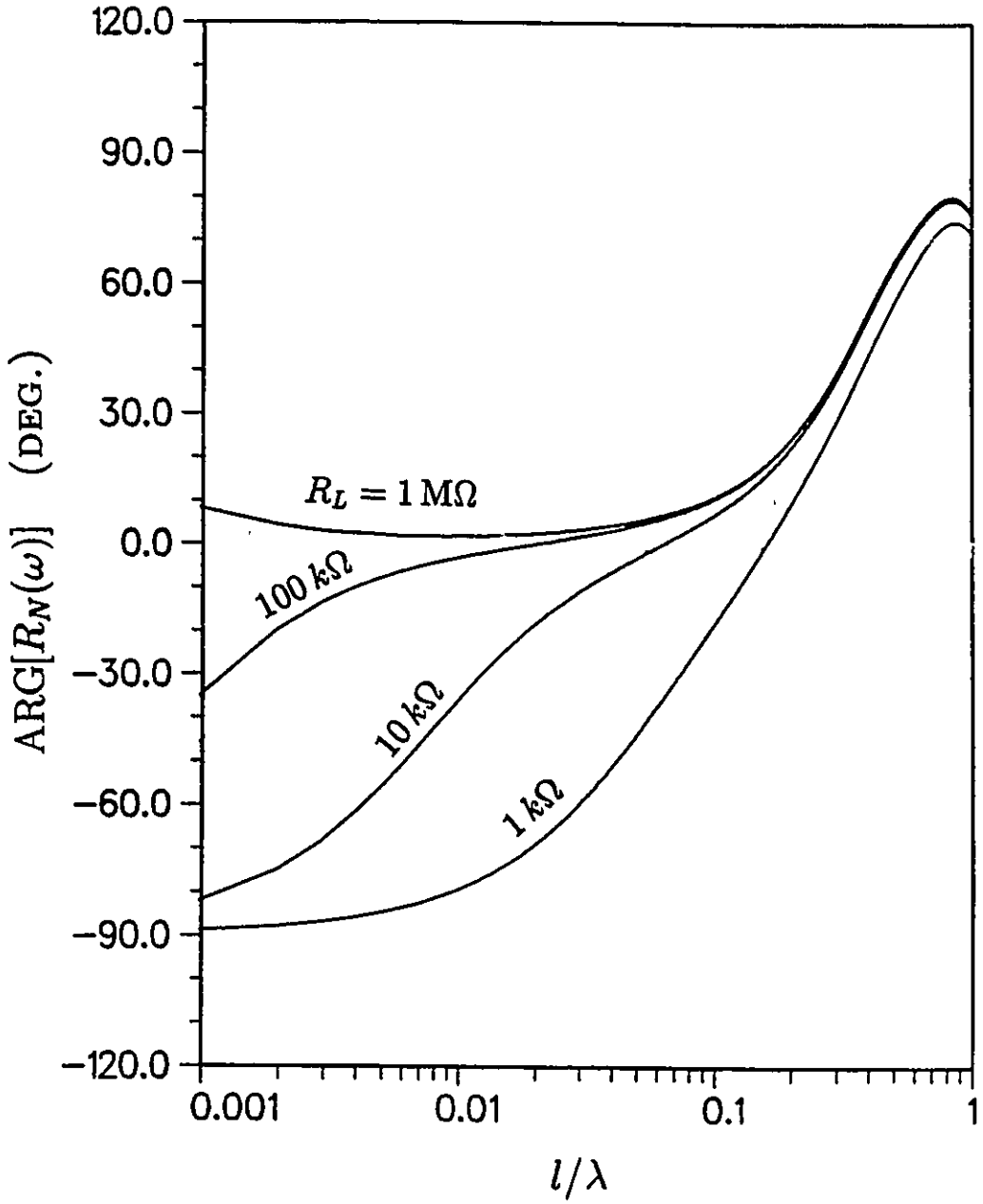


Figure 36: ARG($R_N$) of the WK dipole with a high-resistance termination. Terminal resistance $R_L$ is shown as a parameter.

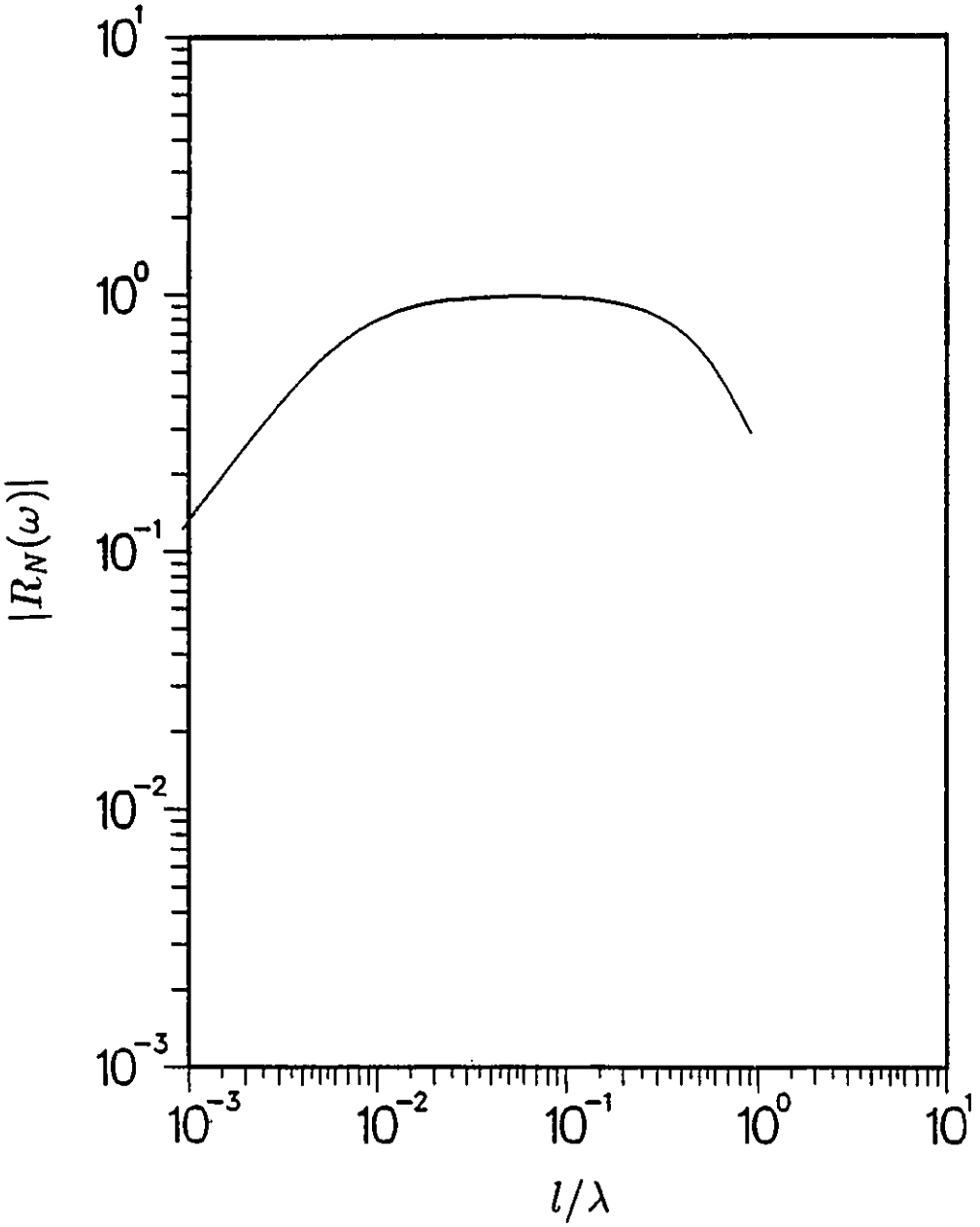


Figure 37: $|R_N|$ of the WK dipole with 10 kΩ termination- from NEC.

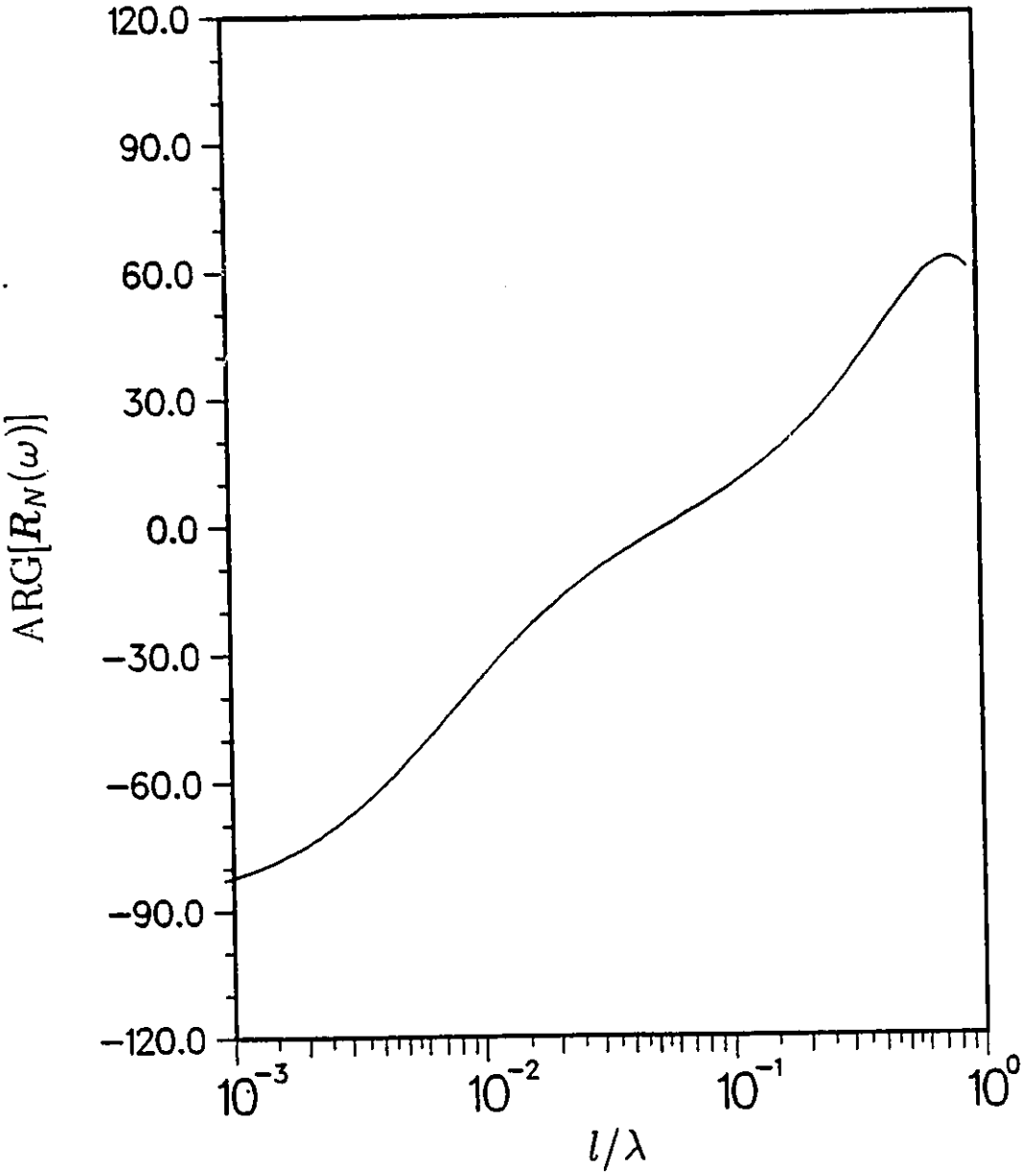


Figure 38: ARG($R_N$) of the WK dipole with 10 kΩ termination- from NEC.

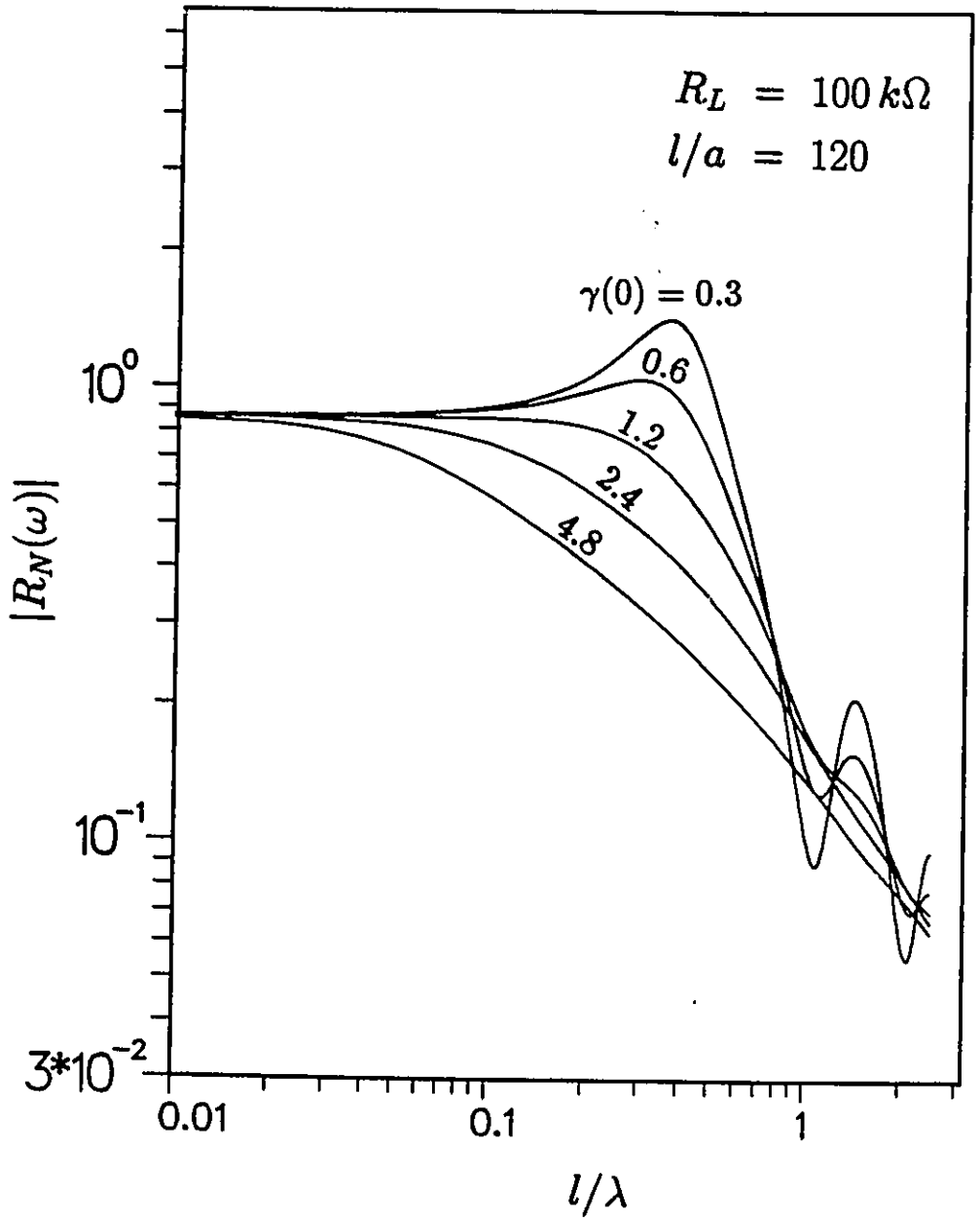


Figure 39: $|R_N|$ of various loaded dipoles with 100 kΩ terminations.

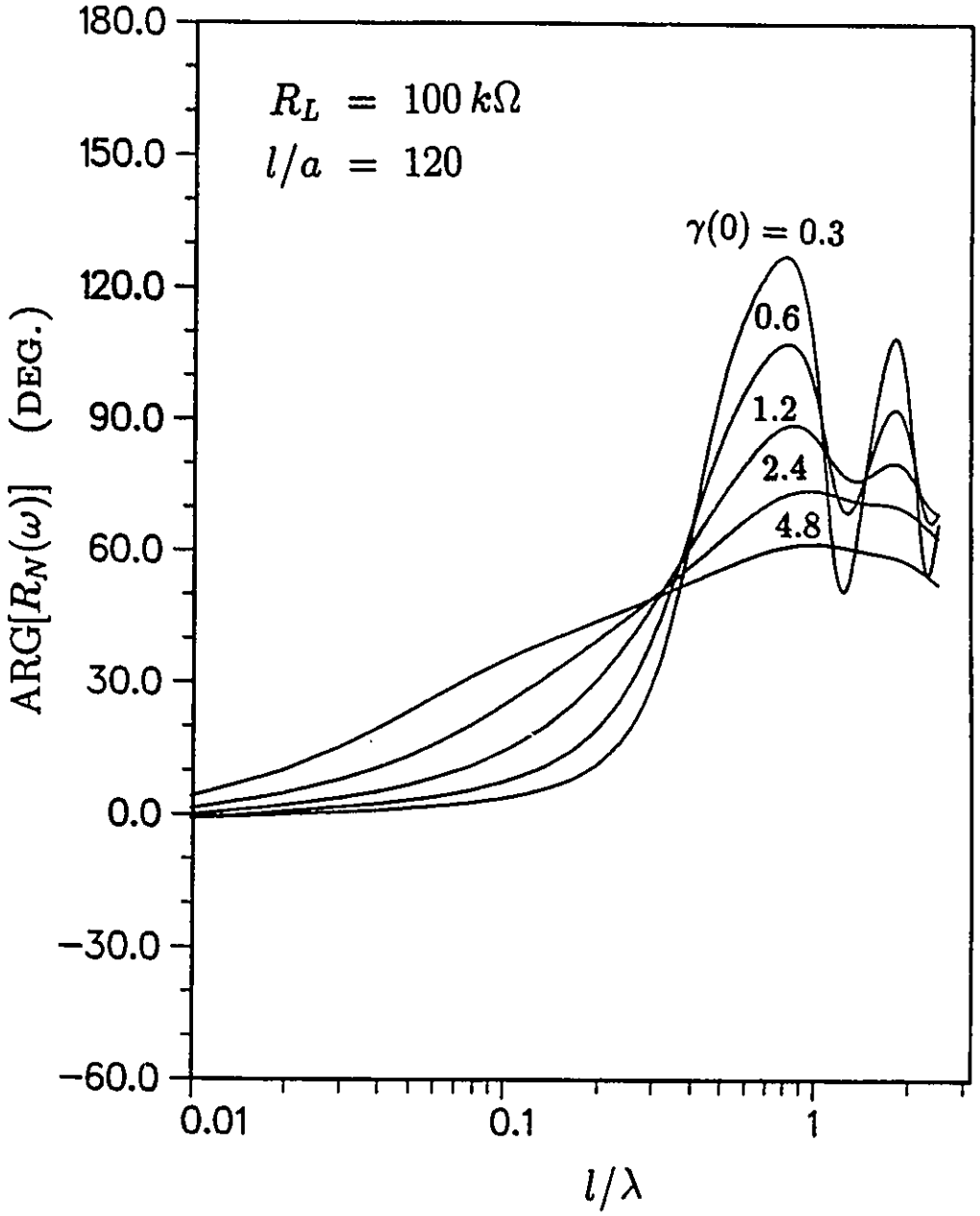


Figure 40: ARG($R_N$) of various loaded dipoles with 100 kΩ terminations.

# Chapter 5

# THE V-ANTENNA

## 5.1 Introduction

In the previous chapter, it was demonstrated that the Wu-King (WK) resistively-loaded straight dipole antenna has a broad receiving bandwidth with non-dispersive phase characteristics. However, in order to achieve this bandwidth, this antenna requires a high-impedance termination ($> 10$ k$\Omega$). This is not a limitation at frequencies below 1 GHz as active (FET) oscilloscope probes with megaohm impedances are commercially available. Further higher impedances can be obtained using electronic buffer amplifiers and photonic modulators [45, 46].

Some natural and man-made transient electromagnetic fields have sub-nanosecond rise times and, hence, gigahertz bandwidths. For high fidelity reception of such fields, receiving antennas operating up to 10 GHz (or higher) are required. Unfortunately, commercially available high-impedance (active) oscilloscope probes don't operate above 1 GHz. To extend any broadband antenna beyond 1 GHz, one has to either design a broadband active (electronic or photonic) high-impedance probe or use commercially available low-impedance (50 $\Omega$ or 500 $\Omega$) broadband passive probes.

As far as sub-nanosecond pulse reception is concerned, the WK antenna has two limitations. First is the bandwidth. The bandwidth obtained from a WK antenna with a 50 $\Omega$

or 500 Ω probe is not adequate for transient field measurements. Second is the sensitivity. The upper roll-off frequency of the WK antenna is mainly determined by the length. From the numerical results presented in the previous chapter, it can be seen that the wavelength at the upper roll-off frequency is approximately equal to the dipole length. A WK antenna operating up to 10 GHz is only a few centimeters long and therefore has a very low sensitivity.

To address these problems, one must look beyond the electrically-small sensors and WK-antennas. Only an electrically-large antenna can yield a good sensitivity at multi-gigahertz frequencies. One such electrically-large antenna considered in the past is the TEM horn. Both unloaded and resistively-loaded TEM horns have been developed [22, 24]. Nonetheless, the complicated geometry of this antenna does not allow an efficient and accurate theoretical analysis. Hence, most developments are based on previous experiment results, empirical formulae or approximate analytical expressions [25].

We selected the thin-wire resistively loaded V-antenna as a potential pulse receiver. The rationale behind this selection is as follows. Let us first compare the receiving characteristics of *perfectly conducting* straight dipoles with those of V-dipoles. The first null in the receiving transfer function of the perfectly conducting straight dipole occurs approximately at $f_n = c/l$, *i.e.* when the dipole is $2\lambda$ long. Yet, the first null of a perfectly conducting V-dipole occurs at much higher frequencies. For example, a V-dipole with a 75° V-angle has the first null approximately at $f_n = 5c/l$. In a resistively loaded straight dipole, the receiving transfer function null is not clearly visible. However, the effect of the null is still present as demonstrated by a rapid fall of the dipole response at higher frequencies. Consequently, when a V-dipole is loaded with a distributed resistance, the response is expected to fall off at higher frequencies very slowly, facilitating operation at higher frequencies.

In this chapter, unloaded and resistively loaded thin-wire V-antennas are analyzed. The time-domain integral equation for the V-antenna is derived in Section 5.2 and it is solved numerically in the time domain, using the stepping-in-time method, in Section 5.3. A

frequency-domain analysis of the V-antenna is also performed, using the Numerical Electromagnetic Code (NEC), which is based on the Method of Moments [101, 102, 103]. Numerical results are presented, both in time and frequency domains, in Section 5.4. It can be seen from these results that the resistively loaded V-antenna *alone* does not have a flat frequency response over a broad frequency range. Hence, the possibility of shaping the frequency response of the V-antenna is discussed in Section 5.5. It is shown that, using a Response Equalizer Circuit (REC), a flat frequency response can be achieved over a broad bandwidth, even with low impedance (50 or 500 Ω) terminations. For a given termination and a given sensitivity, the V-antenna with REC has a much higher upper-roll-off frequency and much lower lower-roll-off frequency, compared with the WK straight dipole antenna.

## 5.2 The Integral Equation

Let us consider the electric field $\vec{E}^s(P,t)$ produced at a point P in free space by a current element $\vec{I}(S,t)$ and a charge element $q(S,t)$ located at point S, as shown in Figure 41(a). If $\vec{R}_s$ is the vector from S to P, the electric field is given by [60]

$$\begin{aligned} 4\pi\epsilon\vec{E}^s(P,t) = & \\ & \frac{q(S,\tau)\vec{R}_s}{R_s^3} + \frac{[\vec{I}(S,\tau).\vec{R}_s]\vec{R}_s}{cR_s^4} \\ - & \frac{\vec{R}_s \times [\vec{I}(S,\tau) \times \vec{R}_s]}{cR_s^4} - \frac{\vec{R}_s \times [\dot{\vec{I}}(S,\tau) \times \vec{R}_s]}{c^2 R_s^3} \end{aligned} \tag{159}$$

where $R_s = |\vec{R}_s|$ and $\tau = t - R_s/c$.

Let the point P be on the surface of the top wire and the point S be on the axis of the bottom wire of a V-dipole, as shown in Figure 41(b). The unit vectors along the top and bottom wires are $\hat{p}$ and $\hat{s}$, respectively. The V-angle of the antenna is $\theta_v$ and the angle between $\hat{s}$ and $\vec{R}_s$ is $\theta_s$. It is assumed here that the current and its associated charge is concentrated at the wire axis. This "thin-wire" assumption should be valid as long as the wire radius is much shorter than all the wavelengths considered. For the derivation of the integral equation for the V-antenna, we need to evaluate the component of the scattered

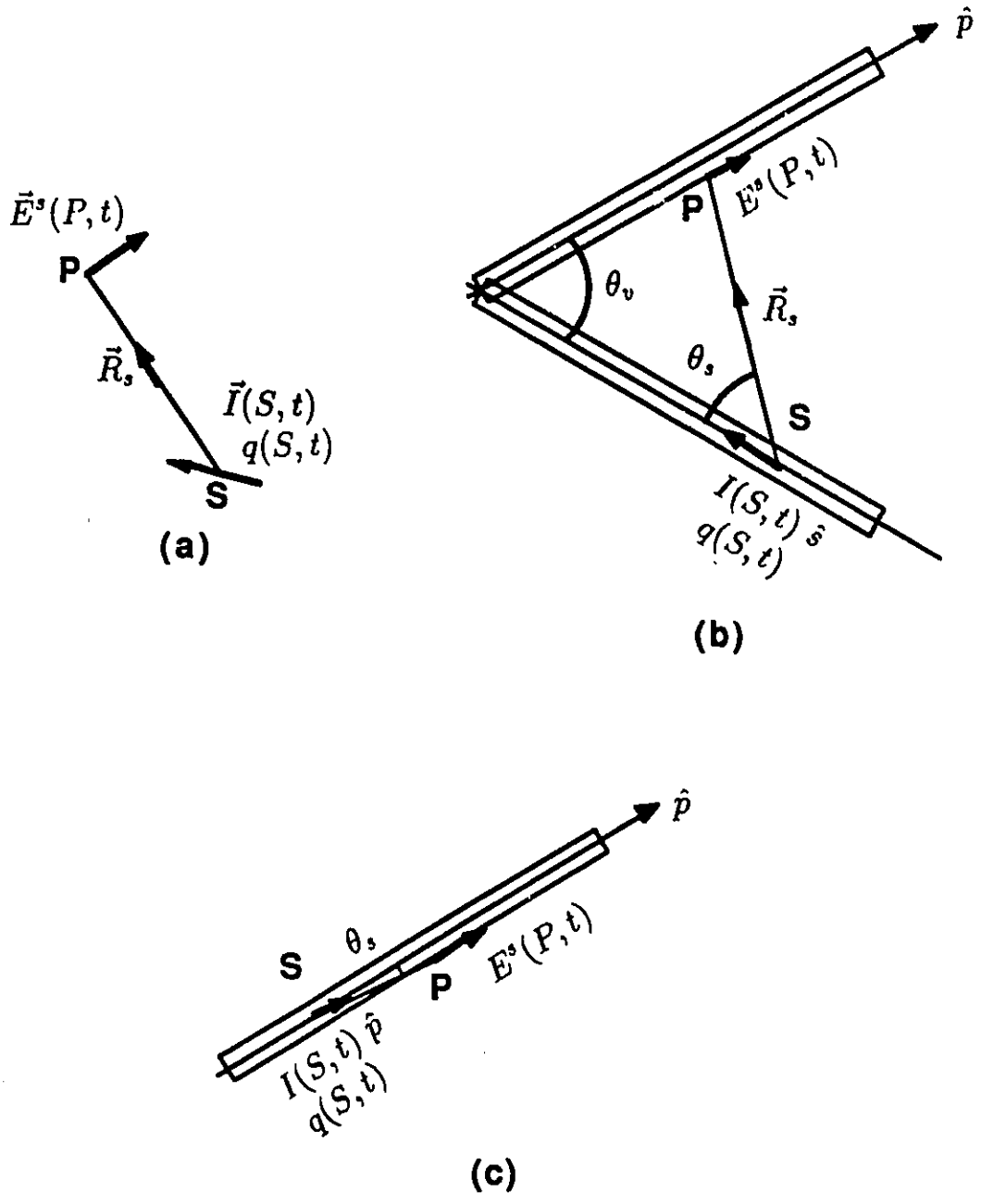


Figure 41: Current and charge elements in the V-dipole.

electric field tangential to the top wire surface, given by

$$E^s(P,t) = \vec{E}^s(P,t).\hat{p}\,. \tag{160}$$

The elemental current at S in the bottom wire can be expressed as

$$\vec{I}(S,t) = I(S,t)\,\hat{s}. \tag{161}$$

Now equation (159) is scalar multiplied by $\hat{p}$ to obtain $4\pi\epsilon E^s(P,t)$. Then, expression (161) is substituted for $\vec{I}(S,t)$. Vector multiples are replaced using the following equations:

$$\vec{R}_s.\hat{p} = -R_s\cos(\theta_v+\theta_s) \tag{162}$$

$$(\hat{s}.\vec{R}_s)(\vec{R}_s.\hat{p}) = -R_s^2\cos\theta_s\cos(\theta_v+\theta_s) \tag{163}$$

$$[\vec{R}_s\times(\hat{s}\times\vec{R}_s)].\hat{p} = -R_s^2\sin\theta_s\sin(\theta_v+\theta_s). \tag{164}$$

Finally, one obtains the tangential electric field produced at the surface of the top wire by an elemental source on the axis of the bottom wire as

$$\begin{aligned}4\pi\epsilon E^s(P,t) = &\\ &-\frac{q(S,\tau)}{R_s^2}\cos(\theta_v+\theta_s)-\frac{I(S,\tau)}{cR_s^2}\cos(\theta_v+2\theta_s)\\ &+\frac{\dot{I}(S,\tau)}{c^2R_s}\sin\theta_s\sin(\theta_v+\theta_s).\end{aligned} \tag{165}$$

Next, consider the case where the elemental source S is on the axis of the top wire, as shown in Figure 41(c). When $\theta_v = 180°$, the bottom wire is identical to the top wire. Hence, the expression for the scattered electric field due to an elemental source in the top wire can be obtained simply by substituting $\theta_v = 180°$ in expression (165). That is,

$$\begin{aligned}4\pi\epsilon E^s(P,t) = &\\ &\frac{q(S,\tau)}{R_s^2}\cos\theta_s+\frac{I(S,\tau)}{cR_s^2}\cos 2\theta_s-\frac{\dot{I}(S,\tau)}{c^2R_s}\sin^2\theta_s.\end{aligned} \tag{166}$$

The total scattered field is obtained by integrating the field from elemental sources over the two wires:

$$4\pi\epsilon E^s(P,t) =$$

$$\int_{bottom\ wire} \left\{ -\frac{q(S,\tau)}{R_s^2}\cos(\theta_v+\theta_s) - \frac{I(S,\tau)}{cR_s^2}\cos(\theta_v+2\theta_s) + \frac{\dot{I}(S,\tau)}{c^2R_s}\sin\theta_s\sin(\theta_v+\theta_s)\right\} ds$$
$$+ \int_{top\ wire} \left\{ +\frac{q(S,\tau)}{R_s^2}\cos\theta_s + \frac{I(S,\tau)}{cR_s^2}\cos 2\theta_s - \frac{\dot{I}(S,\tau)}{c^2R_s}\sin^2\theta_s\right\} ds. \tag{167}$$

The total tangential electric field, *ie.* the sum of the tangential scattered field and the tangential incident field, is given by

$$E^t(P,t) = E^s(P,t) + E^i(P,t). \tag{168}$$

For a perfectly conducting V-antenna, $E^t(P,t)$ must be zero. When the antenna is loaded with a surface resistance $\rho(P)$,

$$E^t(P,t) = \rho(P)\, J(P,t) = \rho(P)\,\frac{I(P,t)}{2\pi a} \tag{169}$$

where $J(P,t)$ is the current density, $I(P,t)$ is the current at P and $a$ is the wire radius. Substitution of (169) in (168) leads to

$$\frac{2\epsilon}{a}\rho(P)I(P,t) = 4\pi\epsilon E^s(P,t) + 4\pi\epsilon E^i(P,t). \tag{170}$$

Finally, expression (167) is substituted for $4\pi\epsilon E^s(P,t)$ and the following integral equation[1] for the resistively loaded V-antenna is obtained:

$$4\pi\epsilon E^i(P,t) =$$
$$\frac{2\epsilon}{a}\rho(P)I(P,t)$$
$$- \int_{bottom\ wire} \left\{ -\frac{q(S,\tau)}{R_s^2}\cos(\theta_v+\theta_s) - \frac{I(S,\tau)}{cR_s^2}\cos(\theta_v+2\theta_s) + \frac{\dot{I}(S,\tau)}{c^2R_s}\sin\theta_s\sin(\theta_v+\theta_s)\right\} ds$$
$$- \int_{top\ wire} \left\{ +\frac{q(S,\tau)}{R_s^2}\cos\theta_s + \frac{I(S,\tau}{cR_s^2}\cos 2\theta_s - \frac{\dot{I}(S,\tau)}{c^2R_s}\sin^2\theta_s\right\} ds. \tag{171}$$

[1]This is essentially an integro-differential equation. Nonetheless, it is normally referred to as an integral equation, for convenience.

The charge $q(S,t)$ is directly related to the current $I(S,t)$ by the continuity equation. Therefore, the only unknown in the integral equation is the current, which is a function of two variables- space and time. The integral equation can be solved for the current, directly in the time domain, as shown in the next section. Alternatively, (171) can be transformed to the frequency domain and solved using conventional frequency-domain numerical methods. The frequency-domain solution can be transformed to the time domain later, using numerical Fourier transform techniques.

## 5.3 The Numerical Solution

The time-domain integral equation for the V-antenna is solved numerically in this section. The algorithm developed here is based on the stepping-in-time method. The stepping-in-time method is a specialization of the method of moments (MOM) where causality is exploited. This allows us to calculate the current distribution in the two wires, step by step, in time. The excitation (incident field or applied voltage) waveform is arbitrary as long as it is causal and sufficiently bandlimited to justify the thin-wire assumption.

### 5.3.1 Expansion and Testing

The unknown in integral equation (171) is the wire current, which is a function of two variables- space and time. Therefore, one needs 2-D expansion functions and 2-D testing functions. In the following analysis, the roof-top function shown in Figure 42(a) is used for expansion. It is a triangular function in time and a pulse function in space. The $\Delta T$ in this figure is the time step. Use of triangular functions in time means the current is interpolated linearly along time axis. Pulse expansion in space means each wire is divided into many segments and the current is assumed to be uniform along each segment. Therefore, according to continuity equation, no charge exists along the segment. However, the discontinuity of current distribution at segment boundaries leads to concentrated charges at these discrete locations. This is obviously an approximation to the actual continuous charge distribution. The advantage of using pulses for spatial expansion is that one doesn't have to perform an

explicit matrix inversion in solving the integral equation. The spatial length of each segment $\Delta Z$ is equal to $2c\Delta T$. In this analysis, two dimensional Dirac functions are used for testing. In other words, the equality in (171) is enforced only at several points on space-time plane. In space, Dirac testing functions are located at the center of each segment. In time, they are at $j\Delta T$ where $j$ is a positive integer.

We are only interested in the reception of electromagnetic pulses incident in the boresite direction of the V-antenna. The V-dipole is therefore symmetrically excited and the current in the bottom wire is identical to that in the top wire, both in magnitude and phase. The charge on the bottom wire is the negative of the corresponding charge on the top wire. Therefore, one has to solve only for the current in the top wire. In turn, testing points are needed only on the top wire.

Figure 42(b) shows an infinitely thin V-dipole with each wire divided into $N$ number of segments. The general $i^{th}$ testing point is located at a distance

$$x_i = (2i - 1)c\Delta T \tag{172}$$

from the terminals. Also shown is the $l^{th}$ segment on the bottom wire. The center of this segment is at a distance

$$x_l = (2l - 1)c\Delta T \tag{173}$$

from the terminals. A V-dipole with finite thickness is shown in Figure 42(c). It can be noted that the only geometrical difference between the two is the small displacement of testing points (from the axis of the top wire to the surface).

### 5.3.2 Scattered Field from Bottom Wire

One may substitute the current expansion described in the previous section in the integral equation (171) and proceed mathematically towards the numerical solution. However, physically it makes more sense, if one considers each term in (171) separately. On the right hand side of (171), there is one term due to the distributed resistance, three terms due to the scattering from top wire and three more terms due to scattering from the bottom wire. Consider the contribution from the bottom wire. The objective of this section is to derive

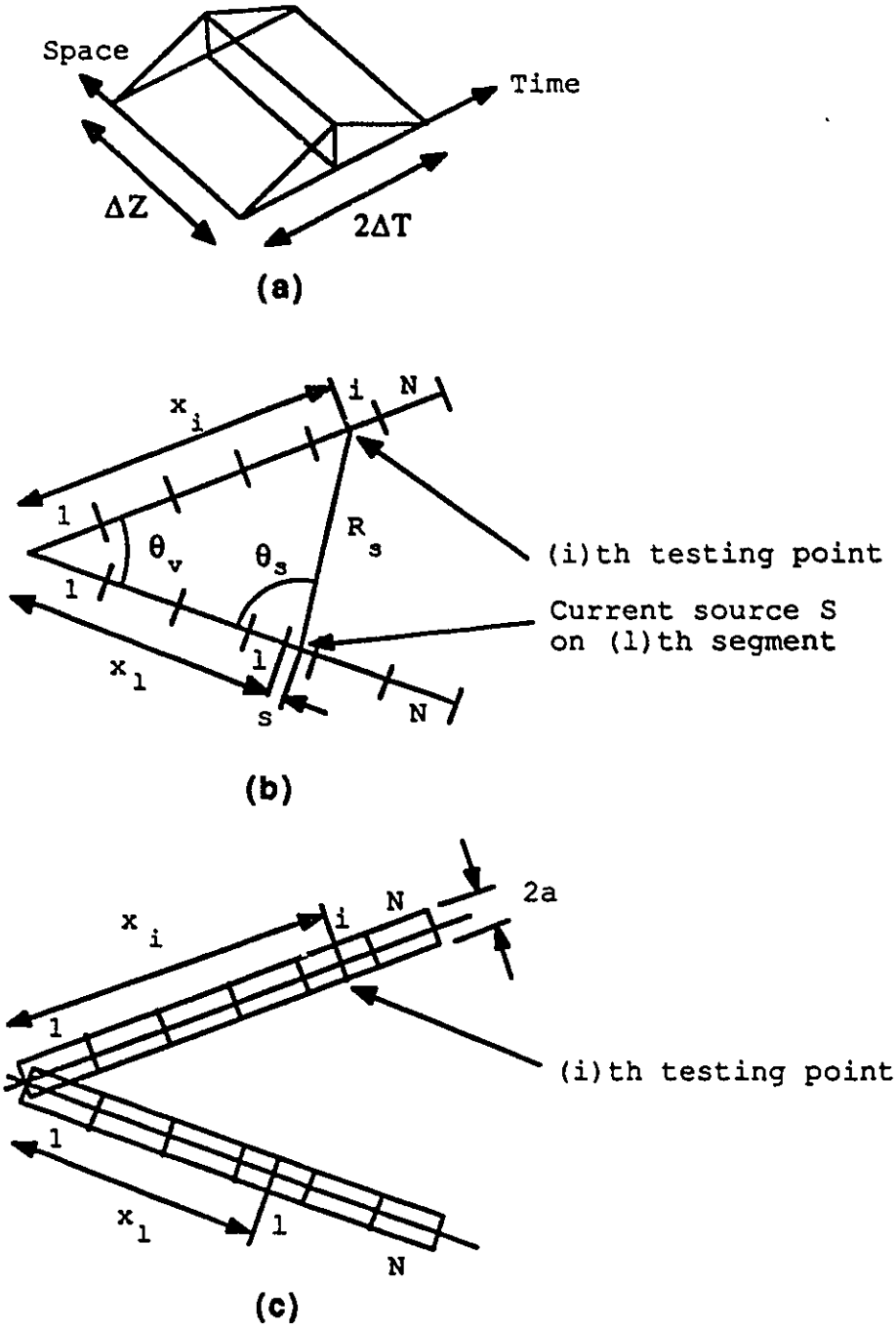


Figure 42: Segmentation of the V-dipole for numerical analysis. (a) roof-top expansion function (b) zero thickness wire (c) finite-thickness wire.

an expression for the value of the electric field at the $(i,j)$ testing point, produced by the $l^{th}$ segment current and its associated boundary-charges.

For convenience, the scattered field contribution from a bottom wire elemental source, given by (165), is divided into three parts as follows:

$$X(s) = -\frac{q(S,\tau)}{R_s^2}\cos(\theta_v + \theta_s) \tag{174}$$

$$Y(s) = -\frac{I(S,\tau)}{cR_s^2}\cos(\theta_v + 2\theta_s) \tag{175}$$

$$Z(s) = \frac{\dot{I}(S,\tau)}{c^2 R_s}\sin\theta_s \sin(\theta_v + \theta_s). \tag{176}$$

Charges exist only at segment boundaries and therefore only the two ends of the $l^{th}$ segment need to be considered when evaluating $X(s)$.

Let the elemental current source be located at a distance $s$ from the center of the $l^{th}$ segment, as shown in Figure 42(b). For the moment, assume that the V-dipole is infinitely thin. Later, the expression derived for the infinitely thin case is modified and the finite thickness of the dipole is accounted for. The spatial separation between the source point and testing point is given by

$$\begin{aligned} R_s^2 = {} & s^2 + 2sc\Delta T[(2l-1) - (2i-1)\cos\theta_v] \\ & + c^2\Delta T^2[(2i-1)^2 + (2l-1)^2 - 2(2i-1)(2l-1)\cos\theta_v]. \end{aligned} \tag{177}$$

Also from Figure 42(b),

$$\sin\theta_s = \frac{x_l - x_i\cos\theta_v}{R_s} \tag{178}$$

$$\cos\theta_s = \frac{x_i\sin\theta_v}{R_s} \tag{179}$$

Substitution of the above expressions into (175) and (176) leads to

$$Y(s) = \frac{I(s,\tau)}{c}\left[\frac{2x_i(x_l+s)\sin^2\theta_v}{R_s^4} - \frac{\cos\theta_v}{R_s^2}\right] \tag{180}$$

$$Z(s) = \frac{\dot{I}(s,\tau)\, x_i(x_l+s)\sin^2\theta_v}{c^2 R_s^3}. \tag{181}$$

If the currents at $j^{th}$ time step is to be calculated,

$$t = j\Delta T$$

and therefore

$$\tau(s) = j\Delta T - \frac{R_s}{c}.$$

Typical curves of $\tau$ versus $s$ for a single segment are sketched in Figures 43(a)-(c). The $\tau$ curve may very well span across many time steps. For example, the curve shown in Figure 43(c) spans across three time steps. Therefore, one needs to divide this segment again into three parts and calculate the contribution to the scattered field from each part separately. A generic part of the $l^{th}$ segment is shown in Figure 43(d).

The electric field due to currents in the generic part is calculated as follows. At one end of this part, $s = s_1$, $R_s = R_{s1}$, $\tau = \tau_1$ and the current is $C_1$ where

$$\begin{aligned} R_{s1}^2 &= s_1^2 + 2s_1 c\Delta T[(2l-1) - (2i-1)\cos\theta_v] \\ &\quad + c^2\Delta T^2[(2i-1)^2 + (2l-1)^2 - 2(2i-1)(2l-1)\cos\theta_v] \qquad (182) \\ \tau_1 &= j\Delta T - \frac{R_{s1}}{c}. \qquad (183) \end{aligned}$$

At the other end, $s = s_2$, $R_s = R_{s2}$, $\tau = \tau_2$ and the current is $C_2$ where

$$\begin{aligned} R_{s2} &= s_2^2 + 2s_2 c\Delta T[(2l-1) - (2i-1)\cos\theta_v] \\ &\quad + c^2\Delta T^2[(2i-1)^2 + (2l-1)^2 - 2(2i-1)(2l-1)\cos\theta_v] \qquad (184) \\ \tau_2 &= j\Delta T - \frac{R_{s2}}{c}. \qquad (185) \end{aligned}$$

The $\tau$ curve of the generic part falls within one segment and one time slot. Hence, the current $I(s,\tau)$ in this part has a linear variation with time $\tau$. One may therefore write

$$I(s,\tau) = \left[\frac{\tau_2 - \tau(s)}{\tau_2 - \tau_1}\right] C_1 + \left[\frac{\tau(s) - \tau_1}{\tau_2 - \tau_1}\right] C_2. \qquad (186)$$

It is necessary to express this current as a function of $s$. For that purpose, substitute $\tau(s) = j\Delta T - R_s/c$ where $R_s$ is a function of $s$ as stated in (177). Also substituting for $\tau_1$ and $\tau_2$ from (183) and (185), one obtains

$$I(s,\tau) = \left(\frac{R_s - R_{s2}}{R_{s1} - R_{s2}}\right) C_1 + \left(\frac{R_{s1} - R_s}{R_{s1} - R_{s2}}\right) C_2. \qquad (187)$$

Similarly,

$$\dot{I}(s,\tau) = \frac{C_2 - C_1}{\tau_2 - \tau_1} = \frac{c(C_2 - C_1)}{R_{s1} - R_{s2}}. \qquad (188)$$

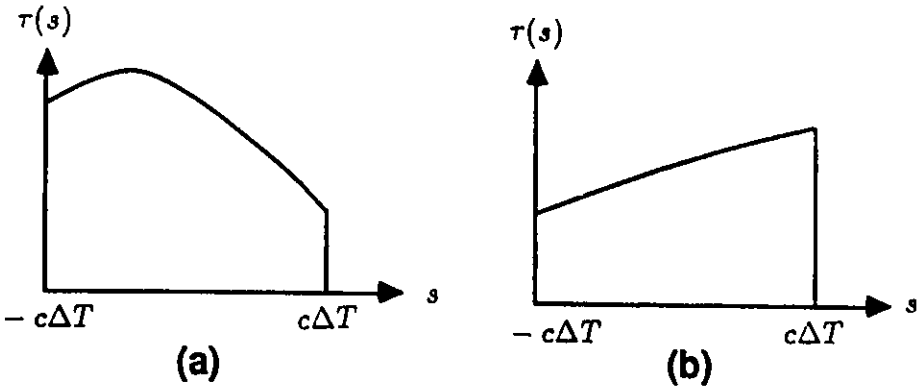


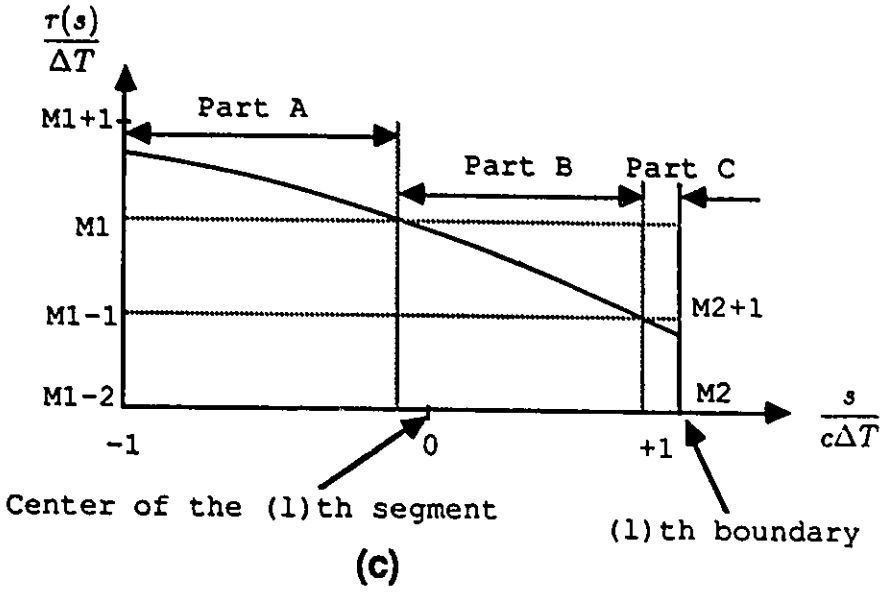


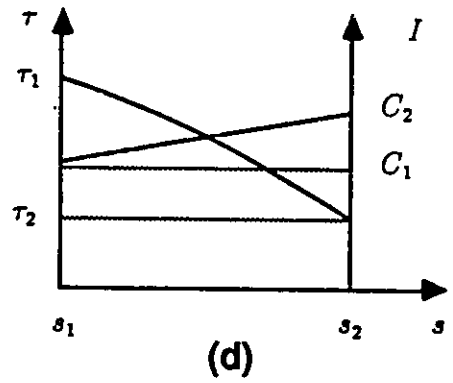


Figure 43: Typical $\tau$ curves of a segment.

These expressions are now substituted in (180) and (181) to find the electric field produced by the elemental current source at $s$. This results

$$cY(s) = \left[\left(\frac{R_s - R_{s2}}{R_{s1} - R_{s2}}\right) C_1 + \left(\frac{R_{s1} - R_s}{R_{s1} - R_{s2}}\right) C_2\right] \cdot \left[\frac{2x_i(x_l + s)\sin^2\theta_v}{R_s^4} - \frac{\cos\theta_v}{R_s^2}\right] \tag{189}$$

$$cZ(s) = \left(\frac{C_2 - C_1}{R_{s1} - R_{s2}}\right) \cdot \left[\frac{x_i(x_l + s)\sin^2\theta_v}{R_s^3}\right] \tag{190}$$

Finally, the total electric field produced by the current in the generic part is obtained by integrating $Y(s)$ and $Z(s)$ from $s_1$ to $s_2$. As shown in Appendix A, this results

$$\begin{aligned} c(Y_t + Z_t) = & \\ & - \cos\theta_v \left(\frac{C_2 - C_1}{R_{s2} - R_{s1}}\right) \ln\left(\frac{R_{s2} + s_2 + x_l - x_i\cos\theta_v}{R_{s1} + s_1 + x_l - x_i\cos\theta_v}\right) \\ & + \cos\theta_v \left[\frac{C_2 s_2}{R_{s2}^2} - \frac{C_1 s_1}{R_{s1}^2}\right] - \left(\frac{x_l\cos\theta_v - x_i}{R_{s1}R_{s2}}\right)\left[\frac{C_1 R_{s2}}{R_{s1}} - \frac{C_2 R_{s1}}{R_{s2}}\right] \end{aligned} \tag{191}$$

where

$$Y_t = \int_{s_1}^{s_2} Y(s)ds$$

and

$$Z_t = \int_{s_1}^{s_2} Z(s)ds.$$

Now consider a V-dipole with radius $a$, as shown in Figure 42(c). The axes of the two wires meet at the terminals. The only difference between this case and the zero-thickness case is that the testing points are now on the surface of the top wire that is a distance $a$ away from the axis. This can be accounted for, by replacing $x_i$ and $x_l$ in the above expressions by $x_i + a\cot\theta_v$ and $x_l + a\,\mathrm{cosec}\,\theta_v$, respectively. The resulting expressions are

$$\begin{aligned} R_{s1}^2 = & \\ & s_1^2 + 2s_1\{c\Delta T[(2l-1) - (2i-1)\cos\theta_v] - a\sin\theta_v\} - 2ac\Delta T(2l-1)\sin\theta_v + a^2 \\ & + c^2\Delta T^2[(2i-1)^2 + (2l-1)^2 - 2(2i-1)(2l-1)\cos\theta_v] \end{aligned} \tag{192}$$

$$\begin{aligned} R_{s2}^2 = & \\ & s_2^2 + 2s_2\{c\Delta T[(2l-1) - (2i-1)\cos\theta_v] - a\sin\theta_v\} - 2ac\Delta T(2l-1)\sin\theta_v + a^2 \end{aligned}$$

$$+c^2\Delta T^2[(2i-1)^2+(2l-1)^2-2(2i-1)(2l-1)\cos\theta_v] \tag{193}$$

$$\begin{aligned} c(Y_t+Z_t) = & \\ - \quad & \cos\theta_v\left(\frac{C_2-C_1}{R_{s2}-R_{s1}}\right)\ln\left(\frac{R_{s2}+s_2+x_l-x_i\cos\theta_v-a\sin\theta_v}{R_{s1}+s_1+x_l-x_i\cos\theta_v-a\sin\theta_v}\right) \\ + \quad & \cos\theta_v\left[\frac{C_2s_2}{R_{s2}^2}-\frac{C_1s_1}{R_{s1}^2}\right]-\left(\frac{x_l\cos\theta_v-x_i}{R_{s1}R_{s2}}\right)\left[\frac{C_1R_{s2}}{R_{s1}}-\frac{C_2R_{s1}}{R_{s2}}\right]. \end{aligned} \tag{194}$$

This expression for the electric field due to currents in the generic part is very general. It can be used in the analysis of wire antennas with arbitrary shapes.

When $\theta_v < 90°$, there is always a bottom wire segment which has a peaked $\tau$ curve as shown in Figure 43(a). Let us denote this segment by $l_{pk}$. In fact, $l_{pk}$ is the bottom-wire segment closest to the $i^{th}$ testing point. All the segments to the left of $l_{pk}$ (*i.e.* $l < l_{pk}$) have $\tau$ curves with positive slopes, like in Figure 43(b). All segments to the right (*i.e.* $l > l_{pk}$) have negative slopes. Using simple geometry, it can be shown that

$$l_{pk} = \mathrm{INT}[(i-\frac{1}{2})\cos\theta_v+\frac{1}{2\psi}\sin\theta_v]+1 \tag{195}$$

where

$$\psi = \frac{c\Delta T}{a} \tag{196}$$

and INT represents the integer function. The point on the bottom wire axis that is closest to the $i^{th}$ testing point (denoted by $s_{pk}$), and the distance between these two points $R_{spk}$ are given by

$$s_{pk} = (2i-1)c\Delta T\cos\theta_v+a\sin\theta_v-(2l_{pk}-1)c\Delta T \tag{197}$$

$$R_{spk} = (2i-1)c\Delta T\sin\theta_v-a\cos\theta_v. \tag{198}$$

The value of $\tau$ at $s_{pk}$ is given by

$$\tau_{pk} = j\Delta T-\frac{R_{spk}}{c} = j-(2i-1)\sin\theta_v+\frac{1}{\psi}\cos\theta_v. \tag{199}$$

All the bottom wire segments are subdivided wherever the $\tau$ curve cuts the time slot boundaries, as shown in Figure 43(c). Further, the $l_{pk}$ segment is subjected to an additional division at $s_{pk}$. Within a general segment $l(\neq l_{pk})$, there can be up to three parts. The

contribution from these parts to the scattered electric field is determined as follows. The first step is to determine the number of parts in a general $l^{th}$ segment. Let $M_1$ be the latest time step before $\tau(-c\Delta T)$ and $M_2$ be the latest time step before $\tau(c\Delta T)$, as shown in Figure 43(c). For all segments other than $l_{pk}$, the number of parts is equal to $|M_1 - M_2| + 1$. Now consider the most complicated case, where the segment is divided into three parts, as in Figure 43(c). For Part A,

$$s_1 = -c\Delta T \tag{200}$$

$$s_2 = -U \pm \sqrt{U^2 - V} \tag{201}$$

where only the value that falls within the segment is selected (*i.e.* $-c\Delta T < s_2 < c\Delta T$). In above expressions, $U$ and $V$ are given by

$$U = x_l - x_i \cos\theta_v - a \sin\theta_v \tag{202}$$

$$V = x_l^2 + x_i^2 - 2x_l x_i \cos\theta_v - 2ax_l \sin\theta_v + a^2 - (j - M_1)^2 c^2 \Delta T^2. \tag{203}$$

Let the current of the $l^{th}$ segment at $m^{th}$ time step be $I_{l,m}$ (this current flows from left to right in the top wire; right to left in bottom wire). The current at the two ends of Part A can be written as

$$C_1 = I_{l,M_1}\left[M_1 + 1 - \frac{\tau(s_1)}{\Delta T}\right] + I_{l,M_1+1}\left[\frac{\tau(s_1)}{\Delta T} - M_1\right] \tag{204}$$

$$C_2 = I_{l,M_1} \tag{205}$$

Substitution of above expressions for $s_1, s_2, C_1$ and $C_2$ into expressions (192)-(194) gives the electric field produced by Part A currents. The contribution from other parts of the $l^{th}$ segment can be determined similarly. Contributions from all the parts in all the bottom-wire segments are combined to find the total scattered electric field due to bottom wire currents. In this discussion, it was assumed that the currents $I_{l,M_1+1}$ etc. are already known. However, there may be cases where $M_1 + 1 = j$ and hence $I_{l,M_1+1}$ is yet unknown. These cases are identified and treated separately in Section 5.3.4.

Finally, one needs to evaluate the electric field produced by the charges on the bottom wire. As mentioned previously, charges exist only at segment boundaries. The boundary

between the $l^{th}$ and $(l+1)^{th}$ segments is denoted as the $l^{th}$ boundary, as shown in Figure 43(c). From (174), the contribution from this boundary is given by

$$X = -\frac{q(l,\tau)}{R_{sl}^2}\cos(\theta_v + \theta_s) \tag{206}$$

where $q(l,\tau)$ is the charge at the $l^{th}$ boundary at $t = \tau$; $R_{sl}$ and $\tau$ here are given by

$$R_{sl}^2 = [4l^2 + (2i-1)^2 - 4l(2i-1)\cos\theta_v]c^2\Delta T^2 - 4alc\Delta T\sin\theta_v + a^2 \tag{207}$$

$$\tau = j\Delta T - \frac{R_{sl}}{c}. \tag{208}$$

Expansion of (206) and substitution for $\sin\theta_s$ and $\cos\theta_s$, from (178) and (179), leads to

$$\begin{aligned} cX &= -\frac{cq(l,\tau)}{R_{sl}^3}[x_l\cos\theta_v - x_i + c\Delta T\cos\theta_v] \\ &= -\frac{c^2\Delta T q(l,\tau)}{R_{sl}^3}[2l\cos\theta_v - 2i + 1]. \end{aligned} \tag{209}$$

The charge $q(l,\tau)$ can be expressed in terms of currents in the $l^{th}$ and $(l+1)^{th}$ segments, as

$$\begin{aligned} q(l,\tau) = &\sum_{k=0}^{M_2}\Delta T(I_{l+1,k} - I_{l,k}) \\ &-\frac{\Delta T}{2}(I_{l+1,M_2} - I_{l,M_2})(M_2 + 1 - j + \frac{R_{sl}}{c\Delta T})^2 \\ &+\frac{\Delta T}{2}(I_{l+1,M_2+1} - I_{l,M_2+1})(j - M_2 - \frac{R_{sl}}{c\Delta T})^2. \end{aligned} \tag{210}$$

When evaluating the charge at the free end (*i.e.* $l = N$ = number of segments), the currents with $(l+1)$ subscripts are neglected. At the wire junction, both segments carry the same current in opposite directions and therefore there is no charge. The contribution to the electric field from all the bottom-wire charges at segment boundaries are calculated using (209) and (210) and summed. This, when added to the total contribution from the bottom wire currents calculated before, gives the total electric field produced by the bottom wire, at $(i,j)$ testing point.

### 5.3.3 Scattered Field from Top Wire

In this section, the electric field produced by the top wire currents, at the $(i,j)$ testing point is determined. Since all the testing points are on the top wire, the problem is similar to

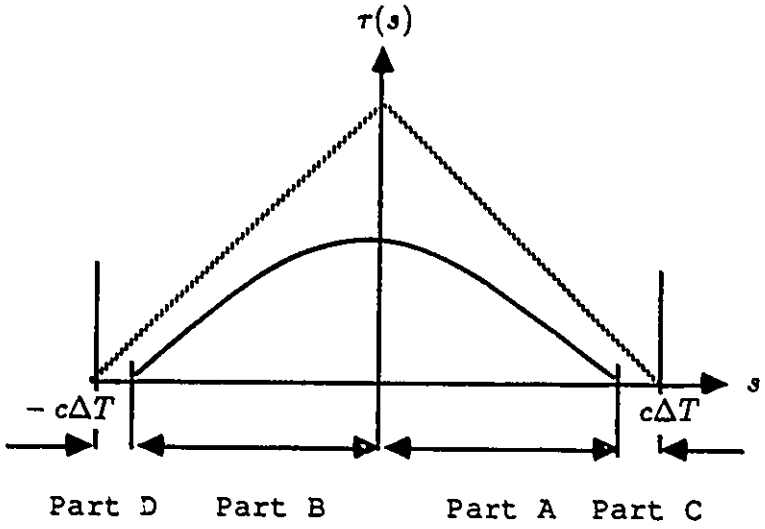


Figure 44: $\tau$ curve for the $i^{th}$ top-wire segment.

a straight dipole or monopole. Expressions for straight dipoles have already been derived in the previous chapter. Instead of quoting those expressions, one may re-derive them here using the more general expression (194). This allows one to check the expressions derived in the previous chapter as well as expression (194).

The bottom wire of a V-dipole is indistinguishable from the top wire when $\theta_v = 180°$. One can therefore use expression (194), with $\theta_v = 180°$, to calculate electric field produced by top wire currents. Let the tangential electric field at the $(i,j)$ testing point be $E^s_{i,j}$. The contribution to $E^s_{i,j}$ from the $(i,k)$ roof-top function $(k \leq j)$ can be determined as follows. The $\tau$ curve for this case is shown in Figure 44. The $i^{th}$ top wire segment is divided into four parts. The electric field created by the currents in Part A is calculated first. Using the notation for the generic part shown in Figure 43(d), one obtains

$$s_1 = 0 \tag{211}$$

$$s_2 = \sqrt{(c\Delta T)^2 - a^2} \tag{212}$$

$$R_{s1} = a \tag{213}$$

$$R_{s2} = c\Delta T \tag{214}$$

$$C_1 = I_{i,j}(1 - \frac{a}{c\Delta T}) + I_{i,j-1}(\frac{a}{c\Delta T}) \tag{215}$$

$$C_2 = I_{i,j-1}. \tag{216}$$

These expressions are substituted in (194), together with

$$\theta_v = 180^\circ \tag{217}$$

$$x_i = (2i-1)c\Delta T \tag{218}$$

$$x_l = -(2i-1)c\Delta T, \tag{219}$$

and hence the contribution to the electric field from Part A currents is obtained as

$$\begin{aligned} &ac(Y_t + Z_t) = \\ &\quad -\frac{I_{i,j}}{\psi}\ln(\psi + \sqrt{\psi^2 - 1}) + \frac{I_{i,j-1}}{\psi}\ln(\psi + \sqrt{\psi^2 - 1}) \\ &\quad -\frac{I_{i,j-1}}{\psi^2}\sqrt{\psi^2 - 1} \end{aligned} \tag{220}$$

where

$$\psi = \frac{c\Delta T}{a}.$$

By symmetry, Part B currents give exactly the same contribution. The contribution from Parts C currents is determined next. In this case,

$$s_1 = \sqrt{(c\Delta T)^2 - a^2} \tag{221}$$

$$s_2 = c\Delta T \tag{222}$$

$$R_{s1} = c\Delta T \tag{223}$$

$$R_{s2} = \sqrt{(c\Delta T)^2 + a^2} \tag{224}$$

$$C_1 = I_{i,j-1} \tag{225}$$

$$C_2 = I_{i,j-1}(2 - \frac{\sqrt{(c\Delta T)^2 + a^2}}{c\delta T}) + I_{i,j-2}(\frac{\sqrt{(c\Delta T)^2 + a^2}}{c\delta T} - 1) \tag{226}$$

Substitution of these in (194) leads to

$$\begin{aligned} ac(Y_t + Z_t) = & \\ & \frac{1}{\psi}(I_{i,j-2} - i_{i,j-1}) \ln \left[ \frac{\psi + \sqrt{\psi^2+1}}{\psi + \sqrt{\psi^2-1}} \right] \\ - \quad & I_{i,j-1} \left( \frac{2 - \sqrt{\psi^2+1}}{\psi^2+1} - \frac{\sqrt{\psi^2-1}}{\psi^2} \right) - I_{i,j-2} \left( \frac{\sqrt{\psi^2+1} - \psi}{\psi^2+1} \right). \end{aligned} \tag{227}$$

The contribution from currents in Part D is equal to that from Part C. Finally, the contribution from the charges at segment boundaries is calculated. These boundary charges are in fact due to currents in the $i^{th}$ segment as well as neighboring segments. For the moment, only the charges associated with $i^{th}$ segment currents are considered. Substitution of expressions (217)-(219) in (209) leads to

$$cX = \frac{c^2 \Delta T q(\tau)}{(c^2 \Delta T^2 + a^2)^{3/2}} \tag{228}$$

where $q(\tau)$ is the charge accumulated at the left end of segment $i$. In turn, there is a $-q(\tau)$ charge accumulated at the right end of the same segment. The total electric field at $(i,j)$ testing point is therefore equal to twice of that given by (228). The charge $q(\tau)$ due to currents in the $i^{th}$ segment is given by

$$\begin{aligned} q(\tau) \quad = \quad & -\frac{I_{i,j-1}\Delta T}{2} \left[ 2 - \sqrt{1 + \frac{a^2}{c^2 \Delta T^2}} \right]^2 - I_{i,j-2} \Delta T \left[ 1 - \frac{1}{2} \left( \sqrt{1 + \frac{a^2}{c^2 \Delta^2}} - 1 \right)^2 \right] \\ & -\Delta T \sum_{k=1}^{j-3} I_{i,k}. \end{aligned} \tag{229}$$

Substituting this in (228), one obtains

$$\begin{aligned} acX = & \\ & -\frac{I_{i,j-1}}{2} \frac{(2\psi - \sqrt{\psi^2+1})}{(\psi^2+1)^{3/2}} - I_{i,j-2} \frac{[\psi^2 - \frac{1}{2}(\sqrt{\psi^2+1} - \psi)^2]}{(\psi^2+1)^{3/2}} \\ & - \sum_{k=1}^{j-3} I_{i,k} \frac{\psi^2}{(\psi^2+1)^{3/2}}. \end{aligned} \tag{230}$$

The total electric field at $(i,j)$ testing point due to the $i^{th}$ top-wire segment is obtained by adding contributions from currents in all the parts and those from the charges at the two

boundaries. The final expression can be written in the form

$$4\pi\epsilon ac E^s_{i,j}|_i = \quad A_0 I_{i,j} + A_1 I_{i,j-1} + A_2 I_{i,j-2} + A_3 \sum_{k=1}^{j-3} I_{i,k} \tag{231}$$

where the coefficients are given by

$$A_0 = -\frac{2}{\psi}\ln(\psi + \sqrt{\psi^2 - 1}) \tag{232}$$

$$A_1 = \frac{4}{\psi}\ln(\psi + \sqrt{\psi^2 - 1}) - \frac{2}{\psi}\ln(\psi + \sqrt{\psi^2 + 1}) - \frac{3\psi^2 - 1}{(\psi^2 + 1)^{3/2}} \tag{233}$$

$$A_2 = \frac{2}{\psi}\ln(\psi + \sqrt{\psi^2 + 1}) - \frac{2}{\psi}\ln(\psi + \sqrt{\psi^2 - 1}) - \frac{2\psi^2 + 1}{(\psi^2 + 1)^{3/2}} \tag{234}$$

$$A_3 = -\frac{2\psi^2}{(\psi^2 + 1)^{3/2}}. \tag{235}$$

It may be noted that the expressions for these coefficients are identical to those derived in the previous chapter, using direct integration.

The electric field at the $i^{th}$ testing point due to currents and charges in other top wire segments can be determined similarly. The procedure is lengthy, and not included here. The final expression for the electric field at $(i,j)$ testing point $E^s_{i,j}$ due to currents and charges in the $(i \pm l)^{th}$ segment $(l > 0)$ can be written as

$$\begin{aligned} &4\pi\epsilon ac E^s_{i,j}|_{i\pm l} = \\ &\quad B_{0,l} I_{i\pm l,j-2l+1} + B_{1,l} I_{i\pm l,j-2l} + B_{2,l} I_{i\pm l,j-2l-1} \\ &\quad + B_{3,l} I_{i\pm l,j-2l-2} + B_{4,l} \sum_{k=1}^{j-2l-3} I_{i\pm l,k} \end{aligned} \tag{236}$$

where the coefficients are given by

$$\begin{aligned} B_{0,l} = &-\frac{1}{\psi}\sinh^{-1}\sqrt{4l^2\psi^2 - 1} + \frac{1}{\psi}\sinh^{-1}[(2l-1)\psi] \\ &+ \frac{(2l-1)}{2}\frac{(4l-1)\psi^2 - 1}{[(2l-1)^2\psi^2 + 1]^{3/2}} \end{aligned} \tag{237}$$

$$\begin{aligned} B_{1,l} = &\frac{1}{\psi}\{2\sinh^{-1}\sqrt{4l^2\psi^2 - 1} - \sinh^{-1}\sqrt{(2l+1)^2\psi^2 - 1} - \sinh^{-1}[(2l-1)\psi]\} \\ &\frac{(2l-1)(2\psi^2 + 1)}{2[(2l-1)^2\psi^2 + 1]^{3/2}} \end{aligned} \tag{238}$$

$$B_{2,l} = \frac{1}{\psi}\ln\left[\frac{(2l+1)\psi+\sqrt{(2l+1)^2\psi^2-1}}{2l\psi+\sqrt{4l^2\psi^2-1}}\right] - \frac{1}{\psi}\ln\left[\frac{(2l+1)\psi+\sqrt{(2l+1)^2\psi^2+1}}{(2l+1)\psi+\sqrt{(2l+1)^2\psi^2-1}}\right] - \frac{(2l+1)[(4l+3)\psi^2-1]}{2[(2l+1)^2\psi^2+1]^{3/2}} + \frac{(2l-1)\psi^2}{[(2l-1)^2\psi^2+1]^{3/2}} \quad (239)$$

$$B_{3,l} = \frac{1}{\psi}\sinh^{-1}[(2l+1)\psi] - \frac{1}{\psi}\sinh^{-1}\sqrt{(2l+1)^2\psi^2-1} + \frac{(2l-1)\psi^2}{[(2l-1)^2\psi^2+1]^{3/2}} - \frac{(2l+1)(2\psi^2+1)}{2[(2l+1)^2\psi^2+1]^{3/2}} \quad (240)$$

$$B_{4,l} = \psi^2\left\{\frac{2l-1}{[(2l-1)^2\psi^2+1]^{3/2}} - \frac{2l+1}{[(2l+1)^2\psi^2+1]^{3/2}}\right\}. \quad (241)$$

During the computation process, the contribution to $E^s_{i,j}$ from the $i^{th}$ segment is calculated using (231). As the current $I_{i,j}$ is unknown at $(i,j)$ testing point, the $A_0 I_{i,j}$ term is neglected in this calculation. This term is taken care of when the current $I_{i,j}$ is calculated, as described in the next section. Contribution to $E^s_{i,j}$ from all the other segments is calculated using (236). All these contributions, when added together, give the electric field at $(i,j)$ testing point due to all (known) top wire currents and charges.

### 5.3.4 Code Description

The stepping-in-time numerical solution described in the previous section was implemented in FORTRAN. A listing of the code named VDIP is given in Appendix E. The VDIP code is briefly described in this section. Some of the equations derived in the previous section were modified to increase the speed of computation and reduce round-off errors. Such changes are also described in this section.

The expressions for the scattered field due to top wire segments in (231) and (236) involve a summation of currents. Computation of this summation at each time step is avoided by replacing it with a quantity related to the charge at $i^{th}$ segment boundary $Q_{i,j}$, defined as

$$Q_{i,j} = \sum_{k=1}^{j} I_{i,k} - I_{i+1,k}. \quad (242)$$

It should be noted that $Q_{i,j}$ accounts not only for the charge due to $i^{th}$ segment currents

but also for the charge due to $(i+1)^{th}$ segment currents. Hence, some of the coefficients in (232)-(235) and (237)-(241) should be modified accordingly.

The coefficient $A_0$ is not contributed by any charge and is therefore left unmodified. The term "self-charge" is used to describe the charge accumulated at the two boundaries of a segment due to its own currents. The charge accumulated at the two boundaries of a segment due to currents in the neighboring segments is called "neighbor's charge". The coefficients $A_1$ and $A_2$ include only self-charge at *both* boundaries. The coefficient $A_3$ is now modified as

$$A_3 = -\frac{\psi^2}{(\psi^2+1)^{3/2}} \tag{243}$$

and the expression (231) is re-written as

$$4\pi\epsilon ac E^s_{i,j}|_i =$$
$$A_0 I_{i,j} + A_1 I_{i,j-1} + A_2 I_{i,j-2} + A_3(Q_{i,j-3} - Q_{i-1,j-3}). \tag{244}$$

Hence, the term $A_3$ accounts for both self- and neighbor's charges at *both* boundaries of $i^{th}$ segment. In VDIP code, coefficients $A_0 - A_3$ are denoted by ASEL0-ASEL3, coefficients $B_{0,l} - B_{4,l}$ by AMUT0(L)-AMUT4(L) and $I_{i,j}$ by C(I,J).

The coefficients $B_{0,l} - B_{4,l}$ in expressions (237)-(241) include only self-charges at *both* boundaries of the $(i \pm l)^{th}$ segment. Consider the $(i+1)^{th}$ segment. The effect of the self-charge due to $(i+1)^{th}$ segment currents at the $i^{th}$ boundary is already accounted for, up to $(j-3)$ time step, by $A_3 Q_{i,j-3}$. Therefore, the contribution from self-charge at the $i^{th}$ boundary should be excluded from $B_{2,1}, B_{3,1}$ and $B_{4,1}$. However, $B_{0,1}$ and $B_{1,1}$ will continue to carry these contributions. All coefficients from $B_{2,1}$ to $B_{4,1}$ will continue to carry the self-charge contributions from the $(i+1)^{th}$ boundary. $B_{0,1}$ and $B_{1,1}$ do not have such contributions. Further, the neighbor's charge contribution at the $(i+1)^{th}$ boundary is added to $B_{4,1}$.

When this procedure is extended for a general $(i \pm l)^{th}$ segment, one finally obtains the following expressions for the scattered field:

$$4\pi\epsilon ac E^s_{i,j}|_{i\pm l} =$$

$$B_{0,l}I_{i\pm l,j-2l+1} + B_{1,l}I_{i\pm l,j-2l} + B_{2,l}I_{i\pm l,j-2l-1}$$
$$+B_{3,l}I_{i\pm l,j-2l-2} \pm B_{4,l}Q_{i\pm l,j-2l-3} \tag{245}$$

where the coefficients are given by

$$B_{0,l} = -\frac{1}{\psi}\sinh^{-1}\sqrt{4l^2\psi^2-1} + \frac{1}{\psi}\sinh^{-1}[(2l-1)\psi]$$
$$+\frac{(2l-1)}{2}\frac{(4l-1)\psi^2-1}{[(2l-1)^2\psi^2+1]^{3/2}} \tag{246}$$

$$B_{1,l} = \frac{1}{\psi}\{2\sinh^{-1}\sqrt{4l^2\psi^2-1} - \sinh^{-1}\sqrt{(2l+1)^2\psi^2-1} - \sinh^{-1}[(2l-1)\psi]\}$$
$$\frac{(2l-1)(2\psi^2+1)}{2[(2l-1)^2\psi^2+1]^{3/2}} \tag{247}$$

$$B_{2,l} = \frac{1}{\psi}\ln\left[\frac{(2l+1)\psi+\sqrt{(2l+1)^2\psi^2-1}}{2l\psi+\sqrt{4l^2\psi^2-1}}\right]$$
$$-\frac{1}{\psi}\ln\left[\frac{(2l+1)\psi+\sqrt{(2l+1)^2\psi^2+1}}{(2l+1)\psi+\sqrt{(2l+1)^2\psi^2-1}}\right]$$
$$-\frac{(2l+1)[(4l+3)\psi^2-1]}{2[(2l+1)^2\psi^2+1]^{3/2}} \tag{248}$$

$$B_{3,l} = \frac{1}{\psi}\sinh^{-1}[(2l+1)\psi] - \frac{1}{\psi}\sinh^{-1}\sqrt{(2l+1)^2\psi^2-1}$$
$$-\frac{(2l+1)(2\psi^2+1)}{2[(2l+1)^2\psi^2+1]^{3/2}} \tag{249}$$

$$B_{4,l} = -\frac{(2l+1)\psi^2}{[(2l+1)^2\psi^2+1]^{3/2}}. \tag{250}$$

The only exception is the field scattered from the first segment on top wire. This particular segment does not have any charge whatsoever at its left-hand boundary (which is also one terminal of the antenna). Therefore, all contributions from the left-hand-boundary-charge (if any) should be eliminated from all the $A$-coefficients when $i = 1$ and from all the $B$-coefficients when $i - l = 1$. This modification is quite straightforward and made directly in the VDIP code. Tables 2-4 summarize how the self- and neighbor's charges are taken care of.

In the VDIP code, it is assumed that $\theta_v < 90°$. Therefore, for every testing point $i$, there is a bottom wire segment with a peaked $\tau$ curve, denoted by $l_{pk}$. For all testing points ($i = 1, \ldots, N$), $l_{pk}$ is determined using (195). Values of $s_{pk}$ and $R_{spk}$ in (197) and (198) are

| time step | $(i-1)^{th}$ boundary | | $i^{th}$ boundary | |
|---|---|---|---|---|
| | self | neighbor's | self | neighbor's |
| $j$ | x | x | x | x |
| $j-1$ | $A_1$ | $B_{0,1}$ | $A_1$ | $B_{0,1}$ |
| $j-2$ | $A_2$ | $B_{1,1}$ | $A_2$ | $B_{1,1}$ |
| $\leq j-3$ | $A_3$ | $A_3$ | $A_3$ | $A_3$ |
| x = no charge | | | | |

Table 2: Allocation of charges at the two ends of the $i^{th}$ segment

| time step | $i^{th}$ boundary | | $(i+1)^{th}$ boundary | |
|---|---|---|---|---|
| | self | neighbor's | self | neighbor's |
| $j-1$ | $B_{0,1}$ | $A_1$ | x | x |
| $j-2$ | $B_{1,1}$ | $A_2$ | x | x |
| $j-3$ | $A_3$ | $A_3$ | $B_{2,1}$ | $B_{0,2}$ |
| $j-4$ | $A_3$ | $A_3$ | $B_{3,1}$ | $B_{1,2}$ |
| $\leq j-5$ | $A_3$ | $A_3$ | $B_{4,1}$ | $B_{4,1}$ |
| x = no charge | | | | |

Table 3: Allocation of charges at the two ends of the $(i+1)^{th}$ segment

| time step | $(i+l-1)^{th}$ boundary | | $(i+l)^{th}$ boundary | |
|---|---|---|---|---|
| | self | neighbor's | self | neighbor's |
| $j-2l+1$ | $B_{0,l}$ | $B_{2,l-1}$ | x | x |
| $j-2l$ | $B_{1,l}$ | $B_{3,l-1}$ | x | x |
| $j-2l-1$ | $B_{4,l-1}$ | $B_{4,l-1}$ | $B_{2,l}$ | $B_{0,l+1}$ |
| $j-2l-2$ | $B_{4,l-1}$ | $B_{4,l-1}$ | $B_{3,l}$ | $B_{1,l+1}$ |
| $\leq j-2l-3$ | $B_{4,l-1}$ | $B_{4,l-1}$ | $B_{4,l}$ | $B_{4,l}$ |
| x = no charge | | | | |

Table 4: Allocation of charges at the two ends of the $(i+l)^{th}$ segment

also calculated for each $i$ and normalized so that $\epsilon_{pk} = s_{pk}/(c\Delta T)$ and $\rho_{pk} = R_{spk}/(c\Delta T)$. The distance between the $i^{th}$ testing point and the $l^{th}$ bottom-wire segment boundary $R_{sl}$ is calculated according to (207) and normalized so that $\rho_{i,l} = R_{sl}/(c\Delta T)$.

The contribution to $4\pi\epsilon acE^s$ at the $i^{th}$ testing point, from the $l^{th}$ (bottom-wire) boundary-charge is given by (209). This can be rewritten as

$$acX = \frac{D_{i,l}q(l,\tau)}{\Delta T}$$

where

$$D_{i,l} = \frac{(2i - 1 - 2l\cos\theta_v)}{\psi\rho_{i,l}^3}$$

and $q(l,\tau)$ is calculated according to (210). $D_{i,l}$ is represented in VDIP by BCHRG(I,J) and $q(i,\tau)/\Delta T$ by SIGMA(L). TAU(L) denotes $\tau/\Delta T$ where $\tau$ is given by (208). Currents on the $l^{th}$ and $(l+1)^{th}$ segments at $t = \tau$ is given by CL(L) and CR(L), respectively.

The contribution from bottom wire currents and charges is calculated as follows. Consider the $l^{th}$ segment and $l^{th}$ boundary where $l \neq l_{pk}$. The number of parts in $l^{th}$ segment is determined first. If it is one, computation is done by Module 1; if 2, by Module 2 and if 3, by Module 3. In each module, the current contribution from each part is determined, according to (194), by subroutine BCRNT. The inputs to the subroutine are A1,A2,EPS1,EPS2,RHO1 and RHO2, which are in fact equal to $C_1, C_2, s_1/(c\Delta T), s_2/(c\Delta T), R_{s1}/(c\Delta T)$ and $R_{s2}/(c\Delta T)$, respectively. The output CONT is equal to $ac(Y_t + Z_t)$. In each module, these input parameters for each part are calculated first, as explained in Section 5.3.2 [see equations (192), (193) and (200)-(205)]. Then the subroutine is called and contributions from all the parts are summed. Finally, the contribution from charge at the $l^{th}$ boundary is calculated and added to the current contribution.

The $l_{pk}$ segment is first divided into two sections at $s_{pk}$ (given by (197)). The section to the right of $s_{pk}$ is handled by Module 1A or Module 2A, depending upon whether this section has only one part or two parts. The section to the left of $s_{pk}$ is handled by Module 1B or Module 2B, similarly.

In the stepping-in-time technique, the scattered field due to all currents and charges are calculated at the $(i,j)$ testing point. Then, the incident field is added to obtain the total

electric field at $(i,j)$ testing point. Finally, the total field is divided by the surface resistance at $i^{th}$ segment and the surface current in $i^{th}$ segment at $j^{th}$ time-step is determined. However, the expressions for the scattered field may involve currents and charges at the $j^{th}$ time-step itself, which are unknown when the scattered field at the $(i,j)$ testing point is evaluated. Hence, the scattered field at the $(i,j)$ testing point is divided into two parts- the known part and the unknown part. Obviously, the term $A_0 I_{i,j}$ in expression (244) is one contributor to the unknown part. This is found to be the only unknown term as far as the top wire is considered.

The number of unknown terms in the expression for the scattered field from the bottom wire depends on the testing point $i$, $\theta_v$ and $\psi$. It can be seen that the expression for the scattered field at the $1^{st}$ testing point (on the top wire) created by the segment 1 currents in the bottom wire involves $I_{1,j}$ which is in fact the unknown being calculated. This is because

$$R_{spk}|_{i=1} = c\Delta T \sin\theta_v - a\cos\theta_v < c\Delta T$$

or

$$\sin\theta_v - \frac{1}{\psi}\cos\theta_v < 1$$

for all $\psi$ and $\theta_v$ ($< 90°$). Let this unknown term be $UI_{i,j}$. $U$ is represented in the code by EXTRA. If the wire is too thick and $\theta_v$ is too small, a fraction of the charge at the $1^{st}$ segment-boundary can be unknown as well. In the VDIP, we assume that this does not occur. This assumption is correct only if the testing point and the segment-boundary are separated by a distance greater than $c\Delta T$, *i.e.*

$$R_{sl}|_{l=1,i=1} \geq c\Delta T.$$

Substituting for $R_{sl}$ from (207), one obtains

$$4 - \cos\theta_v - \frac{4}{\psi}\sin\theta_v + \frac{1}{\psi^2} \geq 0. \tag{251}$$

It is also assumed that all the necessary bottom-wire currents and charges are known when the scattered fields at all other testing points ($i \neq 1$) are evaluated. This requires that

$$R_{spk}|_{i=2} = 3c\Delta T \sin\theta_v - a\cos\theta_v \geq c\Delta T$$

or

$$3\sin\theta_v - \frac{1}{\psi}\cos\theta_v \geq 1. \tag{252}$$

The conditions (251) and (252), together with $\theta_v < 90°$, set the limitations of the VDIP code in its present form.

The waveform of the incident pulse is computed by the external function PULSE. The electric field of the incident pulse is assumed to be vertically polarized. The tangential component of the incident electric field is therefore equal to $\sin(\theta_v/2)$ times the incident pulse. Finally, the current $I_{i,j}$ $(i \neq 1)$ is calculated according to (171). This can be rewritten as

$$\begin{aligned} 4\pi\epsilon ac E^i_{i,j} &= 2\epsilon c\rho_i I_{i,j} - A_0 I_{i,j} \\ &- 4\pi\epsilon ac E^s_{i,j}|_{\text{due to known currents}} \end{aligned} \tag{253}$$

or

$$I_{i,j} = \frac{\frac{aE^i_{i,j}}{30} - 4\pi\epsilon ac E^s_{i,j}|_{\text{due to known currents}}}{\frac{\rho_i}{60\pi} - A_0}. \tag{254}$$

When $i = 1$, the current is calculated according to

$$I_{1,j} = \frac{\frac{aE^i_{1,j}}{30} - 4\pi\epsilon ac E^s_{1,j}|_{\text{due to known currents}}}{\frac{\rho_i}{60\pi} - A_0 - U}. \tag{255}$$

After all segment currents at the $j^{th}$ time step are calculated, the $Q_{i,j}$ for the segment boundaries are calculated according to

$$Q_{i,j} = Q_{i,j-1} + I_{i,j} - I_{i+1,j}. \tag{256}$$

## 5.4 Numerical Results

Unloaded and resistively loaded V-antennas are analyzed and numerical results are presented in this section. Frequency-domain analysis of the antennas is carried out using the NEC code and the results are presented in Section 5.4.1. The time-domain response of

the antennas for different incident electromagnetic pulses is calculated using two different methods. In one method, the frequency-domain results obtained from NEC are numerically transformed to the time domain using FFT techniques. The other method is using the VDIP code described in the previous section, to analyze the antennas directly in the time domain. This method also provides the spatio-temporal distribution of the current and charge on the antenna for pulse (or arbitrary) excitations. Time-domain results obtained from both methods are presented in Section 5.4.2.

Numerical results presented in this section are for V-monopoles of 30 cm length and 1 mm diameter. This small diameter has to be used in order to satisfy NEC guidelines. The monopole has a wedge angle of 15°. In the case of the resistively loaded V-monopole, the loading profile has been determined from the Wu-King formula, as follows. For a monopole with length $l$ and radius $a$, the necessary internal resistance at a distance $s$ from the driving point is given by

$$r(s) = \frac{r(0)\, l}{l - s} \tag{257}$$

where $r(0)$ is the internal resistance at the driving point given by

$$r(0) = \frac{\xi}{2\pi l} \Re(\Psi) \tag{258}$$

in which

$$\Psi = 2[\sinh^{-1} \frac{l}{a} - C(2ka, 2kl) - jS(2ka, 2kl)] + \frac{j}{kl}(1 - e^{-j2kl}) \tag{259}$$

with

$$C(\alpha, x) = \int_0^x \frac{1 - \cos\sqrt{u^2 + \alpha^2}}{\sqrt{u^2 + \alpha^2}}\, du \tag{260}$$

$$S(\alpha, x) = \int_0^x \frac{\sin\sqrt{u^2 + \alpha^2}}{\sqrt{u^2 + \alpha^2}}\, du \tag{261}$$

It should be noted that the above expressions have been originally derived for the straight WK antenna. Nonetheless, it has been found that the value of $r(0)$ given by (258) is appropriate even for V-antennas. A lower distributed resistance leads to resonant ripples in the receiving transfer function. Hence, expression (258) has been used to calculate $r(0)$ of the resistively loaded V-antenna, which gives 2.2 kΩ/m for a 30 cm long, 1 mm thick monopole.

### 5.4.1 Frequency-Domain Results

The input impedance $Z_{in}$ of the loaded V-monopole has been calculated in the frequency range from 10 MHz to 10 GHz, using NEC. Each arm of the V-dipole has been divided into 100 segments in the analysis. The input resistance $R_{in}$ and the capacitive input reactance $-X_{in}$ of the loaded V-monopole are shown in Figure 45. It can be seen that at lower frequencies, where the monopole is electrically small, the input impedance of the loaded antenna can be represented by a constant capacitance ($\approx$ 6.6 pF) and a constant resistance ($\approx$ 150 $\Omega$), in series. This low-frequency input resistance is almost totally due to the loss resistance, which is determined by the current distribution along the wire. The current distribution is virtually constant at low frequencies and, hence, so is the input resistance.

The unloaded and loaded V-monopoles are excited by a uniform plane wave incident in the boresite direction. For a 1 V/m incident field, the currents at the short-circuited terminals $I_{sc}$ are calculated and the results are shown in Figures 46 and 47. The resonance peaks in the unloaded antenna are well reflected in Figure 46. The short-circuit current of the loaded antenna has a much smoother variation with frequency. A more familiar parameter of a dipole or monopole antenna is the effective height $h_{eff}$, which is defined as the open-circuited terminal voltage for a 1 V/m incident wave, and is equal to $I_{sc}Z_{in}$. The magnitude of the effective height $|h_{eff}|$ of the loaded antenna is shown in Figure 48. This is constant at low frequencies as for any other electrically-small antenna, but decreases with frequency in the electrically-large region. Considering the linear-log scale used, one may notice an interesting phenomenon that this drop of $|h_{eff}|$ is very slow, specially at higher frequencies.

The receiving transfer function of the antenna is defined as

$$R(\omega) = \frac{V_L(\omega)}{E^i(\omega)} \tag{262}$$

where $E^i$ is the incident electric field component on the plane of the monopole and $V_L$ is the voltage across antenna terminals. This transfer function can be considered as the *terminated* effective height of the antenna because the antenna is now terminated with a finite impedance rather than being open-circuited. $|R(\omega)|$ is related to the effective area

$A_{eff}(\omega)$ of the antenna by

$$A_{eff}(\omega) = |R(\omega)|^2 \xi G_L(\omega) \tag{263}$$

where $G_L(\omega)$ is the input conductance of the termination. It is related to the gain $G(\omega)$ of the antenna by

$$G(\omega) = \frac{4\pi\xi}{c^2}|R(\omega)|^2 f^2 G_L(\omega). \tag{264}$$

The following expression obtained from the Norton equivalent circuit theorem was used for the calculation of receiving transfer function:

$$R(\omega) = \frac{I_{sc}}{\frac{1}{Z_{in}} + \frac{1}{Z_L}} \tag{265}$$

where $Z_L$ is the termination impedance. The receiving transfer function magnitude of the loaded antenna with different resistive terminations is shown in Figure 49. The phase of the receiving transfer function is shown in Figure 50. It can be seen that only the 50 $\Omega$ termination has broadband receiving characteristics, even though it has the least sensitivity. The upper roll-off frequency obtained with highly resistive terminations ($R_L \geq 5\,k\Omega$) is too low for sub-nanosecond pulse reception. The bandwidth provided by the 500 $\Omega$ is not sufficient for most pulse applications. Therefore, one has to look into ways of reshaping the receiving transfer function. This is done in Section 5.5.

### 5.4.2 Time-Domain Results

#### From NEC and FFT

Frequency-domain results obtained using NEC (and presented in the previous section) have been transformed to the time domain, numerically, using a FFT code. Two bandlimited incident pulse waveforms are considered. One incident pulse has a truncated Gaussian spectrum given by

$$E_1^i(f) = \begin{cases} e^{-0.022f^2}, & f \leq 10.2 \text{ GHz} \\ 0, & f > 10.2 \text{ GHz} \end{cases}. \tag{266}$$

This spectrum has 3dB bandwidth of 4 GHz and it is truncated at the -10 dB level. The waveform of this incident pulse $e_1^i(t)$ approximates a Gaussian pulse, as shown by the dotted

line in Figure 53. The other incident pulse has a rectangular spectrum given by

$$E_2^i(f) = \begin{cases} 1, & f \leq 9.6 \text{ GHz} \\ 0, & f > 9.6 \text{ GHz} \end{cases} \tag{267}$$

and hence the 'sinc' waveform shown in Figure 51- dotted line. Among the common bandlimited waveforms, the sinc pulse has the fastest rise time (transition duration) for a given bandwidth. This particular sinc pulse has a 10-90% rise time of 34 ps and half-magnitude pulse width (PWHM) of 63 ps.

The short-circuited terminal current waveform $i_{sc}(t)$ of the unloaded antenna excited by the sinc pulse, incident in boresite direction, is shown in Figure 51. The short-circuited terminal current of the loaded antenna, under identical excitation, is shown in Figure 52. The loaded antenna is then terminated with a 500 Ω resistive load (such as an oscilloscope probe). Figure 53 shows the terminal voltage waveform of the antenna, for the approximately Gaussian incident pulse excitation. Figure 54 shows the same results but for sinc incident pulse excitation. It can be seen that the output of the antenna has been stretched considerably. This is mainly due to the relatively larger attenuation of high-frequency components, as seen in Figure 49. It should be noted here that $v_L(t)$ shown in these figures is the voltage waveform at the antenna terminals and therefore it excludes the common 20 dB attenuation of passive 500 Ω probes.

### From VDIP

Some of the time-domain results obtained from the VDIP code are presented below. One advantage of the direct time-domain analysis is the facility to provide the spatio-temporal distribution of the currents and charges on the antenna. This allows us to understand the physics of the system which seems difficult with frequency-domain data alone.

Figure 55 shows the spatio-temporal distribution of the current induced in the unloaded antenna, when a short Gaussian electromagnetic pulse is incident in the boresite direction. The terminals of the antenna are short-circuited. Each arm of the V-dipole was divided into 80 segments in the analysis. Figure 56 shows the spatio-temporal variation of charge on the

same antenna. The incident pulse takes approximately 1 ns to pass the 30 cm long antenna. During the presence of the incident pulse, the antenna captures some energy and stores it in the near field. Since the antenna is lossless and the terminals are short-circuited, the only loss mechanism is due to radiation. Therefore, the current and charge stays for an extended period of time even after the incident pulse disappears. The current and charge 'pulses' travel back and forth along the wire due to reflections at the free ends. As it is difficult to read the current values form the 3-D plot, some 2-D cross-sectional views are shown in Figures 57 and 58. Figure 57 shows the current waveform at a few locations on the wire. Figure 58 shows the current distribution along the wire at a few instances (snap-shots).

When the loaded antenna is excited by a short Gaussian pulse incident in boresite direction, the spatio-temporal variation of current is as shown in Figure 59 and the charge is as shown in Figure 60. The terminals are short-circuited. The major difference between this and the unloaded case is the rapid attenuation of current and charge pulses as they travel towards the open ends. This must be due to the tapered internal resistance of the wires. The current and charge pulses virtually disappear at the open ends. Again, Figure 61 shows the current waveform at a few locations on the wire. Figure 62 shows the current distribution along the wire at a few points in time.

In order to validate the VDIP code, the response of the unloaded and loaded antennas excited by the sinc pulse is calculated and compared with NEC results. As the ideal sinc pulse is strictly bandlimited and time-unlimited, one has to truncate the waveform at some point, for time-domain analysis. The incident pulse used for time-domain analysis is shown by the dotted line in Figure 63(a). It is an approximation to the ideal sinc pulse shown in Figure 63(b)- dotted line. The short-circuited terminal current of the unloaded antenna is calculated using VDIP and the results are shown in Figure 63(a). For comparison, the results obtained from NEC and FFT for the ideal sinc pulse excitation (previously shown in Figure 51) are shown again in Figure 63(b). It can be seen that the results from the two methods compare very well. The short-circuited terminal current of the loaded antenna calculated using VDIP is shown in Figure 64(a), which also compares very well with the NEC and FFT results shown in Figure 64(b) (as well as in Figure 52).

## 5.5 Shaping the Receiving Response

Results presented in the previous section suggest that even the resistively loaded V-antenna may not be a good pulse receiving antenna. In particular, the upper roll-off frequency and the bandwidth obtained with the 500 Ω probe is not suitable for pulse applications. At the same time, these results prove our original assumption that at higher frequencies, the drop of response occurs very slowly with frequency. Hence, we have the option to sacrifice the peak sensitivity by a small factor and increase the upper roll-off frequency by a larger factor. However, this should be done in such a way that the final frequency response of the system is flat over a broad frequency range, unlike those shown in Figure 49. We will systematically address this problem of re-shaping the receiving frequency response of the loaded antenna in this section.

Consider a V-monopole terminated *only* with a capacitance $C_e$. This external capacitance, together with the monopole input capacitance, forms a capacitive voltage divider at lower frequencies and hence produces a flat transfer function, as shown in Figure 65- dashed line. Nonetheless, at higher frequencies, the monopole is no longer predominantly capacitive. The capacitance $C_e$ virtually short circuits the antenna terminals at higher frequencies and hence the response drops to zero. The voltage division ratio (at low frequencies) can be controlled by varying the external capacitance.

On the other hand, if the monopole is terminated with a small resistance $R_e$ alone, it will produce a useful response only at higher frequencies, as shown in Figure 65- dotted line. This suggests that the low-frequency response produced by $C_e$ and the high-frequency response produced by $R_e$ can be effectively combined by using a series RC termination. The low- and high-frequency responses can be made equal by selecting proper values for $R_e$ and $C_e$. The receiving transfer function magnitude obtained with such a Response Equalizer Circuit (without the probe) is shown in Figure 65- solid line. It can be seen that the response variation is less than 3 dB for all frequencies up to 10 GHz.

The configuration of a new V-monopole antenna with a Response Equalizer Circuit (REC) and an oscilloscope probe is sketched in Figure 66. This monopole configuration

is useful for ground-plane applications such as scattering range measurements. A V-dipole version can also be implemented for free-space measurements. Now consider the effect of the oscilloscope probe when it is connected to the V-monopole with the REC. The finite resistance of the probe obviously affects the response at very low frequencies. For a given monopole and REC, the lower roll-off frequency is determined by the probe resistance $R_p$. For a given probe, a flat in-band response can be achieved by adjusting the REC capacitance $C_c$. This optimization was carried out for 50 Ω and 500 Ω probes. The resulting receiving transfer function magnitudes are shown in Figure 67 and the phases in Figure 68. It is seen that with the 500 Ω probe, 3-dB bandwidth better than 25 MHz-10 GHz is possible. It should be noted that at 10 GHz, the monopole is 10 $\lambda$ long.

The above numerical results can be compared with the results obtained for a corresponding WK straight monopole antenna. A 2-cm-long WK monopole has approximately the same peak sensitivity ($\approx$ 10 mV/(Vm$^{-1}$)) as the V-monopole with REC and a 500 Ω probe. For a 1 mm thick WK monopole, $r(0)$ is found from (258) as 16.4 kΩ/m. The receiving transfer function of this WK monopole was calculated using NEC. The magnitude of receiving transfer function is shown in Figure 69, for different values of probe resistance $R_p$. The phase of the transfer function is shown in Figure 70. Comparing Figures 67 and 69, it can be seen that for a given probe resistance, the new antenna has a much broader bandwidth and a higher sensitivity than the WK monopole. With a 500 Ω probe, the lower roll-off frequency of the WK monopole is about 50 MHz, the upper roll-off frequency is about 6.5 GHz, and sensitivity is less than 7 mV/(Vm$^{-1}$) (neglecting the probe attenuation). At 6.5 GHz, the WK monopole is only 0.46$\lambda$ long.

The time-domain response of the loaded V-antenna with the REC and a 500 Ω probe was calculated using frequency-domain data and FFT. The terminal voltage waveform $v_L(t)$ to the approximately Gaussian incident pulse, shown in Figure 71, closely resembles the incident pulse waveform $e_1^i(t)$. This may be compared with the response of the same V-monopole but without REC, shown in Figure 53. For comparison, the response of the WK monopole (with a 500 Ω probe) to the same incident pulse is shown in Figure 72. Highly attenuated low-frequency components have caused the undershoot in the WK monopole

response. The response of the V-monopole with REC to the sinc incident pulse is shown in Figure 73. Even this very broadband pulse, which has a width much less than 100 ps, can be received by the REC-assisted V-antenna without any significant fidelity errors. The response of the V-monopole without REC, to the sinc incident pulse was shown in Figure 54. The response of the WK antenna to the same incident pulse is shown in Figure 74.

## 5.6 Discussion

For a resistively-loaded V-antenna, the slow roll-off of $|h_{eff}|$ means that a large increase of bandwidth is possible by sacrificing a smaller amount of sensitivity. In our new antenna, the REC is used for this purpose. Comparing graphs in Figures 48 and 65, we find that the bandwidth improvement due to REC is by a factor of more than 10 (without probe) but the loss of sensitivity is only by a factor of 4. In a resistively-loaded straight dipole antenna, $|h_{eff}|$ falls-off rapidly at higher frequencies and hence such a trade-off would not be profitable. Therefore, REC would not be useful with WK and other straight dipole antennas.

The good lower roll-off frequency of the new antenna, even with a 500 Ω probe, can be explained as follows. Due to the longer length and the V-shape, the V-monopole has a much higher input capacitance compared with the corresponding WK monopole. Further, at lower frequencies, the REC capacitance $C_e$ is effectively added to the monopole capacitance and hence significantly lowers the roll-off frequency.

In summary, the WK resistively loaded straight antenna terminated with a readily available low-impedance (50 Ω or 500 Ω) oscilloscope probe does not have an adequate bandwidth for transient field measurements. Therefore, a new broadband antenna based on the resistively-loaded V-antenna has been developed. With a given oscilloscope probe, the new antenna gives a much broader bandwidth compared with the WK antenna. It is estimated to have a 3-dB bandwidth from 25 MHz to 10 GHz when used with a commercially available 500 Ω passive probe (Tektronix P6150). The sensitivity is approximately 1 $\mathrm{mV/(Vm^{-1})}$, taking into account the 20 dB attenuation of the 500 Ω probe. With a 50 Ω

termination, the new antenna has a 3-dB bandwidth from 110 MHz to above 10 GHz, and a sensitivity better than 4 $mV/(Vm^{-1})$.

Wide bandwidth and non-dispersive phase characteristics of the V-antenna make it very suitable for measuring fast electromagnetic pulses and transients. The width of the pulse can be as short as 70 picoseconds (or the transition duration of the transient, as short as 35 ps). The antenna with a 500 Ω probe is suitable for making measurements up to 40 ns. Even with a 50 Ω termination, measurements can be made up to 9 ns, without noticing the lower rolling-off effect. Since many time-domain scattering ranges have the operational time window between 8 ns and 12 ns, the new antenna with a 50 Ω termination can be used to improve the sensitivity and the resolution of scattering measurements. For comparison, the 10-mm tall L-antenna described in [39] has a sensitivity of 5.8 $mV/(Vm^{-1})$. However, in order to have an operational time window of 9 ns, the antenna has to be at least 135 cm long!

The new V-antenna can also be used in many time-domain unguided-wave measurement systems, which require broadband antennas. It also has potential applications in baseband (impulse) radar and target identification systems. The directivity of the new antenna can be a limitation in some applications, which require omni-directional antennas.

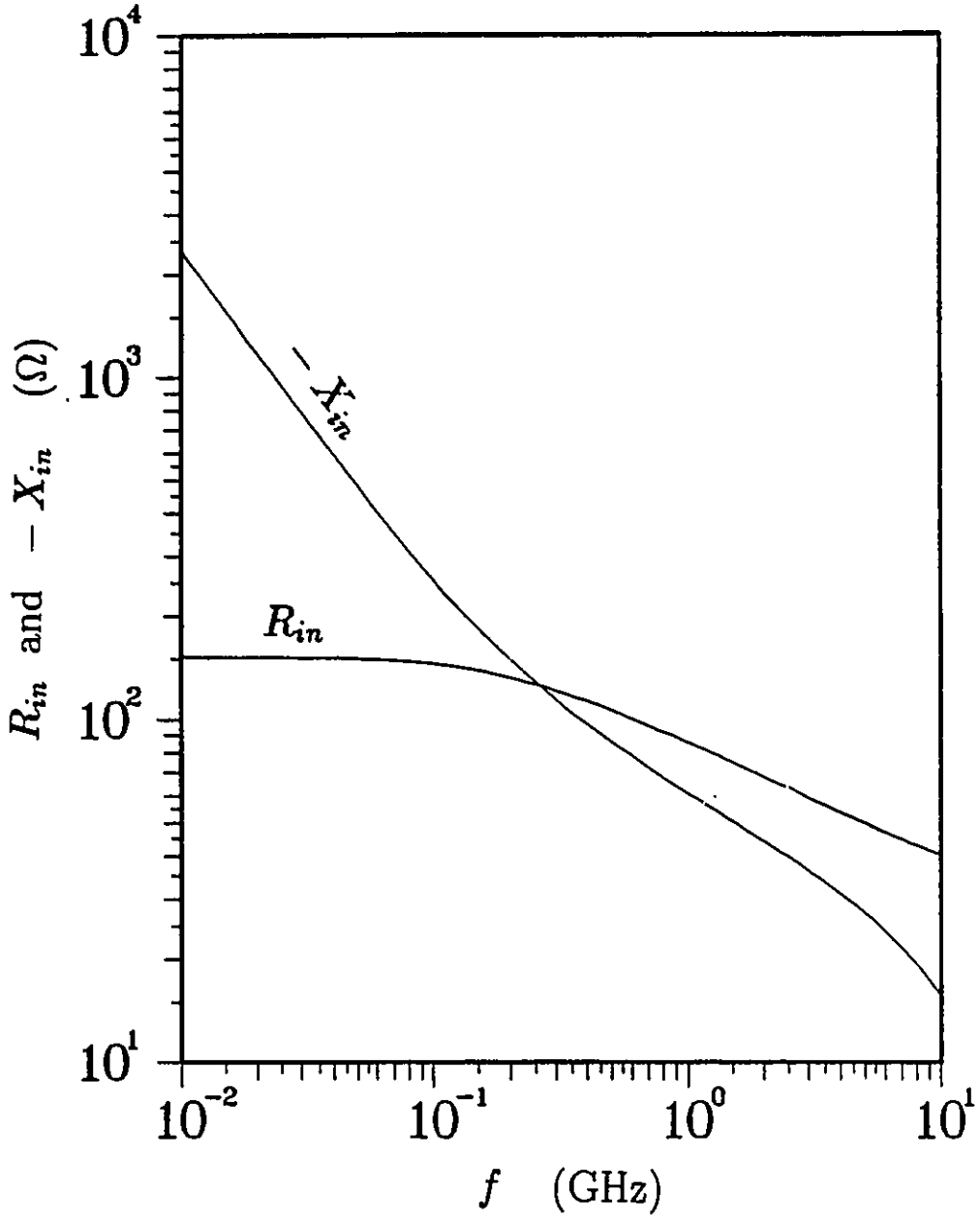


Figure 45: Input resistance ($R_{in}$) and the capacitive input reactance ($-X_{in}$) of the resistively loaded V-monopole versus frequency.

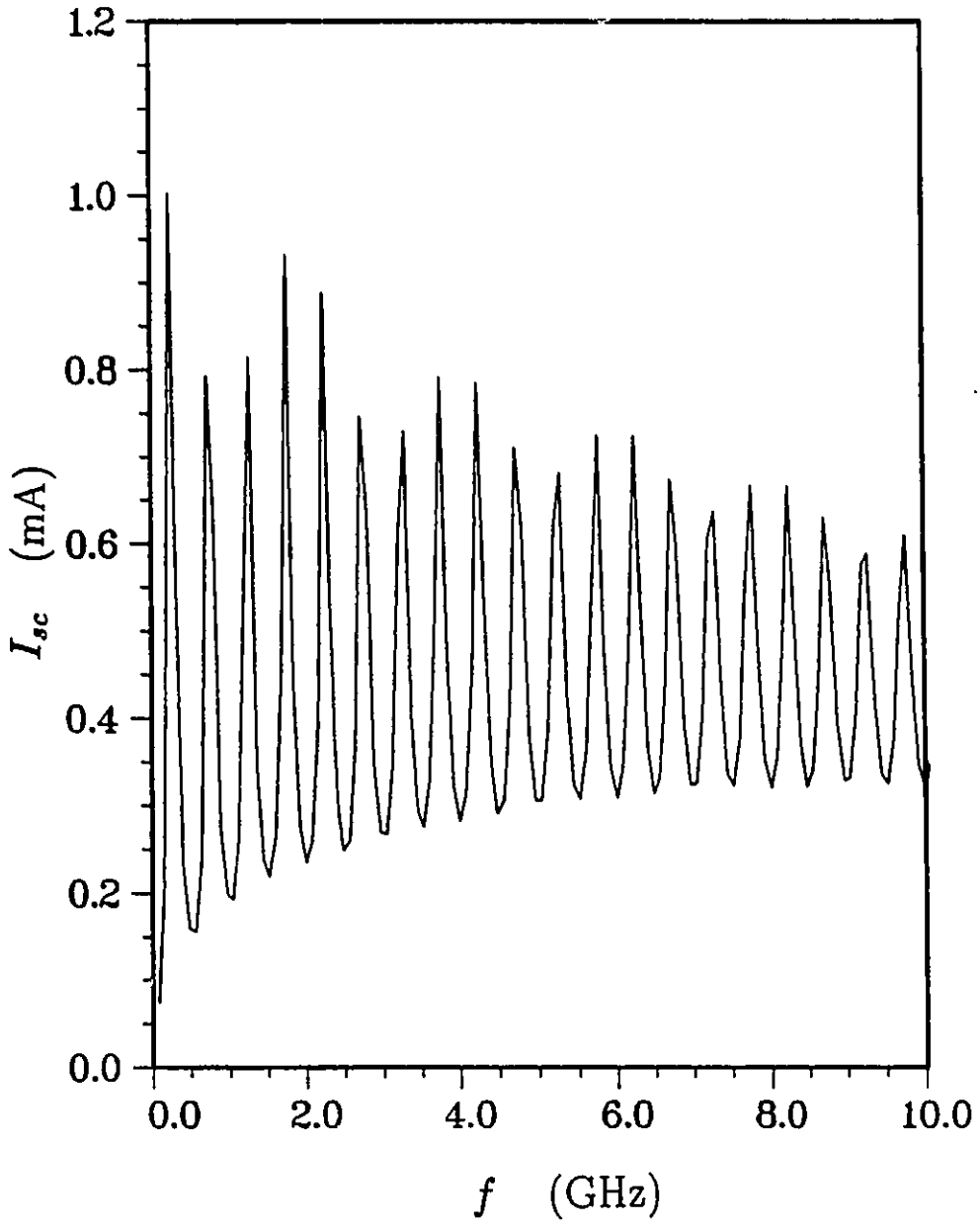


Figure 46: Short-circuit current of the unloaded V-antenna.

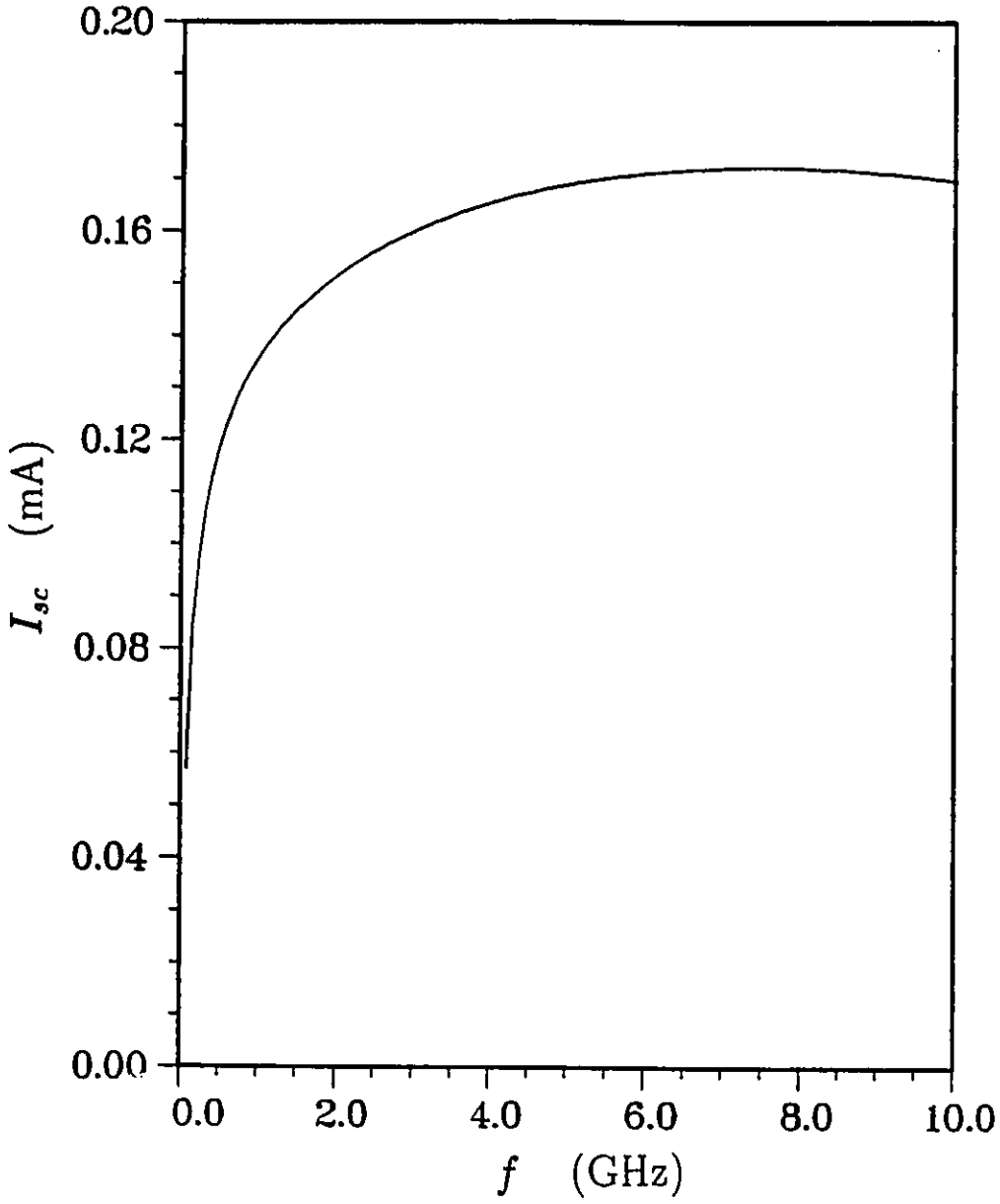


Figure 47: Short-circuit current of the loaded V-antenna.

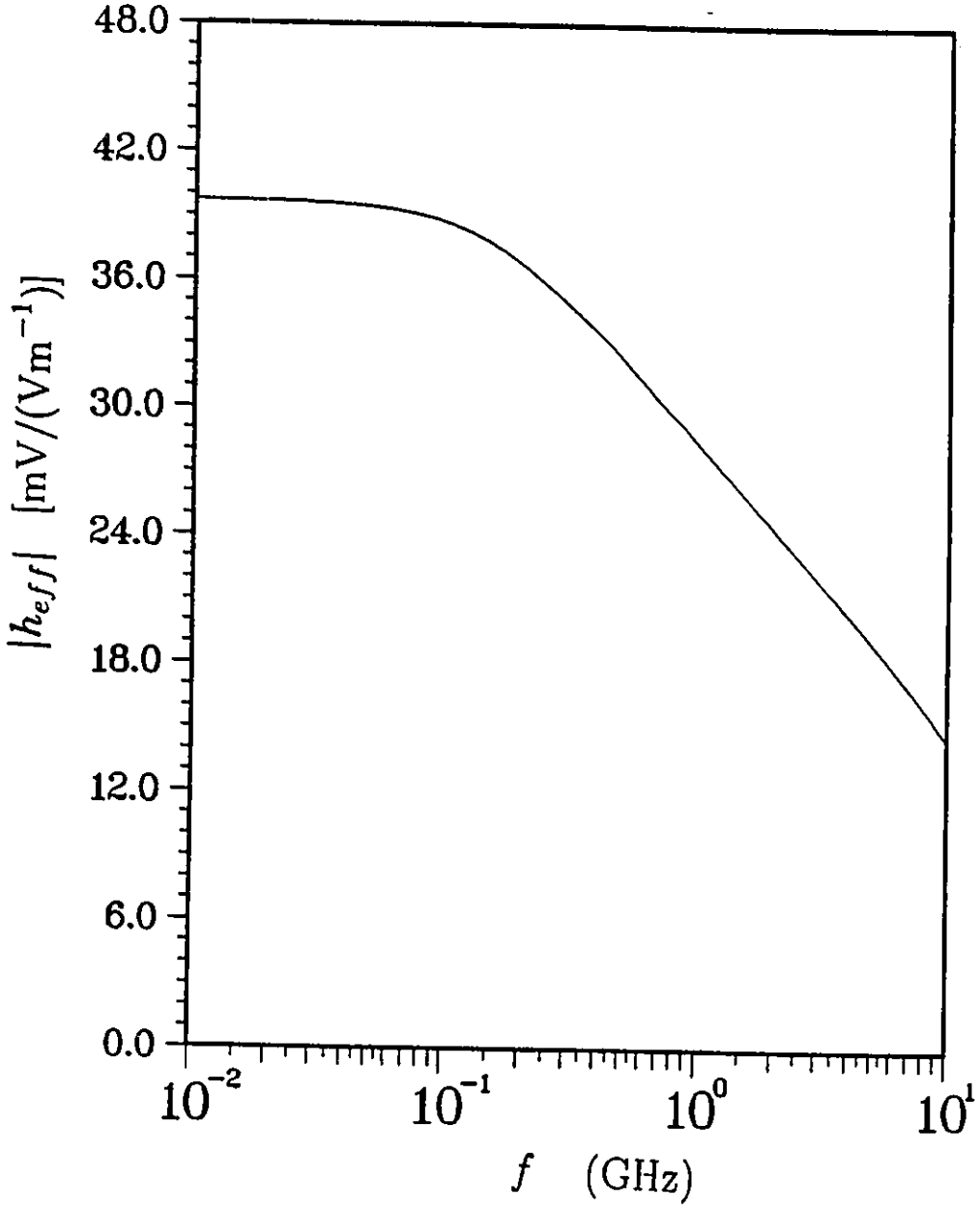


Figure 48: Effective height of the loaded V-antenna.

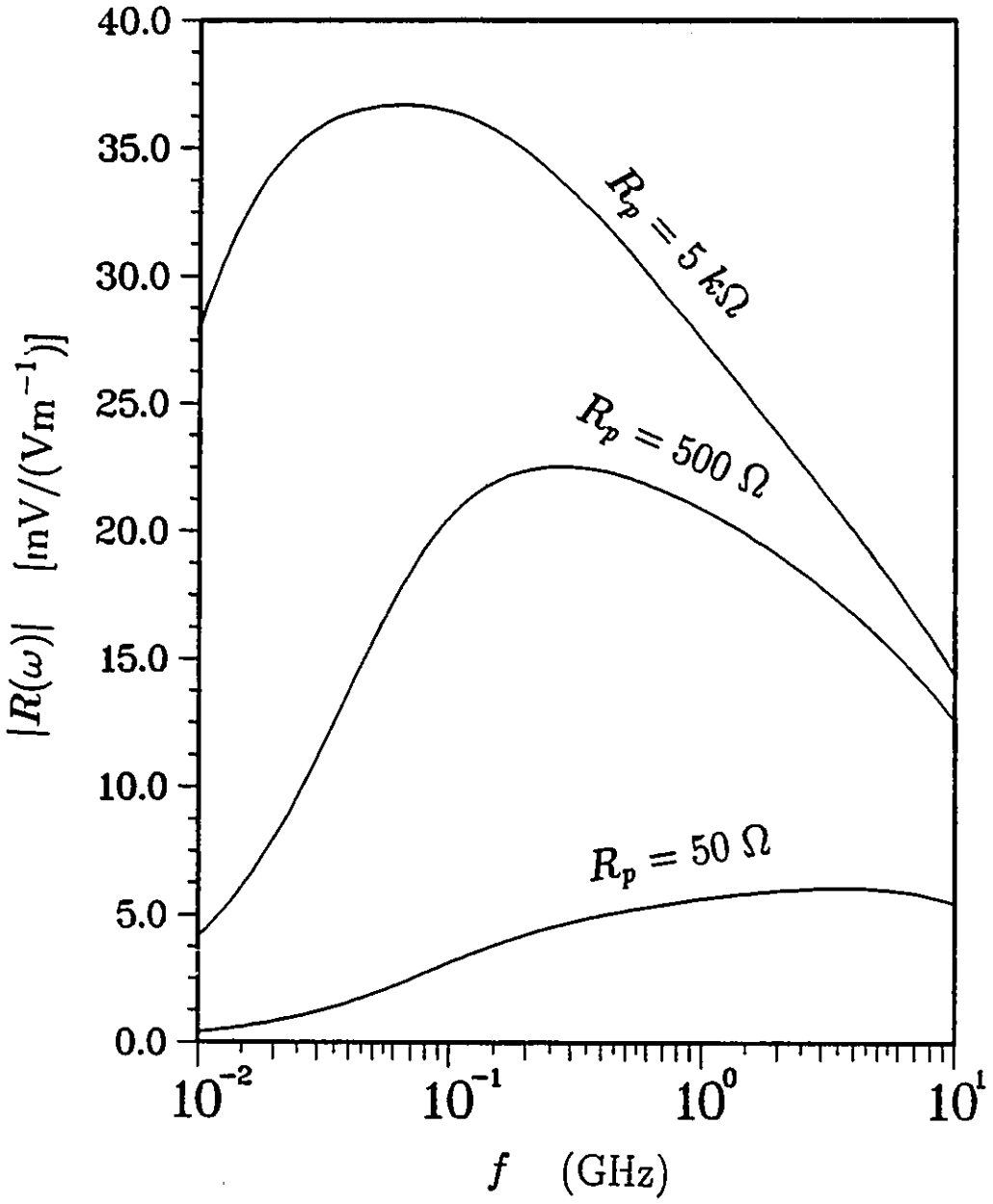


Figure 49: $|R|$ of the loaded V-antenna with a resistive termination. $R_p$ is the terminal resistance.

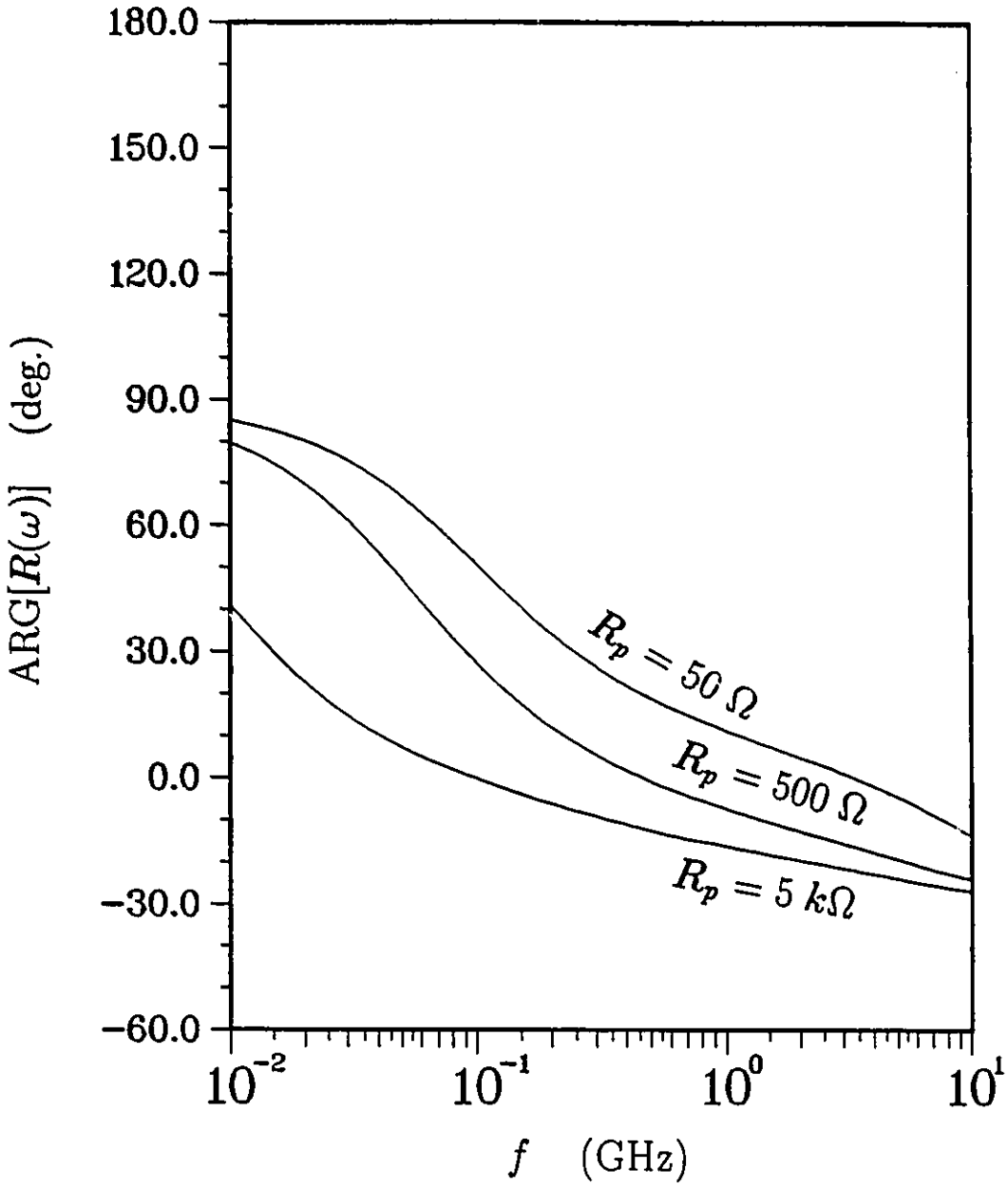


Figure 50: ARG($R$) of the loaded V-antenna with a resistive termination. $R_p$ is the terminal resistance.

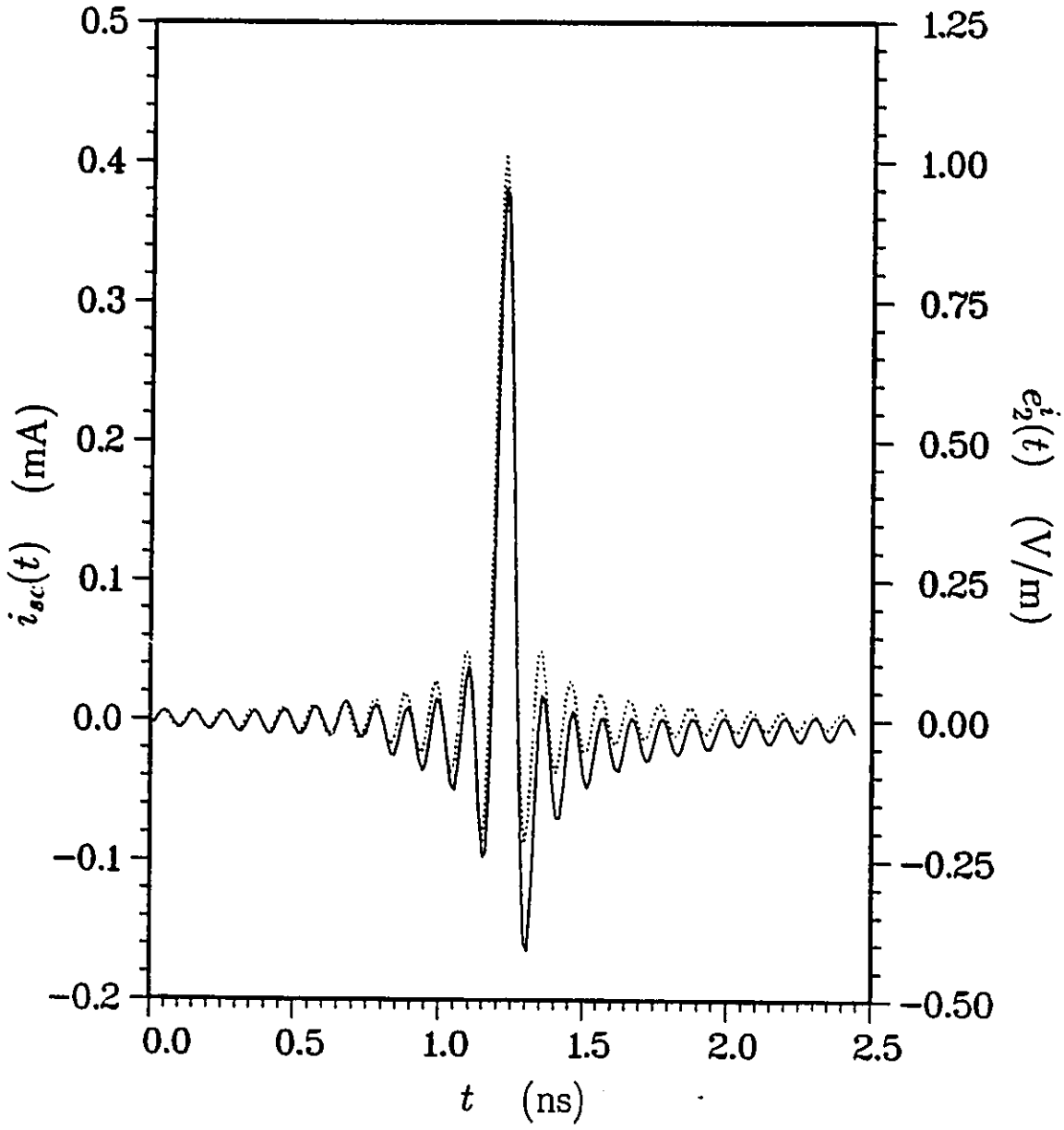


Figure 51: Short-circuit current of unloaded V-antenna to the sinc incident pulse (shown in dotted line).

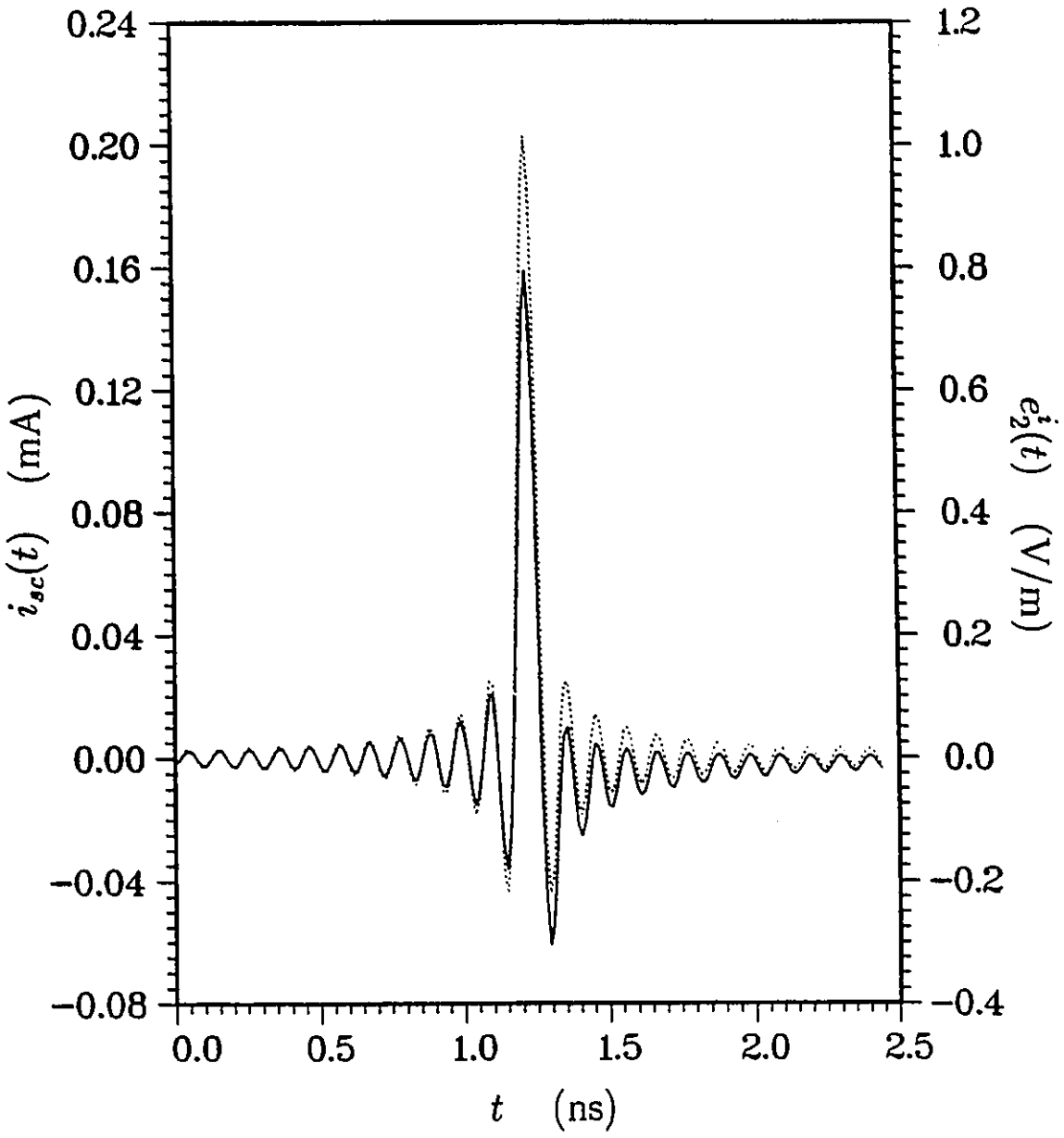


Figure 52: Short-circuit current of loaded V-antenna to the sinc incident pulse (shown in dotted line).

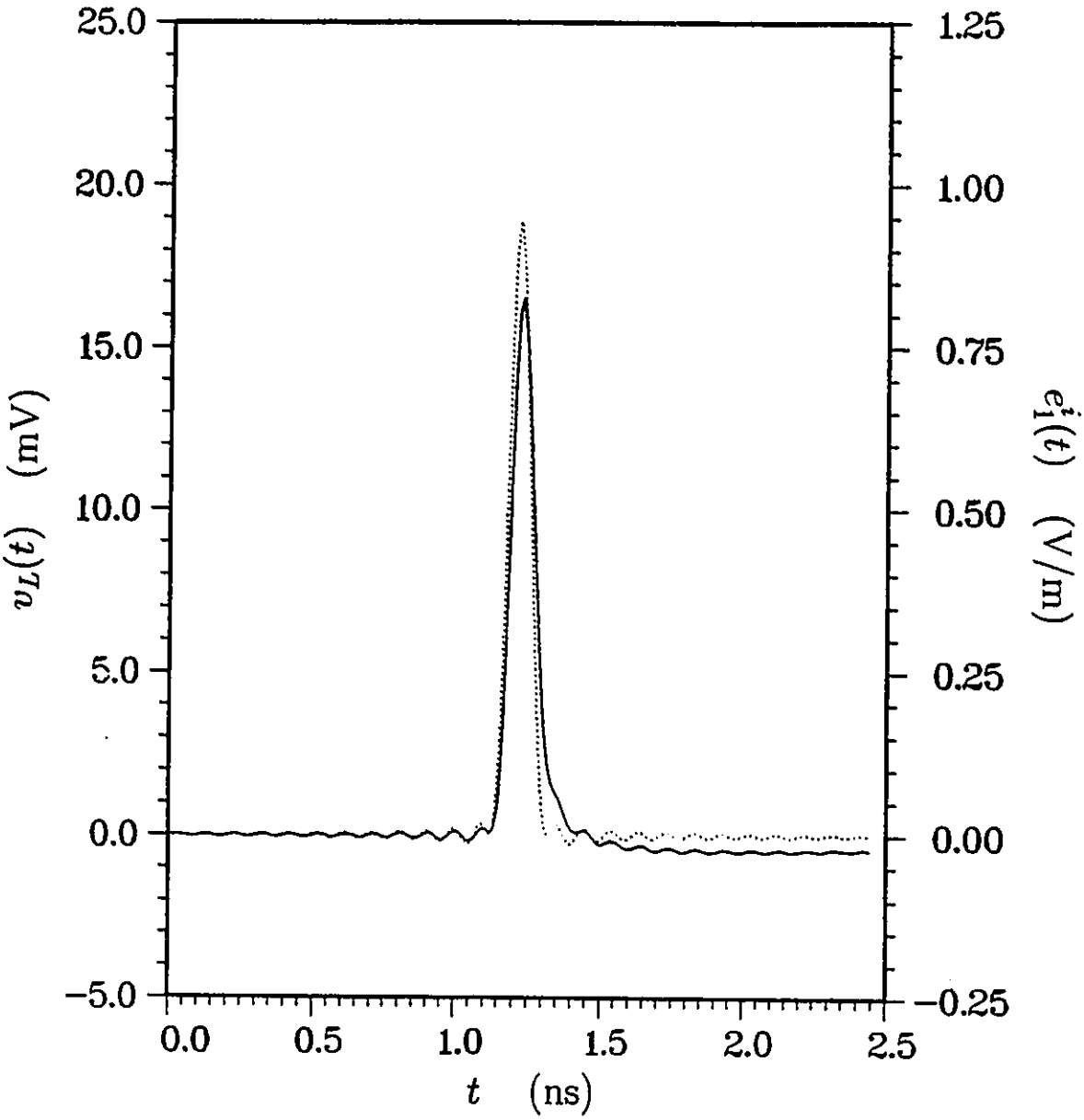


Figure 53: Response of the loaded V-antenna to the approximately Gaussian incident pulse (shown in dotted line). Termination is 500 Ω.

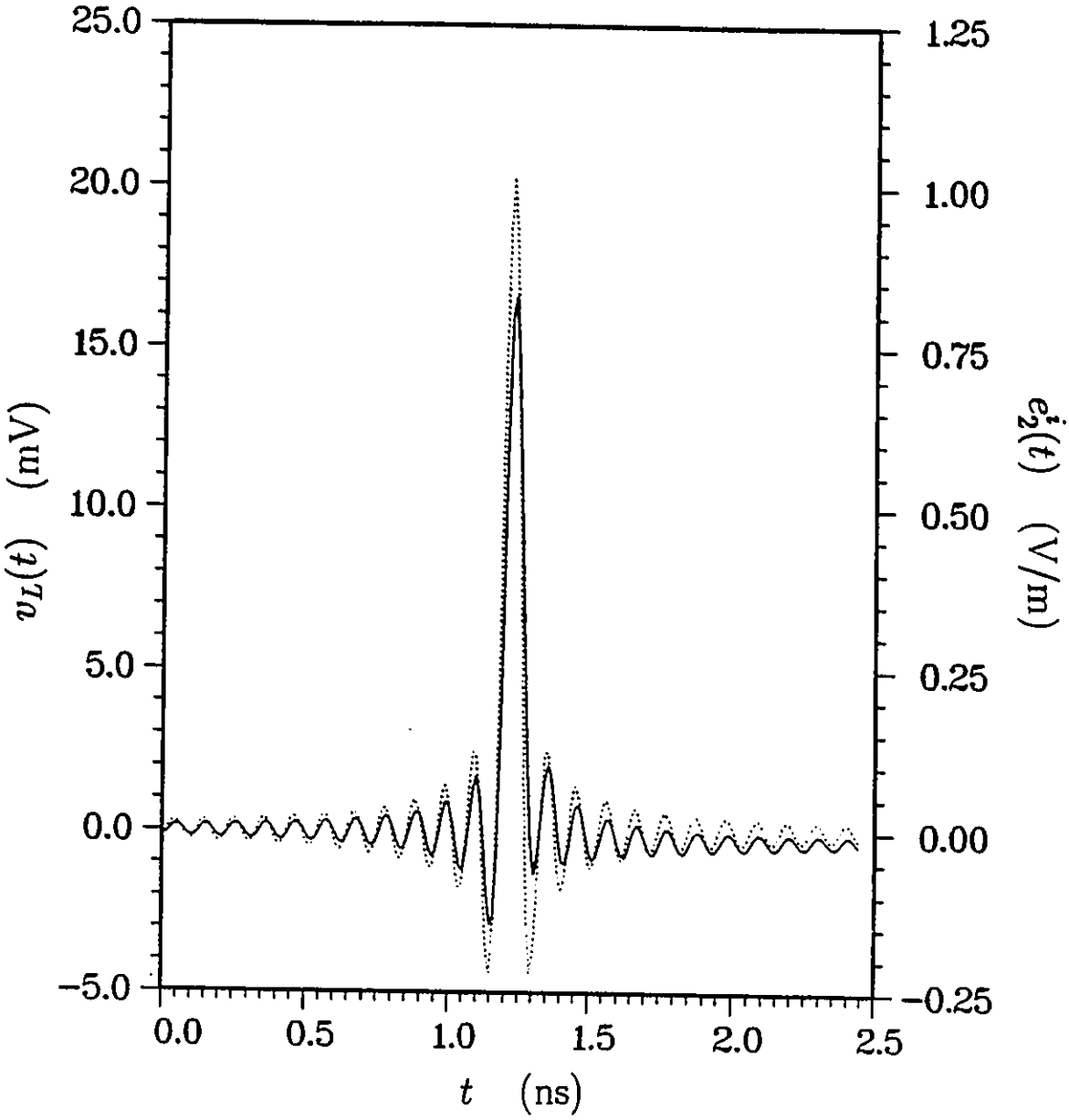


Figure 54: Response of the loaded V-antenna to the sinc incident pulse (shown by dotted line). Termination is 500 Ω.

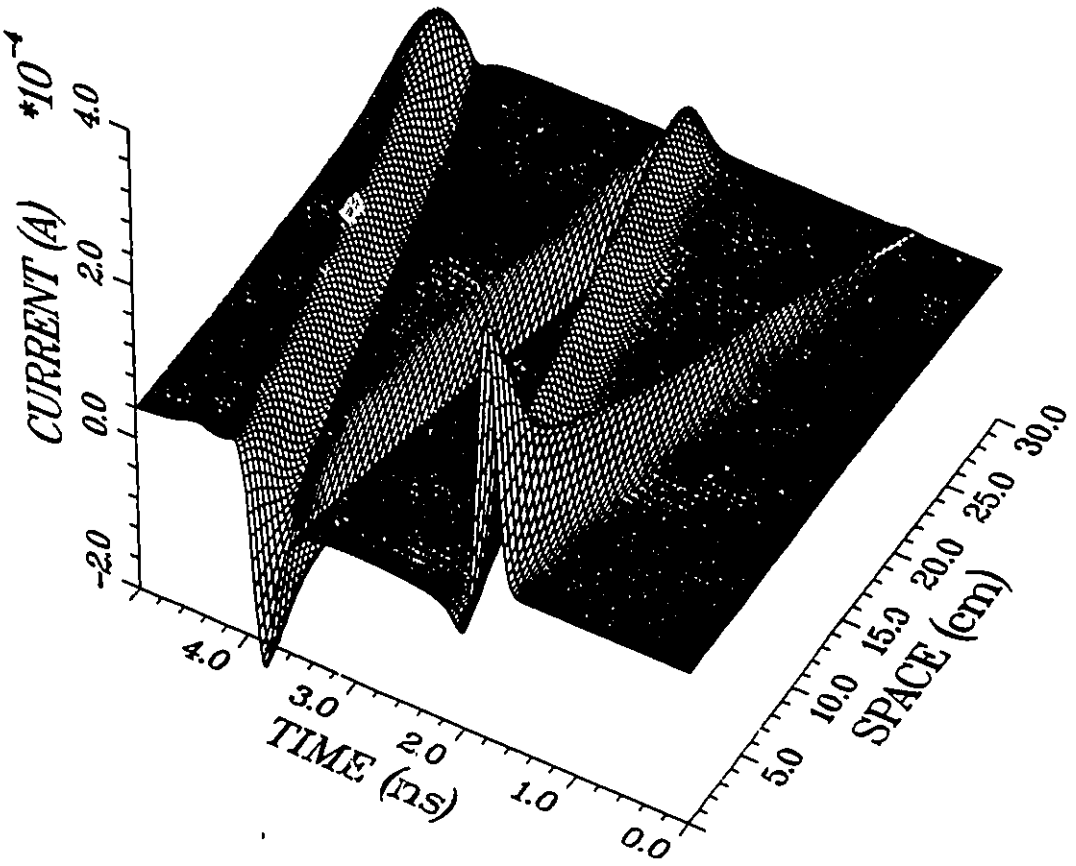


Figure 55: 3-D plot of current in the unloaded V-antenna, for short Gaussian pulse excitation.

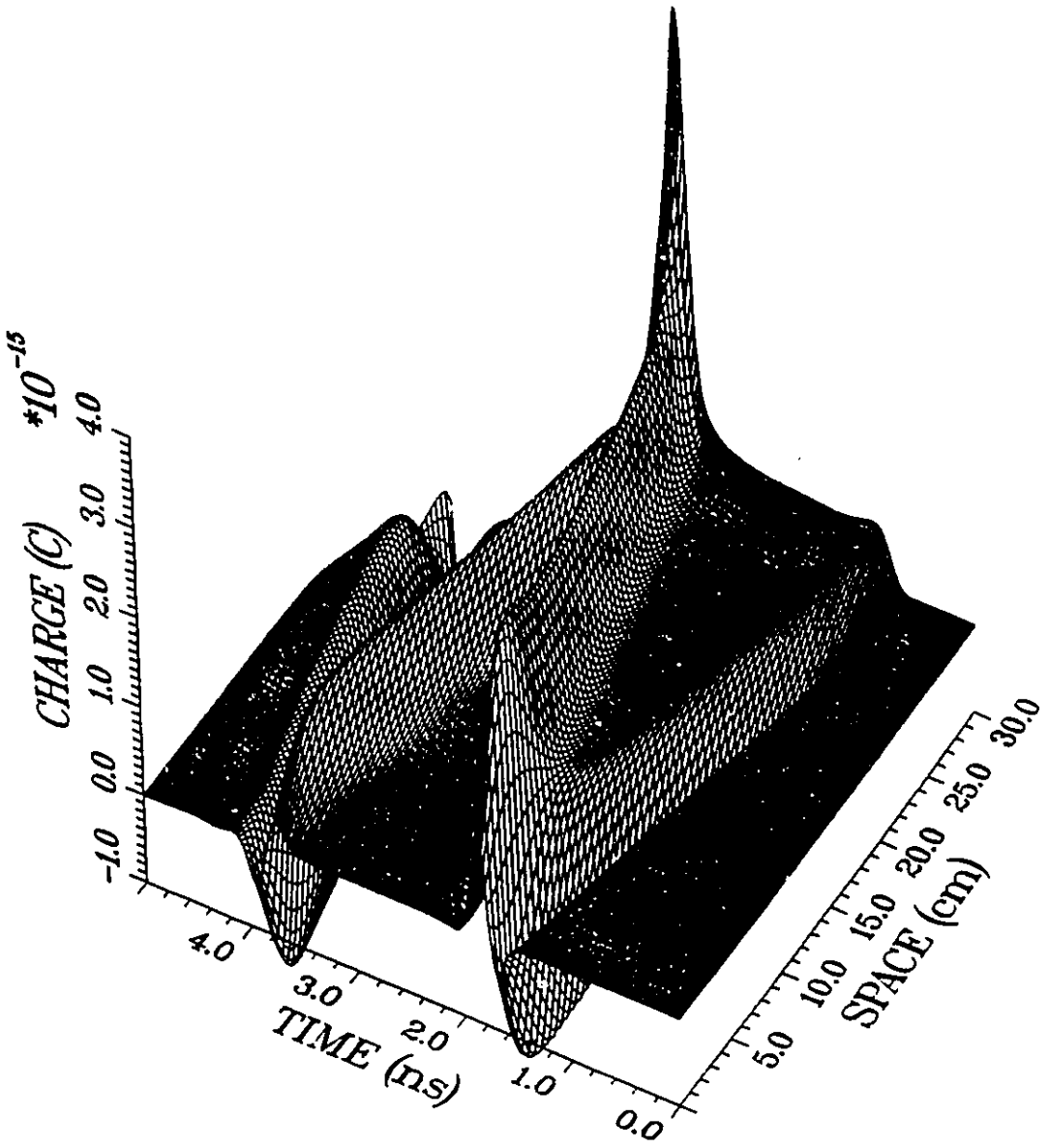


Figure 56: 3-D plot of charge in the unloaded V-antenna, for short Gaussian pulse excitation.

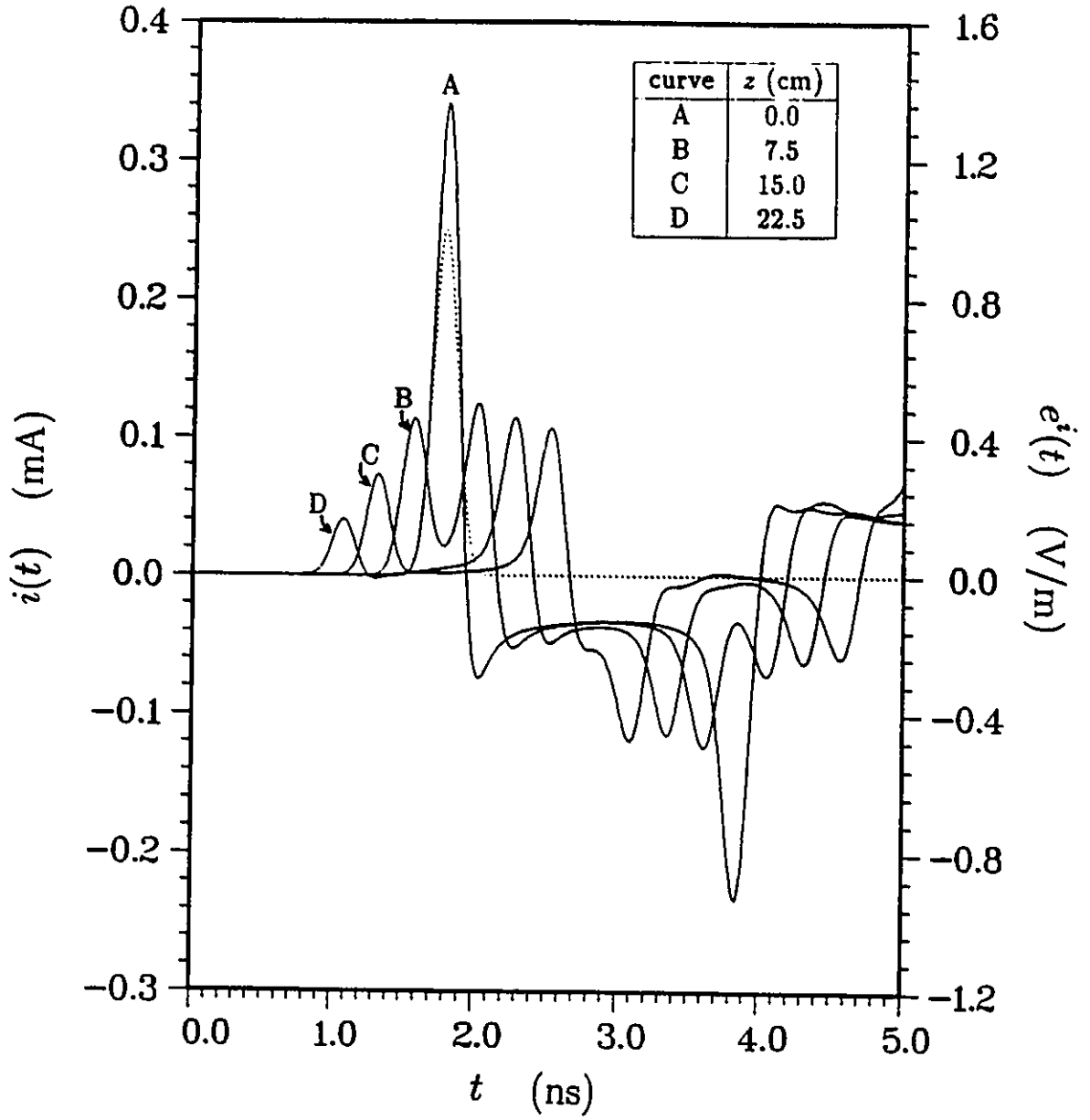


Figure 57: Current waveform at different points on an unloaded V-antenna, excited by a short Gaussian incident pulse. Distance from the terminals to the point is $z$.

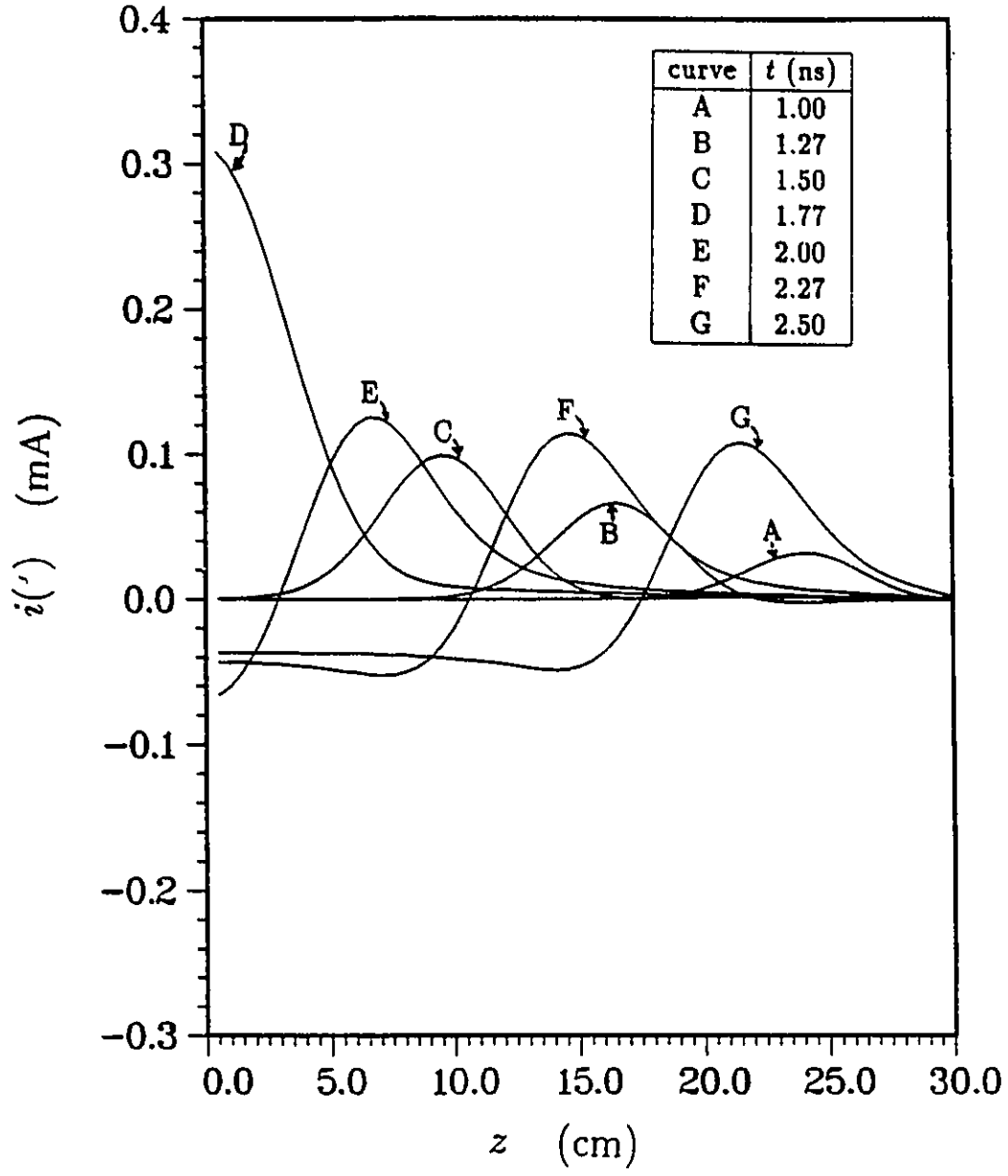


Figure 58: Snap-shots of the current distribution in an unloaded V-antenna, excited by a short Gaussian incident pulse.

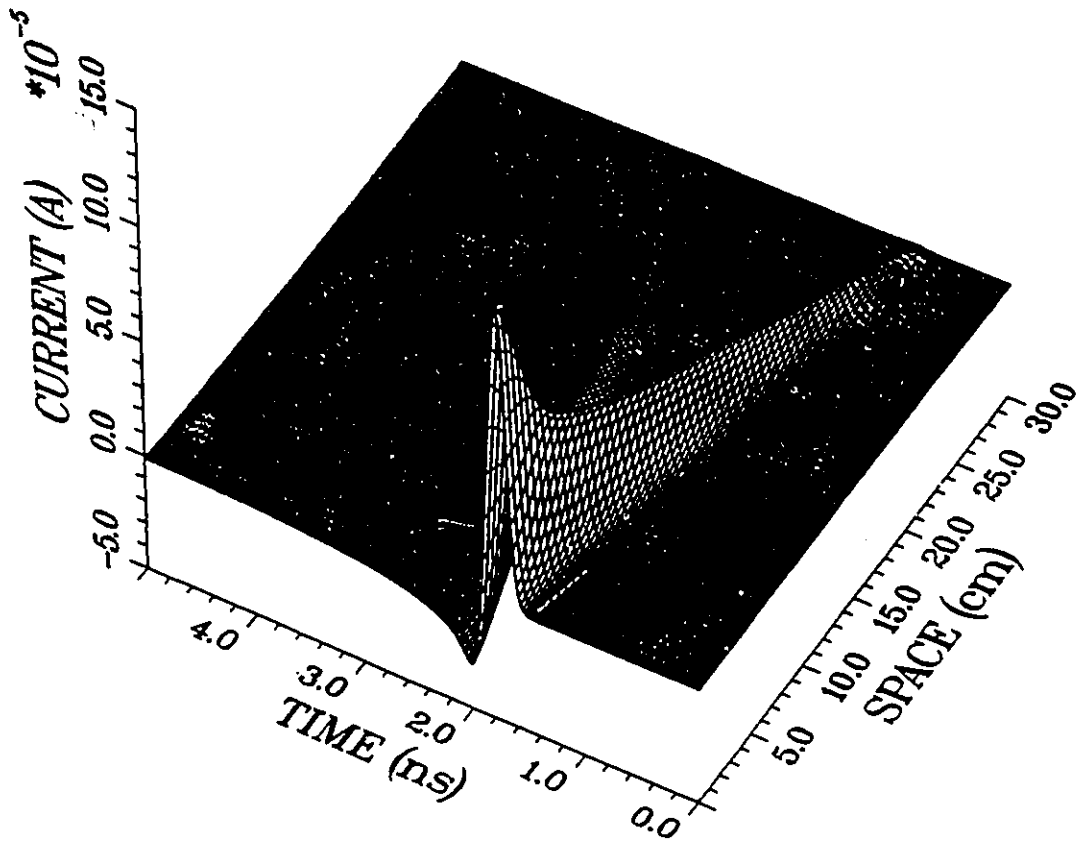


Figure 59: 3-D plot of current in the loaded V-antenna, for short Gaussian pulse excitation.

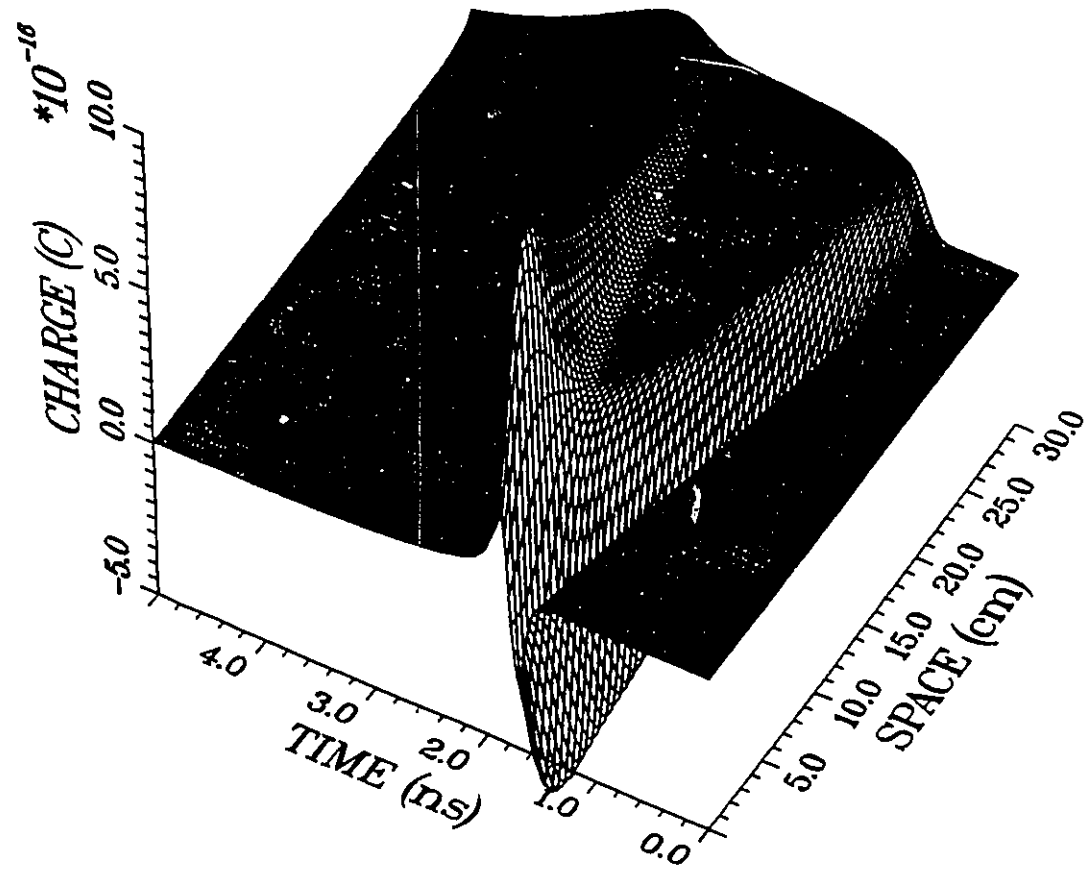


Figure 60: 3-D plot of charge in the loaded V-antenna, for short Gaussian pulse excitation.

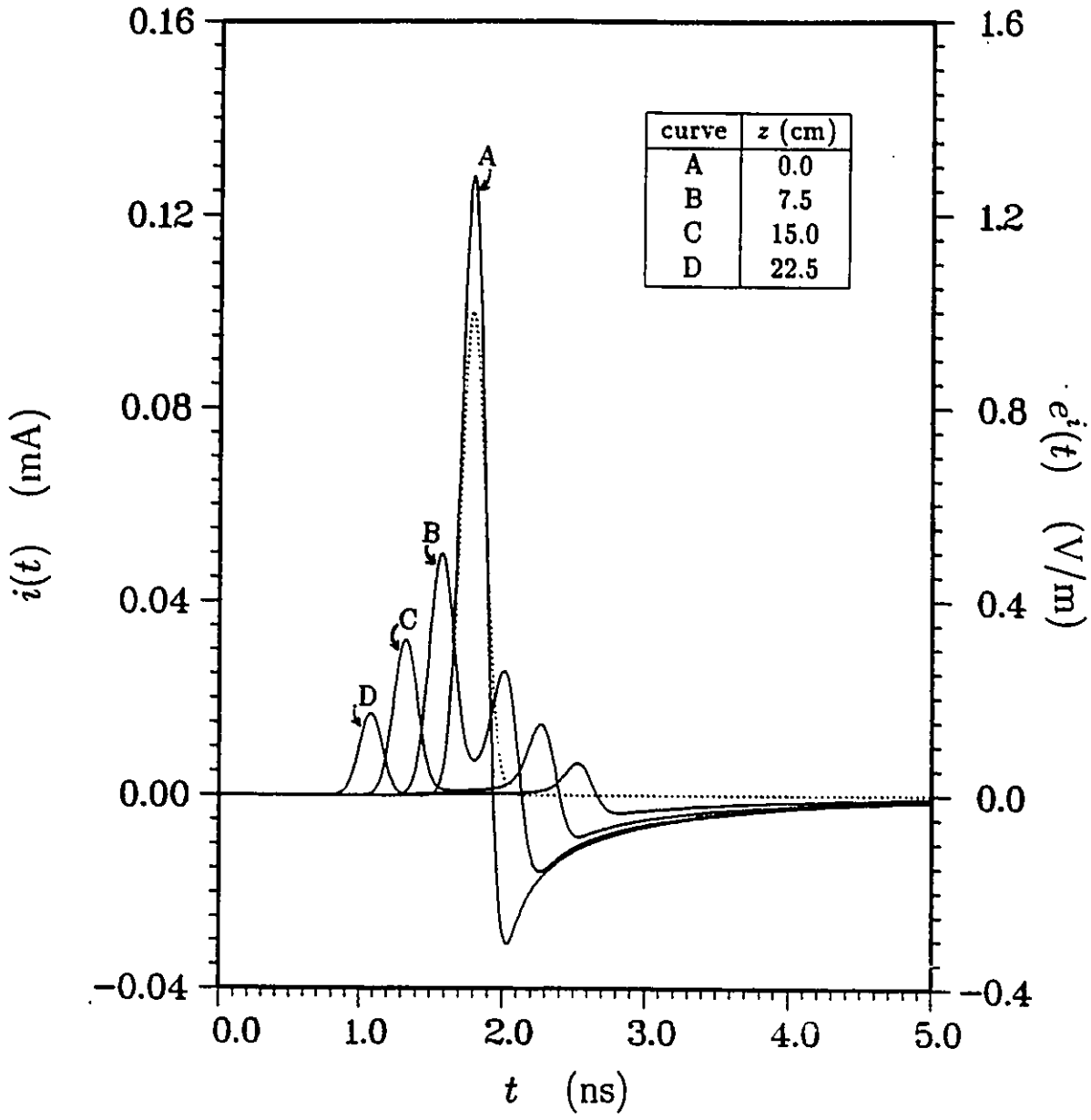


Figure 61: Current waveform at different points on a loaded V-antenna, exited by a short Gaussian incident pulse. Distance from the terminals to the point is $z$.

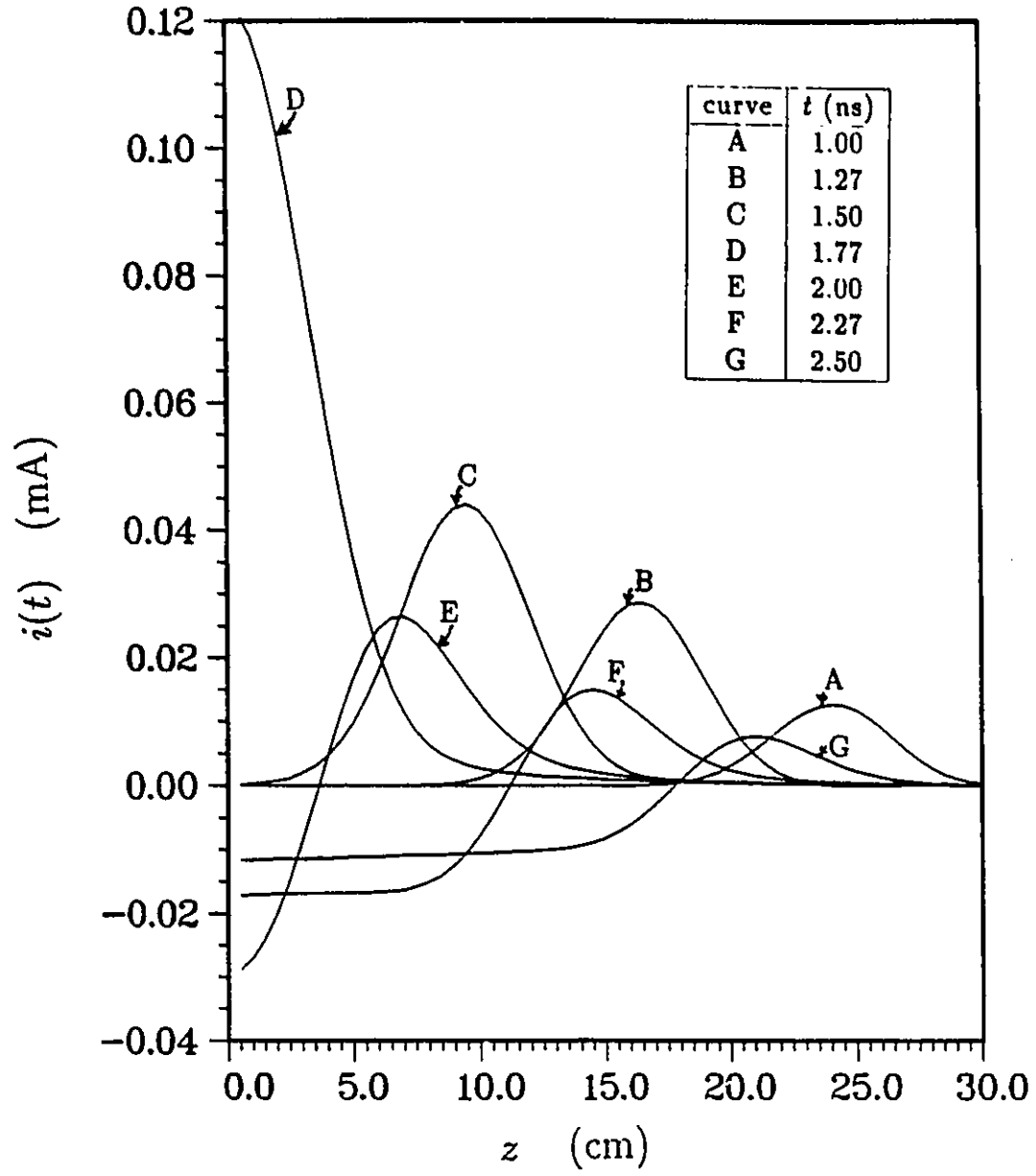


Figure 62: Snap-shots of the current distribution in a loaded V-antenna, excited by a short Gaussian incident pulse.

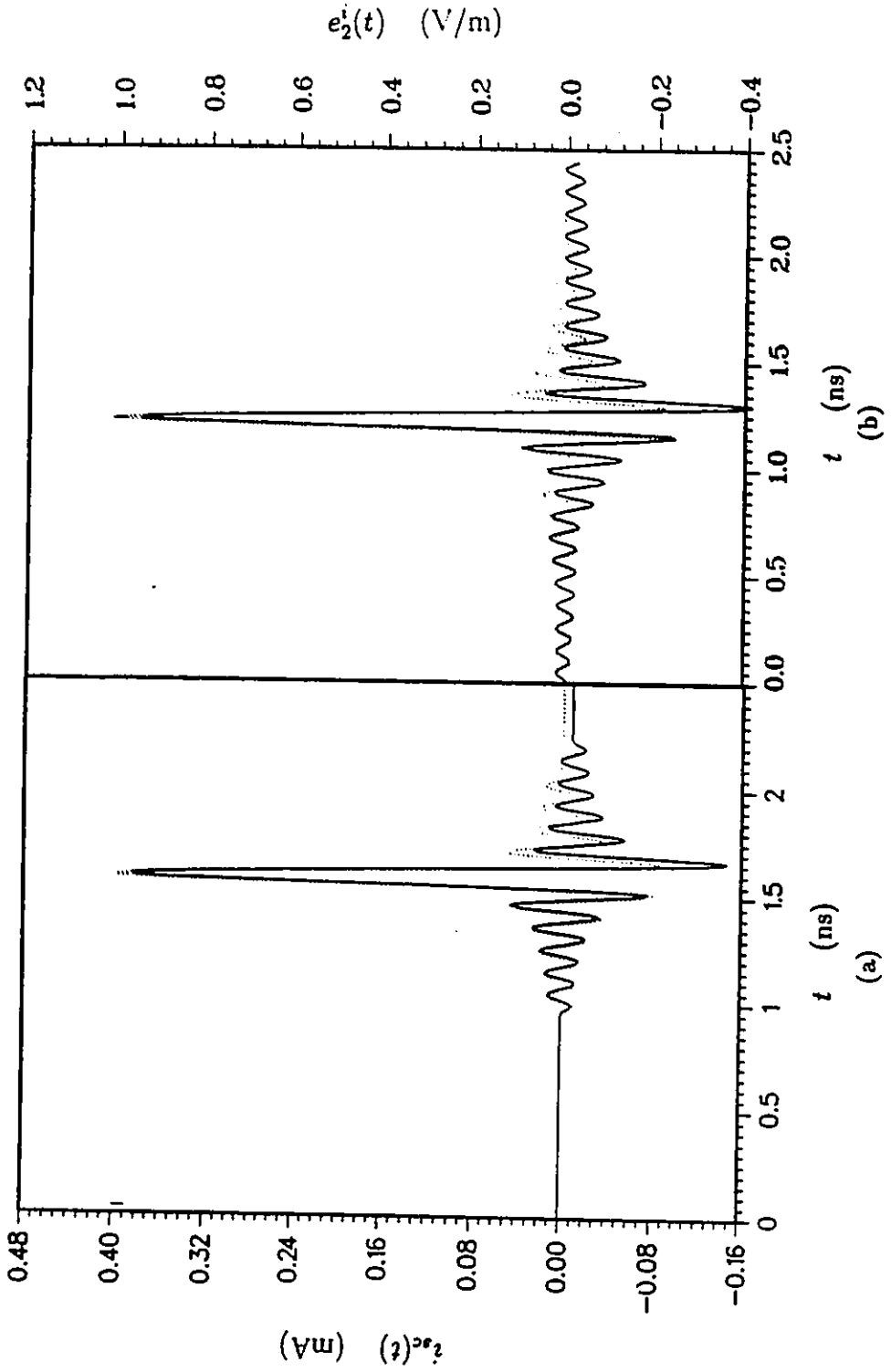


Figure 63: Short-circuit current of the unloaded V-antenna.
(a) from VDIP, (b) from NEC and FFT. Incident pulses are shown by dotted lines.

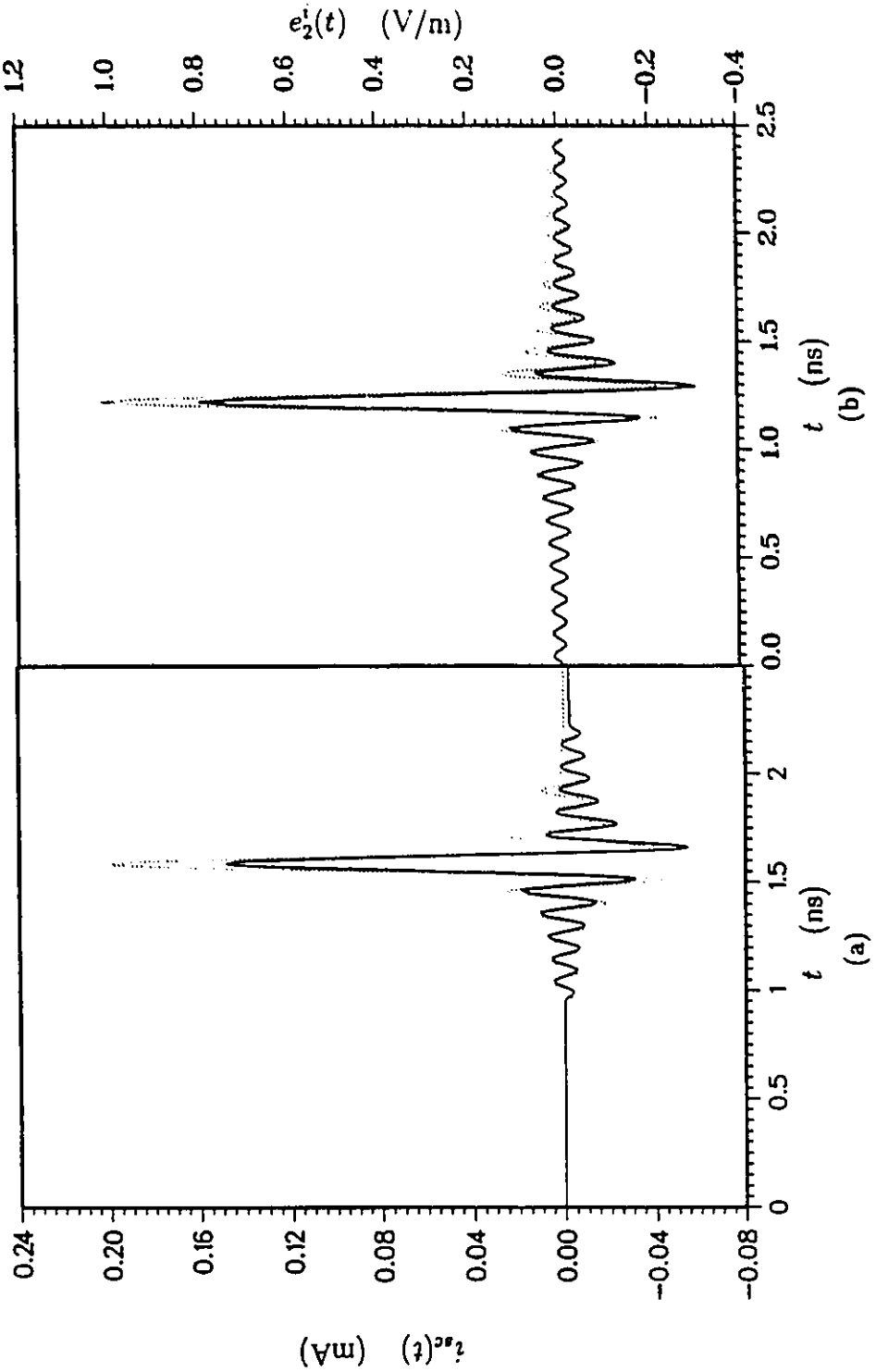


Figure 64: Short-circuit current of the loaded V-antenna.
(a) from VDIP, (b) from NEC and FFT. Incident pulses are shown by dotted lines.

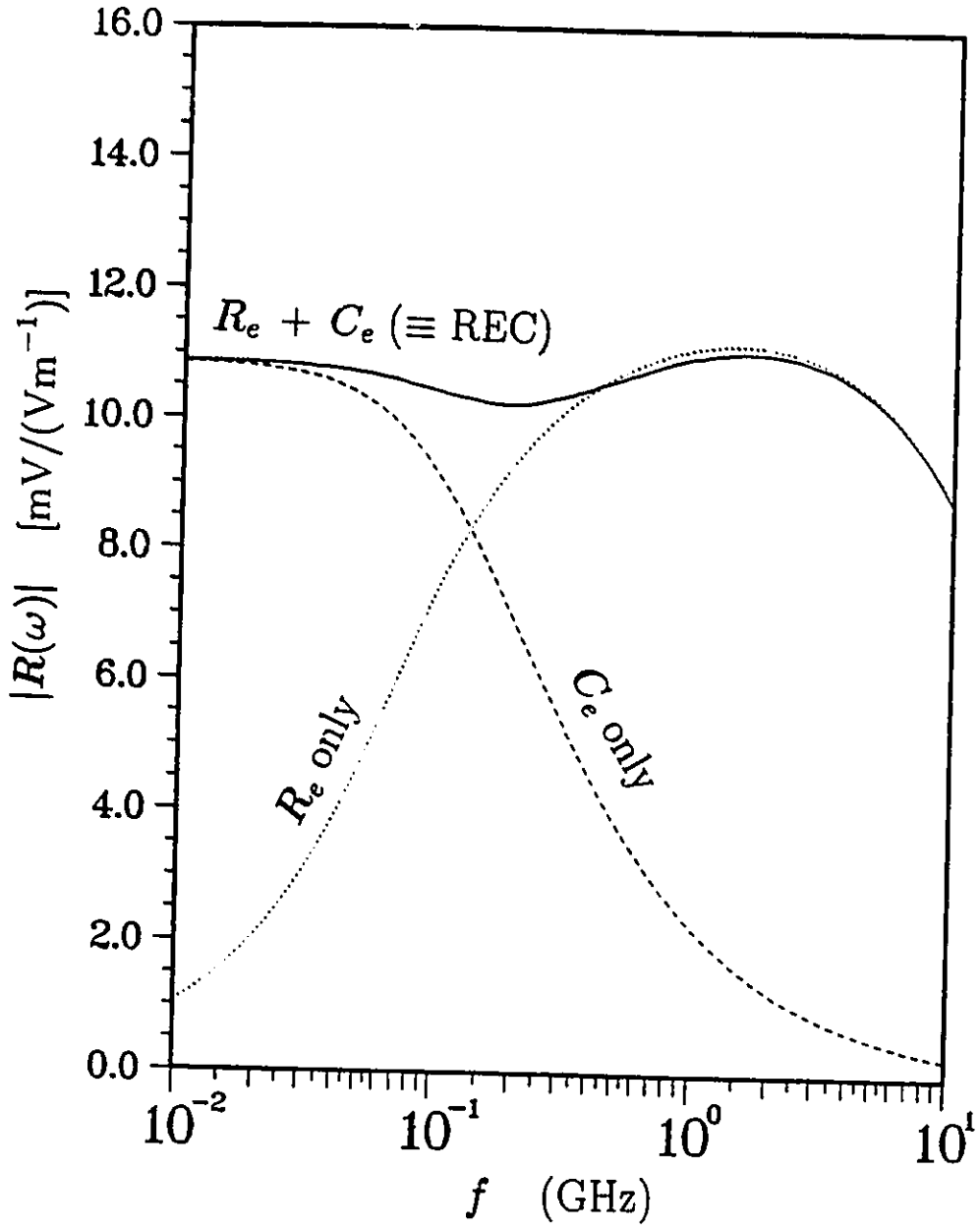


Figure 65: Frequency response of the loaded antenna for various terminations. Dotted line- 125 Ω resistance, dashed line- 9 pF capacitance, solid line- 125 Ω and 9 pF in series.

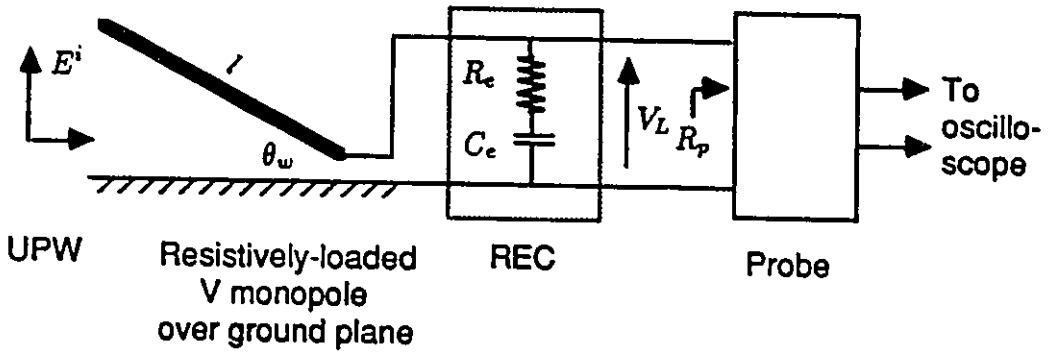


Figure 66: V-monopole antenna with REC.

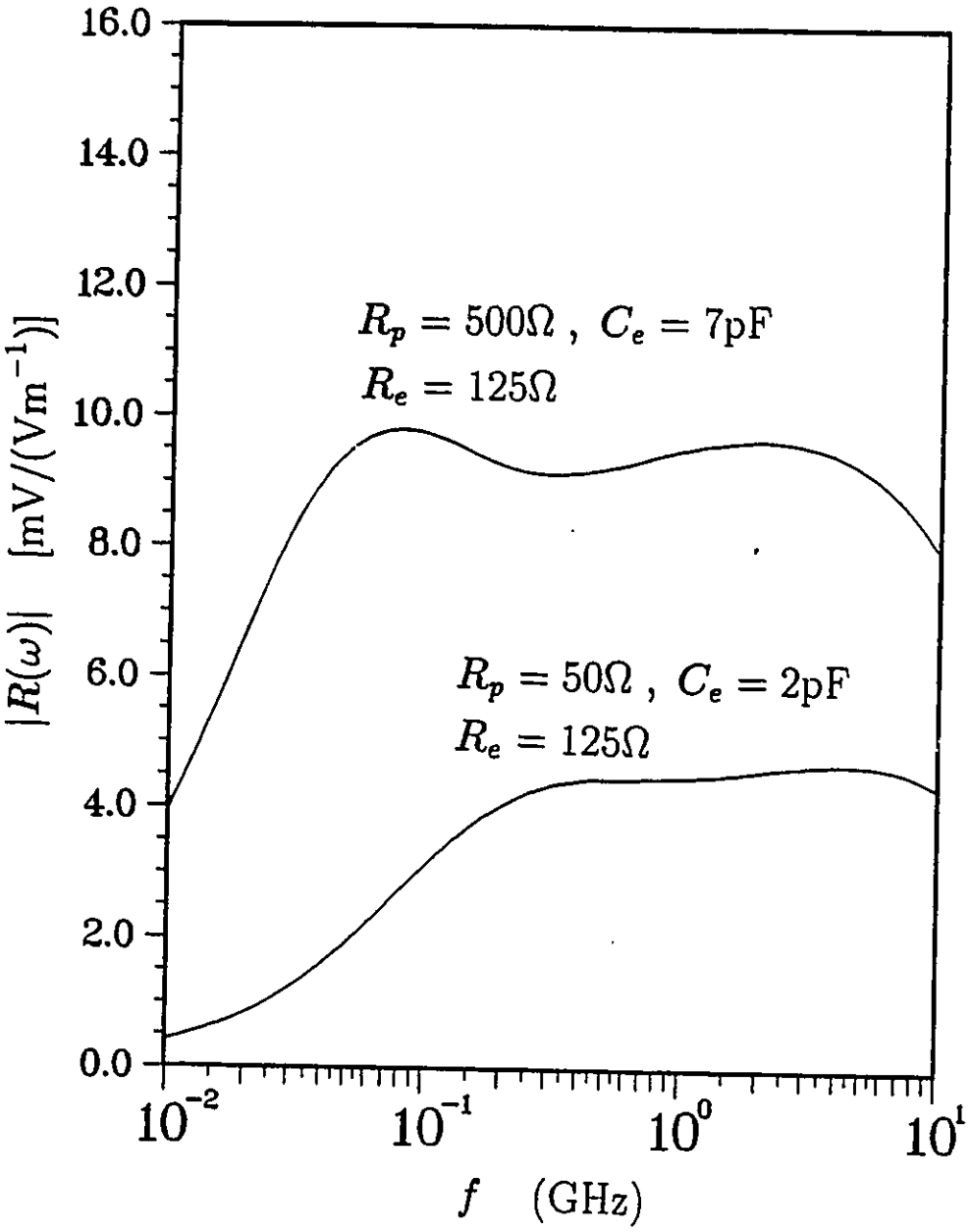


Figure 67: $|R|$ of the loaded V-antenna with REC. $R_e$= REC resistance, $C_e$= REC capacitance, $R_p$= probe resistance.

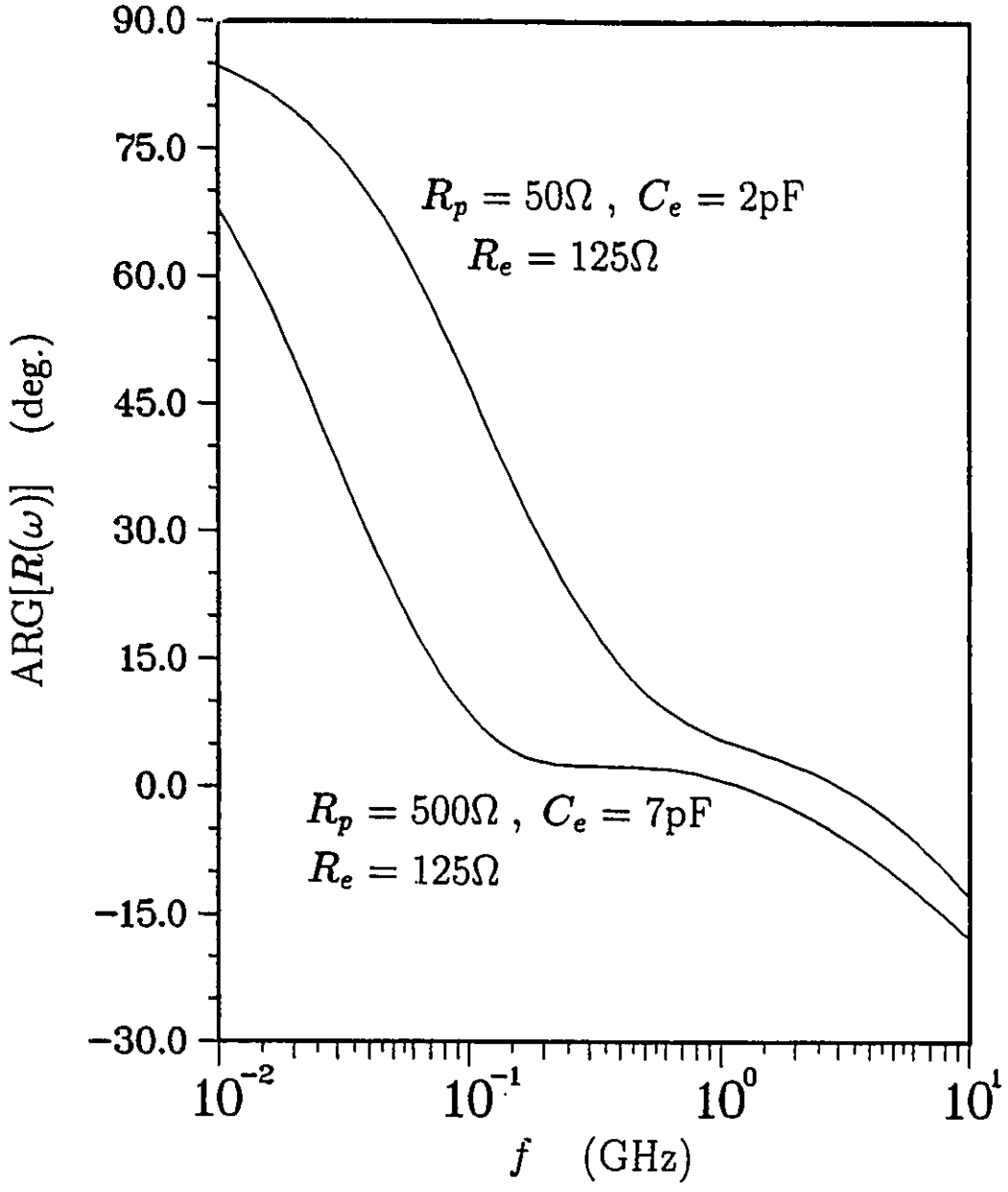


Figure 68: ARG($R$) of the loaded V-antenna with REC. $R_e$= REC resistance, $C_e$= REC capacitance, $R_p$= probe resistance.

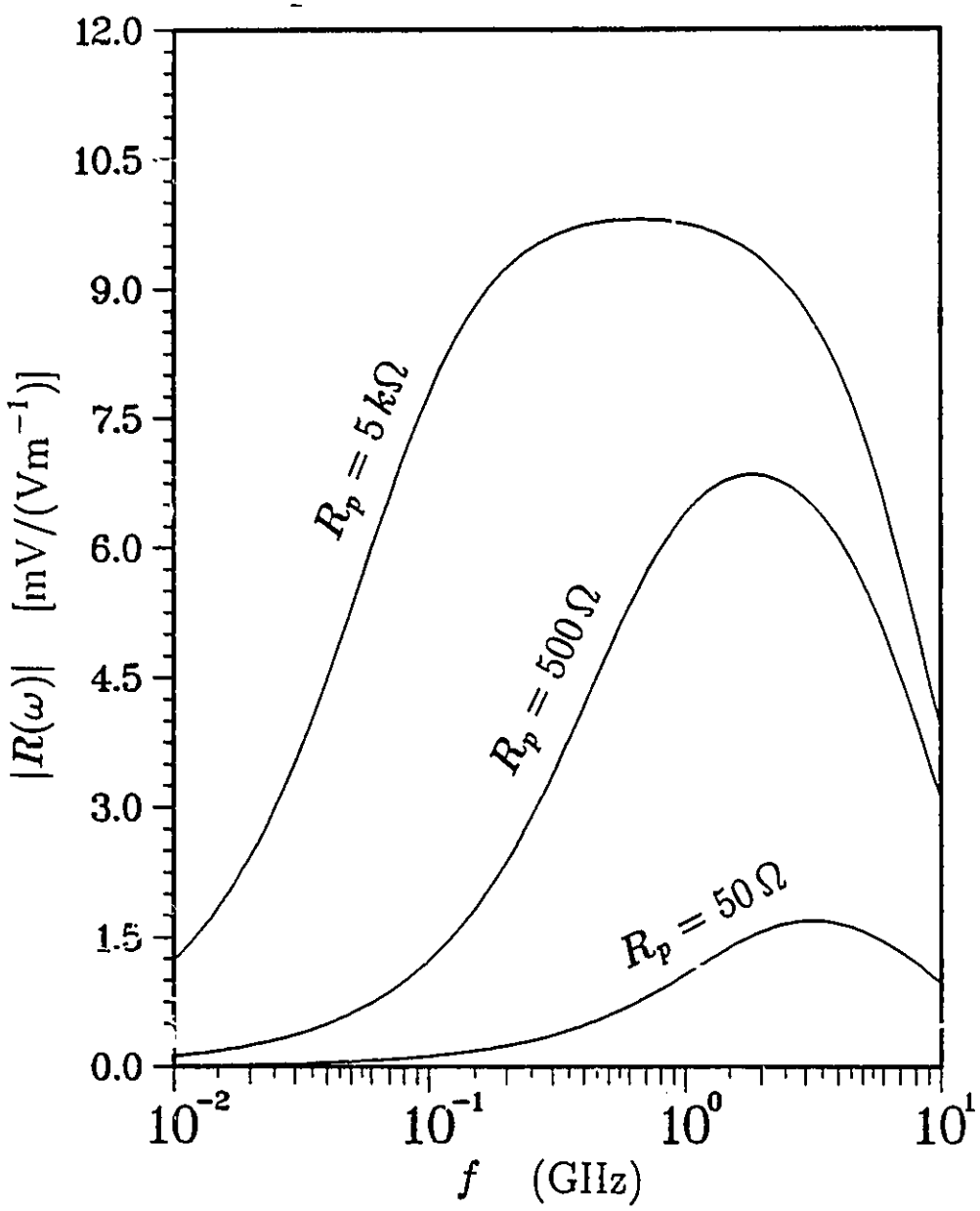


Figure 69: $|R|$ of the WK-antenna for different terminations. $R_p$= probe resistance.

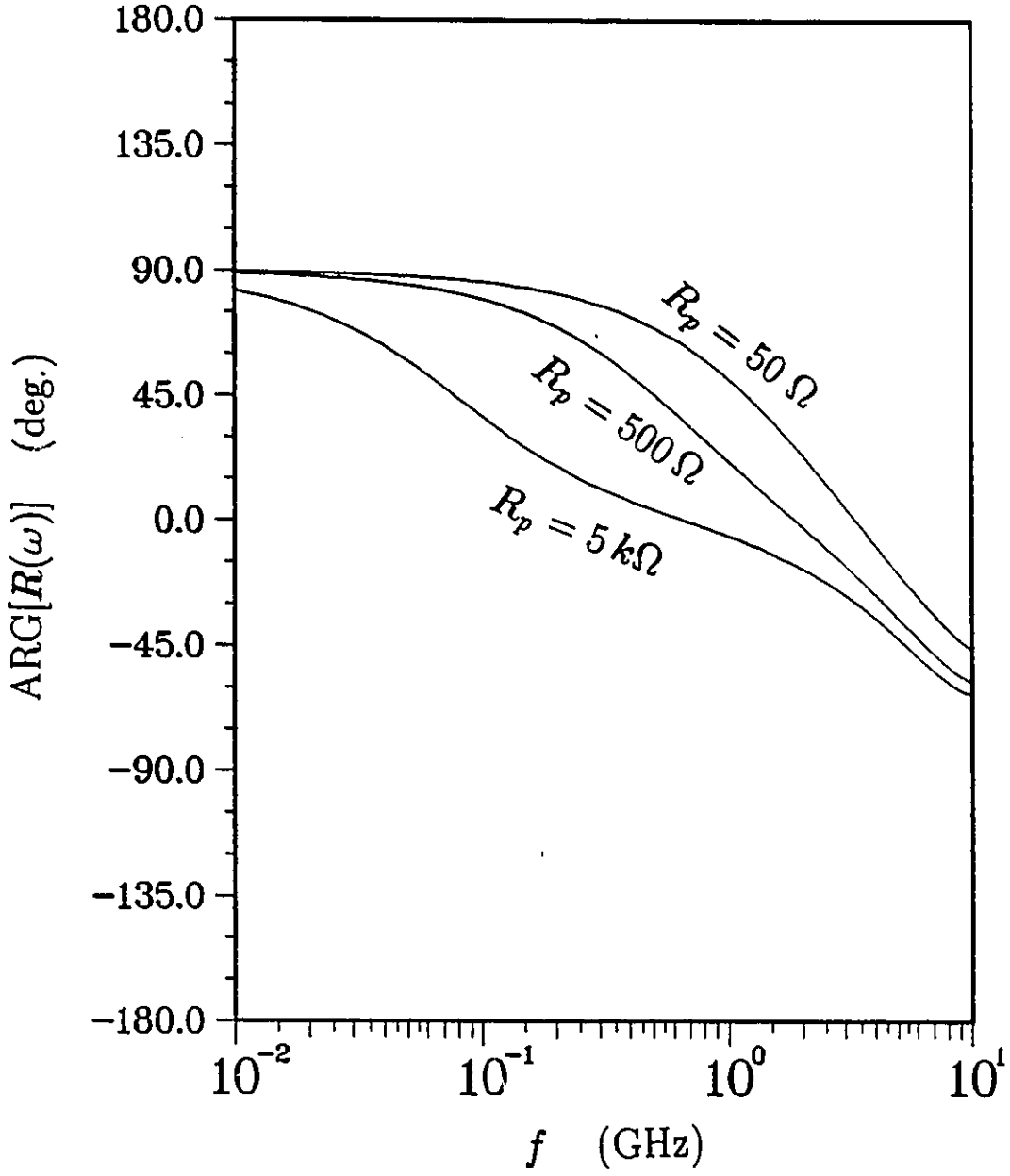


Figure 70: ARG($R$) of the WK-antenna for different terminations. $R_p$= probe resistance.

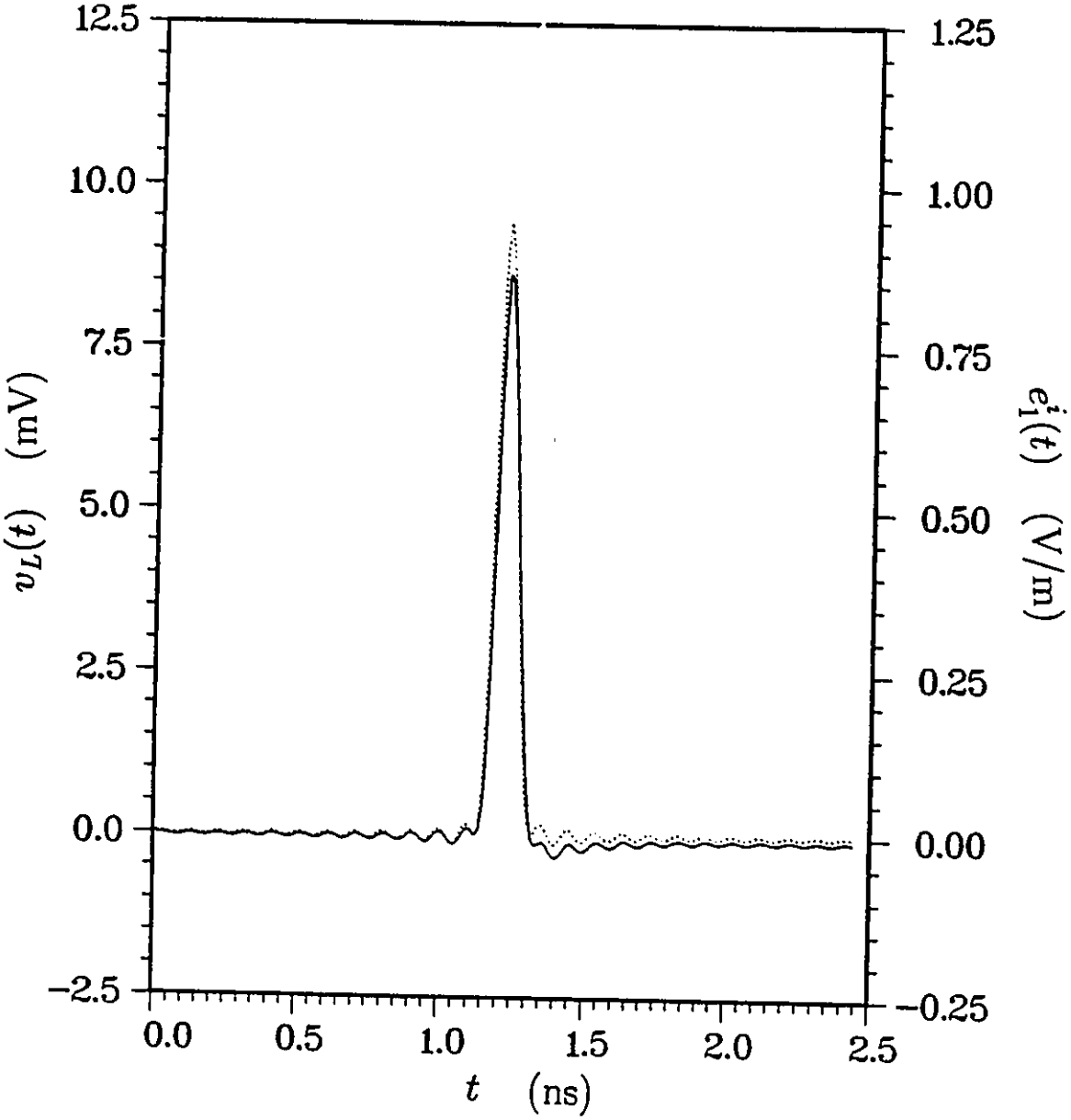


Figure 71: Response of the V-antenna with REC, to the approximately Gaussian pulse. Probe resistance is 500 Ω.

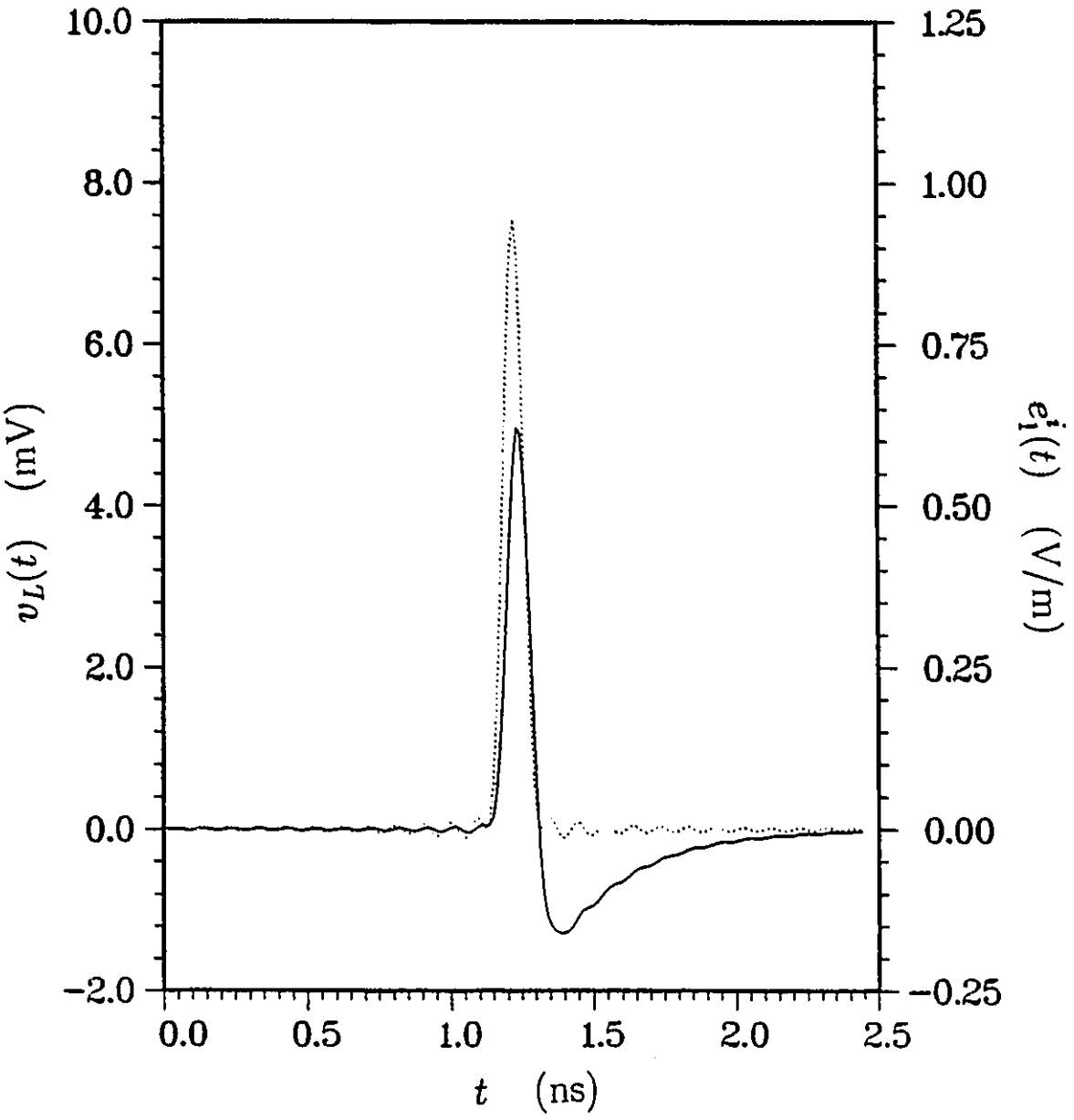


Figure 72: Response of the WK-antenna, to the approximately Gaussian pulse. Probe resistance is 500 Ω.

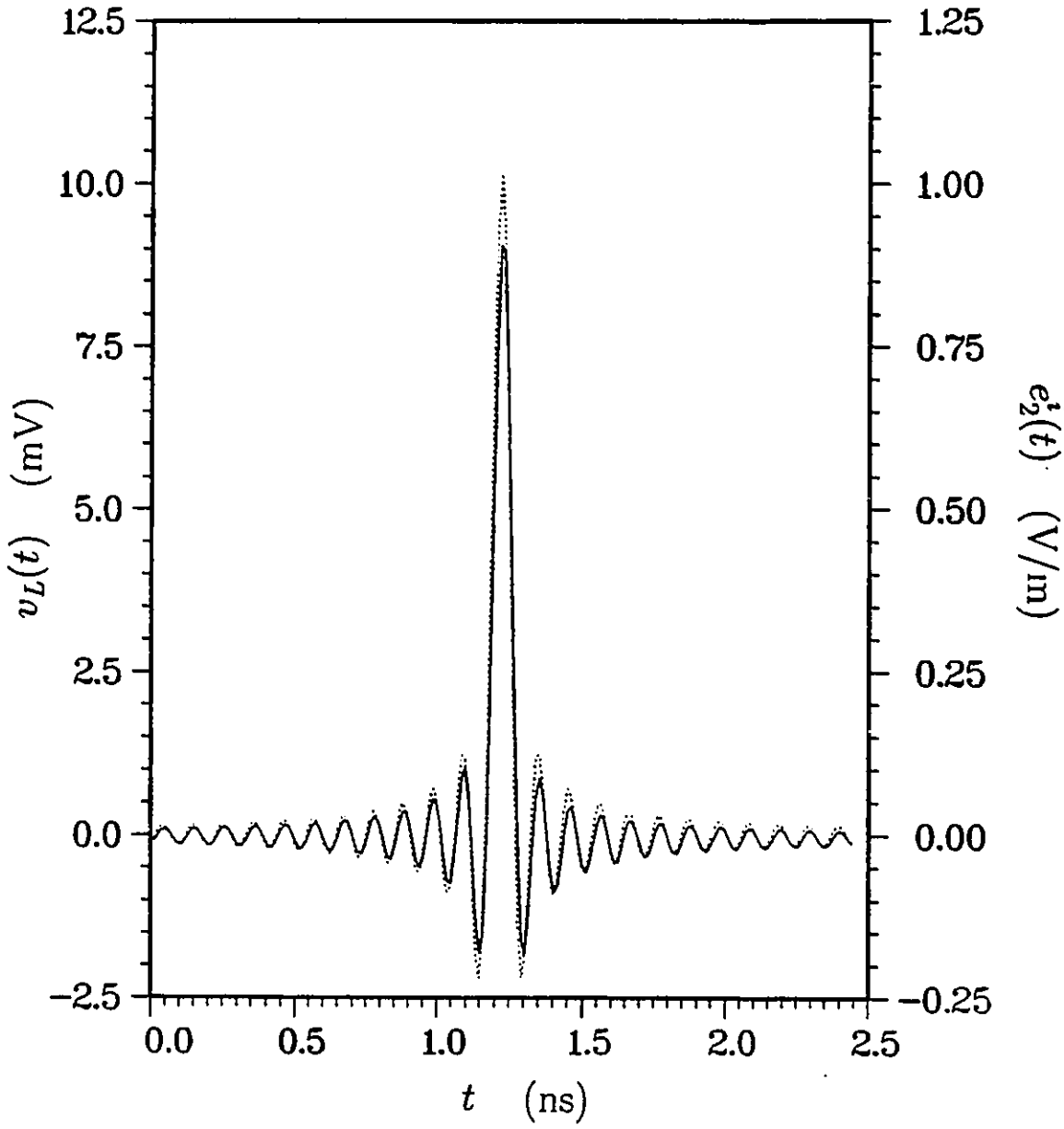


Figure 73: Response of the V-antenna with REC, to the sinc pulse. Probe resistance is 500 Ω.

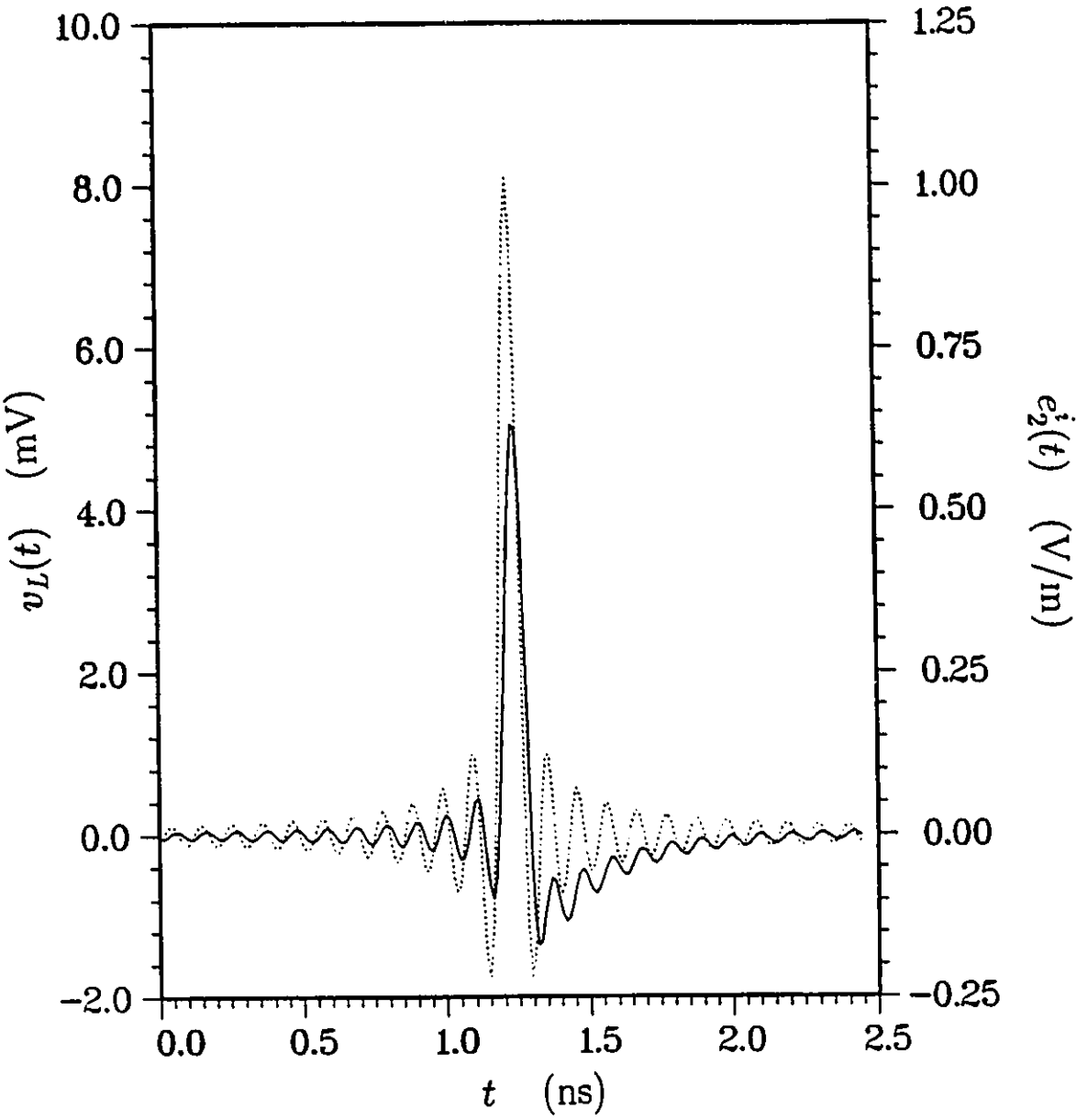


Figure 74: Response of the WK-antenna to the sinc pulse. Probe resistance is 500 Ω.

# Chapter 6

# EXPERIMENTS

## 6.1 Introduction

Two experimental antennas were fabricated and their receiving characteristics were investigated. One experimental antenna is similar, at least in principle, to the resistively loaded V-antenna described in Chapter 5. The other antenna is a Wu-King straight (vertical) monopole, terminated with a high-impedance electronic circuit. A time-domain antenna range was built and used to test the two experimental antennas in the time domain. The V-antenna was also tested in the frequency domain, using a TEM cell and automatic network analyzers (HP 8510B and HP 3577A).

The time-domain and frequency-domain techniques used for obtaining the receiving characteristics of the experimental antennas are presented in Section 6.2. Section 6.3 describes the fabrication of the two experimental antennas. Measurement results are given in Section 6.4, in both time and frequency domains, and they are further discussed in Section 6.5.

## 6.2 Measurement Techniques

Since the experimental antennas were expected to be broadband, it was necessary to test their performance over a wide frequency range. Broadband frequency-domain data can be

obtained by measuring the response of an antenna to a known incident electromagnetic pulse and taking the Fourier transform of the response. Such time-domain measurements have two advantages over conventional frequency-domain measurements: they directly indicate pulse-receiving performance of the antenna, and unnecessary reflections from objects sufficiently away from the measurement set-up can be safely removed (gated out). Therefore, the two antennas were first tested in the time domain. A time-domain antenna range was built for this purpose. The construction and operation of the time-domain antenna range are described in Subsection 6.2.1.

The upper frequency limit of the time-domain antenna range depends on the quality of the transmitting antenna and the ground plane as well as the spectrum of the transmitted pulse. The lower frequency limit is determined by the physical size of the range. The range at the University of Ottawa has a lower frequency limit of about 100 MHz. Therefore, an alternative frequency-domain technique was used to test the experimental V-antenna at lower frequencies. Two automatic network analyzers and a TEM cell were used for this purpose. This technique is described in Subsection 6.2.2. The experimental WK-antenna was too long to be tested in the TEM cell.

### 6.2.1 Time-Domain Measurements

Time-domain measurements were performed using the time-domain antenna range shown in Figure 75. The range was built inside an existing anechoic chamber. A 2.3-m high monocone antenna was built and erected over the ground plane. The half-cone angle of the monocone antenna is 4.4°. According to expression (1) in Chapter 2, the characteristic impedance (input impedance if it were infinite) of this antenna is 196 Ω. The monocone antenna was excited by an approximately Gaussian pulse generated by a Picosecond Pulse Labs (PSPL) 1000C impulse generator. The transmitted pulse was received by the antenna under test and fed to a Tektronix 11802 digital sampling oscilloscope through a 8-m SMA cable. The waveform observed on the oscilloscope was plotted on a HP plotter and was also stored in a personal computer.

When the monocone antenna is excited by the impulse generator, a current pulse is

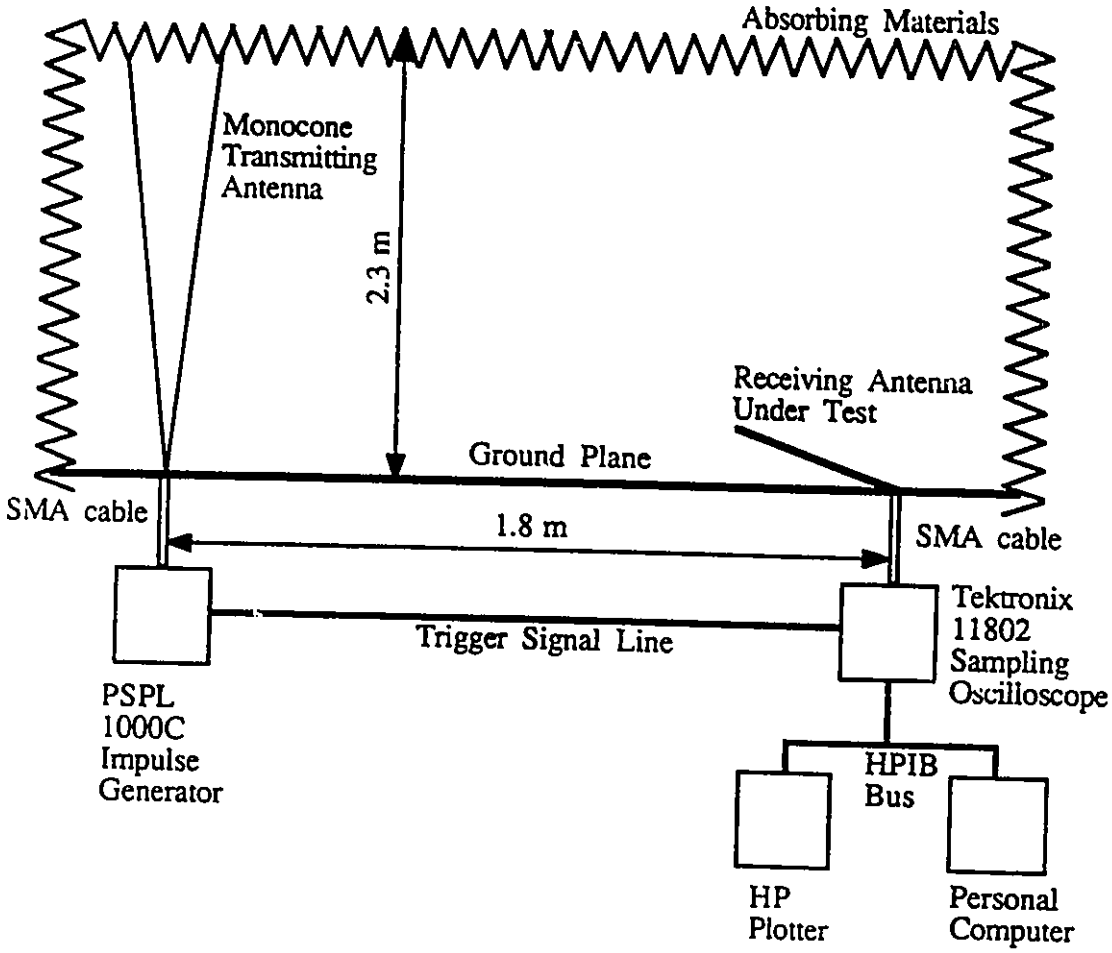


Figure 75: The time-domain antenna range inside the anechoic chamber.

induced in the antenna. This current pulse propagates along the antenna at the speed of light. It in turn generates a hemispherical pulsed electromagnetic field in the vicinity of the antenna. As described by expressions (4) and (5) in Chapter 2, the waveforms of the transmitted electric and magnetic field pulses are identical to the waveform of the impulse generator. However, in 7.6 ns, the current pulse reaches the open end of the monocone antenna, and as a result, undesired reflections are generated. The level of these reflections are kept to a minimum by burring the end of the antenna in absorbing materials. Nonetheless, the reflections cannot be totally eliminated and therefore accurate measurements are possible only within a time window of about 7 ns.

First, the pulse output of the PSPL generator was measured. The generator was connected to the Tektronix 11802 sampling oscilloscope through a SMA cable (which was also used to connect the receiving antenna and the oscilloscope in the range). The waveform recorded by the scope $v_g(t)$, shown in Figure 76, has a PWHM of 520 ps. A commercial signal processing software package (DaiDisp) was used to process this waveform. The Fourier transform of the PSPL generator output voltage waveform (through the cable) $V_g(\omega)$, calculated using DaiDisp, is shown in Figure 77. The energy density spectrum of the pulse was calculated and integrated. It was found that approximately 99% of the energy is below 1.4 GHz. Therefore, the frequency-domain results obtained using this impulse generator may not be reliable above approximately 1.4 GHz because of the very low signal to noise ratio.

The following procedure was used to compute the frequency-domain receiving transfer function of the antenna. First, the received signal was recorded during the reflection-free time window of the range. Then, the Fourier transform of the received waveform $V_r(\omega)$ was calculated. The overall transfer function in the antenna range $F(\omega)$ is defined as

$$F(\omega) = \frac{V_r(\omega)}{V_g(\omega)}. \tag{268}$$

The receiving transfer function of the antenna $R(\omega)$ is given by

$$R(\omega) = \frac{F(\omega)}{A(\omega)} \tag{269}$$

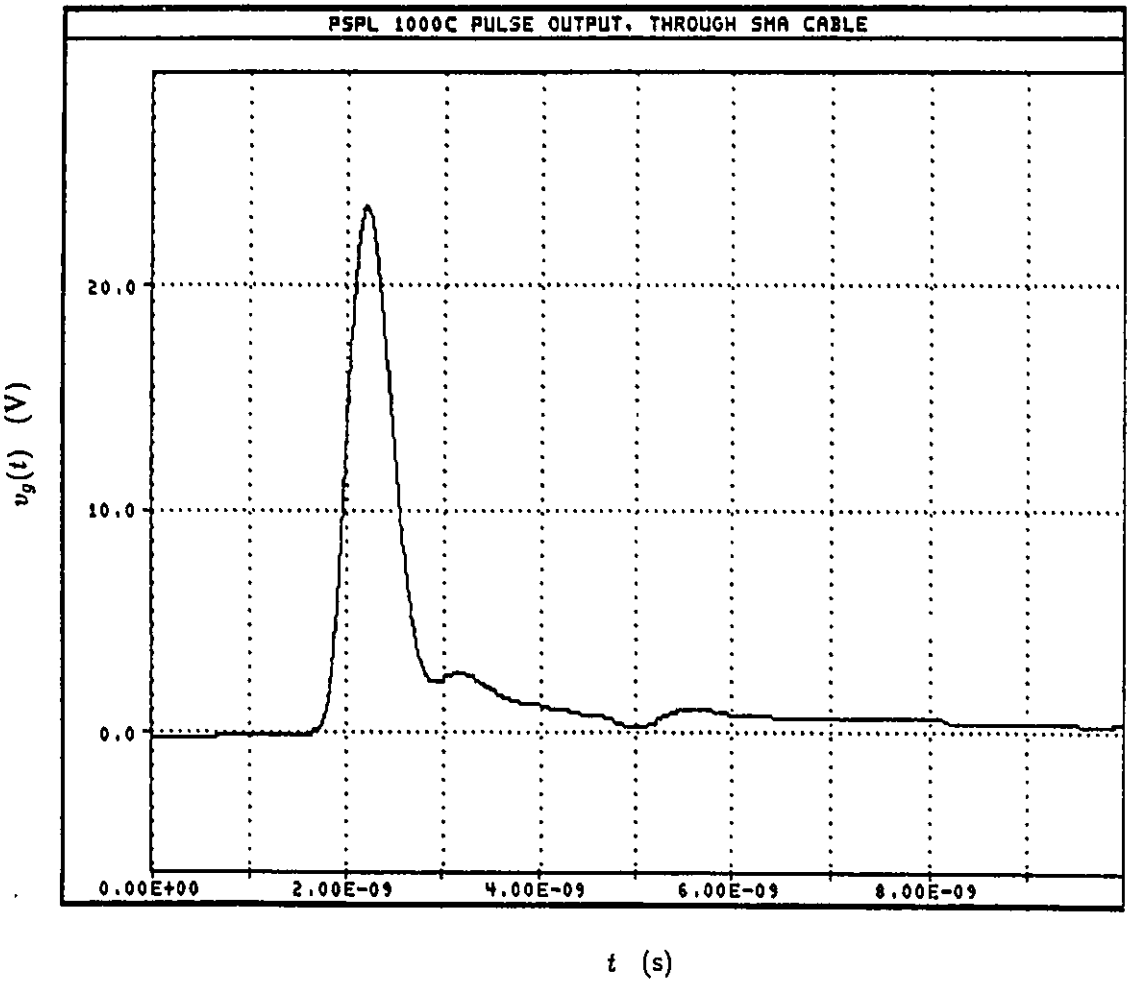


Figure 76: The output pulse of the PSPL 1000C generator.

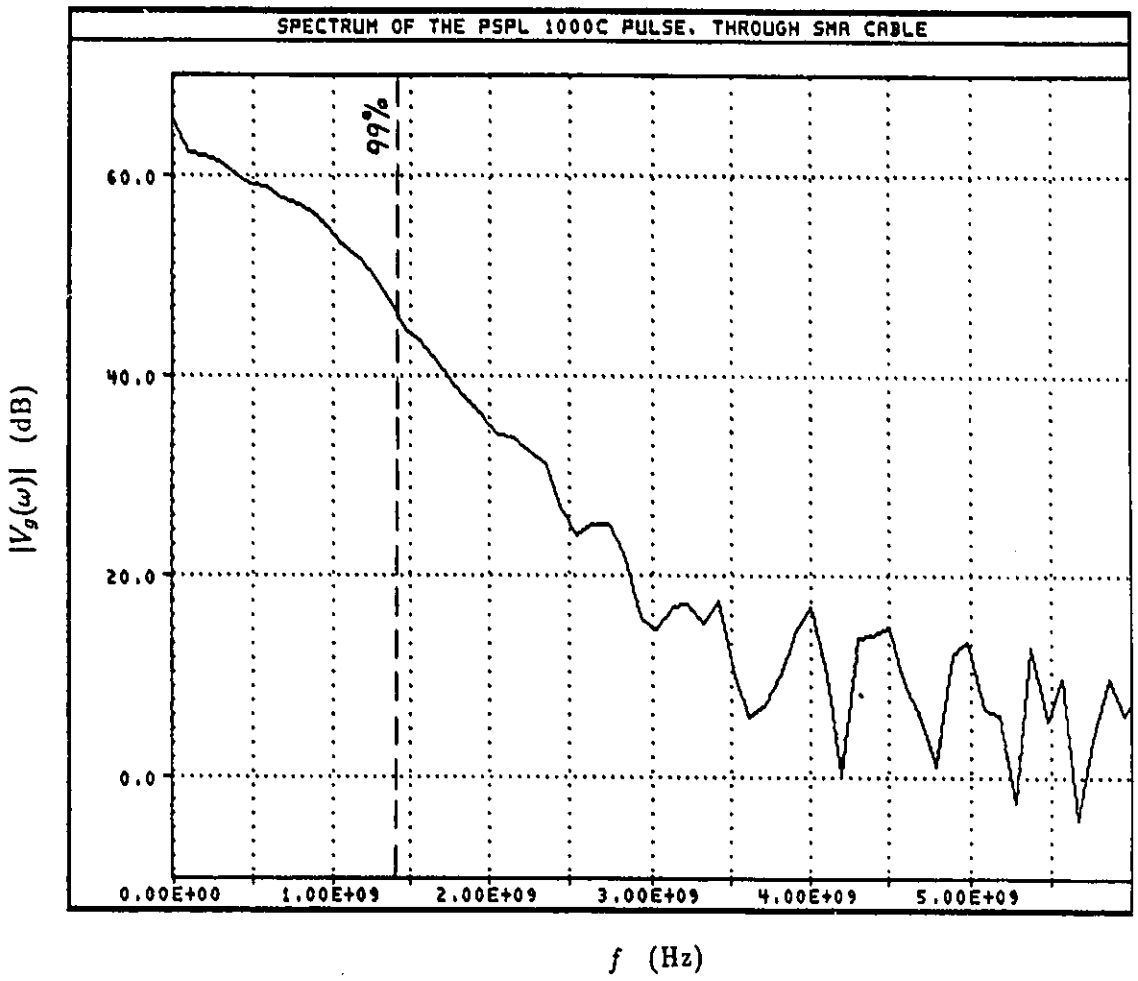


Figure 77: The spectrum of the PSPL 1000C generator output. Reference level (0 dB) corresponds to $10^{-11}$ V/Hz.

where $A(\omega)$ is the field attenuation in the range given by

$$A(\omega) = \frac{E^i(\omega)}{V_g(\omega)} \tag{270}$$

with $E^i(\omega)$ being the incident electric field at the location of the receiving antenna. Considering the mismatch at the input of the monocone antenna and using the field expressions (2) and (3) in Chapter 2, the field attenuation at a distance $d$ from the monocone antenna is found as $0.489/d$. The receiving transfer function of the antenna was calculated using expressions (268) and (269).

### 6.2.2 Frequency-domain measurements

Frequency-domain measurements of the experimental V-antenna were performed inside a TEM cell (IFI CC104). The measurement arrangement is shown in Figure 78. The TEM cell has approximately 45-cm wide and 30-cm high useful area. These dimensions of the cell allow the propagation of higher order modes at frequencies above 300 MHz, and therefore TEM cell measurements are unreliable above 300 MHz. The overall transfer function (forward transmission coefficient) of the system ($S_{21}$) was measured using HP 8510B or HP 3577A network analyzers. The receiving transfer function of the antenna is simply given by

$$R(\omega) = \frac{S_{21}(\omega)}{h} \tag{271}$$

where $h$ is the half-height of the TEM cell.

## 6.3 Experimental Antennas

### 6.3.1 The V-antenna

It is very difficult to realize a tapered distributed resistance on a thin-wire antenna. Therefore, the experimental V-monopole antenna was fabricated using thin-film technology. A picture of the experimental V-antenna is shown in Figure 79. A very thin ($\approx$ 3 mils) resistive layer of a Nickel-Chromium alloy was deposited on a thin flexible Kapton substrate. The thickness of the layer was kept constant along the length of the monopole. This layer

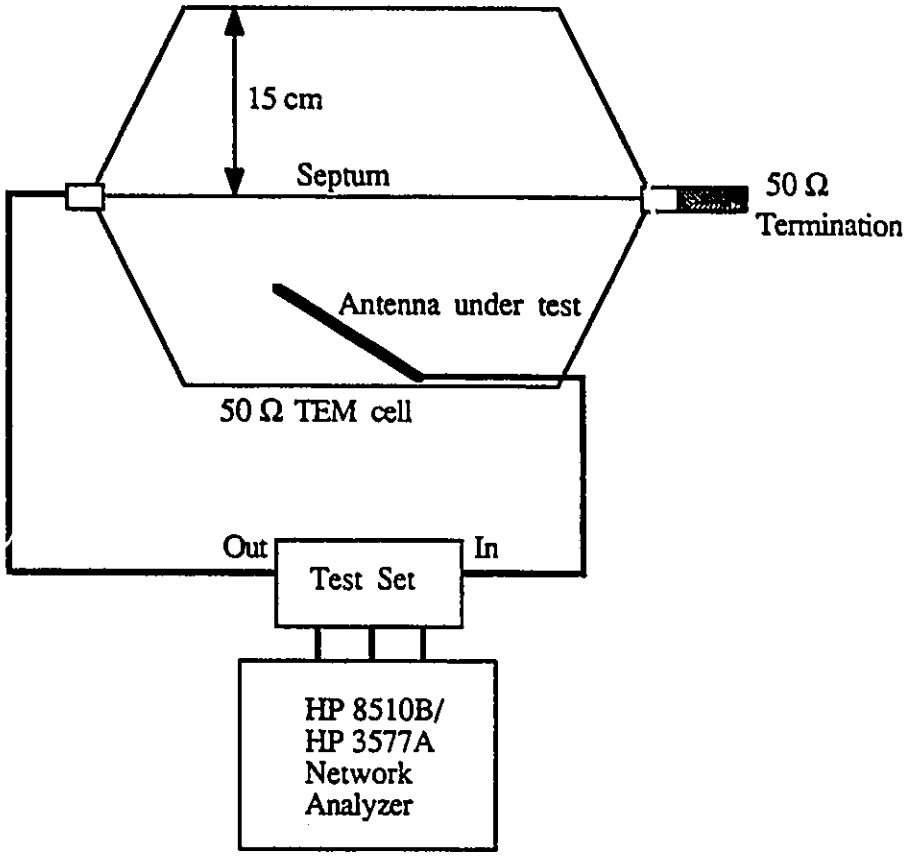


Figure 78: Frequency-domain antenna measurement arrangement.

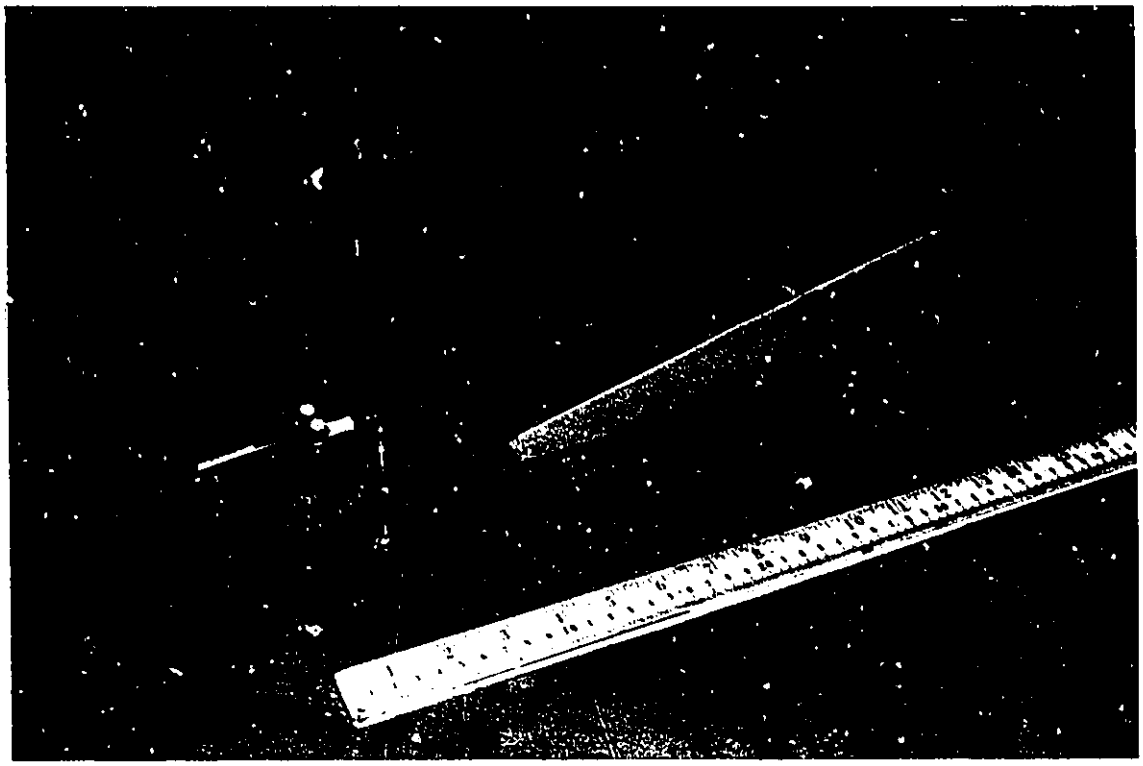

Figure 79: Photograph of the experimental V-antenna.

has a surface resistance of approximately 17 Ω/square. The necessary parabolic distributed resistance profile was achieved by linearly tapering the width of the layer, as done in [35]. The resistive layer is approximately 30 cm long; its width is 1 cm at the wider end. Gold contacts were also deposited on Kapton in order to achieve a good electrical contact between the monopole and the REC elements. The thin Kapton substrate was glued to a thicker (1.5 mm) polycarbonate substrate, which provides the necessary mechanical support.

To realize the REC, a surface mount chip resistor and a ceramic chip capacitor were connected to the gold contacts. The monopole was placed on a copper ground plane to form a wedge angle of 15°, with the support of a styroform wedge. A Tektronix P6150- 500 Ω passive probe was used to pick up the voltage induced across the REC.

### 6.3.2 The Wu-King Monopole

A Wu-King resistively loaded straight monopole antenna was fabricated by depositing a nickel-chromium alloy resistive thin film on a Kapton substrate. The film has a surface resistance of approximately 30 Ω/square. The required parabolic resistance profile was realized by linearly tapering the width of the film. The resistive film was 15 cm long and 1 cm wide at the terminal end. A gold contact was also deposited at the terminal, to provide a good electrical contact between the film and the receiver circuit. The Kapton substrate was glued to a thicker plastic substrate, which serves as a mechanical support.

For broadband operation, the Wu-King antenna needs a high input impedance termination. Therefore, a high-impedance FET source follower/ operational amplifier circuit described in [104] was used at the output of the monopole antenna. This receiver circuit has an input impedance of the order of 100 MΩ, and a 3-dB roll-off frequency of about 300 MHz. The circuit was implemented on a printed circuit board using surface mount components. The monopole was also installed, vertically, on the same printed circuit board. The input of the receiver circuit was connected to the gold contact in the monopole.

## 6.4 Experimental Results

### 6.4.1 The V-antenna

The V-antenna was first tested in the time-domain antenna range, as explained in 6.2.1. The distance from the V-antenna terminals to the monocone antenna was 1.8 m. A 100-Ω resistor and a 10-pF capacitor was used in the REC. The signal received by the antenna is shown in Figure 80. The signal has a PWHM of 568 ps, which compares well with the 520-ps PWHM of the generator pulse. For comparison, the generator pulse (attenuated by 72 dB) is also shown in Figure 80.

It can be seen that the V-antenna is capable of receiving a 520 ps pulse, without significant distortions. During the first few nanoseconds, the transmitted and received signals are almost identical. However, after the major pulse, the received signal exhibits an undesirable oscillatory response. Since the reflections from the top-end of the monocone antenna and the edges of the ground plane are not expected for at least 7 ns, this undesired response must be due to a secondary receiving process associated with the V-antenna. The REC circuit, copper ground plane and the probe ground plane connector in the V-antenna form a small loop antenna. At higher frequencies, this loop may be able to pick up a signal and cause distortions in the received signal.

The response of the V-antenna without REC is shown in Figure 81. As theoretically predicted in Chapter 5, the received pulse has a larger magnitude and a stretched trailing edge (See Figures 53 and 71 for theoretical results).

The frequency-domain receiving response of the V-antenna was computed from the time-domain measurement results, using the FFT. The antenna response measured in the time-domain range may contain undesired reflections 7 ns after the major pulse. Therefore, the received signal was truncated at 7 ns from the beginning of the major pulse. Then, the FFT of the received signal was computed using DaiDisp signal processing software, and the receiving transfer function of the V-antenna was evaluated using (268) and (269). The receiving transfer function of the V-antenna, with 100 Ω and 10 pF REC elements, is shown in Figure 82. Also shown are the spectra of the transmitted signal $|V_g(\omega)|$ and the received

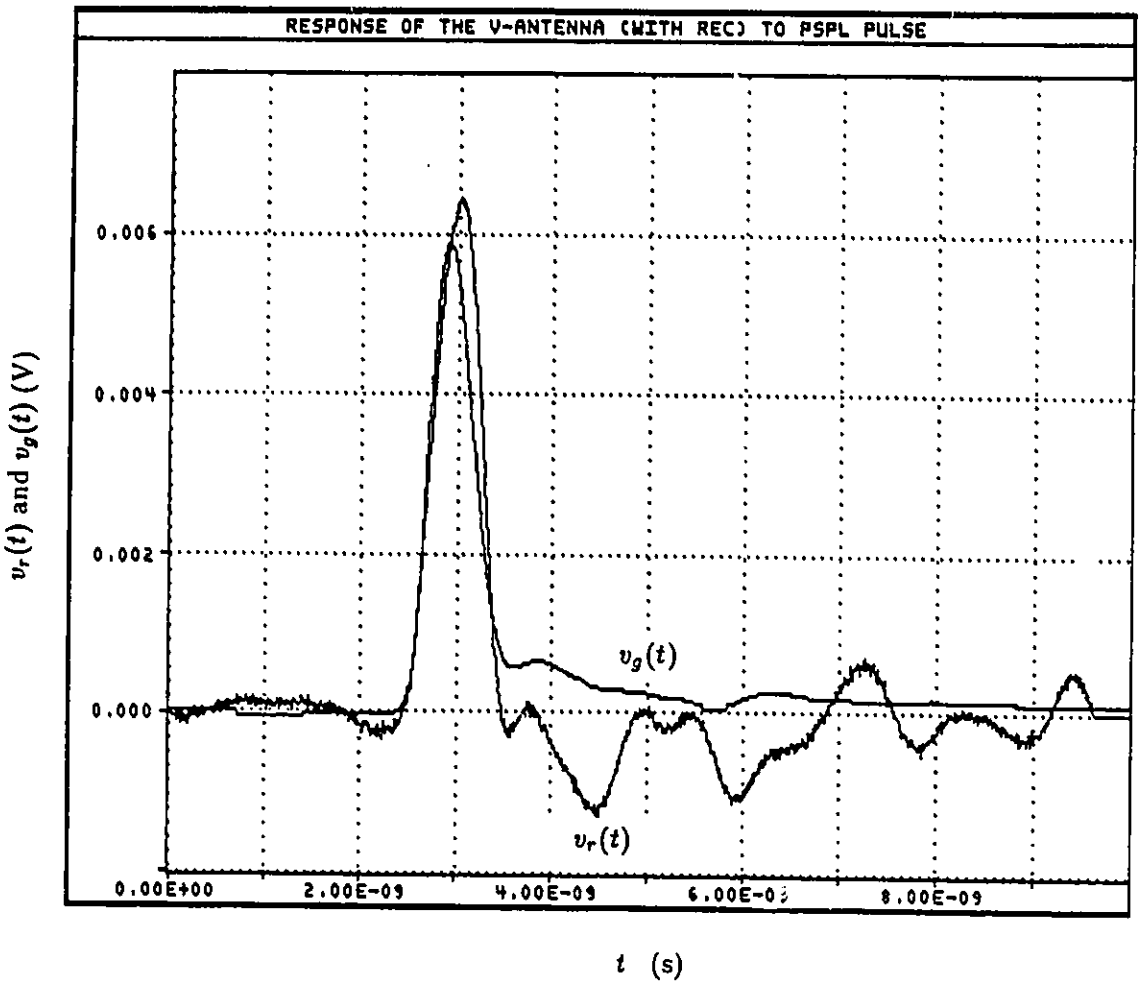


Figure 80: The time-domain response $v_r(t)$ of the experimental V-antenna, with REC. The generator pulse $v_g(t)$ (attenuated by 72 dB and aligned on the rising edge) is also shown for comparison.

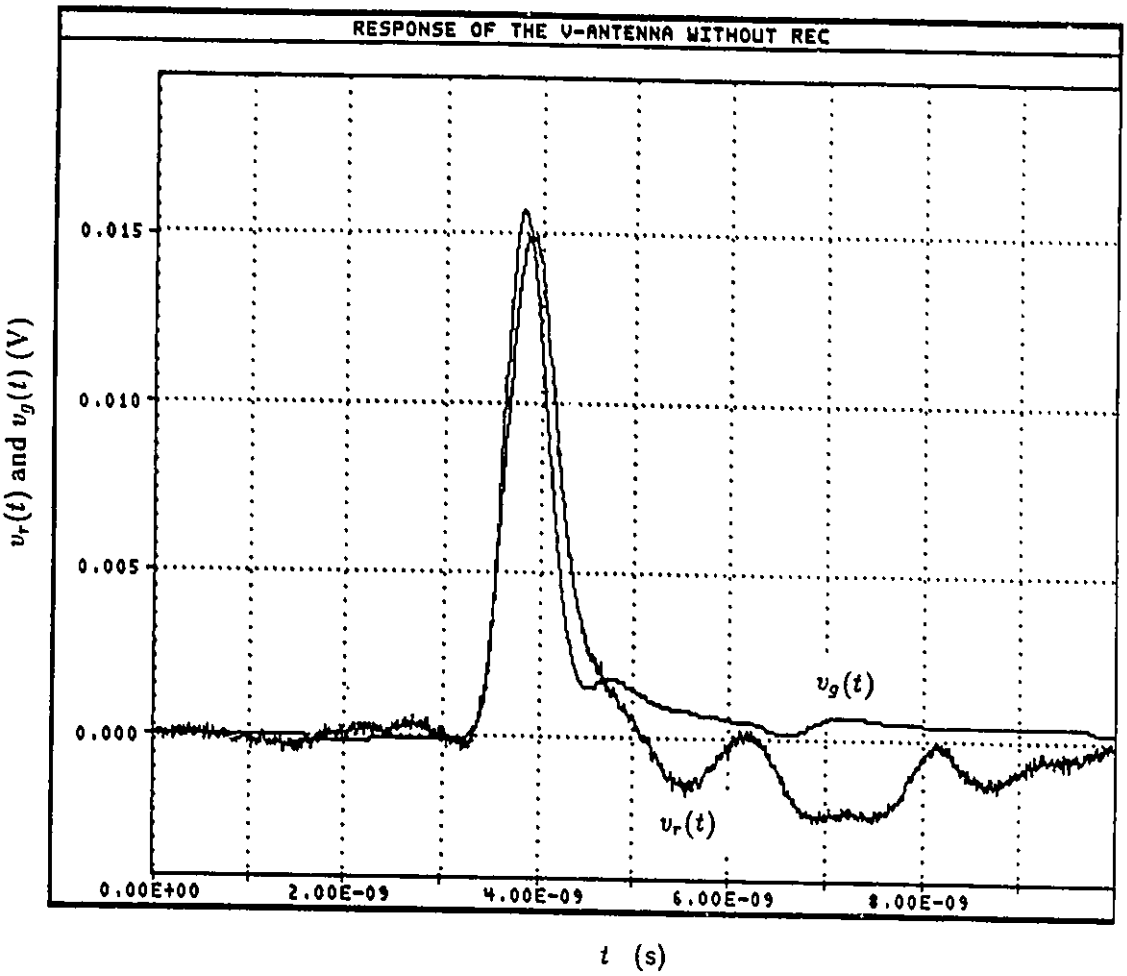


Figure 81: The time-domain response $v_r(t)$ of the experimental V-antenna, without REC. The generator pulse $v_g(t)$ (attenuated by 63.5 dB and aligned on the rising edge) is also shown for comparison.

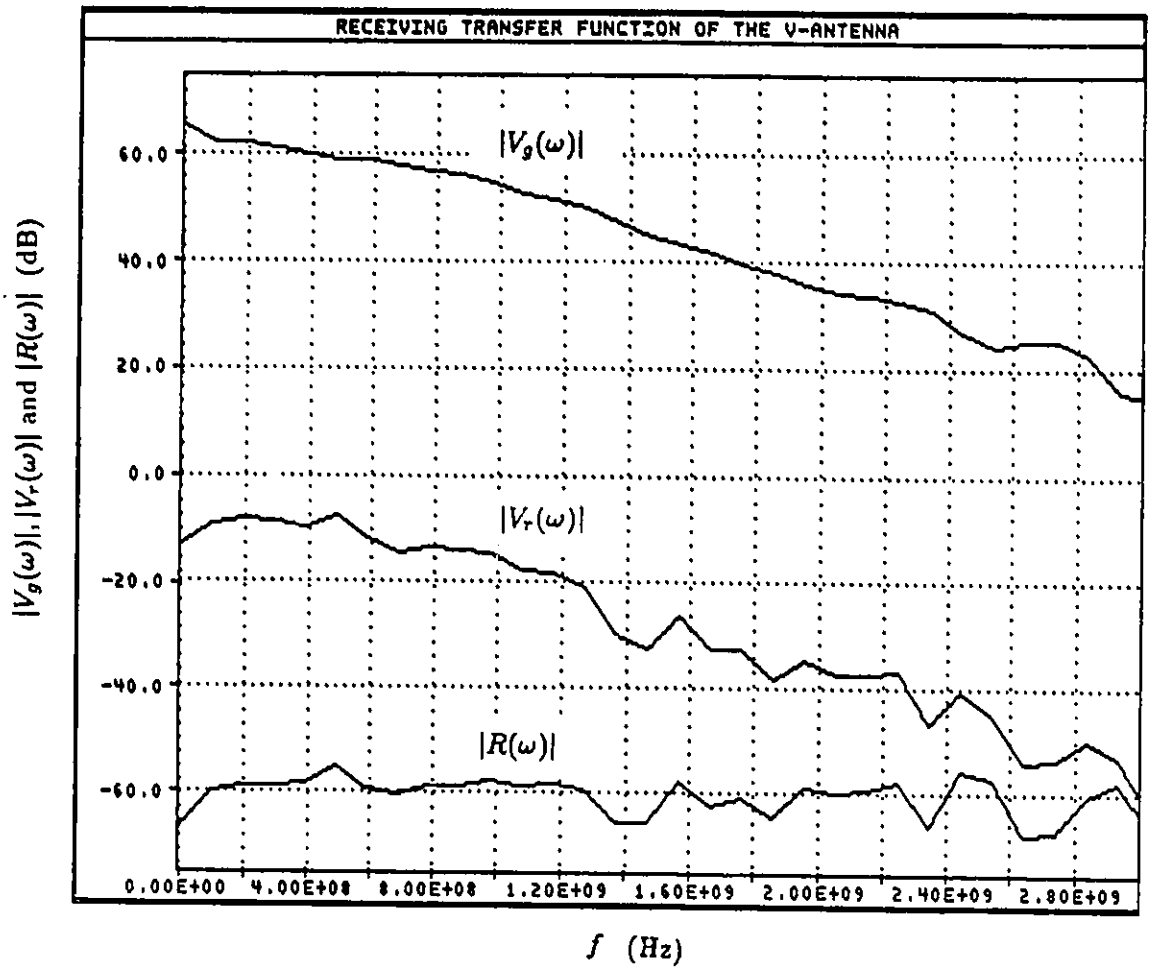


Figure 82: The receiving transfer function $|R(\omega)|$ of the experimental V-antenna, with REC. The spectra of the transmitted signal $|V_g(\omega)|$ and the received signal $|V_r(\omega)|$ are also shown.

signal $|V_r(\omega)|$. In the frequency range from 100 MHz to 1.3 GHz, the variations in $|R(\omega)|$ are within $\pm 3$ dB. The average value of $|R(\omega)|$ in this frequency range is approximately -59 dB or 1.12 mV/(Vm$^{-}$1), which compares well with the theoretical estimate of 1.0 mV/(Vm$^{-}$1) for a *thin-wire* V-antenna (Chapter 5). In the frequency range from 1.3 GHz to 3.0 GHz, the variations in $|R(\omega)|$ are within $\pm 6$ dB. However, the frequency domain results are not reliable above 1.4 GHz, as the generator output pulse has 99% of its spectral energy below this frequency. Reliable high-frequency data can be obtained using faster impulse generators, which are very expensive and not available to the author.

The V-antenna was tested also in the frequency domain, using the TEM cell and network analyzers, as explained in Subsection 6.2.2. The forward transmission coefficient $|S_{21}|$ was measured in the frequency range from 45 MHz to 500 MHz using a HP 8510B network analyzer, and the results are shown in Figure 83. The V-antenna REC resistance and capacitance were 220 $\Omega$ and 22 pF, respectively. As described in Subsection 6.2.2, these measurement results are questionable at frequencies above 300 MHz due to possible overmoding of the TEM cell. At lower frequencies, only the TEM mode propagates and therefore the transmission coefficient $S_{21}$ represents the receiving transfer function $R(\omega)$ of the antenna, according to expression (271). It can be seen from Figure 83 that the variation of the receiving transfer function is within $\pm$ 0.7 dB, in the frequency range from 100 MHz to 300 MHz.

The transmission coefficient (inside the TEM cell) was measured at lower frequencies, using a HP 3577A network analyzer. The magnitude and phase of $S_{21}$ are plotted in Figure 84, from 1 MHz to 200 MHz. The low-frequency roll-off of the antenna response can be seen in this figure. The 3-dB roll-off frequency was found to be 33.5 MHz. For comparison, the theoretical value for a *thin-wire* V-antenna is 25 MHz (Chapter 5).

### 6.4.2 The Wu-King Monopole

The Wu-King straight monopole was tested in the time-domain antenna range, as explained in 6.2.1, with the monopole placed at 2 m from the monocone antenna. The signal received by the monopole antenna, during the initial 10 ns period, is shown in Figure 85.

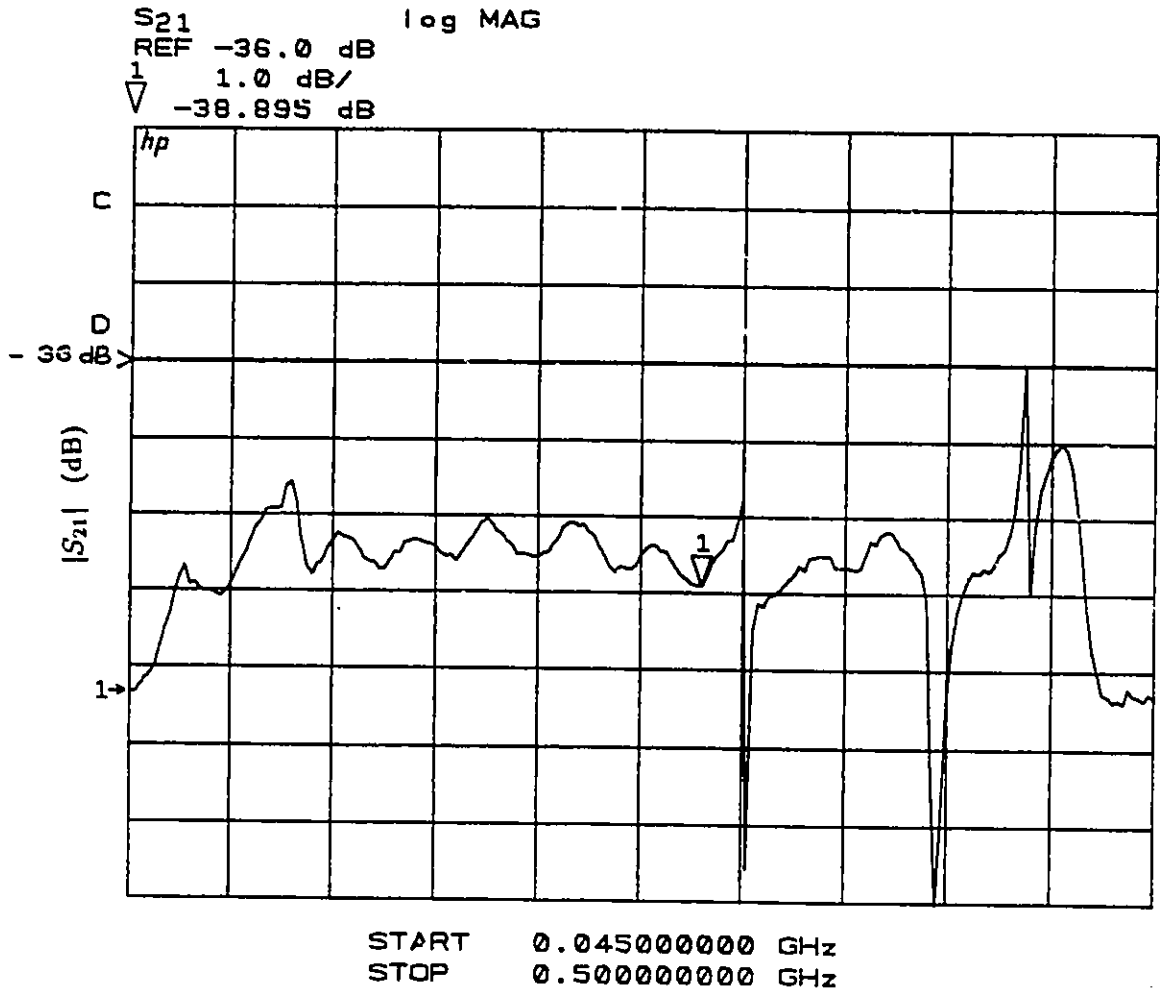


Figure 83: The transmission coefficient $|S_{21}|$ of the experimental V-antenna inside the TEM cell, measured using the HP 8510B network analyzer.

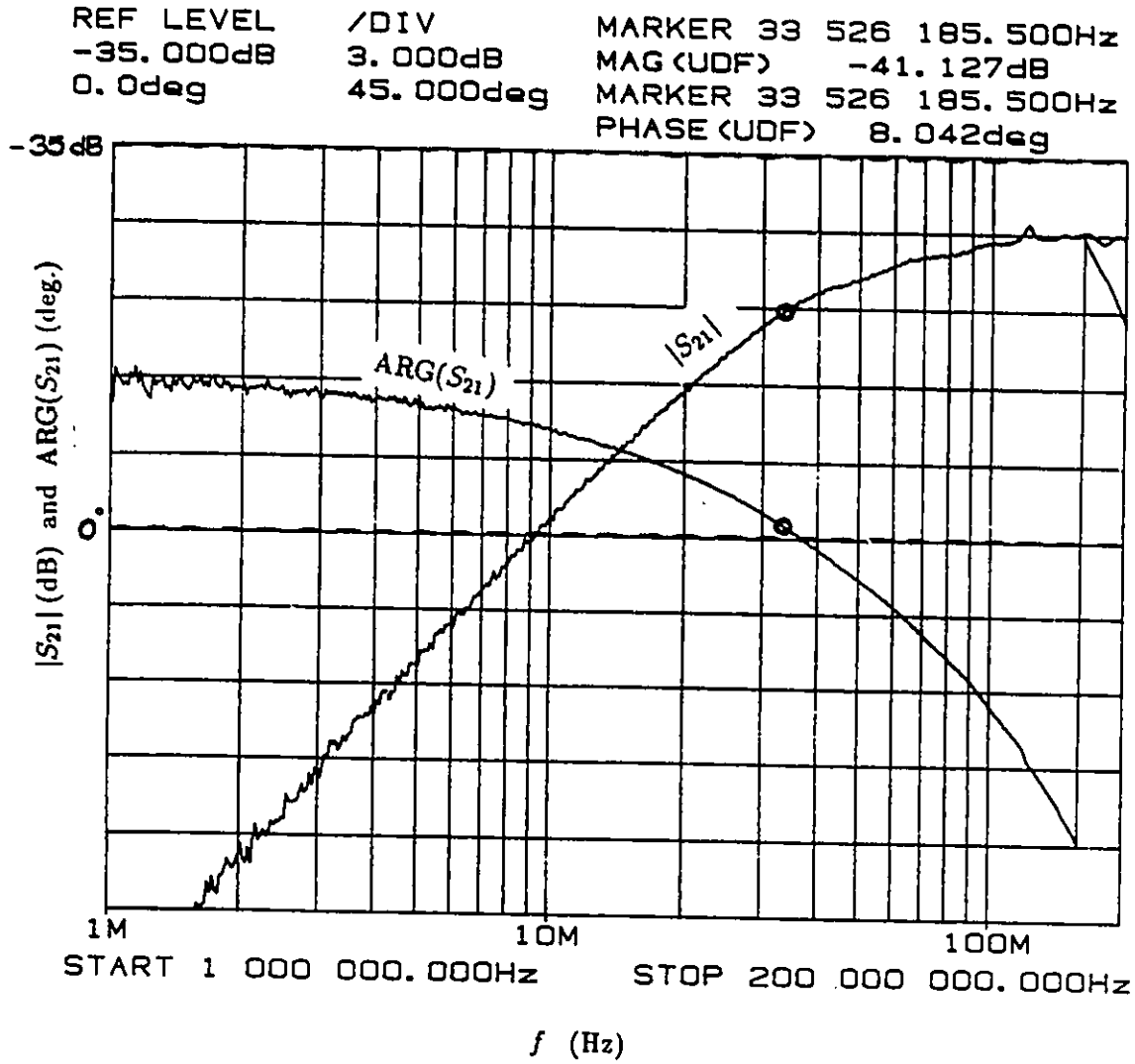


Figure 84: The transmission coefficient $S_{21}$ of the experimental V-antenna inside the TEM cell, measured using the HP 3577A network analyzer.

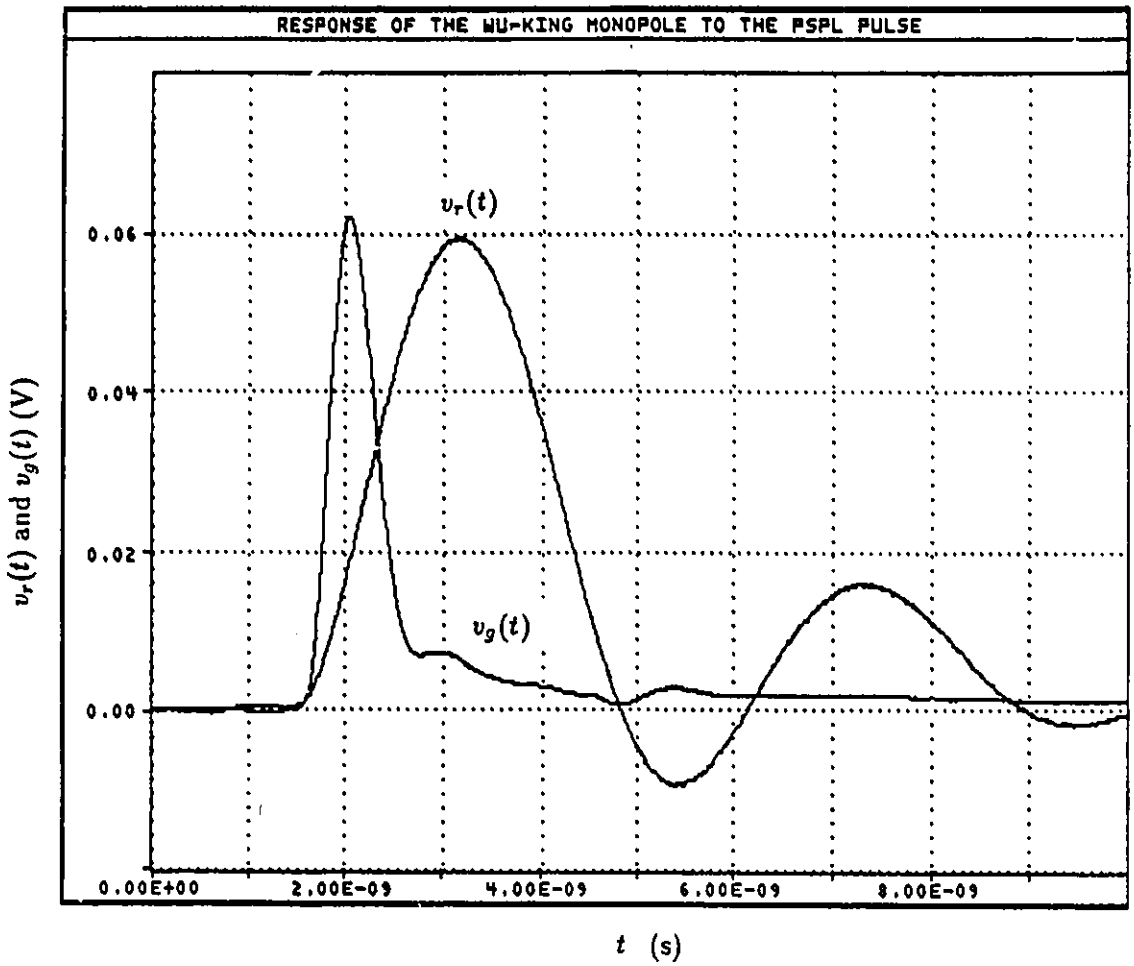


Figure 85: The initial time-domain response $v_r(t)$ of the experimental Wu-King antenna. The generator pulse $v_g(t)$ (attenuated by 52 dB) is also shown for comparison.

Frequency-domain receiving characteristics of the straight monopole were obtained using DaiDisp software and FFT techniques, as for the V-antenna. The receiving transfer function $|R(\omega)|$ of the straight monopole antenna is shown in Figure 86, in the frequency range from 100 MHz to 2 GHz. The antenna has a sensitivity of -33 dB, or 22 mV/(Vm$^{-1}$). The 3 dB upper roll-off frequency is approximately 300 MHz, which corresponds to the upper roll-off frequency of the active receiver circuit.

## 6.5 Discussion

As shown in 6.4.1, the experimental V-antenna is capable of receiving a 520 ps electromagnetic pulse without significant distortions. The pulse has a 99% spectral content at frequencies below 1.4 GHz. Therefore, the antenna is expected to be receiving without distortion at least up to 1.4 GHz. For the evaluation of receiving characteristics at higher frequencies, one would have to use a faster pulse generator.

In the experimental V-antenna, the REC was implemented using lumped elements. Since the frequency responses of the chip resistors and capacitors were not available from the supplier, they were measured using a HP 8510B network analyzer. The chips were soldered between the inner outer conductors of a 3.6-mm, 50-Ω coaxial line open end. The reflection coefficient at the other end of the coaxial line was measured using the network analyzer. Connector reflections were eliminated by gating the time-domain response. The attenuation and time delay caused by the coaxial line were compensated for, using display enhancement functions in the network analyzer.

Figure 87 shows the measured reflection coefficient $S_{11}$ for a nominal 100 Ω surface mount chip resistor. The same data are plotted on a Smith Chart, in Figure 88. The tested chip resistor had a DC resistance of 98 Ω, which dropped to 79 Ω at 10 GHz. The capacitive reactance of 18 Ω, measured at 10 GHz, may be partly due to the fringe-field capacitance of the coaxial line open end. The drop of the resistance from 98 Ω to 79 Ω should not cause a significant deterioration in the REC performance.

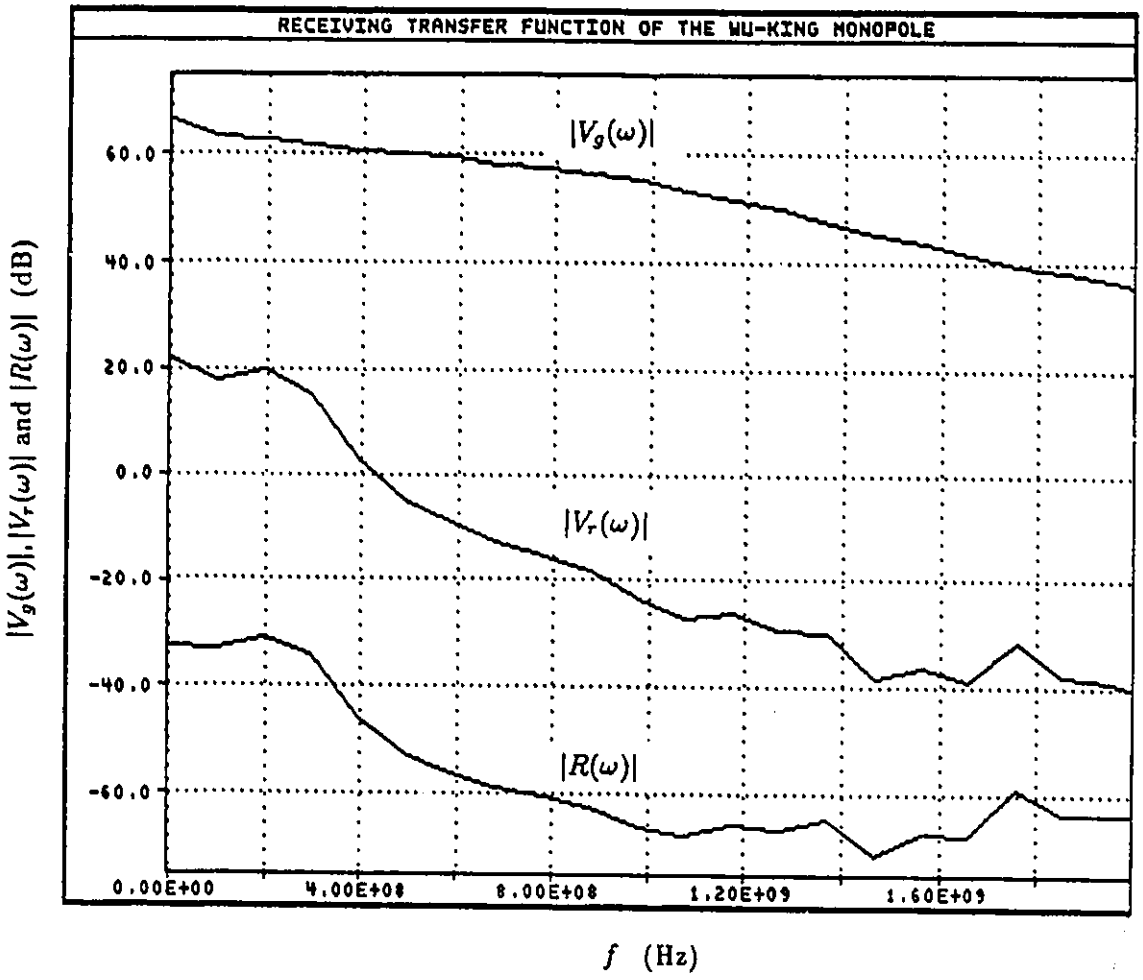


Figure 86: The receiving transfer function $|R(\omega)|$ of the experimental Wu-King antenna. The spectra of the transmitted signal $|V_g(\omega)|$ and the received signal $|V_r(\omega)|$ are also shown.

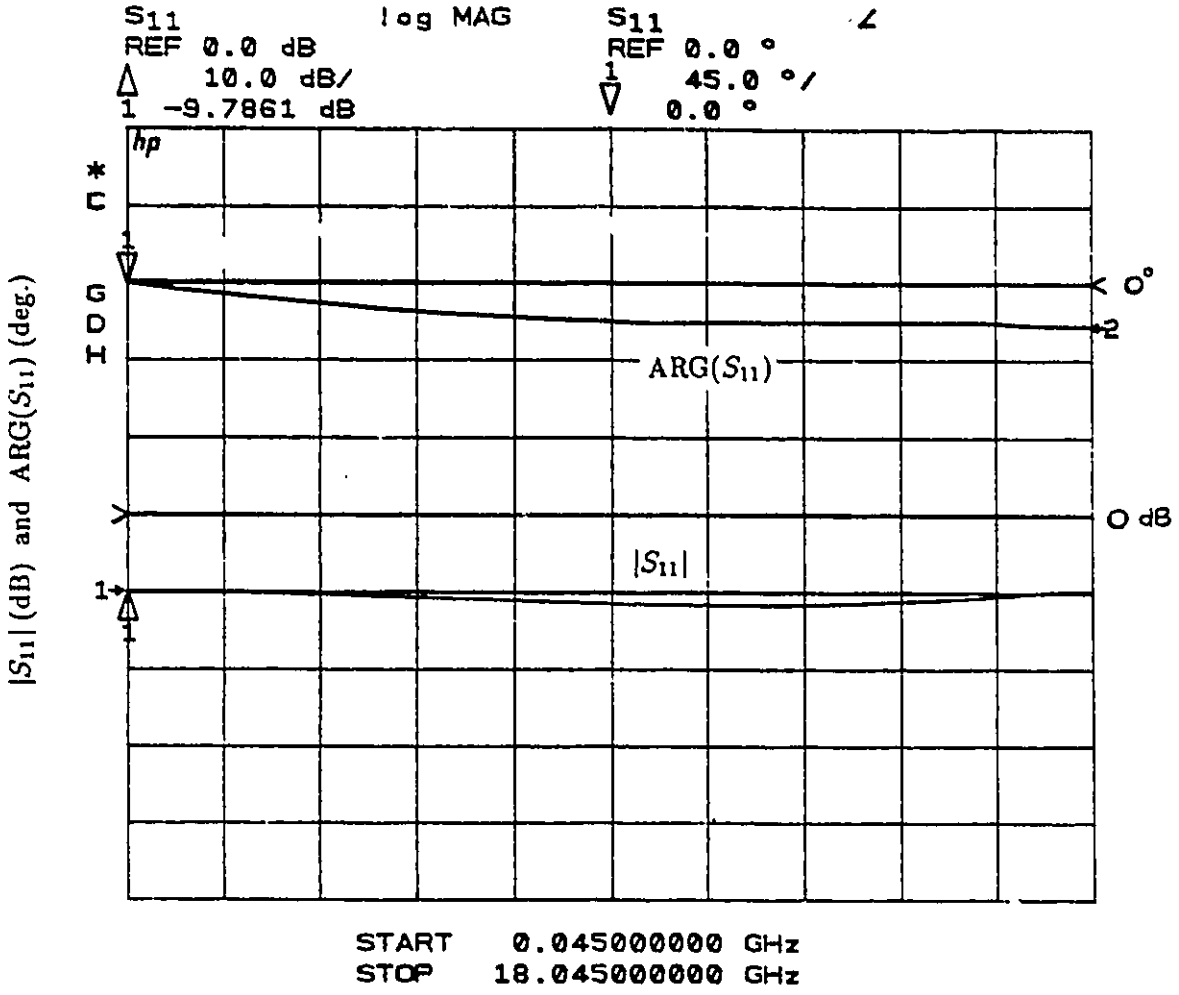


Figure 87: The reflection coefficient $S_{11}$ of a 50-$\Omega$ open-ended coaxial line, with a 100 $\Omega$ chip resistor attached.

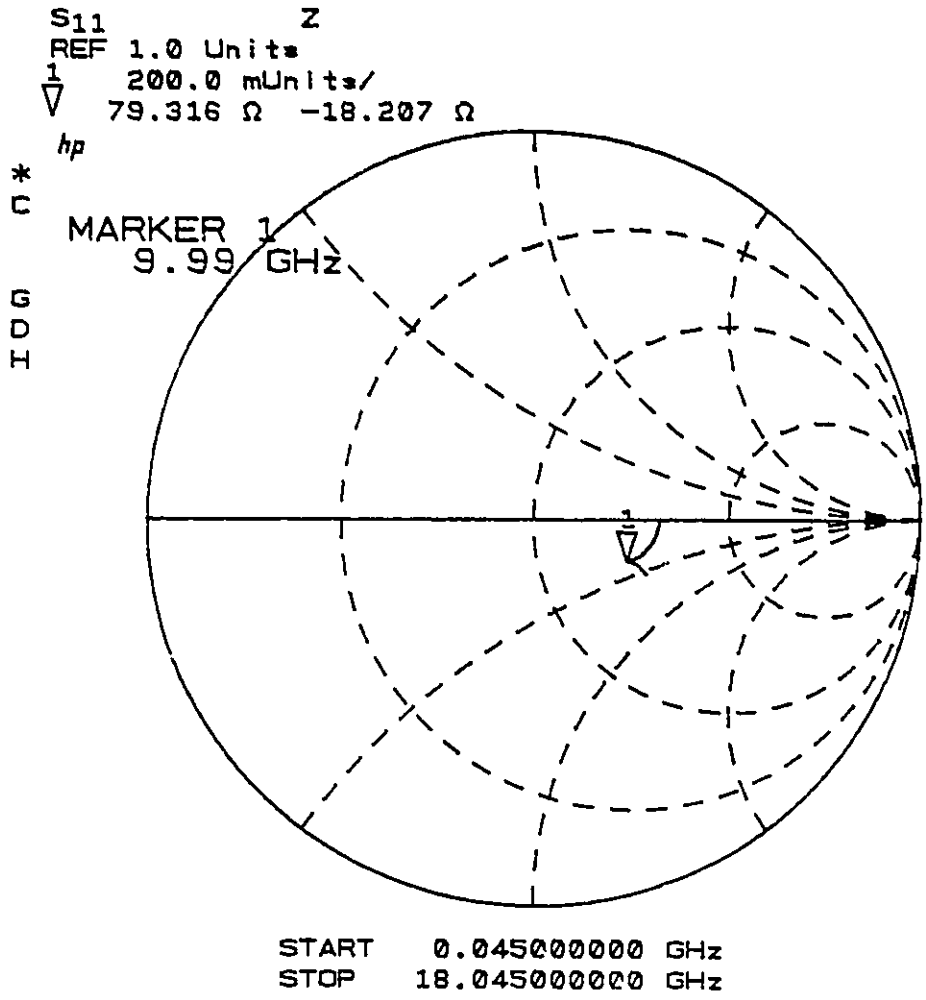


Figure 88: The reflection coefficient $S_{11}$ and the input impedance $Z$ of a 50 Ω open-ended coaxial line, with a 100 Ω chip resistor attached.

Several surface mount ceramic chip capacitors were also measured similarly, and a resonance phenomenon was observed in all cases. The worst results were obtained with a 100 pF capacitor, which resonated at 560 MHz. These results are shown on a Smith Chart in Figure 89. The 10 pF capacitor used in the V-antenna resonated at 1.6 GHz. It was noted that all the measured chip capacitors had a parasitic inductance of about 1 nH. Since the chip capacitor behaves like an inductor at higher frequencies, it can effectively open-circuit the REC. This may profoundly change the performance of the V-antenna. The effect of the parasitic inductance on the receiving transfer function of the antenna is to be evaluated.

In the V-antenna, the REC, the ground plane and the ground plane connector for the oscilloscope probe form a triangular loop that is perpendicular to the incident magnetic field. This loop has an area of approximately 0.5 $cm^2$ and hence can pick up a voltage of about 1 $mV/(Vm^{-1})$ at 1 GHz. This induced voltage is 90° out of phase relative to the incident field, and it drops across an inductive reactance of about 100 Ω (due to the self-inductance of the loop), the impedance of the chip capacitor (very small at 1 GHz), the resistance of the chip resistor (100 Ω) and the input impedance of the probe (500 Ω). It develops a voltage of about .85 mV at the probe input (for a 1 V/m incident field). Taking into account the 20 dB attenuation of the probe, this secondary path can generate a signal of about .085 $mV/(Vm^{-1})$ at the output of the antenna, at 1 GHz. This is approximately 7.5% of the desired output (primary signal) of the antenna. The secondary signal is out of phase with respect to the primary one and is frequency dependent. Thus, it could contribute to the undesired oscillations of the antenna time-domain response. The physical length of the REC and the area of the loop should be minimized in future designs.

In summary, an experimental V-antenna was fabricated and measured in both time and frequency domains. This antenna is capable of receiving a 529-ps Gaussian pulse, without significant distortions. In the frequency domain, the antenna has a sensitivity of 1.12 $mV/(Vm^{-1})$ and a flat receiving response from 35 MHz to 3 GHz. It was not possible to measure the response beyond 3 GHz, due to limitations of the pulse generators available. However, it is suspected that the resonance of the chip capacitors used in the antenna might cause problems at higher frequencies. An experimental Wu-King straight monopole

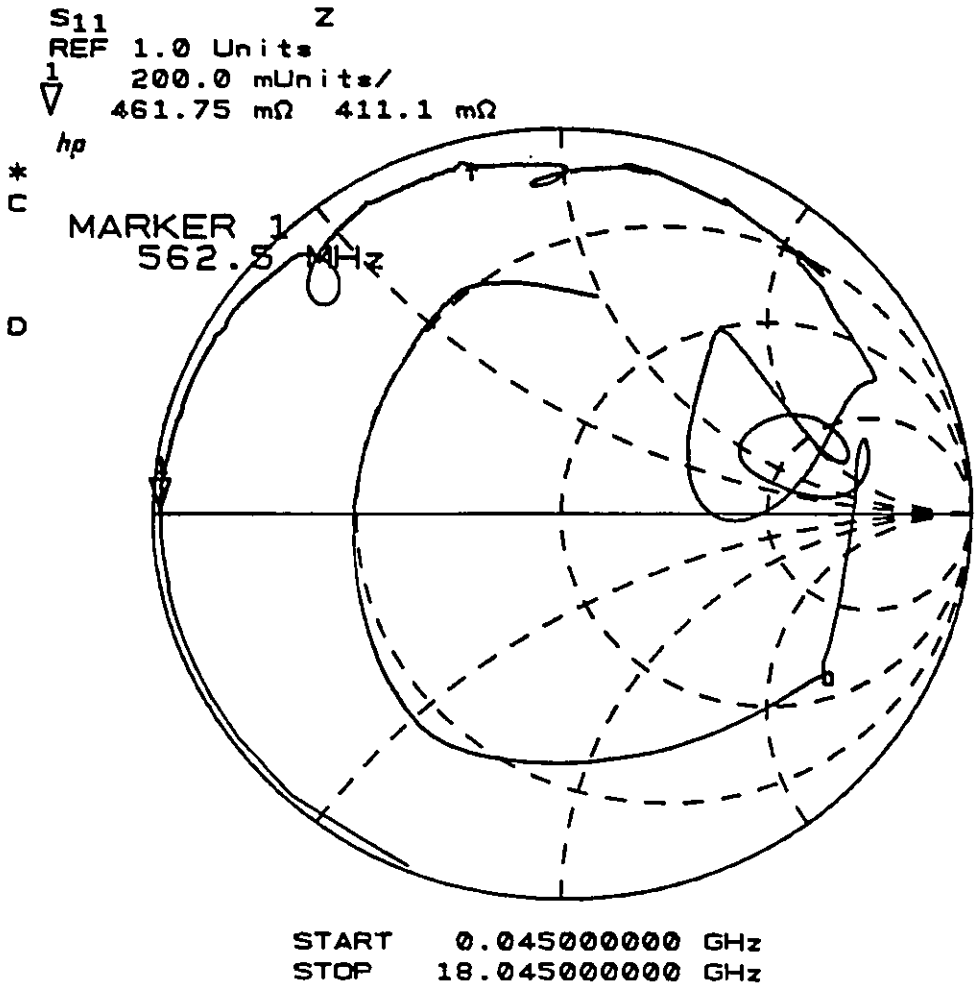


Figure 89: The reflection coefficient $S_{11}$ of a 50 Ω open-ended coaxial line, with a 100 pF ceramic chip capacitor attached.

was also fabricated and tested in the time-domain range. This antenna was too tall for the TEM cell and therefore was not tested in the frequency domain. It has a sensitivity of 22 $mV/(Vm^{-1})$ and a upper roll-off frequency of about 300 MHz, which is limited by the bandwidth of the active receiver circuit.

# Chapter 7

# FINAL WORDS

## 7.1 For the Future

The novel subnanosecond pulse-receiving antenna presented in Chapter 5 is an example which illustrates the possibility of achieving a broad non-dispersive bandwidth using resistively loaded V-monopoles (or dipoles) and passive support circuits. One may optimize the wedge-angle $\theta_w$ (or V-angle $\theta_v$) and the REC parameters $R_e$ and $C_e$, for better performance. This optimization requires heavy computing resources and is to be done in the future. The passive 500Ω probe used in one of the new designs is nothing but a lumped 450Ω resistor connected to a 50 Ω coaxial cable, in series. Therefore, the probe also functions as a 10:1 voltage divider. One may replace the probe by a different resistor and a 50 Ω transmission line. Such a design will allow one to alter $R_p$ and the voltage division ratio and hence compromise the lower roll-off frequency of the antenna against sensitivity.

The most general V-antenna is indeed a resistively loaded "TEM" horn with arbitrarily-shaped plates and a Response Equalizer Circuit. The analysis and optimization of this two-dimensional structure needs extensive computing power. With the availability of powerful workstations and efficient numerical techniques, it might be practical in the near future.

A major difficulty was observed when accommodating a complicated lumped circuit, such as the REC and the probe shown in Figure 66, in a time-domain algorithm. First,

such terminations are hard to implement in the algorithm. Then, whenever the value of one of lumped elements is changed, the whole calculation has to be repeated, making it very inefficient. This problem does not arise in the frequency domain, thanks to the Norton (or Thévenin) equivalent circuit solution. All one needs to know is the short-circuit current $I_{sc}$ (or open-circuit voltage $V_{oc}$) and the input admittance $Y_a$ (or input impedance $Z_a$) of the antenna. Then, the frequency-domain receiving response can be calculated for any complicated termination using these equivalent circuits.

One may analyze the transmitting and receiving antenna in the time domain, and then obtain frequency-domain Norton parameters $Y_a$ and $I_{sc}$ using FFT. After calculating the frequency-domain receiving response for a given termination using Norton's circuit, the time-domain receiving response can be obtained with the help of IFFT. Nonetheless, this procedure is not only awkward but also has some limitations. To apply FFT, one has to calculate the terminal current waveform of the transmitting and receiving antenna until it virtually diminishes. Or else, the response has to be windowed and it will add more errors to the final result.

Alternatively, one may apply the Norton's equivalent circuit principle directly in time-domain, and hence avoid the FFT and IFFT operations. The use of Norton's equivalent circuit, directly in time domain, may not have been discussed in the literature. Therefore, it is outlined here.

Consider the receiving antenna shown in Figure 90(a). The objective is to calculate the load voltage waveform $v_L(t)$ for an arbitrary load, without switching to the frequency domain. The frequency-domain Norton equivalent circuit for the terminated receiving antenna is shown in Figure 90(b) where $I_{sc}(\omega)$ is the frequency-domain short-circuit current and $Y_a(\omega)$ is the antenna admittance. The frequency-domain load voltage $V_L(\omega)$ is given by

$$[Y_a(\omega) + Y_L(\omega)]V_L(\omega) = I_{sc}(\omega). \tag{272}$$

This expression when transformed to the time domain, results

$$[y_a(t) + y_L(t)] * v_L(t) = i_{sc}(t) \tag{273}$$

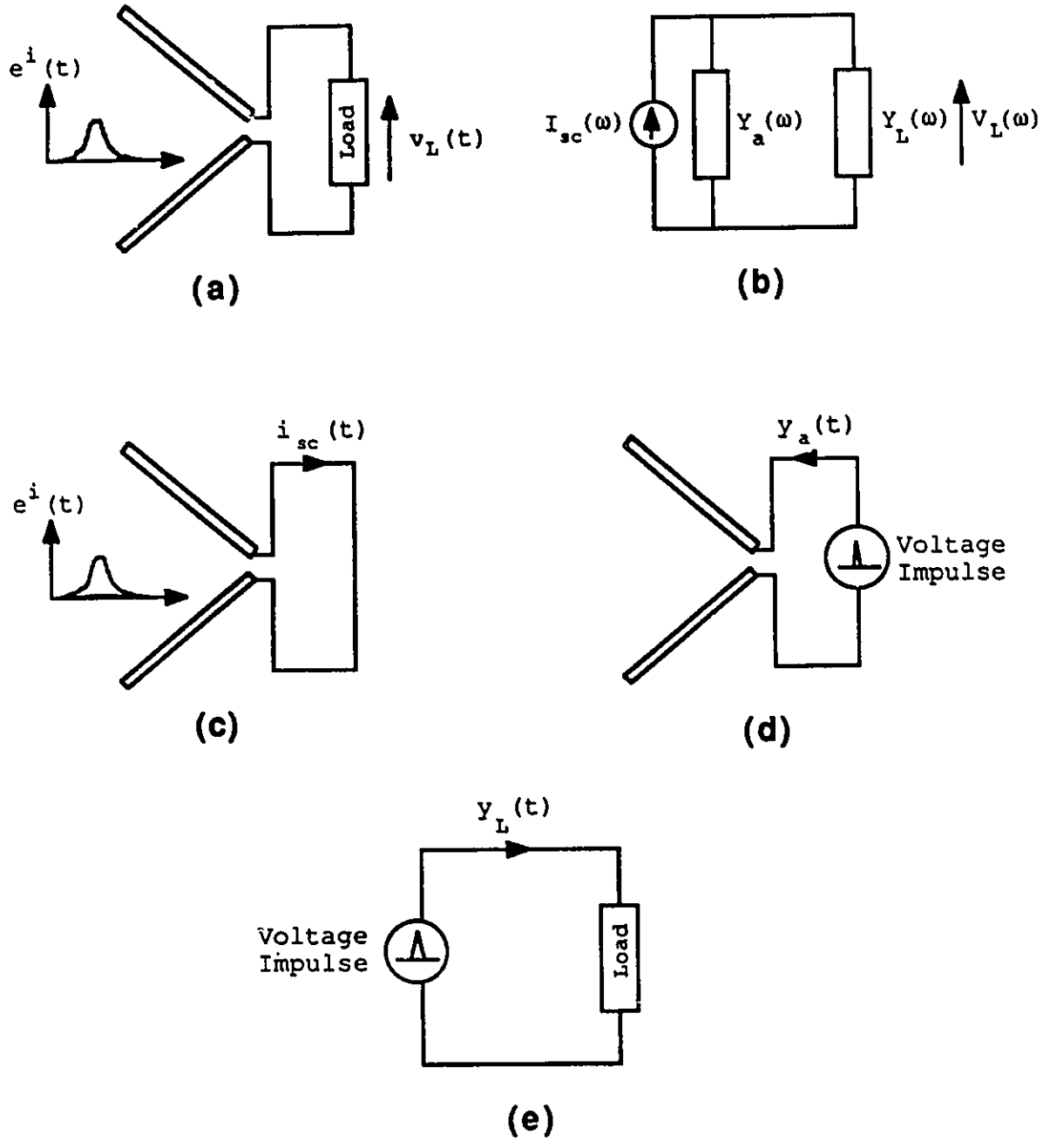


Figure 90: Norton equivalent circuit parameters.

where $i_{sc}(t)$ is the short-circuited terminal current of the receiving antenna (shown in Figure 90(c)), $y_a(t)$ is the input current of the antenna for an input voltage impulse (shown in Figure 90(d)), and $y_L(t)$ is the input current of the termination for an input voltage impulse (shown in Figure 90(e)). The asterisk indicates the convolution operation, defined as

$$x(t) * h(t) = \int_{-\infty}^{\infty} x(t-\theta)h(\theta)d\theta. \tag{274}$$

If the two signals are causal, i.e.

$$x(t) = h(t) = 0, \quad t \leq 0,$$

this simplifies to

$$x(t) * h(t) = \int_{0}^{t} x(t-\theta)h(\theta)d\theta. \tag{275}$$

As $y_a(t)$, $y_L(t)$ and $v_L(t)$ are all causal, equation (273) is essentially a Volterra integral equation of first kind [105]. Its solution can be expressed as

$$v_L(t) = [y_a(t) + y_L(t)] *^{-1} i_{sc}(t) \tag{276}$$

where $*^{-1}$ indicates the deconvolution operation. Various numerical deconvolution techniques have been described in the literature [106, 107].

$i_{sc}(t)$ and $y_a(t)$ of an antenna can be obtained from a code like VDIP. For some simple terminations, $y_L(t)$ may be obtained analytically. Otherwise, $Y_L(\omega)$ can be computed in the frequency domain, and then transformed using IFFT. In either case, it may be convenient to "smooth" $y_L(t)$, by convolving it with another pulse $x(t)$, such that

$$y_{Lx}(t) = y_L(t) * x(t).$$

The waveform of $x(t)$ is arbitrary as long as it covers the whole frequency spectrum of the incident pulse waveform $e^i(t)$. Nonetheless, it may be convenient to use the same pulse waveform for both $x(t)$ and $e^i(t)$. The transmitting antenna response is also smoothed accordingly, i.e.

$$y_{ax}(t) = y_a(t) * x(t).$$

Physically, $y_{ax}(t)$ is the input current of the transmitting antenna for an input voltage with waveform $x(t)$. $y_{Lx}(t)$ is the input current of the termination for an input voltage with waveform $x(t)$. They can be numerically evaluated more easily, when compared with $y_a(t)$ and $y_L(t)$, due to the lack of singularities. Finally, the load voltage waveform $v_L(t)$ is obtained by numerically solving the following deconvolution problem:

$$v_L(t) = [y_{ax}(t) + y_{Lx}(t)] *^{-1} [i_{sc}(t) * x(t)] \tag{277}$$

If $v_L(t)$ is needed in the time interval $0 < t < t_o$, one has to calculate $y_{ax}(t)$, $y_{Lx}(t)$ and $i_{sc}(t)$ *only* in this time interval. This is one advantage of using Norton's equivalent circuit in the time domain. In the frequency-domain approach, one has to calculate $y_a(t)$ and $i_{sc}(t)$ until they virtually diminish.

## 7.2 Conclusions

It was shown in Chapter 3 that a circular loop antenna with a uniform distributed resistance has a broad receiving bandwidth, at least for uniform plane waves incident in $\theta = 90°, \phi_o = 180°$ direction. Nonetheless, the antenna is dispersive and is therefore not suitable for the reception of electromagnetic pulses or transients. One may consider the use of loop antennas with *nonuniform* resistive and reactive loads, for the reception of pulses.

The WK nonreflecting straight dipole, when terminated with a 50 Ω transmission line, does not have a sufficient bandwidth for the reception of electromagnetic pulses. One way of increasing the bandwidth is by increasing the distributed resistance. This type of design gives a broader bandwidth at the expense of the receiving sensitivity. Broader bandwidth can also be achieved, without sacrificing sensitivity, by terminating the WK antenna with a high-resistance load. Although such a design promises better sensitivity, an active (electronic or optical) transducer is needed to realize the high input resistance. The WK antenna terminated with a highly resistive load has the 'maximally flat' frequency response close to the upper roll-off frequency.

As a solution to the problem of receiving sub-nanosecond pulses and transients, a new broadband antenna has been developed as described in Chapter 5. This antenna consists of

a resistively-loaded V-dipole or monopole, a Response Equalizer Circuit and an oscilloscope probe (or other termination). For a given oscilloscope probe, the new antenna has a higher sensitivity and a much broader bandwidth compared with the WK antenna. It is estimated to have a 3-dB bandwidth from 25 MHz to 10 GHz when used with a commercially available 500 Ω passive probe (Tektronix P6150). The sensitivity is approximately 1 $mV/(Vm^{-1})$, taking into account the 20 dB attenuation of the 500 Ω probe. With a 50 Ω termination, this antenna has a 3-dB bandwidth from 110 MHz to 10 GHz, and a sensitivity better than 4 $mV/(Vm^{-1})$.

The wide bandwidth and non-dispersive phase characteristics of the V-antenna make it very suitable for measuring fast electromagnetic pulses and transients. The width of the pulse can be as short as 70 ps (or the transition duration of the transient, as short as 35 ps). The antenna with 500 Ω probe is suitable for making measurements up to 40 ns. Even with a 50 Ω termination, measurements can be made up to 9 ns, without noticing the lower rolling-off effect. Since many time-domain scattering ranges have the operational time window between 8 ns and 12 ns, the new antenna with 50 Ω termination can be used to improve the sensitivity and the resolution of scattering measurements. For comparison, the 10-mm tall L-antenna described in [39] has a sensitivity of 5.8 $mV/(Vm^{-1})$. However, in order to have a operational time window of 9 ns, the antenna has to be at least 135 cm long!

The new V-antenna can also be used in many time-domain unguided-wave measurement systems, which require broadband antennas. It has potential applications in baseband (impulse) radar and target identification systems. The directivity of the new antenna can be a limitation for some applications, which require omni-directional antennas.

An experimental *thin-film* V-antenna has been fabricated, and measured in both time and frequency domains. This antenna is capable of receiving a 520-ps approximately Gaussian pulse, without significant distortions. It has a sensitivity of 1.12 $mV/(Vm^{-1})$ and a flat receiving response from 35 MHz to 3 GHz. At present, it is not possible to measure the response beyond 3 GHz, due to limitations of the pulse generators available. An experimental Wu-King straight monopole has also been fabricated and tested in the time-domain

range. It has a sensitivity of 22 mV/(Vm$^{-1}$) and a upper roll-off frequency of about 300 MHz, which is limited by the bandwidth of the active receiver circuit.

# Bibliography


[1] Ross, G.F., "Early developments and motivations for time-domain analysis and applications," in *Time-Domain Measurements in Electromagnetics* edited by Miller, E.K., Van Nostrand Reinhold, NY, 1986.

[2] Peters, L., Jr. and Young, J.D., "Applications of subsurface transient radar" in *Time-Domain Measurements in Electromagnetics* edited by Miller, E.K., Van Nostrand Reinhold, NY, 1986.

[3] Bennia, A., Su, W., and Riad, S.M., "Bond verification of space shuttle tiles using time domain techniques," *Conf. Precision Electromagnetic Measurements*, Ottawa, Ontario, June 1990.

[4] Giles, S., "Application of a layer-peeling technique to identify dielectric constants of stratified media," *1990 URSI Radio Science Meeting*, Dallas, Texas, May 1990.

[5] Ross, J.E., Rothwell, E.J., Nyquist, D.P. and Chen, K.M., "Multiple target discrimination using E-pulse techniques," *1990 Antennas and Propagation Symp. Digest*, Dallas, Texas, May 1990.

[6] Ross, G.F., Cronson, H. and Lamensdorf D., "Time domain electromagnetics measurements," short course notes, *IEEE AP-S URSI Symp.*, Syracuse, New York, June 1988.

[7] Van Etten, P., "Electromagnetic field compression by dispersive broadband antennas," *IEEE AP-S Symp.*, 1974, pp. 350-353.

[8] Thansandote, A. *et. al.*, "A broadband E-field sensor," *Conf. Precision Electromagnetic Measurements*, Ottawa, Ontario, June 1990.

[9] Stuchly, M.A. *at. al.*, "Magnetic field sensor for measurement of transients," *Conf. Precision Electromagnetic Measurements*, Ottawa, Ontario, June 1990.

[10] Private communication with Dr. Moto Kanda and Mr. Andy Ondrejka, National Institute for Science and Technology, Boulder, Colorado, April 1990.

[11] Schelkunoff, S.A. and Friis, H.T., *Antennas, Theory and Practice*, John Wiley, 1952.

[12] Carrel, R.L., "The characteristic impedance of two infinite cones of arbitrary cross section," *IRE Trans. Antennas and Propagation*, vol. 6, April 1958, pp. 197-201.

[13] Wait, J.R., "Electromagnetic radiation from conical structures" in *Antenna Theory*, edited by Collin, R.E. and Zucker, F.J., McGraw-Hill, 1969.

[14] Harrison, C.W., Jr. and Williams, C.S., Jr., "Transients in wide-angle conical antennas," *IEEE Trans. Antennas and Propagation*, vol. 13, March 1965, pp. 236-246.

[15] Foltz, H.D. and Davis, J.H., "Characteristic impedance of infinite cones of elliptic cross section," *IEEE Trans. Antennas and Propagation*, vol. 35, December 1987, pp. 1481-83.

[16] Blume, S. and Grafmüller, B., "Biconical antennas and conical horns with elliptic cross section," *IEEE Trans. Antennas and Propagation*, vol. 36, August 1988, pp. 1066-69.

[17] Nagasawa, K. and Matsuzuka, I., "Radiation field consideration of biconical horn antenna with different flare angles," *IEEE Trans. Antennas and Propagation*, vol. 36, September 1988, pp. 1306-10.

[18] Maloney, J.G., Smith, J.S. and Scott, W.R., "Accurate computation of the radiation from simple antennas using the finite-difference time-domain method," *IEEE Trans. Antennas and Propagation*, vol. 38, July 1990, pp. 1059-68.

[19] Shen, H.-M., King, R.W.P. and Wu, T.T., "V-conical antenna," *IEEE Trans. Antennas and Propagation*, vol. 36, November 1988, pp. 1519-25.

[20] Kunz, K.S. *et. al.*, "Lawrence Livermore National Laboratory electromagnetic measurement facility," *IEEE Trans. Electromagnetic Compatibility*, vol. 29, May 1987, pp. 93-103.

[21] Lamensdorf, D., "The transient response of the coaxial horn antenna," *IEEE Trans. Antennas and Propagation*, vol. 18, November 1970, pp. 799-802.

[22] Kanda, M., "Transients in a resistively loaded antenna compared with those in a conical antenna and a TEM horn," *IEEE Trans. Antennas and Propagation*, vol. 28, January 1980, pp. 132-136.

[23] Kanda, M., "Transients in resistively loaded antennas and their comparison with conical antennas and TEM horns," *Int. Symp. Antennas and Propagation Digest*, University of Maryland, MD, May 1978, pp. 13-16.

[24] Kanda, M., "The effects of resistive loading of TEM horns," *IEEE Trans. Electromagnetic compatibility*, vol. 24, May 1982, pp. 245-255.

[25] Theodorou, E.A. *et. al.*, "Broadband pulse-optimized antenna," *IEE Proc.*, vol. 128, pt H, June 1981, pp. 124-130.

[26] Evans, S. *et. al.*, "TEM horn antenna: input reflection characteristics in transmission," *IEE Proc.*, vol. 31, pt H, October 1983, pp. 403-409.

[27] Wu, T.T. and King, R.W.P., "The cylindrical antenna with nonreflecting resistive loading," *IEEE Trans. Antennas and Propagation*, vol. 13, May 1965, pp. 369-373. *Corrected by* Shen, L.C. and King, R.W.P. in the same vol., Nov 1965, p 998.

[28] Shen, L.C. and King, R.W.P., "Cylindrical antenna with tapered resistive loading," *Radio Science*, vol 2, Feb. 1967, pp. 191-201.

[29] Kanda, M., "The characteristics of a linear antenna with tapered resistive and capacitive loading," *International IEEE/AP-S Symp. Digest*, June 1980, pp. 696-699.

[30] Walter, C.H., *Travelling Wave Antennas*, Chapter 8, Dover, 1970.

[31] Sengupta, D.L. and Liu, Y.-P., "Analytical Investigation of Waveforms Radiated by a Resistively Loaded Linear Antenna Excited by a Gaussian Pulse," *Radio Science*, vol. 9, June 1974, pp. 621-630.

[32] Liu, Y.-P. and Sengupta, D.L., "Transient Radiation from a Linear Antenna with Nonreflecting Resistive Loading," *IEEE Trans. Antennas and Propagation*, vol. 22, March 1974, pp. 212-220.

[33] Kanda, M., "A relatively short cylindrical broadband antenna with tapered resistive loading for picosecond pulse measurements," *IEEE Trans. Antennas and Propagation*, vol. 26, May 1978, pp. 439-447.

[34] Kanda, M., "The time-domain characteristics of a travelling wave linear antenna with linear and nonlinear parallel loads," *IEEE Trans. Antennas and Propagation*, vol. 28, March 1980, pp. 267-276.

[35] Kanda, M. and Driver, L.D., "An Isotropic Electric-Field Probe with Tapered Resistive Dipoles for Broadband Use, 100 kHz-18 GHz," *IEEE Trans. Microwave Theory and Technology*, vol. 35, February 1987, pp. 124-130.

[36] Masterson, K.D., Driver, L.D. and Kanda, M., "Photonic probes for the measurement of electromagnetic fields over broad bandwidths," *IEEE 1989 National Symp. on Electromagnetic Compatibility*, Denver, Colorado, May 1989, pp. 1-6.

[37] Masterson, K.D. and Driver, L.D., "Broadband, isotropic, photonic electric-field meter for measurements from 10 kHz to above 1 GHz," *Proceedings of SPIE- The Int. Society for Optical Engineering*, vol. 987, September 1988, pp. 107-118.

[38] Vollmer, E. and Hinken, J.H., "Synthesis method for broad-band tapered wire antennas and its experimental verification," *IEEE Trans. Antennas and Propagation*, vol. 37, August 1989, pp. 959-965.

[39] Shen, H.-M., King, R.W.P. and Wu, T.T., "New sensors for measuring very short electromagnetic pulses," *IEEE Trans. Antennas and Propagation*, vol. 38, June 1990, pp. 838-846.

[40] Baum, C. *et. al.*, "Sensors for electromagnetic pulse measurements both inside and away from nuclear source regions," *IEEE Trans. Antennas and Propagation*, vol. 26, January 1978, pp. 22-35.

[41] Baum, C., "Parameters for some electrically-small electromagnetic sensors," *Sensor and Simulation Notes*, Note XXXVIII, March 1967.

[42] Bolla, L. *et. al.*, "A wide-band measuring system for time-domain measurements," *Electromagnetic Compatibility 1981*, Proceedings of the fourth symposium and technical exhibition on electromagnetic compatibility, Zurich, March, 1981, pp. 413-417.

[43] Baum, C., "The circular parallel-plate dipole," *Sensor and Simulation Notes*, Note 80, March 1969.

[44] Baum, C., "Some further considerations for the circular parallel-plate dipole," *Sensor and Simulation Notes*, Note 86, June 1969.

[45] Kopola, H. *et. al.*, "An optical E-field sensor," *Conf. Precision Electromagnetic Measurements*, Ottawa, Ontario, June 1990.

[46] Thansandote, A. *et. al.*, "Broadband active E-field sensors for measurement of transients," submitted to *IEEE Trans. Instrumentation and Measurements*, 1990.

[47] King, R.W.P. and Schmitt, H.J., "The transient response of linear antennas," *IEEE Trans. Antennas and Propagation*, vol. 10, May 1962, pp. 222-228.

[48] Martin, R.G. *et. al.*, "An approximate analysis of transient radiation from linear antennas," *Int. J. Electronics*, vol. 61, no 3, 1986, pp. 343-353.

[49] Zaiping, N., "Radiation characteristics of travelling-wave antennas excited by non-sinusoidal currents," *IEEE Trans. Electromagnetic Compatibility*, vol. 25, 1983, pp. 24-31.

[50] Franceschetti G. and Papas, C.H., "Pulsed Antennas," *IEEE Trans. Antennas and Propagation*, vol. 22, September 1974, pp. 651-661.

[51] Shen, H.-M. *et. al.*, "Theoretical analysis of the rhombic simulator under pulse excitation,' *IEEE Trans. Electromagnetic Compatibility*, vol. 25, February 1983, pp. 47-55.

[52] Shen, H.-M. *et. al.*, "An experimental investigation of the rhombic EMP simulator under pulse excitation,' *IEEE Trans. Electromagnetic Compatibility*, vol. 25, February 1983, pp. 40-46.

[53] Sato, M. *et. al.*, "Transient response of coupled linear dipole antennas," *IEEE Trans. Antennas and Propagation*, vol. 32, February 1984, pp. 133-140.

[54] Sato, M. and Sato, R., "Transient response between a V-antenna and a collinear dipole antenna," *IEEE Trans. Antennas and Propagation*, vol. 32, November 1984, pp. 1211-17.

[55] Chen, Z.-Q., "Theoretical solutions of transient radiation from travelling-wave linear antennas," *IEEE Trans. Electromagnetic Compatibility*, vol. 30, February 1988, pp. 80-83.

[56] Zhan, J. and Qin, Q.-L., "Analytic solutions of travelling-wave antennas excited by nonsinusoidal currents," *IEEE Trans. Electromagnetic Compatibility*, vol. 31, August 1989, pp. 328-330.

[57] Fang, L. and Wenbing, W., "An analysis of the transient fields of linear antennas," *IEEE Trans. Electromagnetic Compatibility*, vol. 31, Nov 1989, pp. 404-409.

[58] Ross, G.F., "A time domain criteria for the design of wideband radiating elements," *IEEE Trans. Antennas and Propagation*, vol. 16, May 1968, pp. 355-356.

[59] Harmuth, H.F. and Ding-Rong, S., "Antennas for nonsinusoidal waves, I. Radiators," *IEEE Trans. Electromagnetic Compatibility*, vol. 25, 1983, pp. 13-25.

[60] Martin, R.G. *et. al.*, "Some thoughts about the radiation of antennas excited by non-sinusoidal currents," *Int. J. Electronics*, vol. 57, no 5, 1984, pp. 617-625.

[61] Hussain, M.G.M., "Antenna patterns of nonsinusoidal waves with the time variation of a gaussian pulse: part IV," *IEEE Trans. Electromagnetic Compatibility*, vol. 31, February 1989, pp. 48-54.

[62] Wu, T.S., "Transient response of a dipole antenna," *J. Mathematical Physics*, vol. 2, no 6, 1961, pp. 892-894.

[63] Morgan, S.P., "Transient response of a dipole antenna," *J. Mathematical Physics*, vol. 3, no 3, 1962, pp. 564-565.

[64] Latham, R.W. and Lee, K.S.H., "Transient properties of an infinite cylindrical antenna," *Radio Science*, vol. 5, April 1970, pp. 715-723.

[65] Chen K.C., "Transient response of an infinite cylindrical antenna," *IEEE Trans. Antennas and Propagation*, vol. 31, January 1983, pp. 170-172.

[66] Kasevich, R.S., "Pulse response of linear dipole antenna," *IEEE Trans. Antennas and Propagation*, vol. 31, March 1983, pp. 369-371.

[67] Franceschetti, G., "A canonical problem in transient radiation," *IEEE Trans. Antennas and Propagation*, vol. 26, July 1978, pp. 551-555.

[68] Kotulski, J.D.,"Early-time response of the spherical antenna," *IEEE Trans. Antennas and Propagation*, vol. 34, April 1986, pp. 521-527.

[69] Poggio, A.J., "Integral equation solutions of three-dimensional scattering problems," in *Computer Techniques in Electromagnetics* edited by Mittra, R., Pergamon Press, 1973.

[70] Miller, E.K. and Poggio, A.J., "Moment-method techniques in electromagnetics from an applications viewpoint," in *Electromagnetic Scattering* edited by Uslenghi, P.L.E., Academic Press, 1978.

[71] Mittra, R., "Integral equation methods for electromagnetic scattering," in *Transient Electromagnetic Fields* edited by Felsen, L.B., Springer-Verlag, 1976.

[72] Auckenthaler, A.k. and Bennett, C.L., "Computer solution of transient and time domain thin-wire antenna problems," *IEEE Trans. Microwave Theory and Technology*, vol. 19, November 1971, pp. 892-893.

[73] Miller, E.K. *et. al.*, "An integro-differential equation technique for the time-domain analysis of thin wire structures. I. The numerical method," *J. Computational Physics*, vol. 12, 1973, pp. 24-48.

[74] Miller, E.K. and Landt, J.A., "Direct time-domain techniques for transient radiation and scattering from wires," *Proc. IEEE*, vol. 68, Nov 1980, pp. 1396-1423.

[75] Miller, E.K. and Blaricum, M.L.V., "The short-pulse response of a straight wire," *IEEE Trans. Antennas and Propagation*, vol. 21, May 1973, pp. 396-398.

[76] Landt, J.A. and Miller, E.K., "Transient response of the infinite cylinder antenna and scatterer, *IEEE Trans. Antennas and Propagation*, vol. 24, March 1976, pp. 246-250.

[77] Poggio, A.J., "The space-time domain magnetic vector potential integral equations," *IEEE Trans. Antennas and Propagation*, vol. 19, September 1971, pp. 702-704.

[78] Liu, T.K. and Mei, K.K., "A time-domain integral-equation solution for linear antennas and scatterers," *Radio Science*, vol. 8, August 1973, pp. 797-804.

[79] Liu, Y.K., *Time Domain Analysis of Linear Antennas and Scatterers*, Ph.D. dissertation, University of California at Berkeley, 1972.

[80] Rao, S.M., Sarkar, T.K. and Dianat, S.A., "A novel technique to the solution of transient electromagnetic scattering from thin wires," *IEEE Trans. Antennas and Propagation*, vol. 34, May 1986, pp. 630-634.

[81] Mohan, S.A. and Rao, S.M., "Transient scattering from a thin arbitrary wire," *IEEE Trans. Antennas and Propagation*, vol. 36, August 1988, pp. 1188-91.

[82] Baum, C., "The singularity expansion method: background and developments," *IEEE Antennas and Propagation Society Newsletter*, August 1986, pp. 15-23.

[83] Tesche, F.M., "On the analysis of scattering and antenna problems using the singularity expansion technique," *IEEE Trans. Antennas and Propagation*, vol. 21, January 1973, pp. 53-62.

[84] Baum, C.E., "The singularity expansion method," in *Transient Electromagnetic Fields* edited by Felsen, L.B., Springer-Verlag, 1976.

[85] Baum, C.E., "Toward an engineering theory of electromagnetic scattering: The singularity and eigenmode expansion methods," in *Electromagnetic Scattering* edited by Uslenghi, P.L.E., Academic Press, 1978.

[86] Marin, L., "Natural-mode representation of transient scattered fields," *IEEE Trans. Antennas and Propagation*, vol. 21, November 1973, pp. 809-818.

[87] Wu, T.T., "Theory of the thin circular loop antenna," *J. Mathematical Physics*, vol. 3, November 1962, pp. 1301-04.

[88] King, R.W.P. and Prasad, S., *Fundamental Electromagnetic Theory and Applications*, Prentice-Hall, 1986.

[89] Blackburn, R.F. and Wilton, D.R., "Analysis and synthesis of an impedance-loaded loop antenna using the singularity expansion method," *IEEE Trans. Antennas and Propagation*, vol. 26, January 1978, pp. 136-140.

[90] Kanda, M., "Transients in a resistively loaded loop antenna," *Int. Symp. on Electromagnetic Compatibility*, Tokyo, Japan, 1984, pp. 286-290.

[91] Kanda, M., "Time-domain sensors and radiators" in *Time-Domain Measurements in Electromagnetics* edited by Miller, E.K., Van Nostrand Reinhold, NY, 1986.

[92] Harrington, R.F., *Field Computation by Moment Methods*, MacMillan, New York, 1968.

[93] Esselle, K.P. and Stuchly, S.S., "Resistively loaded loop as a pulse-receiving antenna," *IEEE Trans. Antennas and Propagation*, vol. 38, July 1990, pp. 1123-26.

[94] Esselle, K.P. and Stuchly, S.S., "Analysis of the loaded loop antenna," *1989 IEEE AP-S International Symp.*, San Jose, California, June 1989, pp. 363-366.

[95] Burke, G.J. and Poggio, A.J., Numerical Electromagnetic Code (NEC)- Method of Moments, Naval Ocean Systems Center, Technical Document 116, San Diego, California, January 1980.

[96] McLachlan, N.M., *Bessel Functions for Engineers*, Oxford, 1955.

[97] Kanda, M., "An electromagnetic near-field sensor for simultaneous electric and magnetic field measurements," *IEEE Trans. Electromagnetic Compatibility*, vol. 26, August 1984, pp. 102-110.

[98] *IMSL Subroutine Reference Manual*, Edition 9.2, IMSL, Houstan, Texas, 1984.

[99] Watson, G.N., *A Treatise on the Theory of Bessel Functions*, Cambridge Univ. Press, 1966.

[100] Esselle, K.P. and Stuchly, S.S., "Pulse receiving characteristics of resistively loaded dipole antennas," accepted for publication in *IEEE Trans. Antennas and Propagation*, vol. 38, October 1990.

[101] Esselle, K.P. and Stuchly S.S., "An electrically-large antenna for transient electromagnetic field measurements," submitted for publication in *IEEE Trans. Instrumentation and measurements*, 1990.

[102] Esselle, K.P. and Stuchly S.S., "A new broadband antenna for transient electromagnetic field measurements," *1990 IEEE Antennas and Propagation Symp. Digest*, Dallas, Texas, May 1990, pp. 1584-87.

[103] Esselle, K.P. and Stuchly S.S., "Loaded V-antenna for pulse electromagnetic field measurements," *XXIIIrd General Assembly of the URSI*, Prague, Czechoslovakia, August 1990.

[104] Thansandote, A. and Stuchly, S.S., "A broadband active E-field sensor for CW and transient field measurements," submitted for publication in *Electronics Letters*, 1990.

[105] Jerri, A.J., *Introduction to Integral Equations with Applications*, Marcel Dekker, NY, 1985.

[106] Sakar, T.K. *et. al.*, "Deconvolution of impulse response from time-limited input and output: theory and experiment," *IEEE Trans. Antennas and Propagation*, vol. 34, December 1985, pp. 541-546.

[107] Sakar, T.K. *et. al.*, "Impulse response determination in the time domain- theory," *IEEE Trans. Antennas and Propagation*, vol. 30, July 1982, pp. 657-663.

# Appendix A

# The Generic Part

The expression for the electric field produced by the current in the generic part is derived in this appendix. For convenience, the expression for current in (187) is rewritten as

$$I(s,\tau) = \zeta + \eta R_s \tag{278}$$

where

$$\zeta = \frac{R_{s2}C_1 - R_{s1}C_2}{R_{s2} - R_{s1}} \tag{279}$$

$$\eta = \frac{C_2 - C_1}{R_{s2} - R_{s1}}. \tag{280}$$

Substituting this in (180), one obtains

$$\begin{aligned} cY(s) = & -\frac{[\eta\cos\theta_v]}{R_s} - \frac{[\zeta\cos\theta_v]}{R_s^2} + \frac{[2\eta x_i x_l \sin^2\theta_v]}{R_s^3} + \frac{[2\zeta x_i x_l \sin^2\theta_v]}{R_s^4} \\ & + [2\eta x_i \sin^2\theta_v]\frac{s}{R_s^3} + [2\zeta x_i \sin^2\theta_v]\frac{s}{R_s^4}. \end{aligned} \tag{281}$$

The expression for $R_s$ is

$$R_s = [s^2 + 2s(x_l - x_i\cos\theta_v) + x_l^2 + x_i^2 - 2x_l x_i\cos\theta_v]^{1/2}. \tag{282}$$

Expression (281) is to be integrated with respect to $s$, between the limits $s_1$ and $s_2$. Using tables of integrals, it can be shown that

$$cY_t = \int_{s_1}^{s_2} cY(s)ds$$

$$= -\eta\cos\theta_v \ln\left(\frac{R_{s2}+s_2+x_l-x_i\cos\theta_v}{R_{s1}+s_1+x_l-x_i\cos\theta_v}\right) + 2\eta\cos\theta_v\left(\frac{s_2}{R_{s2}}-\frac{s_1}{R_{s1}}\right)+2\eta(x_l\cos\theta_v-x_i)\left(\frac{1}{R_{s2}}-\frac{1}{R_{s1}}\right) + \zeta\cos\theta_v\left(\frac{s_2}{R_{s2}^2}-\frac{s_1}{R_{s1}^2}\right)+\zeta(x_l\cos\theta_v-x_i)\left(\frac{1}{R_{s2}^2}-\frac{1}{R_{s1}^2}\right) \quad (283)$$

where

$$R_{s1} = [s_1^2+2s_1(x_l-x_i\cos\theta_v)+x_l^2+x_i^2-2x_lx_i\cos\theta_v]^{1/2} \quad (284)$$

$$R_{s2} = [s_2^2+2s_2(x_l-x_i\cos\theta_v)+x_l^2+x_i^2-2x_lx_i\cos\theta_v]^{1/2}. \quad (285)$$

Substitution of expressions (279) and (280) into (283) leads to

$$cY_t = -\cos\theta_v\left(\frac{C_2-C_1}{R_{s2}-R_{s1}}\right)\ln\left(\frac{R_{s2}+s_2+x_l-x_i\cos\theta_v}{R_{s1}+s_1+x_l-x_i\cos\theta_v}\right) + \frac{\cos\theta_v}{R_{s2}-R_{s1}}\left(\frac{2C_1s_1}{R_{s1}}+\frac{2C_2s_2}{R_{s2}}-\frac{C_1s_2}{R_{s2}}-\frac{C_2s_1}{R_{s1}}-\frac{C_1s_1R_{s2}}{R_{s1}^2}-\frac{C_2s_2R_{s1}}{R_{s2}^2}\right) - \frac{x_l\cos\theta_v-x_i}{R_{s1}R_{s2}}\left(C_2-C_1+\frac{C_1R_{s2}}{R_{s1}}-\frac{C_2R_{s1}}{R_{s2}}\right). \quad (286)$$

Rearranging equation (190), one obtains

$$cZ(s) = -x_ix_l\sin^2\theta_v\left(\frac{C_2-C_1}{R_{s2}-R_{s1}}\right)\frac{1}{R_s^3} - x_i\sin^2\theta_v\left(\frac{C_2-C_1}{R_{s2}-R_{s1}}\right)\frac{s}{R_s^3} \quad (287)$$

Integration of $cZ(s)$ with respect to $s$, between limits $s_1$ and $s_2$, leads to

$$cZ_t = \int_{s_1}^{s_2} cZ(s)ds = -\frac{\cos\theta_v}{R_{s2}-R_{s1}}\left(\frac{C_2s_2}{R_{s2}}+\frac{C_1s_1}{R_{s1}}-\frac{C_1s_2}{R_{s2}}-\frac{C_2s_1}{R_{s1}}\right)+\frac{x_l\cos\theta_v-x_i}{R_{s1}R_{s2}}(C_2-C_1). \quad (288)$$

Finally, the total field produced by the current in the generic part is found as

$$c(Y_t+Z_t) = -\cos\theta_v\left(\frac{C_2-C_1}{R_{s2}-R_{s1}}\right)\ln\left(\frac{R_{s2}+s_2+x_l-x_i\cos\theta_v}{R_{s1}+s_1+x_l-x_i\cos\theta_v}\right) + \cos\theta_v\left[\frac{C_2s_2}{R_{s2}^2}-\frac{C_1s_1}{R_{s1}^2}\right]-\left(\frac{x_l\cos\theta_v-x_i}{R_{s1}R_{s2}}\right)\left[\frac{C_1R_{s2}}{R_{s1}}-\frac{C_2R_{s1}}{R_{s2}}\right]. \quad (289)$$

# Appendix B

# LLOOP Code Listing

```
C THE FOLLOWING CODE CALULATES RECEIVING RESPONSE OF A UNIFORMLY
C RESISTIVELY LOADED LOOP ANTENNA WITH RADIUS*K=KB AND B/A=BBYA.
C NOTE: KB = INT* STEP WHERE INT= ANY POSITIVE INTEGER AND
C STEP IS DEFINED IN SUBROUTINE 'INT' (DEFAULT=.001)
C
C PHIO = DIRECTION OF THE INCIDENT WAVE, BBYA = RADII RATIO
C ZL = TERMINAL LOAD IMPEDANCE, ZT = TOTAL RESISTIVE LOAD AROUND LOOP.
C
      PARAMETER (LIMIT=14)
      COMPLEX NC(0:LIMIT), AC(0:LIMIT-1), LC(0:LIMIT-1), YC, SUMC
      COMPLEX ISC, SC
      REAL KB, NR(0:LIMIT), NI(0:LIMIT), MMBSIO, MMBSKO
      REAL BESNKB(0:LIMIT), B1(2*LIMIT+2), LM
      PI  = 4.*ATAN(1.)
      PHIO= 0.
      BBYA= 23.6
      ZL  = 0.
      ZT  = 50.
      WRITE (*,*) 'RADIUS RATIO   = ',BBYA
      WRITE (*,*) 'WAVE DIRECTION = ',PHIO
      WRITE (*,*) 'LOAD IMPEDANCE = ',ZL,' OHMS'
      WRITE (*,*) 'TOTAL LOAD     = ',ZT,' OHMS'
      WRITE (*,*) 'LIMIT - 1      = ',LIMIT-1
      DO 1000 J=1, 80
      KB  =J*.05
      CALL INT(0,2.*KB,WEBINT,BESINT,IER)
      IF (IER.NE.0) GO TO 210
      NR(0) = LOG(8.*BBYA)/PI - WEBINT/2.
      NI(0) = - BESINT/2.
      NC(0) = CMPLX( NR(0),NI(0) )
      DO 200 N= 1, LIMIT
      CN = LOG(4.*N) + 0.5772
      DO 220 M= 0, N-1
220   CN = CN - 2./(2.*M+1.)
      CALL INT(N,2.*KB,WEBINT,BESINT,IER)
      IF (IER.NE.0) GO TO 210
      NR(N) = ( CN + MMBSI0(1,N/BBYA,IER1)*MMBSK0(1,N/BBYA,IER2) )/PI
     2        - WEBINT/2.
C     WRITE (*,*) N, NR(N), NR(N)+WEBINT/2.
      NI(N) = - BESINT/2.
      NC(N) = CMPLX( NR(N),NI(N) )
      IF (IER1.NE.0) GO TO 250
      IF (IER2.NE.0) GO TO 250
200   CONTINUE
C
C CALCULATION OF A(N)'S:
C
      AC(0) = KB*NC(1)
C     WRITE (*,*) 0, (1.,0.)/AC(0)
      DO 230 N= 1, LIMIT-1
      AC(N) = KB*( NC(N+1) + NC(N-1) )/2. - (N**2)*NC(N)/KB
C     WRITE (*,*) N, AC(N)
230   CONTINUE
C
C CALCULATING LC(I) COMPLEX VECTOR:
```

```
C
      CALL MMBSJN (KB,LIMIT+1,B1,IER)
      IF (IER.NE.0) GO TO 280
      DO 1300 I=0, LIMIT
      BESNKB(I)= B1(2*I+1)
1300  CONTINUE
      LM    = BESNKB(1)
      LC(0) = LM
      DO 1100 I=1, LIMIT-1
      LM    = ( BESNKB(I-1)- BESNKB(I+1) )*COS(I*PHI0)
      LC(I) = -1.*CMPLX( COS(I*PI/2.), SIN(I*PI/2.) )*LM
1100  CONTINUE
      DO 1200 I=0, LIMIT-1
C     WRITE (*,*) I, LC(I)/AC(I)
1200  CONTINUE
C
C CALCULATION OF APPROXIMATIONS TO Y:
C
      SUMC = 1./(ZT+ CMPLX(0.,120.*PI**2)*AC(0))
      YC   = SUMC*(120.*PI)
      YR   = REAL(YC)
      YI   = AIMAG(YC)
      YM   = SQRT(YR**2+YI**2)
      YA   = ATAN(YI/YR)*(180./PI)
C     WRITE (*,240) 0,YC,YM,YA
      DO 260 N= 1, LIMIT-1
      SUMC = SUMC + 2./( ZT + CMPLX(0.,120.*PI**2)*AC(N))
      YC   = SUMC*(120.*PI)
      YR   = REAL(YC)
      YI   = AIMAG(YC)
      YM   = SQRT(YR**2+YI**2)
      YA   = ATAN(YI/YR)*(180./PI)
C     WRITE (*,240) N,YC,YM,YA
260   CONTINUE
C
C CALCULATE SHORT-CIRCUIT CURRENT:
C
      ISC   = LC(0)/( AC(0) + ZT/CMPLX(0.,120.*PI**2) )
      DO 2000 I=1,LIMIT-1
      ISC   = ISC + LC(I)/( AC(I) + ZT/CMPLX(0.,120.*PI**2) )
2000  CONTINUE
C
C CALCULATE RECEIVING RESPONSE SC:
C
      SC = ISC/( YC*ZL  /(120.*PI) + 1.)
      SM = EXP( REAL(CLOG(SC)))
      SA = AIMAG( CLOG(SC))*(180./PI)
      WRITE (*,270) KB,YC,SC
1000  CONTINUE
240   FORMAT (2X,I2,4(2X,E13.5))
270   FORMAT (2X,F5.2,4(2X,E13.5))
      STOP
210   WRITE (*,*) 'ERROR FROM INT-SUBROUTINE'
      STOP
250   WRITE (*,*) 'ERROR FROM MMBSK0 OR MMBSI0'
```

```
      STOP
280   WRITE (*,*) 'ERROR IN BESNKB'
      STOP
      END
C
C FOLLOWING CODE RETURNS INTEGRAL OF LOMMEL-WEBER AND BESSEL
C FUNCTIONS OF ORDER 2*N OVER THE INTEGRAL FROM 0. TO Z.
C NOTE: Z= INT*STEP WHERE INT= ANY INTEGER GRATER THAN 1
C
      SUBROUTINE INT(N,Z,WEBINT,BESINT,IERROR)
      REAL B(82)
C     ADJUST DIMENSION OF B IF 2N IS GRATER THAN 40.
      STEP   = .001
      SUMWEB = 0.
      IF (N.EQ.0) THEN
              SUMBES = .5
      ELSE
              SUMBES = 0.
      END IF
      LIMIT = Z/STEP
      DO 100 I= 1, LIMIT-1
      CALL WEB2NX (N, I*STEP, WEB2N, IER)
      IF (IER.NE.0) GO TO 110
      IF ((2*N.GT.10).AND.(I*STEP.LE.1.0)) THEN
          BES2N = 0.
      ELSE
          CALL MMBSJN (I*STEP, 2*N+1, B, IER)
          BES2N  = B(4*N+1)
      END IF
      IF (IER.NE.0) GO TO 110
      SUMWEB = SUMWEB + WEB2N
      SUMBES = SUMBES + BES2N
100   CONTINUE
      CALL WEB2NX (N, Z, WEB2N, IER)
      IF (IER.NE.0) GO TO 110
      IF ((2*N.GT.10).AND.(Z.LE.1.0)) THEN
          BES2N = 0.
      ELSE
          CALL MMBSJN (Z, 2*N+1, B, IER)
          BES2N  = B(4*N+1)
      END IF
      IF (IER.NE.0) GO TO 110
      WEBINT = (SUMWEB + WEB2N/2.)*STEP
      BESINT = (SUMBES + BES2N/2.)*STEP
      RETURN
110   IERROR = 1
      END
C
C THIS CALCULATES LOMMEL-WEBER FUNCTION WEB(X) WITH ORDER 2*N
C
      SUBROUTINE WEB2NX (N,X,WEB2N,IER)
      IER=0
      SUM=0.
      M=0
100   VAL = ((-1.)**M)*((X/2.)**(2*M+1))/(GAMMAA(REAL(M-N)+1.5)*
```

```
     2                                                  GAMMAA(REAL(M+N)+1.5))
      SUM = SUM + VAL
      DIF = ABS(VAL)*100./ABS(SUM)
      IF (M+N.GT.33) GO TO 110
      M = M+1
      IF (DIF.GT.1.0E-3) GO TO 100
      WEB2N = SUM*(-1.)**N
      RETURN
110   IER = 1
      END
C
C THIS DETERMINES GAMMA FUNCTION FOR BOTH POSITIVE & NEGATIVE
C ARGUMENTS
C
      FUNCTION GAMMAA(X)
      IF (X.GT.0.) THEN
            GAMMAA = GAMMA(X)
      ELSE
            PI     = 4.*ATAN(1.)
            Y      = PI*(1.-X)
            GAMMAA = Y/(SIN(Y)*GAMMA(2.-X))
      END IF
      END
```

# Appendix C

# SDIP1 Code Listing

```
C*****************************************************************
C*                                                               *
C*                                                               *
C*                            SDIP1                              *
C*                                                               *
C*                                                               *
C*****************************************************************
C DOUBLE PRECISION
C THIS PROGRAM CALCULATES THE CURRENT INDUCED ON A LOADED OR UNLOADED
C LINEAR DIPOLE WHEN EXPOSED TO AN ELECTROMAGNETIC PULSE.
C ONLY BROADSIDE DETECTION IS CONCERNED. IN THE RECEIVING CASE,
C TERMINAL LOAD IS SIMULATED BY LOADING THE CENTER SPACE-SLOT.
C
C
      REAL*8  NEXT,SELF
      REAL*8  ASEL0,ASEL1,ASEL2,ASINH,F,PSI,PI,C,RHO,AEINC,Y,X,DK
      REAL*8  ANEX0,ANEX1,ANEX2,ANEX3,ASEL3
      REAL*8  AMUT0,AMUT1,AMUT2,AMUT3,AMUT4
      REAL*8  RLOAD,SUM,OTHERS,CONT,TOTAL
      REAL*8  LEN,RAD,EINC,R,DELZ,DELT
      INTEGER RANGE, TOP, LIMIT, LIMIT1, LIMIT2
C     TOP SOULD BE EVEN
      PARAMETER (TOP=375, RANGE=30)
      DIMENSION C(-RANGE:RANGE,-2:TOP), RHO(0:RANGE), AEINC(0:TOP)
      DIMENSION CS(-RANGE:RANGE,-2:TOP)
      DIMENSION AMUT0(2*RANGE),AMUT1(2*RANGE),AMUT2(2*RANGE)
      DIMENSION AMUT3(2*RANGE),AMUT4(2*RANGE)
      DIMENSION VLOAD(TOP), XX(TOP), AEINC2(TOP), Z(RANGE+1,TOP)
      DIMENSION EINC(0:TOP),R(0:RANGE),TIME(TOP), XX1(TOP)
      ASINH(X) = DLOG(X+DSQRT(X**2+1.0))
      F1(Y)      = ASINH(DSQRT(Y**2*PSI**2-1.D0))
      PI  = 4.D0*DATAN(1.D0)
      LEN = 1.D0
      RAD = .5/120.D0
      DELZ= LEN/(2*RANGE+1)
      DELT= DELZ/6.D8
      PSI = DELZ/(2.D0*RAD)
      DO 499 J=1,TOP
      TIME(J) = DELT*J*1.D9
499   CONTINUE
C
C INCIDENT FIELD DEFINITION; X = PULSE WIDTH IN TIME-STEPS
C
      AEINC(0)= 0.D0
      DO 500 I= 1, 60
      EINC(I)= DEXP( -10.D0*(TIME(I)-5./6.)**2)
500   CONTINUE
      DO 510 I= 1,60
510   AEINC(I)= RAD*EINC(I)
      DO 511 I= 61,TOP
511   AEINC(I)= 0.D0
C
C DEFINE LOAD RESISTANCE AND RHO(I)
C
      DO 520 I=0,RANGE
```

```
      R(I)=2.d0*60.D0*7.663/(1.D0 -(DBLE(2*I)/(2.D0*range+1.D0)))
520   CONTINUE
      DO 521 I=0,RANGE
      RHO(I)= R(I)*2.D0*PI*RAD
521   CONTINUE
      RLOAD =100.d0
      RHO(0)= RHO(0)+RLOAD*PI/PSI
C
C INITIALIZE ZERO- AND NEGATIVE- TIME CURRENTS
C
      DO 900 I= -RANGE,RANGE
      C(I,0)  = 0.D0
      C(I,-1) = 0.D0
      C(I,-2) = 0.D0
      CS(I,0) = 0.D0
      CS(I,-1)= 0.D0
900   CS(I,-2)= 0.D0
C
C  GENERATING COEFFICIENTS
C
      ASEL0 = -2.D0*F1(1.D0)/PSI
      ASEL1 = 4.D0*F1(1.D0)/PSI - 2.D0*ASINH(PSI)/PSI
     1        + (1.D0-3.D0*PSI**2)/(PSI**2+1.D0)**1.5D0
      ASEL2 = 2.D0*ASINH(PSI)/PSI - 2.D0*F1(1.D0)/PSI
     1        - (2.D0*PSI**2+1.D0)/(PSI**2+1.D0)**1.5D0
      ASEL3 = -2.D0*PSI**2/(PSI**2+1.D0)**1.5D0
C
      DO 301 K=1,2*RANGE
      DK=DBLE(K)
      AMUT0(K) = -1.D0*F1(2.D0*DK)/PSI + ASINH((2.D0*DK-1.D0)*PSI)/PSI
     1           +.5D0*(2.D0*DK-1.D0)*((4.D0*DK-1.D0)*PSI**2-1.D0)/
     2           ((2.D0*DK-1.D0)**2*PSI**2+1.D0)**1.5D0
      AMUT1(K) = 2.D0*F1(2.D0*DK)/PSI - F1(2.D0*DK+1.D0)/PSI
     1           -ASINH((2.D0*DK-1.D0)*PSI)/PSI
     2           +.5D0*(2.D0*DK-1.D0)*(2.D0*PSI**2+1.D0)/
     3           ((2.D0*DK-1.D0)**2*PSI**2+1.D0)**1.5D0
      AMUT2(K) = 2.D0*F1(2.D0*DK+1.D0)/PSI - F1(2.D0*DK)/PSI
     1           -ASINH((2.D0*DK+1.D0)*PSI)/PSI
     2           +(2.D0*DK-1.D0)*PSI**2/
     3           ((2.D0*DK-1.D0)**2*PSI**2+1.D0)**1.5D0
     4           -.5D0*(2.D0*DK+1.D0)*((4.D0*DK+3.D0)*PSI**2-1.D0)/
     5           ((2.D0*DK+1.D0)**2*PSI**2+1.D0)**1.5D0
      AMUT3(K) = ASINH((2.D0*DK+1.D0)*PSI)/PSI - F1(2.D0*DK+1.D0)/PSI
     1           +(2.D0*DK-1.D0)*PSI**2/
     2           ((2.D0*DK-1.D0)**2*PSI**2+1.D0)**1.5D0
     3           -.5D0*(2.D0*DK+1.D0)*(2.D0*PSI**2+1.D0)/
     4           ((2.D0*DK+1.D0)**2*PSI**2+1.D0)**1.5D0
      AMUT4(K) = -(2.D0*DK+1.D0)*PSI**2/
     1           ((2.D0*DK+1.D0)**2*PSI**2+1.D0)**1.5D0
     2           +(2.D0*DK-1.D0)*PSI**2/
     3           ((2.D0*DK-1.D0)**2*PSI**2+1.D0)**1.5D0
301   CONTINUE
C
C START OF CALCULATIONS: SELECT TIME-SLOT
C
```

```
      DO 1000 J = 1,TOP
C
C DEFINE LIMIT
C
      JJ= J/2
      IF (JJ*2.EQ.J) THEN
          LIMIT = JJ
          ELSE
          LIMIT = (J-1)/2
      END IF
      LIMIT1 = MIN(LIMIT,RANGE-I)
      LIMIT2 = MIN(LIMIT,RANGE+I)
C
C SELECT SPACE-SLOT
C
      DO 1010 I= 0, RANGE
C
C CONTRIBUTION TO FIELD FROM VARIOUS KNOWN CURRENTS ARE FOUND FIRST.
C FROM SELF-SPACE-SLOT CURRENTS:
C
       SELF = ASEL1*C(I,J-1)
       IF (J.GE.3) SELF= SELF+ASEL2*C(I,J-2)
       IF (J.GE.4) SELF= SELF+ASEL3*CS(I,J-3)
C
C FROM OTHER SPACE-SLOTS:
C
       OTHERS = 0.D0
       DO 230 L= 1,I+RANGE
       CONT = 0.D0
       IF (J.GT.(2*L-1)) CONT = CONT+AMUT0(L)*C(I-L,J-2*L+1)
       IF (J.GT.(2*L)  ) CONT = CONT+AMUT1(L)*C(I-L,J-2*L  )
       IF (J.GT.(2*L+1)) CONT = CONT+AMUT2(L)*C(I-L,J-2*L-1)
       IF (J.GE.(2*L+3)) CONT = CONT+AMUT3(L)*C(I-L,J-2*L-2)
       IF (J.GE.(2*L+4)) CONT = CONT+AMUT4(L)*CS(I-L,J-2*L-3)
230    OTHERS= OTHERS+ CONT
       DO 231 L=1,RANGE-I
       CONT = 0.D0
       IF (J.GT.(2*L-1)) CONT = CONT+AMUT0(L)*C(I+L,J-2*L+1)
       IF (J.GT.(2*L))   CONT = CONT+AMUT1(L)*C(I+L,J-2*L)
       IF (J.GT.(2*L+1)) CONT = CONT+AMUT2(L)*C(I+L,J-2*L-1)
       IF (J.GE.(2*L+3)) CONT = CONT+AMUT3(L)*C(I+L,J-2*L-2)
       IF (J.GE.(2*L+4)) CONT = CONT+AMUT4(L)*CS(I+L,J-2*L-3)
231    OTHERS= OTHERS+ CONT
220    TOTAL = SELF+ OTHERS
C
C CONTRIBUTION FROM INCIDENT FIELD IS ADDED.
C
C     IF (I.EQ.0) TOTAL = TOTAL + AEINC(J)/30.D0
      TOTAL = TOTAL + AEINC(J)/30.D0
C
C CALCULATE C(I,J)
C
      C(I,J)= TOTAL/( RHO(I)/(60.D0*PI)-ASEL0 )
      CS(I,J)=CS(I,J-1)+C(I,J)
1010  CONTINUE
```

```
C
C IMAGE CURRENTS
C
      DO 1020 I= 0-RANGE,-1
      CS(I,J)= CS(-I,J)
1020  C(I,J) = C(-I,J)
1000  CONTINUE
      DO 5000 J=1,TOP
      XX(J)     = TIME(J)
      AEINC2(J)= EINC(J)
      VLOAD(J) = C(1,J)*RLOAD/1000.
      DO 5010 I=1,RANGE+1
5010  Z(I,J)    = 1000.*C(I-1,J-1)
5000  CONTINUE
C
C
C PLOTTING
C
      CALL ANYDEV
      CALL PAGE (10.,11.)
      CALL NOBRDR
      CALL AREA2D (6.,8.)
      CALL DUPLX
      CALL HEIGHT(0.28)
      CALL HEADIN('RLOAD=100, R(0)=WK, SDIP1.FOR,RANGE=30$',100,.5,2)
      CALL HEADIN('LEN=1m,LEN/RAD=240,-10 PULSE,STEPS=375$',100,0.5,2)
      CALL XNAME ('Time (ns)$',100)
      CALL YNAME ('Current (mA)$', 100)
      CALL XTICKS(8)
      CALL YTICKS(10)
      CALL YAXANG(0.)
      CALL GRAF(0., 2., 10.,-.1,0.1,.4)
      CALL THKFRM(.02)
      CALL FRAME
      CALL CURVE (XX,VLOAD,375,0)
      CALL YGRAXS(-.5,.5,2.,8.,'EINC',-1,6.,0.)
      CALL DOT
      CALL CURVE (XX,AEINC2,250,0)
      CALL RESET('DOT')
      CALL ENDPL(0)
      CALL PAGE(8.5,11.)
      CALL NOBRDR
      CALL AREA2D(8.,9.)
      CALL HEADIN('RLOAD=100, R(0)=WK, SDIP, RANGE=30$',100,.5,2)
      CALL HEADIN('LEN=1m,LEN/RAD=240, -10 PULSE, STEPS=375$',100,.5,2)
      CALL VOLM3D(1.,1.,1.)
      CALL X3NAME('SPACE (m)$',100)
      CALL Y3NAME('TIME (ns)$',100)
      CALL Z3NAME('CURRENT (mA)$',100)
      CALL XTICKS(5)
      CALL YTICKS(4)
      CALL ZTICKS(8)
      CALL VUANGL(-150.,45.,25.)2. 10.
      CALL GRAF3D(0., .1, .5,0.,2.,20.,-.1,.1,.3)
      CALL SURMAT(Z,1, 31,1,375,0)
```

```
      CALL ENDPL(0)
      CALL DONEPL
      STOP
      END
```

# Appendix D

# SDIP2 Code Listing

```
      PARAMETER (L=20,K=250)
      DOUBLE PRECISION A,B,PSI,PI,DK,S1K,S2K,T1,T2,V,VSUM,C,CSUM
      DOUBLE PRECISION X,T,ASINH,F1,F2,SUM1,SUM2,THETA,S10,S20,RD,RL
      DOUBLE PRECISION ALPHA,VL,LEN,RAD,EINC,R,DELZ,DELT
      DIMENSION T1(0:4*L-1), T2(0:4*L-1), V(0:K),VV(K)
      DIMENSION C(-2*L:2*L,0:K), RD(-2*L:2*L), XX(K), YY(K), XXX(K)
      DIMENSION ALPHA(0:K),VL(K),Z(L+1,K/2),EINC(0:K),R(-2*L:2*L)
      DIMENSION TIME(K)
      ASINH(X) = DLOG( X+DSQRT(X**2+1.D0) )
      F1(T) = DLOG(.5D0*PSI/DSIN(T)+DSQRT(1.D0+(.5D0*PSI/DSIN(T))**2))
     1           *(1.D0-DCOS(T))
      F2(T) = (DSQRT(1.D0+(2.D0*DSIN(T)/PSI)**2) - 2.D0*DSIN(T)/PSI )
     1           *(1.D0-DCOS(T))
      OPEN (UNIT=10,FILE='SDIP2',STATUS='NEW')
      LEN = 1.0D0
      RAD = .5D0/120.d0
      PI  = 4.D0*DATAN(1.D0)
      RL  = 100.D00/(120.D0*PI)
      DO 3300 I=0, 2*L
      R(I) = 2.d0*60.D0*7.663D0/(1.D0 - DBLE(I)/(DBLE(2*L)+1.E-3))
3300  R(-1*I) = R(I)
      DELZ = LEN/(4*L)
      PSI  = DELZ/RAD
      DO 3301 I=-2*L,2*L
3301  RD(I)= R(I)*DELZ/(120.D0*PI)
      DELT = DELZ/3.D8
      DO 3302 J=1,K
3302  TIME(J)  = J*DELT*1.D9
      ALPHA(0) = 0.D0
C DEFINE THE INCIDENT WAVEFORM
C
      DO 1100 I=1,60
      EINC(I) = DEXP(-10.D0*(TIME(I)-TIME(20))**2)
1100  CONTINUE
      V(0) = 0.D0
      DO 1101 I=1,60
      V(I) = EINC(I)*DELZ
1101  CONTINUE
      DO 1102 I=61,K
      V(I) = 0.D0
1102  CONTINUE
C CALCULATION OF T1(0) AND T2(0)
C
      SUM1 = .5D0*F1(PI/2.D0)
      SUM2 = .5D0*F2(PI/2.D0)
      DO 3100 I=1,999
      THETA= DBLE(I)*(PI/2.D3)
      SUM1 = SUM1+ F1(THETA)
      SUM2 = SUM2+ F2(THETA)
3100  CONTINUE
      S10 = 2.D0*PSI*ASINH(2.D0/PSI) + 4.D0*ASINH(PSI/2.D0)
     1      + 4.D0*SUM1*(PI/2.D3)
      S20 = -2.D0*DSQRT( 1.D0+4.D0/PSI**2) - PSI*DLOG(2.D0/PSI +
     1      DSQRT( 1.D0+4.D0/PSI**2) ) +4.D0/PSI
     2      - 4.D0*SUM2*(PI/2.D3)
```

```
      T1(0) = (S10+S20)/(8.D0*PI*PI)
      T2(0) = S20/(-8.D0*PI*PI)
C CALCULATION OF T1(K) AND T2(K)
C
      DO 3000 KK=1,4*L-1
      DK  = DBLE(KK)
      A   = DSQRT(DK*DK*PSI*PSI+1.D0) - DK*PSI
      B   = DSQRT((DK+1.D0)*(DK+1.D0)*PSI*PSI+1.D0) - (DK+1.D0)*PSI
      IF (KK.LE.5) THEN
           S1K = 2.D0*PI*DLOG(A/B)
      ELSE
           S1K  = DLOG((DK+1.D0)/DK)*2.D0*PI
     1           - ((2.D0*DK+1.D0)/(DK**2*(DK+1.D0)**2))*.5D0*PI/PSI**2
     2           + ((DK+1.D0)**2+DK**2)*(2.D0*DK+1.D0)*3.D0*PI
     3             /((DK+1.D0)**4*DK**4*16.D0*PSI**4)
      END IF
      IF (KK.LE.15) THEN
           A   = DSQRT(DK*DK + 1.D0/(PSI*PSI))
           B   = DSQRT((DK+1.D0)*(DK+1.D0) + 1.D0/(PSI*PSI))
           S2K = 2.D0*PI*(A-B)
      ELSE
           S2K = - 1.D0 + 1.D0/(2.D0*DK*(DK+1.D0)*PSI**2)
     1             - (3.D0*DK**2+3.D0*DK+1.D0)
     2               /(8.D0*DK**3*(DK+1.D0)**3*PSI**4)
           S2K = 2.D0*PI*S2K
      END IF
      T1(KK) = ((DK+1.D0)*S1K + S2K)/(8.D0*PI*PI)
      T2(KK) = ( DK*S1K + S2K)/(-8.D0*PI*PI)
3000  CONTINUE
C CALCULATION OF CURRENT
C
      DO 1000 N=1,K
      DO 2000 M=N-2*(N/2), 2*L-N+2*(N/2)
      NN = MIN(N, 2*L-M)
      MM = MIN(N, 2*L+M)
      VSUM = V(N) + .5D0*V(N-MM)
      IF (NN.GT.0) VSUM = VSUM + .5D0*V(N-NN)
      DO 9000 I= 1,NN-1
9000  VSUM = VSUM + V(N-I)
      DO 9010 I= 1,MM-1
9010  VSUM = VSUM + V(N-I)
      CSUM  = 0.D0
      DO 100 I=1, MIN( N-1,2*L-M-1 )
      CSUM  = CSUM + ( T1(I)+T2(I-1) +RD(M+I+1)/12.D0 +RD(M+I)/3.D0
     1                               +RD(M+I-1)/12.D0 ) * C(M+I,N-I)
100   CONTINUE
      DO 105 I=1, MIN( N-1,2*L+M-1 )
      CSUM  = CSUM + ( T1(I)+T2(I-1) +RD(M-I+1)/12.D0 +RD(M-I)/3.D0
     1                               +RD(M-I-1)/12.D0 ) * C(M-I,N-I)
105   CONTINUE
      IF (M.EQ.2*L) THEN
C CURRENT IS ZERO. ALPHA IS CALCULATED.
C
      C(M,N)= 0.D0
      ALPHA(N) = CSUM - VSUM/2.D0 + .5D0*RL*C(0,MAX(N-2*L,0))
```

```
      IF (N.GT.4*L) ALPHA(N) = ALPHA(N) - ALPHA(N-4*L)
      ELSE
C CURRENT IS CALCULATED.
C
          IF (M.EQ.0) THEN
          C(M,N) = (VSUM/2.D0 - CSUM + 2.D0*ALPHA(MAX(N-2*L,0)))
     1                                /( 2.D0*T1(0) + .5D0*RL
     2               + RD(1)/12.D0 + RD(0)/3.D0 + RD(-1)/12.D0 )
          ELSE
          C(M,N) = (VSUM/2.D0 - CSUM - .5D0*RL*C(0,MAX(N-M,0))
     1               + ALPHA(MAX(M+N-2*L,0)) + ALPHA(MAX(N-M-2*L,0)))
     2                 /(2.D0*T1(0) + RD(M+1)/12.D0 + RD(M)/3.D0
     3                              + RD(M-1)/12.D0)
          END IF
      END IF
      C(-M,N) = C(M,N)
2000  CONTINUE
1000  CONTINUE
      DO 4004 I=1,K
4004  VL(I) = C(0,I)*1000./(120.*PI)

      DO 4000 I=1,K/2
      XX(I) = TIME(2*I)
      YY(I) = VL(I*2)
4000  CONTINUE
      DO 4050 I=1,K
      VV(I) = V(I)/DELZ
      XXX(I)= TIME(I)
4050  CONTINUE
      DO 4005 I=1,L+1
      DO 4005 J=1,K/2
      Z(I,J)= 1000.*SNGL(C(2*(I-1),2*(J-1)))/(120.*PI)
4005  CONTINUE
      DO 9999 i=1,125
9999  WRITE (10,9998) XX(I),YY(I)
9998  FORMAT(2X,E13.5,2X,E13.5)
C PLOTTING
C
      CALL ANYDEV
      CALL PAGE (9.5,11.)
      CALL NOBRDR
      CALL AREA2D (6.,8.)
      CALL DUPLX
      CALL HEIGHT(0.28)
      CALL HEADIN('LEN=1m, LEN/RAD=240, -10 pulse$',100,.5,2)
      CALL HEADIN('100 Ohm, R(0)=WK, LIU3D, L=20,K=250$',100,0.5,2)
      CALL XNAME ('Time (ns)$',100)
      CALL YNAME ('Current (mA)$', 100)
      CALL XTICKS(4)
      CALL YTICKS(8)
      CALL YAXANG(0.)
      CALL GRAF(0.,2.,10.,-.1,.1,.4)
      CALL THKFRM(.02)
      CALL FRAME
      CALL CURVE (XX,YY,125,0)
```

```
call ygraxs(-.5,.5,2.,8.,'Einc',-1,6.,0.)
call dot
CALL CURVE (XXX,VV,250,0)
CALL RESET('DOT')
CALL ENDPL(0)
CALL PAGE(9.5,11.)
CALL NOBRDR
CALL AREA2D(8.,9.)
CALL HEADIN('100 Ohm, r(0)=WK, LIU3D, L=20,K=250$',100,.5,2)
CALL HEADIN('LEN=1m, LEN/RAD=240, -10 pulse$',100,.5,2)
CALL VOLM3D(1.,1.,1.)
CALL X3NAME('SPACE (m)$',100)
CALL Y3NAME('TIME (ns)$',100)
CALL Z3NAME('CURRENT (mA)$',100)
CALL XTICKS(4)
CALL YTICKS(4)
CALL ZTICKS(5)
CALL VUANGL(-150.,45.,25.)
CALL GRAF3D(0., .1, .5,0.,2.,10.,-.1,.1,.3)
CALL SURMAT(Z,1, 21,1,125,0)
CALL ENDPL(0)
CALL DONEPL
STOP
END
```

# Appendix E

# VDIP Code Listing

```
C
C  ************************************************************
C  *                                                          *
C  *                          VDIP                            *
C  *                                                          *
C  ************************************************************
C
C  -TO ANALYZE V-DIPOLES/MONOPOLES IN TIME DOMAIN.
C  -CALCULATES CURRENTS AND CHARGES INDUCED IN A RESISTIVELY
C   LOADED OR UNLOADED V-ANTENNA.
C  -EXCITATION IS AN UNIFORM FIELD WITH ARBITRARY TIME VARIATION,
C   INCIDENT ALONG BROADSIDE DIRECTION -or- A VOLTAGE SOURCE WITH
C   ARBITRARY TIME VARIATION, CONNECTED TO TERMINALS.
C  -SOURCE WAVEFORM IS SET BY THE SUBROUTINE `PULSE'.
C
C  NOTES: GRAPHING SECTION AT THE END NEEDS `DISSPLA' PACKAGE.
C         NO EXTERNAL SUBROUTINES ARE NEEDED FOR COMPUTING SECTION.
C
C  LEN    = LENGTH OF THE V-ANTENNA ALONG (EACH) WIRE (METERS)
C  RAD    = RADIUS OF THE WIRE (METERS)
C  LENGTH= NUMBER OF SEGMENTS ON (EACH) WIRE
C  SEG    = SEGMENT LENGTH (METERS)
C  SPACE = SPACE DIMENSION (CENTIMETERS)
C  PSI    = SEGMENT LENGTH TO DIAMETER RATIO
C  DELT   = TIME STEP (SECONDS)
C  TIME   = TIME (NANOSECONDS)
C  STEPS = NUMBER OF TIME STEPS TO GO
C  PULSE = INCIDENT ELECTRIC FIELD (VOLTS/METER)
C  AEINC = RAD * INCIDENT ELECTRIC FIELD (VOLTS)
C  THETA = V-ANGLE OF THE DIPOLE (RADIANS), OR
C        = 2 * WEDGE ANGLE OF THE MONOPOLE (RADIANS)
C  R(I)   = SURFACE RESISTANCE ON(I)TH SEGMENT (OHMS/SQUARE)
C  RO     = SURFACE RESISTANCE AT THE DRIVING POINT (OHMS/SQUARE)
C  RL     = HALF THE TERMINAL RESISTANCE OF DIPOLE IN (OHMS), OR
C        = TERMINAL RESISTANCE OF MONOPOLE (OHMS).
C  VO(J) = TERMINAL VOLTAGE OF MONOPOLE (VOLTS), OR
C        = HALF THE TERMINAL VOLTAGE OF DIPOLE (VOLTS)
C  QO(J) = NORMALIZED TIME-INTEGRAL OF TERMINAL CURRENT (AMPERES).
C        = ACTUAL TIME-INTEGRAL/DELT
C
C
C  WRITTEN BY:  KARU P. ESSELLE
C  **********   ***************
C
C               LABORATORY FOR ELECTROMAGNETICS AND MICROWAVES
C               DEPARTMENT OF ELECTRICAL ENGINEERING
C               UNIVERSITY OF OTTAWA
C               OTTAWA, ONTARIO K1N 6N5
C               CANADA
C
C  COPYRIGHT:   KARU P. ESSELLE
C               JUNE, 1990.
C
      INTEGER STEPS,LENGTH
      PARAMETER (STEPS=300,LENGTH=60)
```

```
      DIMENSION R(LENGTH),AMUT0(LENGTH),AMUT1(LENGTH),AMUT2(LENGTH)
      DIMENSION AMUT3(LENGTH),AMUT4A(LENGTH),AMUT4B(LENGTH)
      DIMENSION BCHRG(LENGTH,0:LENGTH)
      DIMENSION C(LENGTH,0:STEPS),Q(LENGTH,0:STEPS),TAU(0:LENGTH)
      DIMENSION M(0:LENGTH),CL(0:LENGTH),CR(0:LENGTH),SIGMA(0:LENGTH)
      DIMENSION RHO(LENGTH,0:LENGTH),LPEAK(LENGTH),RHOPK(LENGTH)
      DIMENSION EPSPK(LENGTH),Q0(0:STEPS),Q1(0:STEPS)
      DOUBLE PRECISION ASINH,X,PSI,PI,AEINC,R,ASEL0,ASEL1,ASEL2,ASEL3,
     1       AMUT0,AMUT1,AMUT2,AMUT3,AMUT4A,AMUT4B,F1,Y,DK,THETA,
     2       BCHRG,TOTAL,C,Q,RHO,TAU,CL,CR,SIGMA,RHOPK,EPSPK,TAUPK,
     3       EXTRA,CONT,CONT1,CONT2,CA,CA1,CA2,CB,CC,EPSA,EPSB,EPSC,
     4       RHOA,RHOB,RHOC,U,V,W1,W2,CD,EPSD,RHOD,CC1,CC2,RL,R0
     5       LEN,RAD,SEG,DELT,Q0
      INTEGER M,LPEAK,MPEAK,MDIF,I,J,L,MMAX,MB,MC,LPK
      REAL XX(STEPS),EI(STEPS),Y1(STEPS),Y2(STEPS),Y3(STEPS),Y4(STEPS),
     1       Y5(STEPS), Z1(LENGTH,STEPS), Z2(LENGTH,STEPS),V0(STEPS),
     2       TIME(STEPS),SPACE(LENGTH)
      COMMON I,L,THETA,PSI
      ASINH(X) = DLOG(X+DSQRT(X**2+1.D0))
      F1(Y) = ASINH(DSQRT(Y**2*PSI**2-1.D0))
      LEN   = 30.D-2
      RAD   = .5D-3
      SEG   = LEN/LENGTH
      PSI   = SEG/(2.D0*RAD)
      DELT  = SEG/6.D8
      PI    = 4.D0*DATAN(1.D0)
      THETA = 30.D0*(PI/180.D0)
      RL    = 0.D0
      R0    = 2.2D0*PI
      open (unit=10,file='vdip',status='new')
C
C  INITIATE CURRENT AND CHARGE AT T=0
C
      DO 100 I=1,LENGTH
      C(I,0) = 0.D0
      Q(I,0) = 0.D0
100   CONTINUE
      Q0(0)  = 0.D0
      Q1(0)  = 0.D0
C
C  LOADING PROFILE
C
      DO 200 I=1,LENGTH
      R(I) = R0/(1.D0-(2.D0*I-1.D0)/(2.D0*LENGTH))
200   CONTINUE
C
C  GENERATING COEFFICIENTS
C
      ASEL0 = -2.D0*F1(1.D0)/PSI
      ASEL1 = 4.D0*F1(1.D0)/PSI - 2.D0*ASINH(PSI)/PSI
     1        + (1.D0-3.D0*PSI**2)/(PSI**2+1.D0)**1.5D0
      ASEL2 = 2.D0*ASINH(PSI)/PSI - 2.D0*F1(1.D0)/PSI
     1        - (2.D0*PSI**2+1.D0)/(PSI**2+1.D0)**1.5D0
      ASEL3 = -1.D0*PSI**2/(PSI**2+1.D0)**1.5D0
C
```

```
      DO 300 K=1,LENGTH
      DK=DBLE(K)
      AMUT0(K) = -1.D0*F1(2.D0*DK)/PSI + ASINH((2.D0*DK-1.D0)*PSI)/PSI
     1           +.5D0*(2.D0*DK-1.D0)*((4.D0*DK-1.D0)*PSI**2-1.D0)/
     2           ((2.D0*DK-1.D0)**2*PSI**2+1.D0)**1.5D0
      AMUT1(K) = 2.D0*F1(2.D0*DK)/PSI - F1(2.D0*DK+1.D0)/PSI
     1           -ASINH((2.D0*DK-1.D0)*PSI)/PSI
     2           +.5D0*(2.D0*DK-1.D0)*(2.D0*PSI**2+1.D0)/
     3           ((2.D0*DK-1.D0)**2*PSI**2+1.D0)**1.5D0
      AMUT2(K) = 2.D0*F1(2.D0*DK+1.D0)/PSI - F1(2.D0*DK)/PSI
     1           -ASINH((2.D0*DK+1.D0)*PSI)/PSI
c     2            +(2.D0*DK-1.D0)*PSI**2/
c     3            ((2.D0*DK-1.D0)**2*PSI**2+1.D0)**1.5D0
     4           -.5D0*(2.D0*DK+1.D0)*((4.D0*DK+3.D0)*PSI**2-1.D0)/
     5           ((2.D0*DK+1.D0)**2*PSI**2+1.D0)**1.5D0
      AMUT3(K) = ASINH((2.D0*DK+1.D0)*PSI)/PSI - F1(2.D0*DK+1.D0)/PSI
c     1            +(2.D0*DK-1.D0)*PSI**2/
c     2            ((2.D0*DK-1.D0)**2*PSI**2+1.D0)**1.5D0
     3           -.5D0*(2.D0*DK+1.D0)*(2.D0*PSI**2+1.D0)/
     4           ((2.D0*DK+1.D0)**2*PSI**2+1.D0)**1.5D0
      AMUT4A(K)= (2.D0*DK+1.D0)*PSI**2/
     1           ((2.D0*DK+1.D0)**2*PSI**2+1.D0)**1.5D0
      AMUT4B(K)= -1.D0*(2.D0*DK+1.D0)*PSI**2/
     1           ((2.D0*DK+1.D0)**2*PSI**2+1.D0)**1.5D0
300   CONTINUE
C
      DO 400 I=1,LENGTH
      LPEAK(I)= INT((I-.5D0)*DCOS(THETA)+.5D0*DSIN(THETA)/PSI)+1
      RHOPK(I)= (2*I-1)*DSIN(THETA)-DCOS(THETA)/PSI
      EPSPK(I)= (2*I-1)*DCOS(THETA)+DSIN(THETA)/PSI-2*LPEAK(I)+1
      IF (ABS(EPSPK(I)).GT.1.D0) THEN
              WRITE (*,*) 'ERROR #1'
              GO TO 2000
              END IF
      IF ((RHOPK(I).LT.1.D0).AND.(I.NE.1)) THEN
              WRITE (*,*) 'RHOPK',I,' LESS THAN 1.'
              STOP
              END IF
      DO 400 L=0,LENGTH
      RHO(I,L)= DSQRT(4*L**2+(2*I-1)**2-4*L*(2*I-1)*DCOS(THETA)
     1                -4*L*DSIN(THETA)/PSI+1/PSI**2)
      BCHRG(I,L)= (2*I-1-2*L*DCOS(THETA))/(PSI*RHO(I,L)**3)
      IF (RHO(I,L).LT.1.D0) THEN
              WRITE (*,*) 'RHO ',I,',',L,' LESS THAN 1.'
              STOP
              END IF
400   CONTINUE
C
C  START OF CURRENT CALCULATIONS
C
      DO 500 J=1,STEPS
      WRITE(*,*) J
      DO 600 I=1,LENGTH
      EXTRA = 0.D0
C
```

```
C  CONTRIBUTION FROM TOP WIRE:
C  FROM (I)TH SEGMENT CURRENT AND (I)TH BOUNDARY CHARGE
C
      TOTAL = ASEL1*C(I,J-1)
      IF (I.EQ.1) TOTAL = TOTAL+C(I,J-1)*.5D0*(2.D0*PSI-
     1   SQRT(PSI**2+1.D0))**2/(PSI**2+1.D0)**1.5D0
      IF (J.GT.2) TOTAL = TOTAL+ASEL2*C(I,J-2)
      IF ((J.GT.2).AND.(I.EQ.1)) TOTAL = TOTAL+C(I,J-2)*
     1   PSI*(PSI-.5D0*(SQRT(PSI**2+1.D0)-PSI)**2)/
     2   (PSI**2+1.D0)**1.5D0
      IF (J.GT.3) TOTAL = TOTAL+ASEL3*Q(I,J-3)
      IF ((J.GT.3).AND.(I.NE.1)) TOTAL = TOTAL-ASEL3*Q(I-1,J-3)
C
C  CONTRIBUTIONS FROM OTHER TOP WIRE CURRENTS AND CHARGES
C
      DO 700 L=1,LENGTH-I
      IF ((J-2*L+1).GT.0) TOTAL = TOTAL+ AMUT0(L)*C(I+L,J-2*L+1)
      IF ((J-2*L  ).GT.0) TOTAL = TOTAL+ AMUT1(L)*C(I+L,J-2*L)
      IF ((J-2*L-1).GT.0) TOTAL = TOTAL+ AMUT2(L)*C(I+L,J-2*L-1)
      IF ((J-2*L-2).GT.0) TOTAL = TOTAL+ AMUT3(L)*C(I+L,J-2*L-2)
      IF ((J-2*L-3).GT.0) TOTAL = TOTAL+ AMUT4B(L)*Q(I+L,J-2*L-3)
700   CONTINUE
      DO 800 L=1,I-1
      IF ((J-2*L+1).GT.0) TOTAL = TOTAL+ AMUT0(L)*C(I-L,J-2*L+1)
      IF ((J-2*L  ).GT.0) TOTAL = TOTAL+ AMUT1(L)*C(I-L,J-2*L)
      IF ((J-2*L-1).GT.0) THEN
                          TOTAL = TOTAL+ AMUT2(L)*C(I-L,J-2*L-1)
         IF (L.EQ.(I-1))  TOTAL = TOTAL+ C(I-L,J-2*L-1)*
     1   .5D0*(2.D0*L+1.D0)*((2.D0*L+2.D0)*PSI-SQRT((2.D0*L+1.D0)**2
     2   *PSI**2+1.D0))**2/((2.D0*L+1.D0)**2*PSI**2+1.D0)**1.5D0
      END IF
      IF ((J-2*L-2).GT.0) THEN
                          TOTAL = TOTAL+ AMUT3(L)*C(I-L,J-2*L-2)
         IF (L.EQ.(I-1))  TOTAL = TOTAL+ C(I-L,J-2*L-2)*
     1   (2.D0*L+1.D0)*(PSI**2-.5D0*(SQRT((2.D0*L+1.D0)**2*PSI**2+1.D0)
     2   -PSI*(2.D0*L+1.D0))**2)/((2.D0*L+1.D0)**2*PSI**2+1.D0)**1.5D0
      END IF
      IF (((J-2*L-3).GT.0).AND.(L.NE.(I-1)))
     1                    TOTAL = TOTAL+ AMUT4A(L)*Q(I-L-1,J-2*L-3)
800   CONTINUE
C
C  TO DETERMINE CONTRIBUTIONS FROM BOTTOM WIRE CURRENTS AND CHARGES,
C  TAU,M,CR,CL AND SIGMA FOR EACH BOUNDARY ARE CALCULATED FIRST.
C
      DO 900 L=0,LENGTH
      TAU(L) = J-RHO(I,L)
      IF (TAU(L).GE.0.D0) THEN
        M(L) = INT(TAU(L))
      ELSE
        M(L) = INT(TAU(L))-1
      END IF
      IF ((TAU(L).LE.0.D0).OR.(L.EQ.LENGTH)) THEN
        CR(L) = 0.D0
      ELSE
        CR(L) = C(L+1,M(L))*(M(L)+1-TAU(L))
```

```
     1         +C(L+1,M(L)+1)*(TAU(L)-M(L))
      END IF
      IF ((TAU(L).LE.0.D0).OR.(L.EQ.0)) THEN
        CL(L) = 0.D0
      ELSE
        CL(L) = C(L,M(L))*(M(L)+1-TAU(L))
     1         +C(L,M(L)+1)*(TAU(L)-M(L))
      END IF
      IF ((TAU(L).LE.0.D0).OR.(L.EQ.0)) THEN
        SIGMA(L) = 0.D0
      ELSE IF (L.EQ.LENGTH) THEN
        SIGMA(L) = -Q(L,M(L))
     1             -.5D0*C(L,M(L)+1)*(TAU(L)-M(L))**2
     2             +.5D0*C(L,M(L))*(M(L)+1-TAU(L))**2
      ELSE
        SIGMA(L) = -Q(L,M(L))
     1             -.5D0*(C(L,M(L)+1)-C(L+1,M(L)+1))*(TAU(L)-M(L))**2
     2             +.5D0*(C(L,M(L))-C(L+1,M(L)))*(M(L)+1-TAU(L))**2
      END IF
900   CONTINUE
C
C  START OF THE CALCULATION OF CONTRIBUTIONS FROM BOTTOM WIRE
C  CURRENTS AND CHARGES (EXCEPT THOSE AT "LPEAK(I)" SEGMENT AND
C  BOUNDARY.
C
      DO 1000 L=1,LENGTH
      IF (L.NE.LPEAK(I)) THEN
C
      MDIF = ABS(M(L)-M(L-1))
      IF (MDIF.EQ.0) THEN
C
C  MODULE #1
C
      EPSA = -1.D0
      EPSB = 1.D0
      CA   = CR(L-1)
      CB   = CL(L)
      RHOA = RHO(I,L-1)
      RHOB = RHO(I,L)
      CALL BCRNT(CA,CB,EPSA,EPSB,RHOA,RHOB,CONT)
      TOTAL= TOTAL+CONT+BCHRG(I,L)*SIGMA(L)
C
C  END OF MODULE #1
C
      END IF
      IF (MDIF.EQ.1) THEN
C
C  MODULE #2
C
      EPSA = -1.D0
      MMAX = MAX(M(L),M(L-1))
         U = (2*L-1)-(2*I-1)*DCOS(THETA)-DSIN(THETA)/PSI
         V = (2*L-1)**2+(2*I-1)**2-2*(2*L-1)*(2*I-1)*DCOS(THETA)
     1       -2.D0*(2*L-1)*DSIN(THETA)/PSI+1.D0/PSI**2-(J-MMAX)**2
        W1 = -U+DSQRT(U**2-V)
```

```
          W2 = -U-DSQRT(U**2-V)
        IF (DABS(W1).LE.1.D0) EPSB=W1
        IF (DABS(W2).LE.1.D0) EPSB=W2
        IF ((DABS(W1).LE.1.D0).AND.(DABS(W2).LE.1.D0)) THEN
              WRITE (*,*) 'ERROR #2'
              GO TO 2000
              END IF
        IF ((DABS(W1).GT.1.D0).AND.(DABS(W2).GT.1.D0)) THEN
              WRITE (*,*) 'ERROR #3'
              GO TO 2000
              END IF
        EPSC = 1.D0
C
        CA = CR(L-1)
        IF (MMAX.GT.0) THEN
        CB = C(L,MMAX)
        ELSE
        CB = 0.D0
        END IF
        CC = CL(L)
C
        RHOA = RHO(I,L-1)
        RHOB = J-MMAX
        RHOC = RHO(I,L)
        CALL BCRNT(CA,CB,EPSA,EPSB,RHOA,RHOB,CONT)
        TOTAL= TOTAL+CONT
        CALL BCRNT(CB,CC,EPSB,EPSC,RHOB,RHOC,CONT)
        TOTAL= TOTAL+CONT+BCHRG(I,L)*SIGMA(L)
C
C  END OF MODULE #2
C
      END IF
      IF (MDIF.EQ.2) THEN
C
C  MODULE #3
C
      EPSA = -1.D0
      IF (M(L).LT.M(L-1)) THEN
        MB = M(L)+2
        MC = M(L)+1
      ELSE
        MB = M(L-1)+1
        MC = M(L-1)+2
      END IF
         U = (2*L-1)-(2*I-1)*DCOS(THETA)-DSIN(THETA)/PSI
         V = (2*L-1)**2+(2*I-1)**2-2*(2*L-1)*(2*I-1)*DCOS(THETA)
     1       -2.D0*(2*L-1)*DSIN(THETA)/PSI+1.D0/PSI**2-(J-MB)**2
        W1 = -U+DSQRT(U**2-V)
        W2 = -U-DSQRT(U**2-V)
      IF (DABS(W1).LE.1.D0) EPSB=W1
      IF (DABS(W2).LE.1.D0) EPSB=W2
      IF ((DABS(W1).LE.1.D0).AND.(DABS(W2).LE.1.D0)) THEN
            WRITE (*,*) 'ERROR #3'
            GO TO 2000
```

```
            END IF
       IF ((DABS(W1).GT.1.D0).AND.(DABS(W2).GT.1.D0)) THEN
            WRITE (*,*) 'ERROR #4'
            GO TO 2000
            END IF
          V = (2*L-1)**2+(2*I-1)**2-2*(2*L-1)*(2*I-1)*DCOS(THETA)
     1       -2.D0*(2*L-1)*DSIN(THETA)/PSI+1.D0/PSI**2-(J-MC)**2
        W1 = -U+DSQRT(U**2-V)
        W2 = -U-DSQRT(U**2-V)
       IF (DABS(W1).LE.1.D0) EPSC=W1
       IF (DABS(W2).LE.1.D0) EPSC=W2
       IF ((DABS(W1).LE.1.D0).AND.(DABS(W2).LE.1.D0)) THEN
            WRITE (*,*) 'ERROR #5'
            GO TO 2000
            END IF
       IF ((DABS(W1).GT.1.D0).AND.(DABS(W2).GT.1.D0)) THEN
            WRITE (*,*) 'ERROR #6'
            GO TO 2000
            END IF
       EPSD = 1.D0
C
       CA = CR(L-1)
       IF (MB.GT.0) THEN
       CB = C(L,MB)
       ELSE
       CB = 0.D0
       END IF
       IF (MC.GT.0) THEN
       CC = C(L,MC)
       ELSE
       CC = 0.D0
       END IF
       CD = CL(L)
C
       RHOA = RHO(I,L-1)
       RHOB = J-MB
       RHOC = J-MC
       RHOD = RHO(I,L)
C
       CALL BCRNT(CA,CB,EPSA,EPSB,RHOA,RHOB,CONT)
       TOTAL= TOTAL+CONT
       CALL BCRNT(CB,CC,EPSB,EPSC,RHOB,RHOC,CONT)
       TOTAL= TOTAL+CONT
       CALL BCRNT(CC,CD,EPSC,EPSD,RHOC,RHOD,CONT)
       TOTAL= TOTAL+CONT+BCHRG(I,L)*SIGMA(L)
C
C  END OF MODULE #3
C
      END IF
      IF (MDIF.GE.3) THEN
            WRITE (*,*) I,J,L,M(L),M(L-1),MDIF
            WRITE (*,*) 'ERROR #7'
            GO TO 2000
```

```
                END IF
        ELSE
C
C  FINALLY, CONTRIBUTIONS FROM THE "LPEAK(I)" SEGMENT CURRENT AND
C  "LPEAK(I)" BOUNDARY CHARGE ARE CALCULATED AND ADDED TO TOTAL.
C
1100   TAUPK= J-RHOPK(I)
       IF (TAUPK.GE.0.D0) THEN
         MPEAK= INT(TAUPK)
       ELSE
         MPEAK= INT(TAUPK)-1
       END IF
C
C  CONTRIBUTION FROM PART-1 OF "LPEAK(I)" SEGMENT
C
       MDIF= MPEAK - M(LPEAK(I))
       IF (MDIF.EQ.0) THEN
C
C  MODULE #1A
C
       LPK = LPEAK(I)
       EPSA= EPSPK(I)
       EPSB= 1.D0
       IF (TAUPK.LE.0.D0) THEN
         CA= 0.D0
       ELSE
         CA= C(LPK,MPEAK)*(MPEAK+1-TAUPK)
     1      +C(LPK,MPEAK+1)*(TAUPK-MPEAK)
       END IF
       CB  = CL(LPK)
       RHOA= RHOPK(I)
       RHOB= RHO(I,LPK)
       CALL BCRNT(CA,CB,EPSA,EPSB,RHOA,RHOB,CONT)
       TOTAL = TOTAL+CONT+BCHRG(I,LPK)*SIGMA(LPK)
C
C  END OF MODULE #1A
C
       END IF
       IF (MDIF.EQ.1) THEN
C
C  MODULE #2A
C
       LPK  = LPEAK(I)
       EPSA = EPSPK(I)
          U = (2*LPK-1)-(2*I-1)*DCOS(THETA)-DSIN(THETA)/PSI
          V = (2*LPK-1)**2+(2*I-1)**2-2*(2*LPK-1)*(2*I-1)*DCOS(THETA)
     1       -2.D0*(2*LPK-1)*DSIN(THETA)/PSI+1.D0/PSI**2-(J-MPEAK)**2
       EPSB = -U+DSQRT(U**2-V)
       IF ((EPSB.LE.EPSA).OR.(EPSB.GE.1.D0)) THEN
              WRITE (*,*) 'ERROR #8'
              GO TO 2000
              END IF
       EPSC = 1.D0
C
```

```
      IF (TAUPK.LE.0.D0) THEN
        CA1= 0.D0
        CA2= 0.D0
      ELSE
        CA1= C(LPK,MPEAK)*(MPEAK+1-TAUPK)
        CA2= DBLE(TAUPK-MPEAK)
      END IF
      IF (MPEAK.GT.0) THEN
        CB = C(LPK,MPEAK)
      ELSE
        CB = 0.D0
      END IF
      CC   = CL(LPK)
C
      RHOA = RHOPK(I)
      RHOB = J-MPEAK
      RHOC = RHO(I,LPK)
      CALL BCRNT(CA1,CB,  EPSA,EPSB,RHOA,RHOB,CONT1)
      CALL BCRNT(CA2,0.D0,EPSA,EPSB,RHOA,RHOB,CONT2)
      IF (I.NE.1) THEN
        TOTAL= TOTAL+CONT1+CONT2*C(LPK,MPEAK+1)
      ELSE
        TOTAL= TOTAL+CONT1
        EXTRA= CONT2
      END IF
      CALL BCRNT(CB,CC,EPSB,EPSC,RHOB,RHOC,CONT)
      TOTAL= TOTAL+CONT+BCHRG(I,LPK)*SIGMA(LPK)
C
C  END OF MODULE #2A
C
      END IF
C     IF (MDIF.GE.2) GO TO 2010
      IF ((MDIF.GE.2).AND.(M(LPEAK(I))).GE.0) THEN
            WRITE(*,*) I,J,L
            GO TO 2010
      END IF
      IF (MDIF.LT.0) THEN
            WRITE (*,*) 'ERROR #8'
            GO TO 2000
            END IF
C
C  CONTRIBUTION FROM PART-2 OF "LPEAK(I)" SEGMENT
C
      MDIF= MPEAK - M(LPEAK(I)-1)
      IF (MDIF.EQ.0) THEN
C
C  MODULE #1B
C
      LPK = LPEAK(I)
      EPSB= EPSPK(I)
      EPSA= -1.D0
      IF (TAUPK.LE.0.D0) THEN
        CB= 0.D0
      ELSE
        CB= C(LPK,MPEAK)*(MPEAK+1-TAUPK)
```

```
     1     +C(LPK,MPEAK+1)*(TAUPK-MPEAK)
      END IF
      CA  = CR(LPK-1)
      RHOB= RHOPK(I)
      RHOA= RHO(I,LPK-1)
      CALL BCRNT(CA,CB,EPSA,EPSB,RHOA,RHOB,CONT)
      TOTAL = TOTAL+CONT
C
C  END OF MODULE #1B
C
      END IF
      IF (MDIF.EQ.1) THEN
C
C  MODULE #2B
C
      LPK  = LPEAK(I)
      EPSA = -1.D0
      EPSC = EPSPK(I)
         U = (2*LPK-1)-(2*I-1)*DCOS(THETA)-DSIN(THETA)/PSI
         V = (2*LPK-1)**2+(2*I-1)**2-2*(2*LPK-1)*(2*I-1)*DCOS(THETA)
     1       -2.D0*(2*LPK-1)*DSIN(THETA)/PSI+1.D0/PSI**2-(J-MPEAK)**2
      EPSB = -U-DSQRT(U**2-V)
      IF ((EPSB.LE.-1.D0).OR.(EPSB.GE.EPSC)) THEN
             WRITE (*,*) 'ERROR #9'
             GO TO 2000
             END IF
C
      CA   = CR(LPK-1)
      IF (MPEAK.GT.0) THEN
        CB = C(LPK,MPEAK)
      ELSE
        CB = 0.D0
      END IF
      IF (TAUPK.LE.0.D0) THEN
        CC1= 0.D0
        CC2= 0.D0
      ELSE
        CC1= C(LPK,MPEAK)*(MPEAK+1-TAUPK)
        CC2= DBLE(TAUPK-MPEAK)
      END IF
C
      RHOA = RHO(I,LPK-1)
      RHOB = J-MPEAK
      RHOC = RHOPK(I)
      CALL BCRNT(CA,CB,EPSA,EPSB,RHOA,RHOB,CONT)
      TOTAL= TOTAL+CONT
      CALL BCRNT(CB,  CC1,EPSB,EPSC,RHOB,RHOC,CONT1)
      CALL BCRNT(0.D0,CC2,EPSB,EPSC,RHOB,RHOC,CONT2)
      IF (I.NE.1) THEN
        TOTAL= TOTAL+CONT1+CONT2*C(LPK,MPEAK+1)
      ELSE
        TOTAL= TOTAL+CONT1
        EXTRA= EXTRA+CONT2
      END IF
C
```

```
C  END OF MODULE #2B
C
      END IF
      IF ((MDIF.GE.2).AND.(M(LPEAK(I)-1)).GT.0) GO TO 2010
      IF (MDIF.LT.0) THEN
            WRITE (*,*) 'ERROR #10'
            GO TO 2000
            END IF
      END IF
1000  CONTINUE
C
C  ADD CONTRIBUTION FROM THE INCIDENT FIELD
c
      AEINC = RAD*DSIN(THETA/2.D0)*
     1        PULSE(J+(2*I-2*LENGTH-1)*DCOS(THETA/2.D0),THETA,LENGTH)
      TOTAL = TOTAL+ AEINC/30.d0
C
C  CALCULATE CURRENT
C
      IF (I.EQ.1) THEN
         C(1,J)= TOTAL/(RL/(60.D0*PSI)+R(1)/(60.D0*PI)-ASELO-EXTRA)
      ELSE
        C(I,J)= TOTAL/(R(I)/(60.D0*PI)-ASELO)
      END IF
600   CONTINUE
C
C  CALCULATE CHARGE
C
      DO 1200 I=1,LENGTH-1
      Q(I,J)= Q(I,J-1)+C(I,J)-C(I+1,J)
1200  CONTINUE
      Q(LENGTH,J)= Q(LENGTH,J-1)+C(LENGTH,J)
      QO(J)      = QO(J-1)+C(1,J)
C
C  OUTPUT VOLTAGE
C
      VO(J) = 1000.*SNGL(C(1,J)*RL)
500   CONTINUE
C
C
C DISSPLA PLOTTING ROUTINE
C
      DO 4098 J=1,STEPS
      XX(J) = J
      TIME(J) = J*DELT*1.E9
      EI(J) = SNGL(PULSE(DBLE(J)-(2*LENGTH-1)*DCOS(THETA/2.D0)
     1                  ,THETA,LENGTH))
      Y1(J) = C(1,J)*1000.
      Y2(J) = C(LENGTH/4,J)*1000.
      Y3(J) = C(LENGTH/2,J)*1000.
      Y4(J) = C(LENGTH*3/4,J)*1000.
      Y5(J) = C(LENGTH,J)*1000.
      WRITE(10,19) TIME(J), EI(J), 1000.*C(1,J)
4098  CONTINUE
19    FORMAT(2X,E16.8,2X,E16.8,2X,E16.8)
```

```
      WRITE (10,*)'STEPS =',STEPS
      WRITE (10,*)'LENGTH=',LENGTH
      WRITE (10,*)'LEN   =',LEN
      WRITE (10,*)'RAD   =',RAD
      WRITE (10,*)'THETA =',THETA
      WRITE (10,*)'SWITCH=',SWITCH
      WRITE (10,*)'R0    =',R0
      WRITE (10,*)'RL    =',RL
      WRITE (10,*)'CAP   =',CAP
      WRITE (10,*)'RP    =',RP
      DO 4099 I=1,LENGTH
      DO 4099 J=1,STEPS
      Z1(I,J)= SNGL(C(I,J))
      Z2(I,J)= SNGL(Q(I,J))*DELT
4099  CONTINUE
C PLOTTING
C
      CALL ANYDEV
      CALL PAGE (9.5,11.)
      CALL NOBRDR
      CALL AREA2D (6.,8.)
      CALL DUPLX
      CALL HEIGHT(0.28)
      CALL HEADIN('9.6 GHz sinc incident pulse$',100,.5,4)
      CALL HEADIN('30-cm, .5-mm, V-antenna$',100,0.5,4)
      CALL HEADIN('Tv=30, R0=2.2*pi - WK, LENGTH=60$',100,.5,4)
      CALL HEADIN('RL=0 Ohm, NO CAP, NO RP, TRANS$',100,.5,4)
      CALL XNAME ('Time (ns)$',100)
      CALL YNAME ('1000*C (Amps)$', 100)
      CALL XTICKS(10)
      CALL YTICKS(8)
      CALL XINTAX
      CALL YAXANG(0.)
      CALL GRAF(0.,.5,2.5,-.08,.04,.24)
      CALL THKFRM(.02)
      CALL FRAME
      CALL CURVE (TIME,v0,300,0)
      call ygraxs(-.4,.2,1.2,8.,' ',-1,6.,0.)
      call dot
      CALL CURVE (TIME,EI,300,0)
      call reset('dot')
      CALL ENDPL(0)
      CALL PAGE(9.5,11.)
      CALL NOBRDR
      CALL AREA2D(8.,9.)
      CALL HEADIN('9.6 GHz sinc incident pulse$',100,.5,4)
      CALL HEADIN('30-cm, .5-mm, V-antenna$',100,.5,4)
      CALL HEADIN('Tv=30, R0=2.2*pi - WK, LENGTH=60$',100,.5,4)
      CALL HEADIN('RL=0 Ohm, NO CAP, NO RP, TRANS$',100,.5,4)
      CALL VOLM3D(1.,1.,1.)
      CALL X3NAME('Space (cm)$',100)
      CALL Y3NAME('Time (ns)$',100)
      CALL Z3NAME('Current (Amp)$',100)
      CALL XTICKS(5)
      CALL YTICKS(5)
```

```
      CALL ZTICKS(4)
      CALL VUANGL(-150.,45.,25.)
      CALL GRAF3D(0., 5., 30.,0.,.5,2.5,-.08E-3,.08E-3,.24E-3)
      CALL SURMAT(Z1,2, 60,4,300,0)
      CALL ENDPL(0)
      CALL DONEPL
      STOP
1     format(2x,i2,5(1x,d12.4))
C ERROR MESSAGES
2000  WRITE (*,*) 'ERROR: LOOKS LIKE A BUG!'
      STOP
2010  WRITE (*,*) 'ERROR: LPEAK SECTION NEEDS MODIFICATION'
      STOP
      END
      DOUBLE PRECISION FUNCTION PULSE(X,THETA,LENGTH)
C
C  FUNCTION TO DETERMINE THE INCIDENT FIELD
C
      DOUBLE PRECISION X,THETA
      INTEGER LENGTH
      IF ((X.LE.0.D0).OR.(X.GE.200.D0)) THEN
        PULSE = 0.D0
      ELSE
c
c  Gaussian Pulse
c        PULSE = DEXP(-.06D0*(X-50.D0)**2)
c
c  `sinc' Pulse
          IF (X.EQ.75.D0) THEN
                  PULSE=1.D0
                  ELSE
                  PULSE= DSIN(.503D0*(X-75.D0))/(.503D0*(X-75.D0))
          END IF
c
      END IF
      END
      SUBROUTINE BCRNT(A1,A2,EPS1,EPS2,RHO1,RHO2,CONT)
C
C  SUBROUTINE TO CALCULATE FIELD CONTRIBUTIONS FROM
C  BOTTOM WIRE CURRENTS
C
      DOUBLE PRECISION A1,A2,EPS1,EPS2,RHO1,RHO2,CONT,THETA,PSI
      INTEGER I,L
      COMMON I,L,THETA,PSI
      IF (DABS(EPS1-EPS2).LE.1.D-6) THEN
        CONT=0.D0
      ELSE
        CONT=(A2*EPS2/RHO2**2-A1*EPS1/RHO1**2)*DCOS(THETA)/PSI
     1       +(A2/RHO2**2-A1/RHO1**2)*((2*L-1)*DCOS(THETA)-(2*I-1))/PSI
     2       -(DCOS(THETA)/PSI)*((A2-A1)/(RHO2-RHO1))*
     3    DLOG((RHO2+EPS2+(2*L-1)-(2*I-1)*DCOS(THETA)-DSIN(THETA)/PSI)/
     4           (RHO1+EPS1+(2*L-1)-(2*I-1)*DCOS(THETA)-DSIN(THETA)/PSI))
      END IF
      END
```